A thesis submitted to the


**Université Louis Pasteur - Strasbourg I**
Ecole et Observatoire des Sciences de la Terre
UMR7517
**and**
**Charles University in Prague**
Faculty of Science
Institute of Petrology and Structural Geology


**of the requirement for the degree of**
**Doctor of Philosophy in Earth Sciences**
**by**


## Pavlína Hasalová


# Microstructural, petrological and geochemical records of pervasive melt transport in the crust


**Jury** **Defended 18th June 2007 in Strasbourg**

| | | |
|---|---|---|
| Prof. Michael Brown | University of Maryland, USA | External reviewer |
| Dr. Holger Stünitz | University Basel, Switzerland | External reviewer |
| Prof. José Honnorez | Université Louis Pasteur, Strasbourg | Internal reviewer |
| Prof. Lukas Baumgartner | University Lausanne, Switzerland | Member of the Jury |
| Dr. Alain Vauchez | University Montpellier, France | Member of the Jury |
| Prof. Karel Schulmann | Université Louis Pasteur, Strasbourg | Supervisor |
| Dr. Norbert Clauer | Université Louis Pasteur, Strasbourg | Co-supervisor |
| Prof. Wali Shah Faryad | Charles University, Praha | Co-supervisor |

# Acknowledgements

At this place I would like to thank all the people that supported me and helped me during my Ph.D. and without whom this thesis would be impossible to finish. So, thanks a lot.......

Firstly, I would like to thank my supervisor Karel Schulmann for the guidance of this work, for many useful discussions, for inspiration and big patience. Great thanks for the introduction in the „magic migmatite world“ and help in the “transformism” combat. Maybe one day it will come through...... But the most valuable for me was his never ending enthusiasm and friendship to geology that even when everything looked impossible kept me going forward. Thanks for the encouragement in getting the best from me.

Many thanks to my co-supervisors Norbert Clauer who enabled me to stay at ULP Strasbourg and Wali Shah Faryad for the support at the Charles University in Prague.

Special thanks to Ondrej Lexa for many unique discussions about microstructures, for the PolyLX and for his computer advices, without which I would be lost. Next thesis I will surely write in LATEX☺. Pavla Štípská is thanked for introducing me into, and helping me with, the pseudosection modeling and for the goodwill to model open-system processes. Is there any equilibrium? Big appreciation goes to Vojtěch Janoušek, who showed me that the geochemistry is more than interesting.

Next there are all my colleagues and friends from Prague – Monika, Lenka, Honza, Racík, Silva, Maruška, Pavel, Prokop, Maky, Lůca, Zůza, Petr, Stano, Kony, Radka, Eliška, Kryštof, Igor and many others unmentioned but not forgotten. I would like to thank them all for their friendship and nice atmosphere.

I am deeply indebted to all my friends from Strasbourg – Jeremie (ba Voilááááá), Julia, Nicolas, Anne, Benoit, Suzon, Julien, Mohamed, Francis, Etienne, Caroline, Manu, Brice ..................... that made my stay in France a really happy one and let me enjoy the time here. Special thanks to Julia, Jeremie , Nico and Benoit for all the smiles, personal support and the nice lunches. Anne is thanked for her superb English-French translation skills and good mood.

Thanks are due to the technical staff of both institutes, especially R. Boutin for the excellent ICP-MS data, J. Míková and V. Erban for the isotopic data, Z. Veselovský and J. Malec for assistance with separation of the heavy minerals, J. Haloda and P. Týcová for operating the EBSD and G. Morvan for the work on the electron microscope. M. Wontrobová, V. Fojtíková, V. Tolar, C. Nothinsen and D. Zill are thanked for the assistance with all the administration tasks. Big appreciations to B. Kiefer for the amazing library servis.

My special thanks belong to the French gouverment that was financing my stays in Strasbourg within the framework of the Co-tutelle program.

Last, but not least, I would like to thank Mark, my mom, dad and sister Lucie who gave the best support I can imagine and stayed by me during good but also during the bad period of my Ph.D. work. Thanks that you are like you are and that you can let me smile.

This work is dedicated to you.

Pavlína

# Introduction

*"Learn from yesterday, live for today, hope for tommorow.*
*The most important thing is to keep the eyes open and do*
*not stop questioning." (A. Einstein)*

This thesis represents the outcome of detailed field, microstructural, petrological and geochemical studies on two large Variscan migmatitic terranes, the Gföhl Unit of the Moldanubian Zone in the Bohemian Massif (Czech Republic) and inVosges Mts. (France). The resulting data obtained by this multidisciplinary approach are used to constrain the origin of the migmatitic rocks and for better understanding of the melt transport in the crust, within the two chosen field areas, but also as a general approach for fields including migmatites. A new possible model - melt infiltration from an external source is proposed to explain the variations in the migmatite appearance and the 'reactive porous melt flow' for the melt movement on a crustal scale.

The Gföhl migmatite-gneiss complex forms the largest (~ 5000 km$^2$) anatectic unit of the Variscan orogenic root domain. It is situated at the eastern margin of the Bohemian Massif and consists of high-grade orthogneisses showing different degree of migmatitization with minor bodies of granulites, peridotites and amphibolites. The Gföhl Unit offers an exceptional opportunity to study the origin of migmatitic rocks, because it provides the possibility to observe directly in the field, spatial and structural relationships between the migmatites and their granitic protolith but with different proportion of melt. This means that one is able to investigate the gradual changes in macroscopic appearance, microstructures and modal proportions of the rock-forming minerals, together with mineral and whole-rock geochemistry, during the advancing migmatitization.

Based on the detail field and microstructural study **(Chapter 1)** we described four types of migmatites in the studied area: (i) Banded orthogneiss (Type I) with distinctly separated monomineralic layers of recrystallized plagioclase, K-feldspar and quartz separated by distinct layers of biotite; (ii) Stromatic migmatite (Type II) composed of plagioclase and K-feldspar aggregates with subordinate quartz and irregular quartz aggregates. The boundaries between individual aggregates are ill-defined and rather diffuse; (iii) Schlieren migmatite (Type III) consists of plagioclase–quartz and K-feldspar–quartz enriched domains and the foliation is marked only by the preferred orientation of biotite and sillimanite dispersed in the rock; (iv) completely isotropic nebulitic migmatite (Type IV). The results of this thesis shows, that they form a continuous sequence developed by melt-present deformation where the banded orthogneisses and nebulitic migmatites are considered as end-members. The banded orthogneiss ($S_1$ compositional banding) is transposed by $D_2$ deformation to stromatic migmatite containing relicts of $S_1$ banded orthogneiss. The stromatic migmatite gradually passes into more isotropic schlieren migmatite alternating with elongated bodies of nebulitic migmatite.

The destruction of the well-equilibrated banded microstructure and the progressive development of the nebulitic migmatites are characterized by many systematic textural changes. In order to quantify these changes, a quantitative textural study was carried out, including grain size analysis, crystal size distribution (CSD), grain shape and orientation and grain boundary analysis. The quantification was realised using the Arc-View GIS PolyLX extension and the PolyLX Matlab toolbox on the main phases (Plg, Kfs, Qtz and Bt) through the whole sequence. The grain size statistics show a continuous decrease of the grain size coupled with a decrease in standard deviation from the banded orthogneiss towards the nebulitic migmatite. The crystal size distribution (CSD) curves indicate a systematic increase of the nucleation rate and a decrease of the growth rate for all felsic phases towards the isotropic nebulitic migmatite. The new phases preferentially nucleate along high-energy like boundaries causing the development of the regular distribution of individual phases. Simultaneously, the modal proportions of felsic phases evolves towards a “granitic minimum” composition. Moreover, this evolutionary trend is accompanied with the decrease in grain shape preferred orientation (SPO) of all felsic phases. All the mentioned textural changes are in agreement with a progressive heterogeneous nucleation of Pl, Kfs and Qtz from melt associated with the resorption of original phases.

To explain these changes observed in the macroscopic study and in the compositional changes a new model of melt infiltration was developed. It evolves an external source where the melt passes pervasively along the grain boundaries through the whole rock volume and changes its macroscopic and microscopic appearance. It is suggested that the individual migmatite types represent different degree of equilibration between the host rock and the passing melt.

The amount of melt and its connectivity are critical parameters controlling the melt mobility and the rheological behaviour of partially molten rocks. In order to constrain these parameters in studied migmatites, the anisotropy of magnetic susceptibility (AMS) and EBSD methods were used. The melt topology in Type I orthogneiss exhibit elongated pockets of melt oriented at a high angle to the compositional banding. It indicates that the melt distribution was controlled by the deformation of the solid framework. Here, the microstructure exhibit features compatible with the combination of dislocation creep and grain boundary sliding deformation mechanisms. The Type II – IV microstructures were developped by granular flow accompanied by a melt-enhanced diffusion and/or direct melt flow. However, the amount of melt present in the rock never exceeded the critical threshold during the deformation to allow free rotation of the biotite grains.

In **Chapter 2** we discuss the petrological aspects of the transition from banded orthogneiss into the nebulitic migmatite. The purpose is to try to understand what sort of fluid could have participated in the mineralogical and whole-rock geochemical evolution, and what could have been its composition, as well as how it may have interacted with the original rock.

The assemblage in the studied sequence is a garnet–biotite–sillimanite–K-feldspar–plagioclase–quartz without muscovite implying that the involved fluid is a granitic melt. The mineral compositions exhibit systematic changes with an increasing degree of disintegration (e.g. increase of $X_{Fe}$ in garnet and biotite, decrease of Ca in plagioclase). This is compatible with the decrease in equilibration temperature and pressure from 790–850°C at 7.5 kbar for a banded orthogneiss to 690–770°C at 4.5 kbar for the nebulitic migmatite (THERMOCALC modelling). The changes in the whole rock analyses indicate open system behaviour interpreted as a result of melt percolation along the grain boundaries. In order to change significantly the whole rock composition a large quantity of melt must have passed through the rocks.

We argue that the studied migmatites did not lose their banded texture due to a high in situ production of melt as it is described in the literature for the majority of metasedimentary diatexites. On the contrary, the arguments presented support the idea that the reactive porous melt flow was responsible for the formation of these migmatites. Additionally, the *P–T* calculations showed that the infiltrating melt equilibrated with the host rock during the retrograde branch of the *P–T* path, i.e. during the exhumation of the Gföhl gneiss complex from the lower crust.

The geochemical section **(Chapter 3)** describes the major- and trace-element as well as Sr-Nd isotopic whole-rock geochemical variation in the individual gneiss and migmatite types. While each of the types shows a distinct geochemical and Sr–Nd isotopic fingerprint, the whole sequence evolves along a regular, and more or less smooth trends in most of the elements. This evolution is in agreement with the proposed melt infiltration process, penetrated by felsic melt derived from an external source. The melt infiltration was modelled as an open-system process, characterised by the changes of the total mass/volume, accompanied by gains/losses in many of the major- and trace-elements. The numerical modelling of the mass balance resulted in identification of a component added by an heterogeneous nucleation of feldspars, quartz and apatite from the passing melt. At the most advanced stages, the chemical variations in the schlieren and nebulitic migmatite require an increasing role for fractional crystallization of the K-feldspar and plagioclase, with accessory amounts of Th-rich monazite ± apatite.

Compiling all the obtained informations it is demonstrated that the sequence of various types of the Gföhl gneisses/migmatites can be interpreted by a process in which, the banded orthogneiss was pervasively, along grain boundaries, penetrated by felsic melt derived from an external source. Such a process of a large melt volume penetrating through rocks at the grain scale without any important signs of segregation and "channelization" may be an important mechanism for the melt transport in a migmatitic crust. As the Gföhl gneiss represents a significant portion of the orogenic root, this process through the lower crust would be a crucial for crustal differentiation, but also for crustal rheology during orogenic events.

**Chapter 4** is a additional chapter, where interesting microstructural, field, AMS and numerical data from migmatities of Vosges Mts. are presented. In this work I have contributed with the microstructural study. I tryed to evaluate textures of the studied migmatites, melt appearance and degree of the melt–rock interaction. The most importante are the estimates of melt percetages, that are discussed together with the AMS data.

This study shows the complex behaviour of solid state rocks and granitic melts in a fertile region of magma segregation. It can be seen, that the pervasive viscous flow in these domains is strongly dependent on the lithology, i.e., mechanical properties of rocks during melting and their pre-melting anisotropy. The diatexites and granites show a very weak degree of anisotropy and a highly variable ellipsoid shapes which may reflect the undisturbed rotation of careers of magnetic anisotropy (biotite) in the freely moving melts. In contrast, rocks with strong pre-RCMP anisotropy and low ability to melt are behaving as rigid bodies. Their behaviour also depends on the amount of granitic liquid. In regions with low amount of melts, the magma is ascending along the main anisotropy in the form of sills. In domains where the magma proportion is high, these lithologies behave as rigid sheet-like bodies passively rotating towards the direction of the flow. Therefore, a correlation between melt proportion and AMS pattern was observed. The low proportion of melt is characterized by the preservation of the homogeneous AMS fabric of the solid state network at high angle to the fabric pattern of the magma flow. In contrast, high melt proportion is identified in the rocks by the disintegration of pre-melting fabric elements and their progressive reorientation towards the directions of main magma flow. Such information allows to estimate the mechanical threshold when the rigid framework is still present and when it becomes disintegrated in viscous magma flow. Such mechanical threshold may be considered an indirect expression of the rheological critical melt percentage or melt escape threshold.

# Contents

## Origin of migmatites by deformation enhanced melt infiltration of orthogneiss: a new model based on quantitative microstructural analysis

## Transforming mylonitic metagranite by open-system interactions during melt flow

## From orthogneiss to migmatite: geochemical assessment of the melt infiltration model in the Gföhl Unit (Moldanubian Zone, Bohemian Massif)



## Influence of mechanical anisotropy and melt proportion on recurrent brittle and ductile response of partially molten crust exemplified by structural and AMS study, Central Vosges, France

# CHAPTER I:

## Origin of migmatites by deformation enhanced melt infiltration of orthogneiss: a new model based on quantitative microstructural analysis

Accepted to Journal of Metamorphic Geology

# Origin of migmatites by deformation enhanced melt infiltration of orthogneiss: a new model based on quantitative microstructural analysis

*Pavlína Hasalová [1,2], Karel Schulmann [1], Ondrej Lexa [1,2] , Pavla Štípská [1],*

*František Hrouda [2,3] , Stanislav Ulrich [2,4], Jakub Haloda [5] and Patrýcie Týcová [5]*

[1] Université Louis Pasteur, CGS/EOST, UMR 7517, 1 rue Blessig, Strasbourg, 670 84, France

[2] Institute of Petrology and Structural Geology, Charles University, Albertov 6, 128 43, Prague, Czech Republic

[3] AGICO, Ječná 29a, 621 00, Brno, Czech Republic

[4] Institute of Geophysics, Czech Academy of Sciences, Boční II/1401, 141 31 Praha 4, Czech Republic

[5] Czech Geological Survey, Klárov 3, 118 21 Prague 1, Czech Republic

## Abstract

A detailed field study reveals a gradual transition from high-grade solid state banded orthogneiss via stromatic migmatite and schlieren migmatite to irregular, foliation-parallel bodies of nebulitic migmatite within the eastern part of the Gföhl Unit (Moldanubian domain, Bohemian Massif). The orthogneiss to nebulitic migmatite sequence is characterized by progressive destruction of well-equilibrated banded microstructure by crystallization of new interstitial phases (Kfs, Pl and Qtz) along feldspar boundaries and by resorption of relict feldspars and biotite. The grain size of all felsic phases decreases continuously, whereas the population density of new phases increases. The new phases preferentially nucleate along high-energy like–like boundaries causing the development of a regular distribution of individual phases. This evolutionary trend is accompanied by a decrease in grain shape preferred orientation (SPO) of all felsic phases. To explain these data, we propose a new petrogenetic model for the origin of felsic migmatites by melt infiltration from an external source into banded orthogneiss during deformation. In this model, infiltrating melt passes pervasively along grain boundaries through the whole rock volume and changes completely its macro- and microscopic appearance. It is suggested that the individual migmatite types represent different degrees of equilibration between the host rock and migrating melt during exhumation. The melt topology mimicked by feldspar in banded orthogneiss forms elongate pockets oriented at a high angle to the compositional banding, indicating that the melt distribution was controlled by the deformation of the solid framework. The microstructure exhibits features compatible with a combination of dislocation creep and grain boundary sliding deformation mechanisms. The migmatite microstructures developed by granular flow accompanied by melt-enhanced diffusion and/or melt flow. However, an AMS study and quartz microfabrics suggest that the amount of melt present did not exceed a critical threshold during the deformation to allow free movements of grains.

**Keywords:** crystal size distribution, melt infiltration, melt topology, migmatites, quantitative textural analysis

## Introduction

Movement of a large volume of granitic melt is an important factor in the compositional differentiation of the continental crust (Fyfe, 1973; Collins & Sawyer, 1996; Brown & Rushmer, 2006) and the presence of melt in rocks profoundly influences their rheology (Arzi, 1978). The migration of melt through the crust is controlled by melt buoyancy and pressure gradients resulting from the combination of gravity forces and deformation (Wickham, 1987; Sawyer, 1994). There are three major mechanisms controlling melt migration through the continental crust: (i) diapirism resulting in upward motion of low-density magma through higher density rocks (Chandrasekhar, 1961; Ramberg, 1981), (ii) dyking that describes melt migration by hydrofracturing of the host rock and transport of melt through narrow dykes (Lister & Kerr, 1991; Petford, 1995), (iii) and migration of a melt through a network of interconnected pores during deformation or compaction of solid matrix (McKenzie, 1984; Wickham, 1987). Brown & Solar (1998a) and Weinberg & Searle (1998) proposed that during active deformation melt moves by pervasive flow and it is essentially pumped through the system parallel to the principal finite elongation in the form of foliation parallel veins. Based on a number of field studies, pervasive melt migration at outcrop scale controlled by regional deformation has been suggested byvarious authors (Collins & Sawyer, 1996; Brown & Solar, 1998b; Vanderhaeghe, 1999; Marchildon & Brown, 2003). These authors argued that magma intrudes pervasively, parallel to the main anisotropy represented by foliation planes (John & Stünitz, 1997), fold hinges and interboudin partitions(Brown, 1994; Brown et al., 1995). It is also commonly observed that vein-like leucosomes are injected into extensional structures provided the magma pressure is high enough (Wickham, 1987; Lucas & St.Onge, 1995) or parallel to axial surfaces of folds (Vernon & Paterson, 2001).

Microscopic studies of natural rocks show orientations of former melt microstructures that are interpreted in terms of grain scale channel networks (Sawyer, 2001). Melt migration pathways at the grain-scale are commonly determined from distribution of melt films and pools (now glass) in experimentally prepared samples or by distribution of mineral phases supposed to preserve the original melt topology in natural rocks (Brown *et al.*, 1999; Rosenberg & Riller, 2000; Rosenberg, 2001). The melt topology in experiments is controlled mainly by differential stress, confining pressure and the amount of melt in the system (Rosenberg, 2001). At static conditions, the melt topology is characterized by equilibrium dihedral (wetting) angles at triple point junctions (Jurewicz & Watson, 1984; Laporte & Watson, 1995; Laporte *et al.*, 1997; Cmíral *et al.*, 1998; Walte *et al.*, 2003) and the mobility of the melt remains very low, even if the melt phase forms an interconnected network along triple-junction grain edges at dihedral angles lower than 60° (Laporte & Watson, 1995; Connolly *et al.*, 1997).

Experimental studies on rock analogues to investigate grain-scale melt flow under laboratory conditions show that during contemporaneous melting and deformation melt connection allows the nucleation of shear bands along which a melt is further segregated (Rosenberg & Handy, 2000, 2001; Barraud *et al.*, 2001). Rosenberg (2001) reviewed the experimental data and concluded that the melt migration and melt flow direction are controlled by incremental shortening and melt pressure gradients between source and areas of melt accumulation.

There have only been a few attempts to quantify melt distribution in rocks using methods of quantitative and computer aided microstructural analysis (Dallain *et al.*, 1999; Tanner, 1999; Marchildon & Brown, 2003). These studies commonly deal with grain contact frequency distributions, grain size evolution and orientation of former melt films (McLellan, 1983; Dougan, 1983; Rosenberg & Riller, 2000). However, modern quantitative microstructural analysis may provide further important information about: (i) reorganization of the rock structure associated with melt migration in terms of grain contact distributions (Lexa *et al.*, 2005); (ii) characterization of dynamic or static conditions of melt movement through rocks using analysis of grain boundaries and shape orientations (Rosenberg & Riller, 2000; Marchildon & Brown, 2002); and (iii) cooling or heating histories of rocks using crystal size distribution theory (Higgins, 1998; Berger & Roselle, 2001).

In this work, we study a sequence of deformed felsic rocks ranging from high-grade banded orthogneiss to fine-grained isotropic migmatite both at macro- and microscale using structural, petrographic and quantitative microstructural analyses. We show that a sequence of banded orthogneiss, stromatic, schlieren and nebulitic migmatites results from progressive deformation in a crustal-scale shear zone in the presence of melt. The microstructural and fabric modifications connected with disintegration of parental banded orthogneiss and development of random mineral microstructure are quantified. We discuss the relationships of the individual rocks types and the possible origin of this sequence in terms of deformation and migmatization of different protoliths, melt infiltration from an external source or *in-situ* melting of the same protolith during progressive deformation. We argue that banded orthogneiss and nebulitic migmatites can be interpreted as end members of a continuous sequence resulting from melt infiltration from an external source during deformation. Finally, we discuss the role of melt for activity of grain scale deformation mechanisms and bulk rheological behaviour of crustal rocks during melt infiltration.

## Geological setting

The Moldanubian zone represents the highest-grade unit of the Bohemian Massif and is interpreted as an internal zone of the Variscan orogen developed during the Variscan convergence (Matte *et al.*, 1990). The Moldanubian zone is comprised essentially of high-grade gneisses and migmatites containing relicts of high-pressure felsic granulites, eclogites and peridotites that are intercalated with mid-crustal rocks (Fig. 1a). Schulmann *et al.* (2005) described the structural and metamorphic evolution of high-grade crustal rocks of the so-called Gföhl Unit and of the adjacent middle crustal units. For the mechanism of exhumation, they proposed a model of vertical extrusion of orogenic lower crust and its lateral spreading in mid-crustal levels due to an indentation of the easterly Brunia promontory. As a consequence of this process, the high-pressure rocks were thrust over adjacent middle crustal units in conjunction with retrogression of original mineral assemblages and partial melting of all the rock types (Štípská *et al.*, 2004).

The onset of the exhumation process is dated by zircon U–Pb ages of *ca.* 340 Ma on felsic granulites, migmatites and mantle-derived syn-tectonically emplaced plutons (van Breemen *et al.*, 1982; Kröner *et al.*, 1988; Holub *et al.*, 1997; Schulmann *et al.,* 2005). Tajcmanová *et al.* (2006) assigned metamorphic conditions of 840°C at 18–19 kbar and 760–790°C at 10–13 kbar to relict steep granulitic fabrics which originated by vertical extrusion of lower crust. These authors also estimated the conditions of re-equilibration of granulites associated with horizontal spreading stage to 720–770°C and 4–4.5 kbar. High pressure rocks of the Gföhl Unit are accompanied by large bodies of biotite–sillimanite Gföhl orthogneiss spatially associated with K-feldspar–sillimanite paragneisses and leucocratic migmatites for which *P-T* conditions of 7–10 kbar and 750°C were estimated by Racek *et al.* (2006).

The area of this study is located at the easternmost termination of the Gföhl Unit (Fig. 1a). The main rock type is represented by the Gföhl orthogneiss with protolith ages 488 ± 6 Ma (U–Pb SHRIMP: Friedl *et al.*, 2004) including small bodies of amphibolite, granulite, eclogite, ultrabasic rock and paragneiss. The Gföhl orthogneiss shows different stages of migmatization characterized by the assemblage of Kfs + Pl + Qtz + Bt ± Grt ± Sill. This migmatized orthogneiss complex is heterogeneously deformed by top to the NE shearing along a large-scale, gently-dipping shear zone (Schulmann *et al.*, 1994). Consequently, the northern margin of this complex is thrust over a footwall comprised of the Náměšt granulite body and Neoproterozoic metagranites of the northeastern continental margin (Urban, 1992).

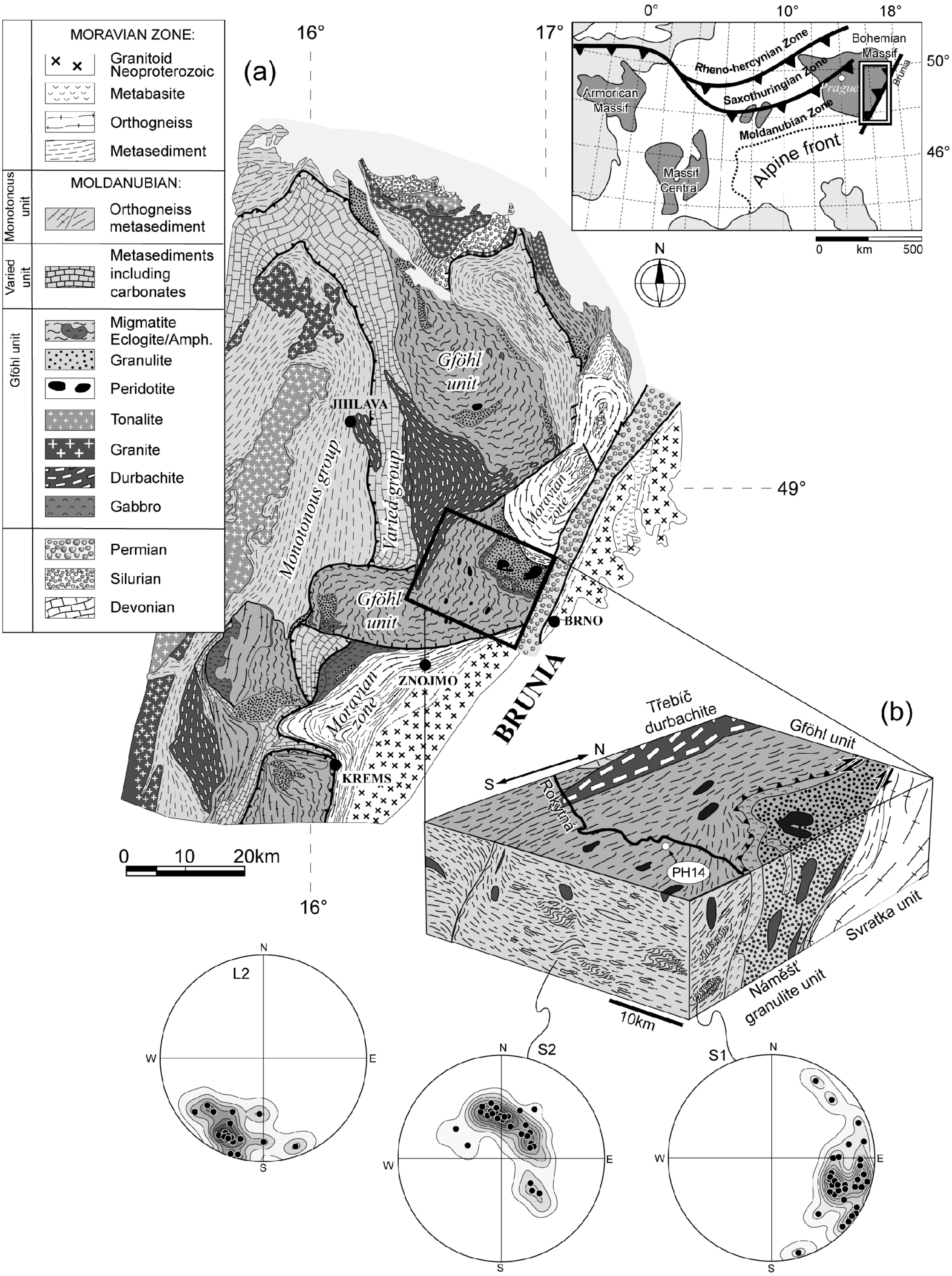


**Fig. 1:** *(a) Geological map of the eastern margin of the Bohemian Massif (modified after Schulmann et al., 2005) with the location of the study area (black rectangle). The upper right inset shows the general location of the Bohemian Massif within the European Variscides. (b) Schematic block diagram displaying the main structural features in the study area (modified after Schulmann et al., 2005). Dominant $S_1$ and $S_2$ fabrics with their orientations are shown. This block diagram is not vertically scaled.*

## Structural evolution

### *Mesoscopic structures*

Two major deformation events are recognized. The first event ($D_1$) is represented by a steep, west-dipping high-grade foliation $S_1$ (Fig. 1b). This fabric is preserved in banded orthogneisses (Type I), as an alternation of recrystallized monomineralic K-feldspar, plagioclase and quartz layers, separated by bands of biotite ± sillimanite (Fig. 2a). Lineation $L_1$ is locally marked by alignment of biotite, sillimanite and by elongation of quartz and feldspar aggregates. This deformation is attributed to an early stage of exhumation of the lower crust along a vertical channel during horizontal shortening of the thickened orogenic root (Schulmann *et al.*, 2005).

The second deformation ($D_2$) is associated with reworking and folding of the $S_1$ compositional layering in banded orthogneiss, so that $S_1$ is only preserved locally in elongate relict domains (Fig. 2a). The $D_2$ shearing is attributed to horizontal flow of hot lower crust in a zone up to ten kilometers wide at a mid-crustal level above the Brunia promontory over distances of several tens of kilometers (Schulmann *et al.*, 2005). Relic domains with gently folded $S_1$ fabric are surrounded by highly deformed zones with tightly folded $S_1$ fabric (Fig. 2). The composite $S_{1\text{–}2}$ fabric is characterized by a banded structure with diffuse boundaries between polymineralic K-feldspar- and plagioclase-rich domains similar to a stromatic migmatite structure (Type II) (Fig. 2b). Locally the $S_1$ fabric is completely transposed and a new $S_2$ foliation is dipping gently to the SW (Fig. 1b). A sub-horizontal, gently S-SW plunging $L_2$ lineation (Fig. 1b) is mostly defined by preferred orientation of sillimanite.

Detailed field observations reveal that with ongoing deformation the Type II rock gradually pass into more isotropic rock (Type III) composed of K-feldspar–quartz and plagioclase–quartz aggregates (Fig. 2c) and containing rootless folds of the deformed $S_1$ fabric. This rock type alternates with irregular bodies or elongate lenses of fine-grained isotropic felsic rock (Type IV, Fig. 2d), which in this region traditionally has been described as a nebulitic migmatite (Matějovská, 1974). Such a structural sequence originated through intense $D_2$ deformation superimposed on an older steep anisotropy and was identified in outcrop scale along several sections. These observations are supported by the existence of macroscopically visible leucosomes or granitic veins that are also parallel to $S_2$ and form isolated elongate pockets and lock-up shear bands.

This area has been extensively studied by Matějovská (1974) and Dudek *et al.* (1974) who used the classical migmatite terminology of Mehnert (1971) for above described rock types. These authors identified Type I rock as banded orthogneiss, rock Type II as stromatic migmatite and rock Type IV as nebulitic migmatite. Rock Type III resembles the schlieren migmatite of Mehnert (1971). Because the Gföhl Unit is considered as one of the largest migmatitic terrains of the Variscan belt, we adapt the traditional migmatite terminology to our rocks.

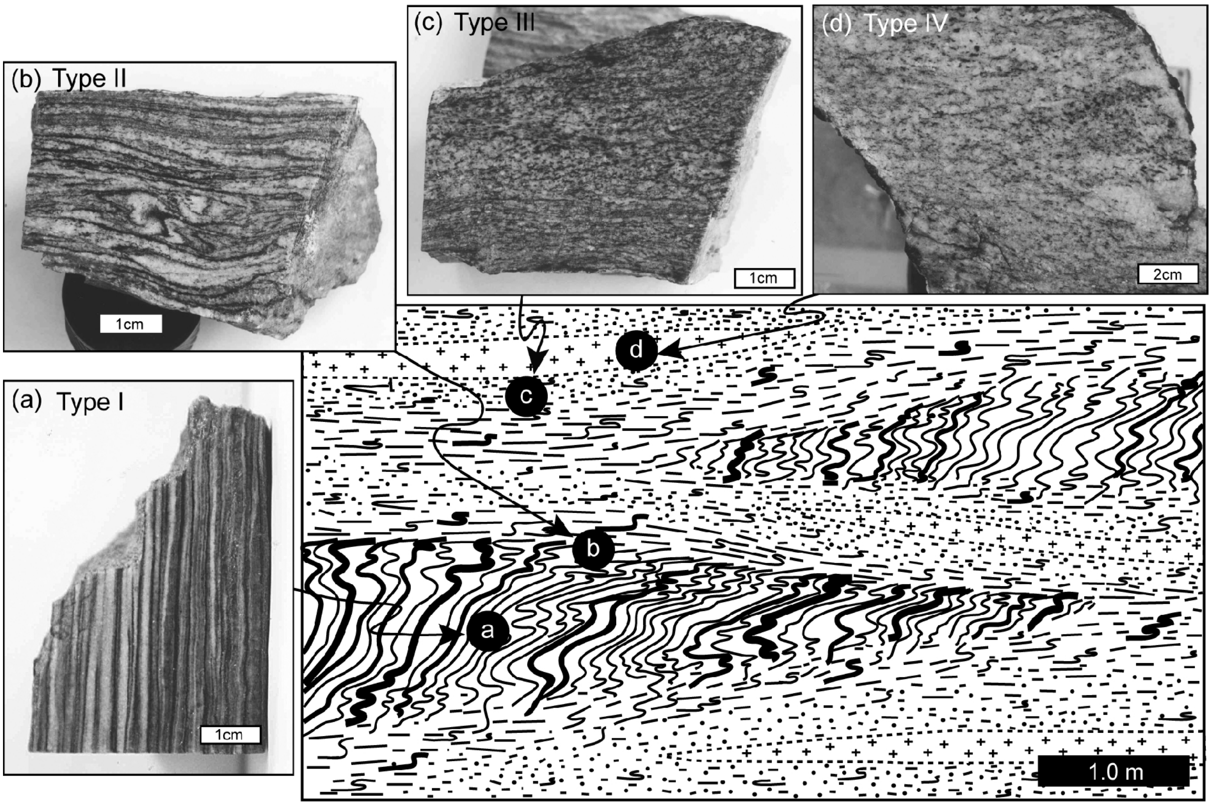


**Fig. 2:** *Schematic representation of the rock relationships at an outcrop scale and photographs of the individual rock types. (a) Banded orthogneiss (Type I); (b) stromatic migmatite (Type II); (c) schlieren migmatite (Type III); and (d) nebulitic migmatite (Type IV). The position of this outcrop in the study area is shown in Fig. 1b.*

## Microstructural observations

The microstructural characteristics including grain size, grain shape and grain boundary geometry were studied in each of the four rock types and in K-feldspar- and plagioclase-rich domains. Thin sections were cut perpendicular to the foliation and parallel to $L_2$ lineation (XZ section). In order to discriminate K-feldspar from plagioclase, the thin sections were stained according to the method of Bailey & Stevens (1960).

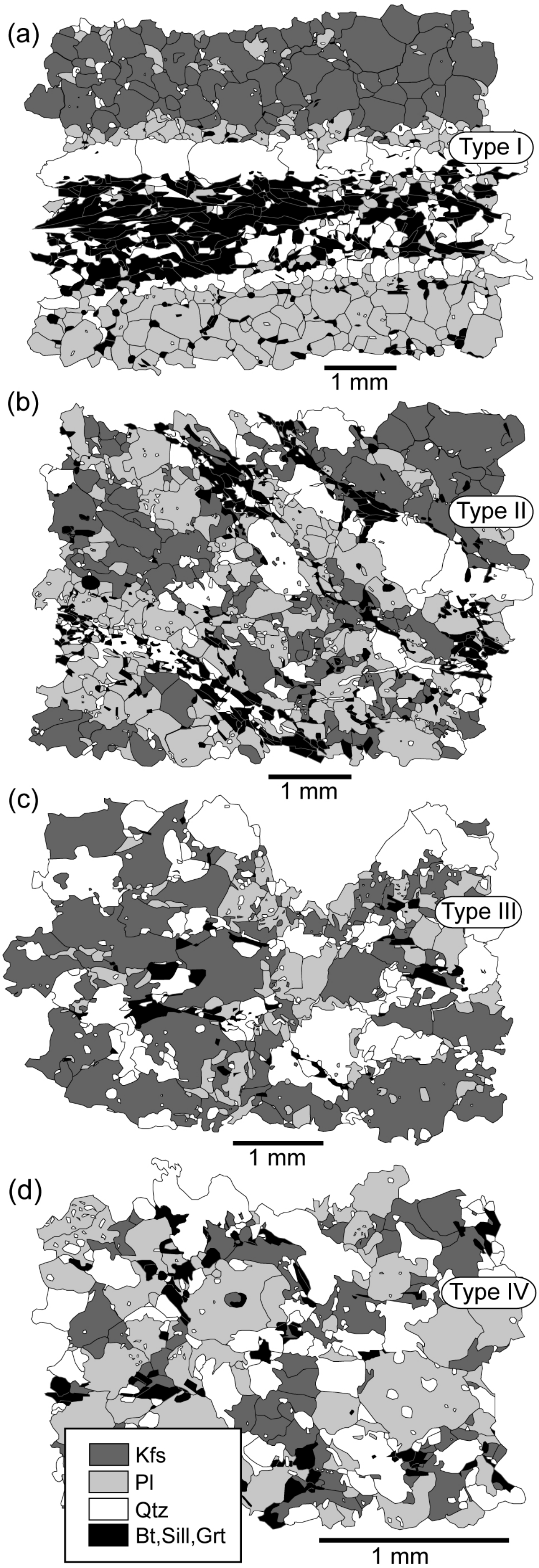


### *Type I: Banded orthogneiss*

This rock type is a fine-grained orthogneiss with 0.25-2.0 mm thick layers of recrystallized plagioclase (30 modal %), K-feldspar (40 modal %) and quartz (20 modal %), separated by discrete layers of biotite (10 modal %) commonly associated with minor sillimanite and garnet (Table 1, Fig. 3a).

K-feldspar forms completely recrystallized aggregates (0.2-0.8 mm grain size) with straight grain boundaries locally meeting in triple point junctions at 120° (Fig. 4a). Numerous rounded inclusions of quartz (0.05 mm) occur preferentially at triple points, along planar boundaries or in cores of feldspar (Fig. 4a). Plagioclase ($An_{10-20}$) is present in K-feldspar aggregates as small interstitial grains or forms thin films preferentially tracing those K-feldspar boundaries that

**Fig. 3:** *Representative digitalized microstructures (X-Z sections) for individual textural types (note differences in scales when making comparisons). (a) Banded orthogneiss (Type I) with distinct monomineralic layers composed of a polygonal mosaic of well-equilibrated plagioclase, K-feldspar and quartz polycrystalline ribbons separated by discrete layers of biotite ± sillimanite ± garnet (sample PH60/B). (b) Stromatic migmatite (Type II) composed of K-feldspar-rich, plagioclase-rich and quartz-rich aggregates separated by relicts of biotite ± sillimanite-rich layers (sample PH60/A). (c) Schlieren migmatite (Type III) showing alternation of K-feldspar- and plagioclase-rich domains interpreted to correspond to an original spatial distribution (K-feldspar domain is shown, sample PH90). (d) Isotropic nebulitic migmatite without any gneissosity (Type IV) composed of equal amounts of K-feldspar, plagioclase and quartz (sample PH59/D).*

are oriented at a high angle to the foliation (Fig. 5a). Rarely, tiny interstitial biotite is present in the K-feldspar-rich bands.

Plagioclase aggregates (0.2-0.5 mm) are composed of an equidimensional polygonal mosaic with straight boundaries, and minor interstitial quartz and biotite (Fig. 4b). The plagioclase grains show abundant twinning and form a foam-like texture with a perfect triple point network of grain boundaries. Plagioclase exhibits normal zoning with homogeneous oligoclase cores ($An_{24–28}$) and more sodic ($An_{10–18}$), clear, 2-10 μm thick rims at boundaries with K-feldspar. Plagioclase grain size continuously decreases from the centre of an aggregate towards its borders. Quartz occurs as small (0.01-0.05 mm) rounded inclusions or interstitial grains whereas K-feldspar exhibits characteristic cuspate shapes (Fig. 5b). Tiny biotite grains (0.1-0.5 mm in length; $X_{Fe}$ = 0.42–0.48, Ti = 0.2–0.27 p.f.u.) commonly occur along the plagioclase boundaries that are sub-parallel to the foliation (Fig. 3a).

Quartz ribbons 0.3-1.0 mm wide are composed of elongate grains with straight grain boundaries perpendicular to the ribbon margin (Fig. 3a). Quartz–feldspar boundaries are gently curved, with cusps that point from feldspar to quartz. Biotite-rich layers commonly show decussate microstructure , which is a textural equivalent of the foam-like texture of the felsic minerals (Vernon, 1976). Contacts between biotite - and plagioclase -rich layers are marked by numerous (< 1 modal %) small idiomorphic garnets (0.05-0.10 mm in size; $X_{Fe}$ = 0.77–0.85).

### *Type II: Stromatic migmatite*

This rock type is composed of plagioclase- and K-feldspar-rich aggregates with subordinate quartz and irregular quartz aggregates (Fig. 3b); modes are given in Table 1. These aggregates are rimmed by relicts of biotite-rich layers commonly intergrown with fibrolitic sillimanite. The ill-defined and rather diffuse boundaries between individual aggregates are characteristic for this textural type (Fig. 3b).

K-feldspar-rich aggregates (0.2-0.8 mm grain size) include abundant small interstitial plagioclase ($An_{17–20}$ in the core and $An_{4–10}$ at the rim) and quartz. K-feldspar forms irregular grains with lobate boundaries. Most of the K-feldspar grain boundaries are decorated by thin interstitial plagioclase ($An_{6–8}$). Quartz is present as inclusions (0.01-0.06 mm) in K-feldspar or forms irregular grains (0.1-0.2 mm) along the K-feldspar boundaries. In plagioclase-rich aggregates (0.1-0.3 mm grain size, $An_{17–20}$), plagioclase grains have straight to lobate boundaries whereas irregularly distributed interstitial quartz has irregular shapes. Similar to the Type I orthogneiss, interstitial K-feldspar shows cuspate shapes.

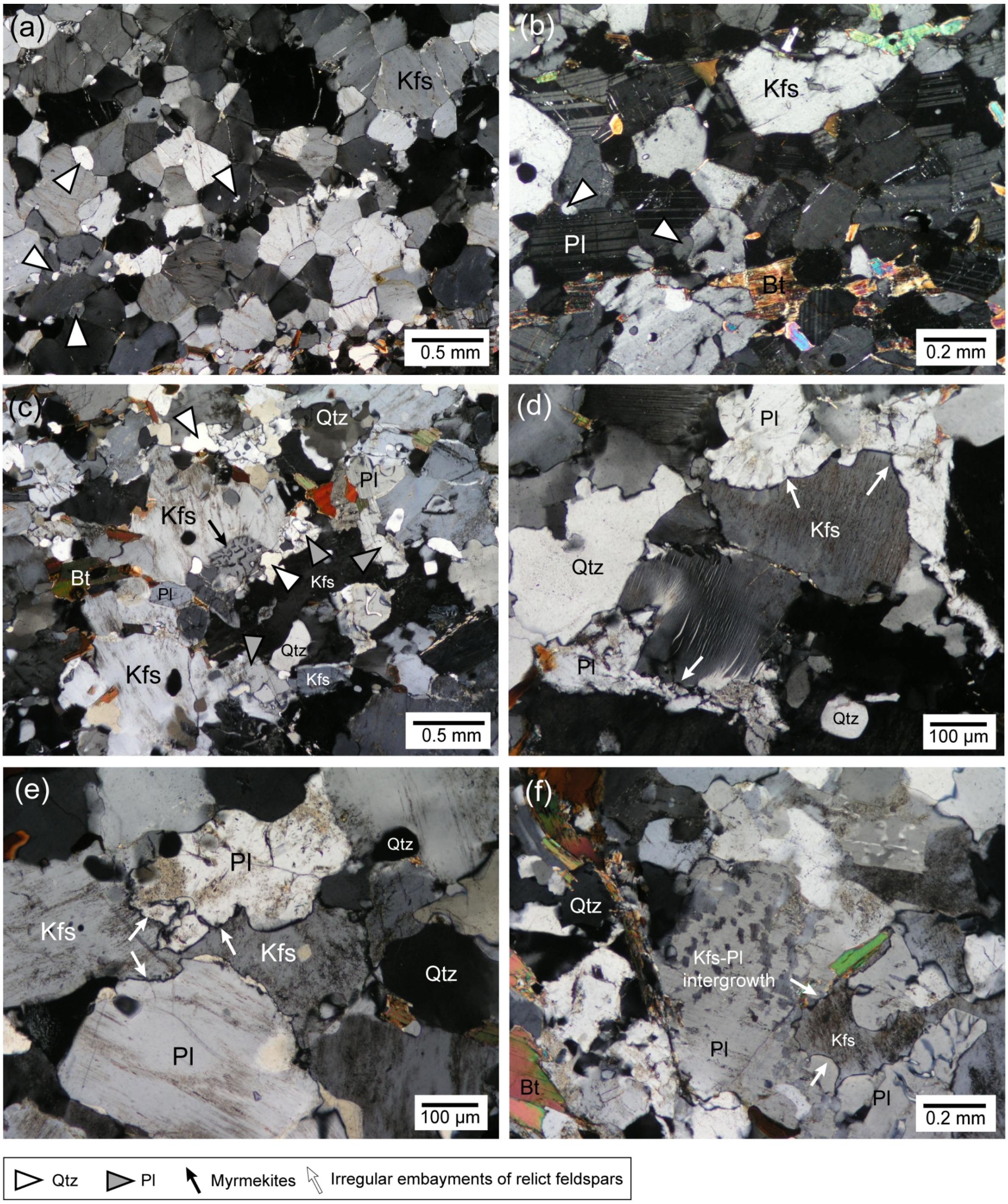


**Fig. 4:** *Photomicrographs showing characteristic textures of the rock sequence (note differences in scales when making comparisons). (a) Type I banded orthogneiss: recrystallized K-feldspar aggregate with straight grain boundaries and numerous smaller rounded quartz grains (white triangles) along the boundaries or in the cores of feldspars (sample PH60/B). (b) Type I banded orthogneiss: well-developed plagioclase polygonal foam-like texture with straight grain boundaries, interstitial quartz (white triangles) and biotite (sample PH60/B). (c) Type III schlieren migmatite: typical microstructure with irregularly shaped feldspar and quartz grains with highly lobate boundaries. Myrmekitic aggregates commonly develop along the K-feldspar boundaries (black arrow). New small interstitial plagioclase (grey triangles), K-feldspar and quartz (white triangles) grains trace almost all the relict feldspar boundaries. Interstitial quartz forms preferentially rounded shapes different from plagioclase which forms thin elongated grains/films coating K-feldspar boundaries (sample PH90). Such a microstructure is typical also for the Type IV. (d) Type III schlieren migmatite: irregular cuspate K-feldspar grain embayed with newly crystallized quartz and plagioclase (sample PH90). (e) Type IV nebulitic migmatite: corroded relics of K-feldspar grains (sample PH59/D). (f) Type III nebulitic migmatite: plagioclase-K-feldspar intergrowths embaying relict K-feldspar grain (sample PH14/D). White arrows in (d), (e) and (f) point to irregular embayments of relict K-feldspar originated through resorption of old K-feldspar grains by newly crystallized material.*

Biotite (15 modal %; $X_{Fe}$ = 0.55–0.59, Ti = 0.18–0.26 p.f.u) is variable in size and appears along plagioclase boundaries mostly parallel to the foliation (Fig. 3b). Small idiomorphic garnet (0.07-0.2 mm in size; $X_{Fe}$ = 0.84–0.91) occurs in the plagioclase-rich aggregates and biotite-rich layers.

### *Type III: Schlieren migmatite*

This textural type does not show macroscopically-visible feldspar-rich aggregates, but stained thin sections reveal the presence of plagioclase–quartz and K-feldspar–quartz-enriched domains (Fig. 3c); modes are given in Table 1. The foliation is marked by preferred orientation of biotite and sillimanite dispersed in the rock.

K-feldspar forms large irregularly-shaped grains (0.1-0.3 mm in size) (Fig. 3c & Fig. 4c) or small cuspate grains along plagioclase boundaries. The most characteristic feature is the presence of irregular embayments of quartz and plagioclase in the K-feldspar grains (Fig. 4d). Myrmekitic aggregates are commonly developed along the K-feldspar boundaries (Fig. 4c). Plagioclase occurs as large irregular twinned grains ($An_{12–16}$ in the core, $An_{2–4}$ at the rim) and as films ($An_{1–4}$) lining the K-feldspar boundaries (Fig. 5c). Entirely dispersed quartz forms large relict grains (0.7-1.0 mm) with undulatory extinction and highly lobate boundaries, abundant irregular interstitial grains lining the K-feldspar boundaries and rounded inclusions (0.02-0.05 mm) in K-feldspar and plagioclase (Fig. 4c). Biotite (10–15modal %; $X_{Fe}$ = 0.76–0.79, Ti = 0.18–0.19 p.f.u.) is homogeneously dispersed and is most prevalent in the plagioclase–quartz domains. Atoll-shaped garnet (0.05-0.25 mm in size; $X_{Fe}$ = 0.96–0.97) appears inside the felsic aggregates, rather than along contacts with biotite.

### *Type IV: Nebulitic migmatite*

This type of rock is composed of almost equal amount of plagioclase, K-feldspar and quartz, and contains minor biotite ($X_{Fe}$ = 0.91–0.93, Ti = 0.01–0.04 p.f.u.), sillimanite and garnet ($X_{Fe}$ = 0.98–1.00) (Fig. 3d), with a weakly developed preferred orientation of the biotite and sillimanite; modes are given in Table 1. K-feldspar (0.10-0.25 mm in size) occurs in the form of irregular grains embayed with quartz and plagioclase. Commonly, the intensity of quartz and plagioclase lobes correlates well with highly cuspate irregular forms of corroded relics of K-feldspar (Fig. 4e). Similarly, the relics of irregular plagioclase (0.05-0.15 mm in size; $An_{6–10}$ in the core and $An_{0–4}$ at the rim) show cuspate boundaries, but with curvature less pronounced than that of the corroded relics of K-feldspar grains. An important feature is the presence of new plagioclase ($An_{0-1}$)–K-feldspar intergrowths embaying corroded relics of K-feldspar grains (Fig. 4f). Quartz (0.04-0.07 mm) with highly lobate boundaries is uniformly distributed in the rock. Biotite of low aspect ratio shows highly corroded cuspate forms filled with quartz, K-feldspar and plagioclase.

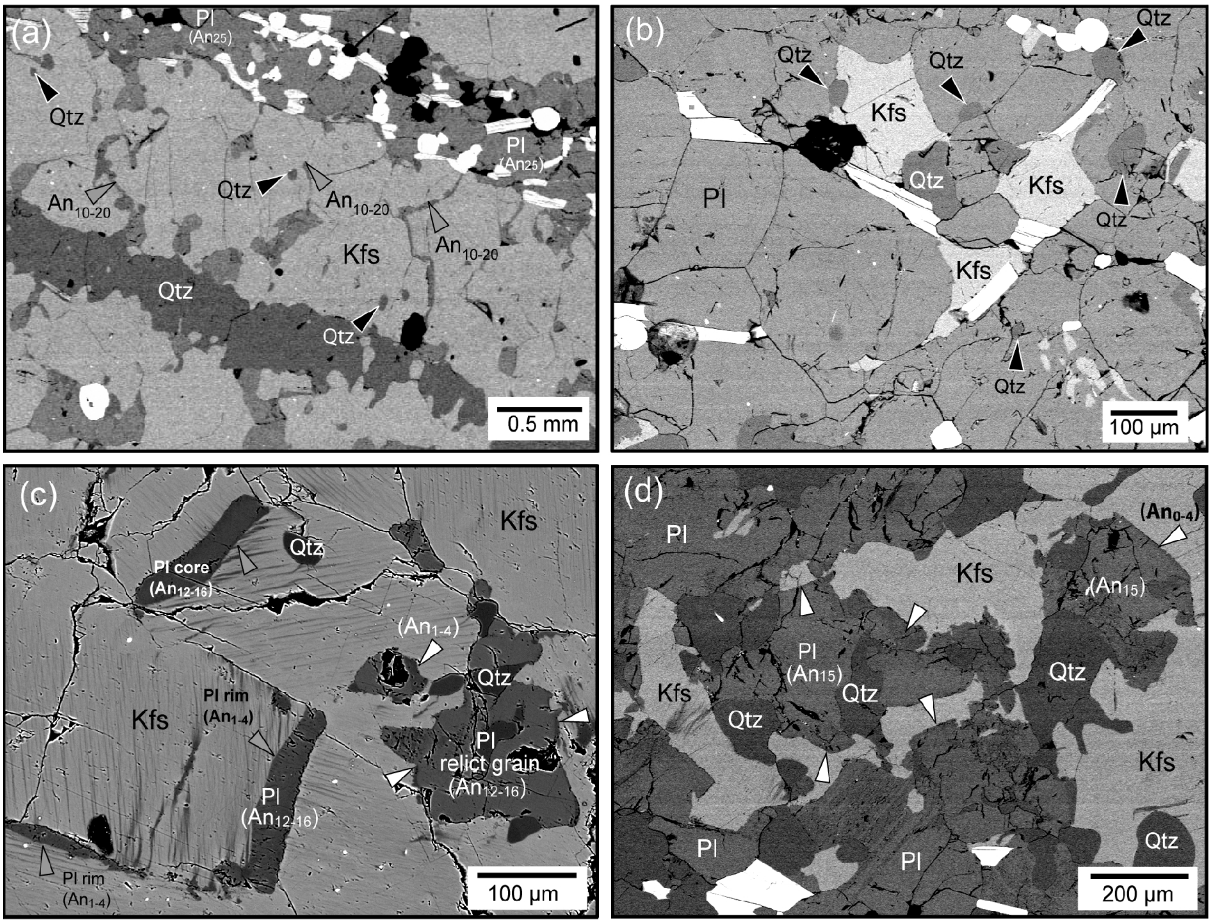


**Fig. 5:** *SEM backscatter images showing the inferred former melt topology (note differences in scales when making comparisons). (a) Type I banded orthogneiss: interstitial plagioclase ($An_{10-20}$), representing the plagioclase component crystallized from the anatectic melt (grey arrow), tracing the K-feldspar boundaries sub-perpendicular to the foliation (sample PH60/B). Black arrows show small rounded quartz grains crystallized along feldspar boundaries. (b) Type I banded orthogneiss: inferred former melt pools with cuspate margins in a plagioclase band (sample PH60/B). The former melt has crystallized to K-feldspar (cuspate melt pools), plagioclase (growing on the old plagioclase grains) and quartz (forming small rounded grains along the feldspar boundaries (black arrow)). (c) Type III schlieren migmatite: more developed interstitial plagioclase (grey arrow) with normal zoning (core = $An_{12-16}$; rim = $An_{1-4}$) and distinct albite rims ($An_{1-4}$) on relict feldspar grains (white arrow) (sample PH90). The interstitial plagioclase is not in optical continuity with any residual plagioclase grains adjacent to it and does not show any preferred orientation, in contrast to plagioclase in Types I and II. (d) Type III schlieren migmatite: new plagioclase inferred to have crystallized from melt (growing on an old plagioclase grain in the form of the discrete albite rims (white arrow)) and quartz grains that resorb relict K-feldspar grains (sample PH14/D).*

### *Summary of modal changes*

Modal composition of the feldspar aggregates in the Type II migmatite does not change significantly compared to the Type I orthogneiss. However, the Type III migmatite is characterized by an important increase in quartz content in feldspar domains (up to 30 modal %) associated with a slight increase of interstitial plagioclase in K-feldspar-rich domains and K-feldspar in plagioclase-rich domains. The proportions of the felsic minerals are equal in the Type IV migmatite.

### *Evidence of melting*

Sawyer (1999, 2001) summarized criteria for recognition of former melt at grain scale in metamorphic rocks. The three most important features are: (i) mineral pseudomorphs after thin melt films along crystal faces, a feature typically observed in melting experiments under dynamic conditions (Jin *et al.*, 1994), (ii) rounded and corroded reactant minerals embayed by surrounding mineral pseudomorphs after melt (Büsch *et al.*, 1974), and (iii) cuspate and lobate areas inferred to represent pools of crystallized melt (Jurewicz & Watson, 1984).

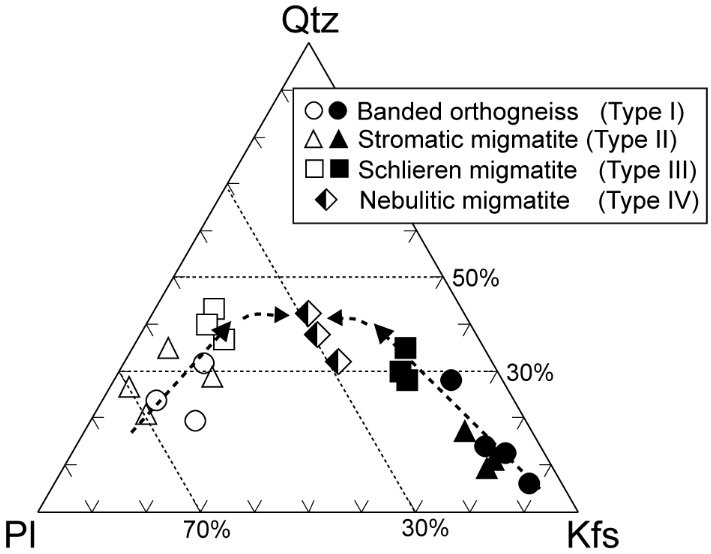


**Fig. 6:** *Modal changes in both plagioclase (open symbols) and K-feldspar (closed symbols) aggregates in different rock types plotted in a quartz–plagioclase–K-feldspar triangle. Arrowed dashed lines indicate evolutionary trend from Type I banded orthogneiss to Type IV nebulitic migmatite.*

The former presence of melt at grain scale was inferred from the following microstructures (Figs. 4 & 5). (i) Plagioclase films between adjacent K-feldspar grains, inferred to represent a plagioclase component crystallized from melt (Fig. 5a, c). This plagioclase is characterized by more albitic composition and by different topology compared to original grains. (ii) Pl–Kfs–Kfs and Kfs–Kfs–Pl dihedral angles commonly lower than 30° (Fig. 5a, c), as observed in granitic melt crystallized under experimental conditions (e.g., Laporte *et al.,* 1997). (iii) Cuspate K-feldspar pools in plagioclase aggregates (Fig. 5b), inferred to represent a K-feldspar component crystallized from melt (Jurewicz & Watson, 1984; Sawyer, 1999, 2001). (iv) Normal zoning of plagioclase from $An_{10–30}$ to $An_{0–15}$ (Sawyer, 1998; Marchildon & Brown, 2001) lining K-feldspar boundaries (Fig. 5c, d). An important feature is the preferential orientation of plagioclase films coating K-feldspar boundaries in Type I orthogneiss and Type II migmatite sub-perpendicular to the foliation (Fig. 5a), in contrast to the Types III and IV migmatites, where these films are wider and do not show any optically visible preferred orientation. Bulbous myrmekite (Fig. 4d) and new highly irregular lobate grains that overgrow partially resorbed corroded feldspar grains (e.g., Fig 4c) are similar to microstructures described as typical of minerals reacting with melt (Mehnert *et al.*, 1973; Büsch *et al.*, 1974; McLellan, 1983).

## Quantitative textural analysis

The quantitative analysis of texture is based on statistical evaluation of grain-size distributions (Kretz, 1966, 1994; Ashworth, 1976; Ashworth & McLellan, 1985; Cashman & Ferry, 1988; Cashman & Marsh, 1988; Higgins, 1998; Berger & Roselle, 2001), spatial distribution of minerals and grain boundary preferred orientations (Panozzo, 1983), and grain contact frequencies (Flinn, 1969; Kretz, 1969; McLellan, 1983; Kruse & Stünitz, 1999). In simple chemical systems, these textural parameters are more sensitive to changes of physical conditions than compositional characteristics. This is due to the high activation energies of chemical reactions needed to produce new crystal growth compared to the small amount of lattice strain energy and grain boundary energy required to drive recrystallization processes (Spry, 1969; Stünitz, 1998).

In this study, we analyzed the texture of three samples from each rock type, and in each sample more than 1000 grains were evaluated in thin section. Due to significant textural variations, the individual K-feldspar-rich and plagioclase-rich domains were analyzed separately. Maps of grains with full topology were manually traced into the ESRI ArcView Desktop GIS environment and grain boundaries were generated using the ArcView PolyLX extension (Lexa, 2003). Analysis of grain size, crystal size distribution (CSD), grain shape preferred orientation (SPO), grain boundaries preferred orientation (GBPO) and grain contact frequencies were obtained using the MATLAB™ PolyLX Toolbox (Lexa, 2003; http://petrol.natur.cuni.cz/~ondro/). The grain sizes of the minerals were evaluated in terms of Feret diameter (diameter of a circle having the same area as the grain). Two methods were used to determine the grain shape preferred orientation (SPO): (1) mean directions using circular statistics, and (2) eigenvalue analysis of Scheidegger's bulk orientation tensor calculated from individual long axes weighted by grain size (Lexa *et al.*, 2005) where degree of SPO is expressed as the eigenvalues ratio Rg. Grain boundary preferred orientation (GBPO) was assessed by similar techniques, but the bulk orientation tensor is formed from the decomposed grain boundaries between chosen phases (Lexa *et al.*, 2005) and the degree of GBPO is expressed as the eigenvalues ratio Rb. Grain contact frequency, used to examine statistical deviation from a random spatial distribution of contact relations between the individual minerals, was evaluated in a manner similar to the method of Kretz (1969, 1994), except that contact frequencies were obtained directly from grain map topologies instead of using line intercepts.

Results of the quantitative microstructural analyses show an evolutionary trend from the banded orthogneiss, through the migmatite types II and III to the nebulitic migmatite. Therefore, in the following sections the rock types are discussed as a sequence in which the Type I orthogneiss and Type IV nebulitic migmatite are considered to be end members of a continuous microstructural evolution.

### *Grain size analysis*

The crystal size distribution (CSD) is an important tool to estimate residence time of magmas in magma chambers, cooling rates in rapidly quenched lavas, as well as to quantify textures related to phenocrysts accumulation and fractionation (Cashman & Marsh, 1988; Marsh, 1988; Higgins, 1998). In metamorphic petrology, CSD is used to obtain quantitative information concerning crystal nucleation and growth rates and nucleation density and/or annealing (Randolph & Larson, 1971; Cashman & Ferry, 1988; Carlson, 1989; Waters & Lovegrove, 2002). Hickey & Bell (1996) proposed that during dynamic recrystallization decreasing strain rate to temperature ratio (e/T) leads to decrease in ratio of nucleation and growth rate (N/G) and development of coarser grain size, whereas increasing e/T leads to increasing N/G and therefore to grain size decrease. This hypothesis is well documented in experimental studies with steel alloys (Sakai & Jonas, 1984) supported by Azpiroz & Fernández (2003) and Lexa *et al.* (2005) in naturally deformed rocks. These authors evaluate the role of recrystallization mechanisms on N/G ratio of the CSD. Crystal size distribution is commonly used in formerly partially molten rocks to evaluate combined process of resorption and grain size decrease of reacting phases in mesosome and nucleation and grain growth and coarsening of minerals crystallizing in leucosomes (Dougan, 1983; McLellan, 1983; Ashworth & McLellan, 1985; Dallain *et al.*, 1999). Because the processes controlling grain size distributions in the crystallization of partially molten rocks are complex and interpretations uncertain, CSD has only rarely been used to describe textural evolution of migmatites (Berger & Roselle, 2001). In this work, we use the

CSD methods as a practical approach to parameterize grain size frequency histograms and visualize their trends in a simple manner.

Grain size statistics were evaluated for the four rock types for plagioclase, K-feldspar and quartz and the results are presented in the form of average grain size, expressed as a median value of the Feret diameter, and grain size range expressed as the difference between the third and first quartiles instead of standard deviation because of the lognormal distribution of measured data (Fig. 7a, Table 1). The results are also summarized as CSD curves (plot of logarithms of population density against crystal size) that were constructed using the method of Peterson (1996); values of the zero-size intercept ($N_0$ - population density interpreted as ratio of nucleation rate to growth rate) and negative inverse of slope (Gt interpreted as a function of growth rate) of the linear parts of the CSD curves are plotted in Fig. 7b, c.

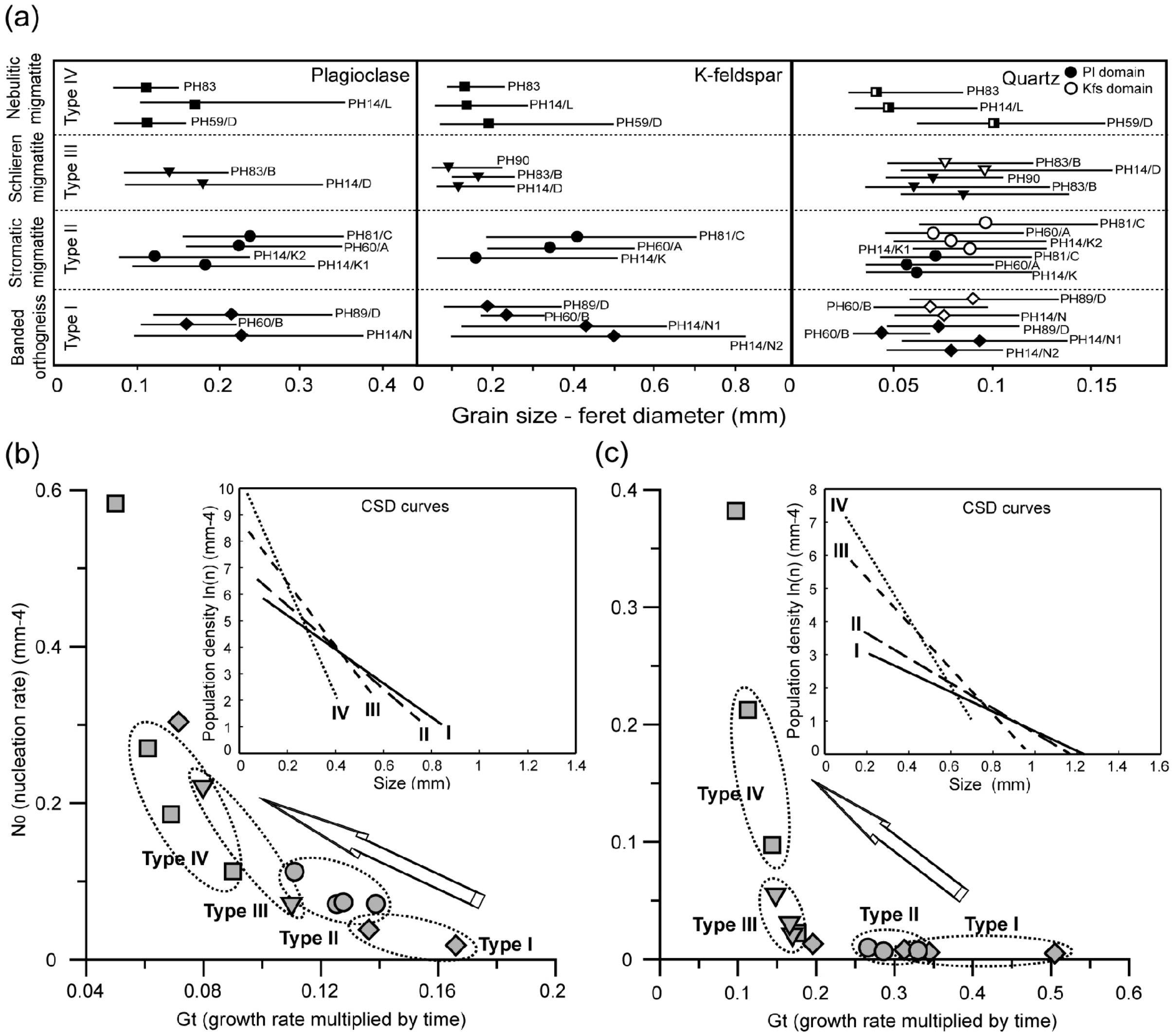


**Fig. 7:** *Grain size statistics and CSD evolution for the rock sequence. (a) Calculated average grain size (median value of the Feret diameter) and range (difference of third and first quartiles) for plagioclase, K-feldspar and quartz. (b, c) Plots of crystal size distribution parameters $N_0$ (corresponding to the nucleation density per size per volume) and Gt (non-dimensional value dependent on the growth rate) with examples of linearized CSD curves (upper right insets) used for Gt and $N_0$ estimates. (b) Plagioclase, (c) K-feldspar. The CSD curves show single lines of four representative samples corresponding to the individual rock types.*

Both plagioclase and K-feldspar in the Type I orthogneiss are characterized by lognormal grain size distribution exhibiting average grain size of about 0.2 mm and 0.2-0.5 mm, respectively. Interstitial quartz yields significantly smaller average grain size of 0.05-0.1 mm in both domains. Quartz grains from polycrystalline ribbons were not evaluated statistically but their grain size of 0.5-2.0 mm was estimated using an optical microscope. The grain size of new interstitial plagioclase in the K-feldspar aggregates is close to 0.1 mm. The grain size distributions from Type I orthogneiss to Type II, Type III and Type IV migmatites are characterized by the following features. The average grain size of plagioclase and K-feldspar decreases compared to Type I orthogneiss (Fig. 7a, Table 1). This is accompanied by a continuous decrease of grain-size range for both feldspars. The interstitial quartz grain size remains fairly constant throughout all the stages of textural evolution, ranging between 0.05 and 0.1 mm, being larger in the K-feldspar than in the plagioclase domains (Fig. 7a). The grain size of minor plagioclase in the K-feldspar domains shows a bimodal distribution that is attributed to the presence of small newly nucleated grains (0.06-0.1 mm) and to larger plagioclase grains (0.2 mm) already present in the feldspar aggregates.

The crystal size distributions (CSD) of plagioclase indicate continuous increase of $N_0$ (nucleation density) values coupled with a decrease of Gt (growth rate) values from Type I orthogneiss towards Type IV migmatite (Fig. 7b, Table 1). In contrast, K-feldspar shows a decrease of Gt values from Type I orthogneiss to Type III migmatite without significant increase of $N_0$ values, which remain very low. From Type III to Type IV migmatite a dramatic increase of $N_0$ values is observed for K-feldspar at almost constant Gt values (Fig. 7c). This evolution is clearly shown by steepening of the slopes of the CSD curves accompanied by increase of their upper intercept with the ordinate axis (insets in Fig. 7b, c).

### *Grain shapes and grain shape preferred orientation (SPO)*

Grain shape or grain aspect ratio together with grain shape preferred orientation analyses (SPO) provide important information about deformation during or after leucosome formation (Mehnert & Büsch, 1968; McLellan, 1983) or about degree of inheritance of original anisotropy (Ashworth, 1979, 1985). Measurements of preferred orientations of inferred melt-filled grain boundaries in rocks give insights to processes of melt draining and melt transfer (Rosenberg & Handy, 2000, 2001; Sawyer, 2001).

Grain shape and shape preferred orientation statistics were evaluated in all the textural types for plagioclase, K-feldspar, quartz and biotite. The results of shape preferred orientation statistic are summarized in a boxplot-type diagram, where the axial ratios of the individual minerals are plotted against bulk SPO (Lexa *et al.*, 2005) for the corresponding minerals (Fig. 8).

Aspect ratios for both K-feldspar and plagioclase show small median values ranging from 1.5 to 1.7 throughout the whole microstructural sequence (Fig. 8, Table 1). Quartz exhibits slightly smaller and stable aspect ratio close to 1.5. An important feature is the continuous decrease of SPO of K-feldspar and plagioclase from Type I orthogneiss to Type IV nebulitic migmatite (Fig. 8, Table 1). Rose diagrams for the rock Types I, II and III show that K-feldspar and plagioclase (Fig. 8b) have weakly inclined SPO with respect to the aggregate elongation direction at an angle of 15° to 30°. Biotite shows a high aspect ratio for Type I orthogneiss (Table 1) and strong SPO parallel with mesoscopic foliation for the Type I, II and III migmatites. In the Type IV migmatite, biotite aspect ratio and preferred orientation are lower and the latter parameter shows bimodal distribution with one maximum sub-parallel to the main foliation and a second one almost perpendicular to it. Interstitial K-feldspar, plagioclase and quartz exhibit always small aspect ratio and weakly developed SPO maxima at an angle of 40°-60° to the foliation for Type I, II and III. The exception is Type IV migmatite, where, in similar fashion to biotite, the interstitial plagioclase shows two maxima, one sub-parallel and one perpendicular to the foliation.

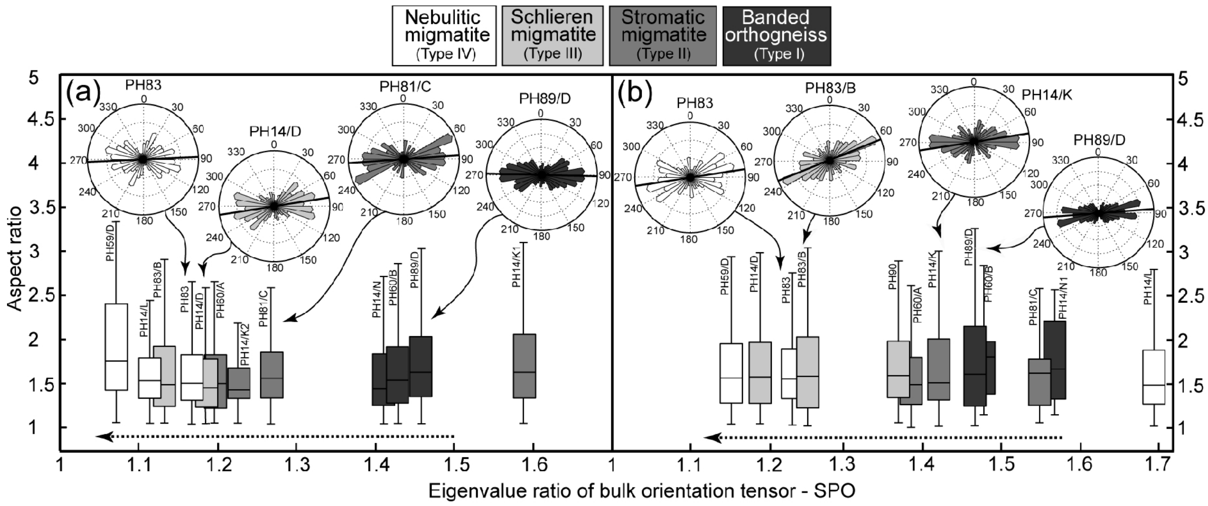


**Fig. 8:** *Plot of grain shape preferred orientation (SPO) of K-feldspar (a) and plagioclase (b). The results are summarized in a box plot of aspect ratios (characterizing the shape of grains) vs. eigenvalue ratios (showing the degree of preferred orientation). Individual boxes show median, and 1st and 3rd quartiles of the aspect ratio. The whiskers represent a statistical estimate of the data range where outliers are not plotted. Representative rose diagrams for individual rock types show maxima orientation in respect to the aggregate elongation direction. The degree of shading corresponds to the individual rock types.*

### *Grain contact frequency analysis and grain boundary preferred orientation (GBPO)*

The grain contact frequency method (Kretz, 1969) allows an examination of the statistical deviation from the hypothesis of random distribution of phases in rocks. In random distribution, the number of contacts of given phases depend only on the total number of grains of each phase present. There are two possible deviations from random distribution: (i) aggregate distribution, where grains of the same phase tend to occur in aggregates in which contacts between grains of the same phase (like–like contacts) predominate; and, (ii) regular distribution, where the grains tend to occur in a regular (chessboard-like) pattern in which contacts between different phases (unlike contacts) are more common. McLellan (1983) reviewed processes responsible for different types of grain distributions. A random distribution should theoretically develop during rapid quenching of granitic melt, whereas regular distribution commonly is interpreted to result from extensive solid-state annealing under very high temperatures (Flinn, 1969; Vernon, 1976; McLellan, 1983; Lexa *et al.*, 2005). These interpretations are based on the assumption of reducing surface energy (Seng, 1936; DeVore, 1959) by elimination of high energy contacts (commonly non coherent like–like contacts) either by reduction of grain boundary area or by nucleation and growth of new phases along such a boundaries (Kim & Rohrer, 2004). In addition, Kruse & Stünitz (1999) and Baratoux *et al.* (2005) proposed that the regular distribution was induced by mechanical mixing and heterogeneous nucleation. According to Vernon (1976) and McLellan (1983), an aggregate distribution results from a solid-state differentiation associated mostly with dynamic recrystallization where development of monomineralic layers results from uneven efficiency of deformation mechanisms simultaneously operating in different phases (Jordan, 1988).

Grain contact frequency and the grain boundary preferred orientation (GBPO) were evaluated for K-feldspar, plagioclase and quartz in all the textural types over the full digitalized area of individual K-feldspar and plagioclase domains. The results are presented in a diagram (Fig. 9), where the value

$$\frac{Observed \quad Expected}{\sqrt{Expected}}$$

or deviation from the random distribution is plotted against the ratio of eigenvalues of the orientation tensor or the degree of GBPO (Lexa *et al.* 2005) . Values of expected frequencies are estimated using Lafeber's method of testing for randomness (Lafeber, 1963; Kretz, 1969). This diagram offers a simple visual evaluation of the relationship between degree of deviation from expected random distribution of grain contacts and grain boundary preferred orientations of like–like and unlike boundaries.

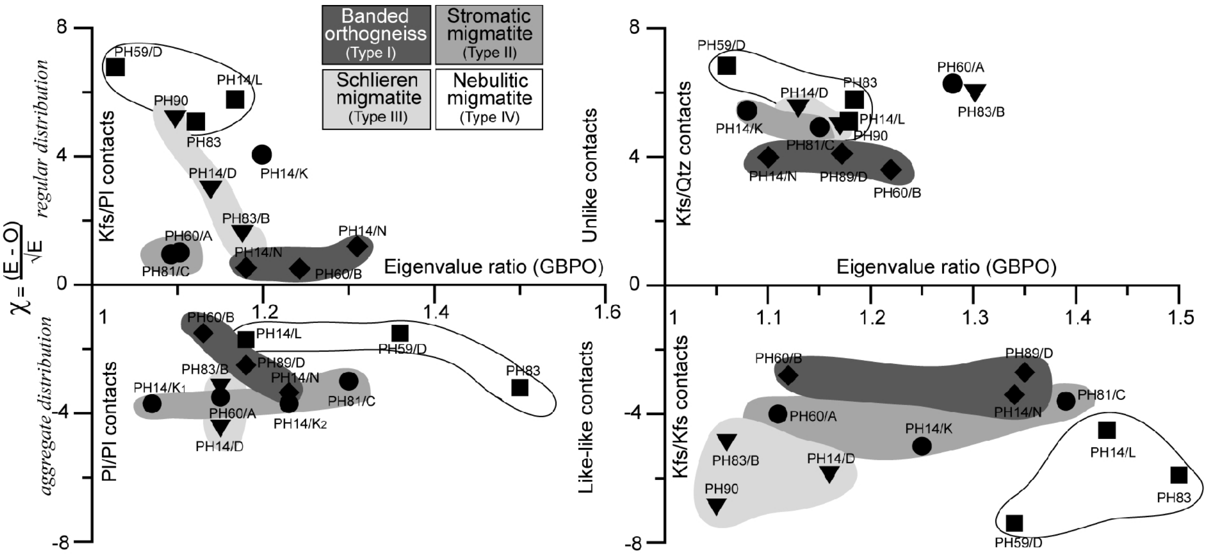


**Fig. 9:** *Grain boundary statistics plotted as the deviation from a random spatial distribution (grain contact frequency) vs. degree of grain boundary preferred orientation (GBPO). For details see text. The degree of shading corresponds to the individual rock types.*

The Type I orthogneiss is characterized by a relatively small proportion of like–like K-feldspar and plagioclase contacts indicating a weak regular distribution (slightly negative values for like–like and positive values for unlike contacts; Fig. 9), despite macroscopically banded texture in which a strong aggregate distribution should be observed. This feature is attributed to a great proportion of minor interstitial grains (Qtz, Bt, Kfs and Pl) lining the K-feldspar and the plagioclase boundaries. Additionally, the number of like–like K-feldspar and plagioclase contacts continuously decreases from Type I orthogneiss to Type IV migmatite, whereas the number of Pl–Kfs, Kfs–Qtz and Pl–Qtz unlike contact continuously increases (negative like–like values and positive unlike values) (Fig. 9). This is in a good accordance with the increasing amount of interstitial phases towards the Type IV migmatite. Quartz exhibits the same strong regular distribution from the Type I orthogneiss to the Type IV migmatite in both feldspar domains.

In K-feldspar-rich aggregates, the degree of GBPO of the K-feldspar like–like boundaries slightly decreases from Type I orthogneiss to Type III migmatite, whereas Type IV migmatite is characterized by an increase in degree of K-feldspar like–like GBPO (Fig. 9, Table 1). The GBPO of plagioclase–plagioclase boundaries in the plagioclase-rich aggregates is similar to the evolution of K-feldspar like–like boundaries. The GBPO of the K-feldspar–quartz boundaries as well as those of K-feldspar–plagioclase boundaries are weak, and decrease throughout the textural evolution (Fig. 9, Table 1).

## Mineral fabric

In rocks deformed in the presence of melt, the textures of quartz and feldspars can be used to evaluate the deformation mechanisms of solid fraction as well as the deformation of crystallizing intragranular melt (Závada *et al.*, in press). The mineral fabrics of ferromagnesian phases can be indirectly assessed using anisotropy of magnetic susceptibility (AMS). The AMS method has been recently used to determine the degree of susceptibility, shape of the fabric ellipsoid and relative contribution of ferro- and para-magnetic minerals to the bulk fabric in migmatites (Ferré *et al.*, 2003, 2004).

### *Anisotropy of magnetic susceptibility (AMS)*

Types III and IV migmatites are macroscopically close to isotropic, so that the mineral alignment defined by the orientation of dispersed biotite is poorly defined (Fig. 2c, d). To better characterize the fabric, we used anisotropy of magnetic susceptibility (AMS) method to determine the internal fabric of these rocks. Oriented samples were collected using a portable drill at four sampling sites covering a section across the well-defined structural sequence. The AMS data were statistically evaluated using the ANISOFT software package (Jelínek, 1978; Hrouda *et al.*, 1990). The low values of mean susceptibility ($<250\ 10^{-6}$ SI) indicate that biotite is the main carrier of the magnetic susceptibility (Ferré *et al.*, 2003). The AMS study reveals a homogeneous pattern of a south-dipping magnetic foliation (Fig. 10b) and SW sub-horizontally plunging magnetic lineation (Fig. 10b) that are consistent with the mesoscopic $D_2$ structural pattern.

According to the degree of AMS (expressed by parameter P', Jelínek, 1981) and shape of the AMS ellipsoid (expressed by parameter T, Jelínek, 1981) the samples are divided in two groups (Fig. 10a). The banded orthogneiss and the Type II migmatite exhibit a strong degree of magnetic anisotropy (P' = 1.14–1.2) and planar shape of the ellipsoid of magnetic susceptibility (T = 0.4–1) (Fig. 10a). These values are typical for metamorphic rocks with well-developed compositional layering and biotite aligned in planar aggregates. Samples from Type III and IV migmatites occur in a region of lower degree of anisotropy (P' = 1.06–1.16) and correspond to a planar–linear fabric (T = 0.1–0.7) (Fig. 10a) marked by more intense magnetic lineation.

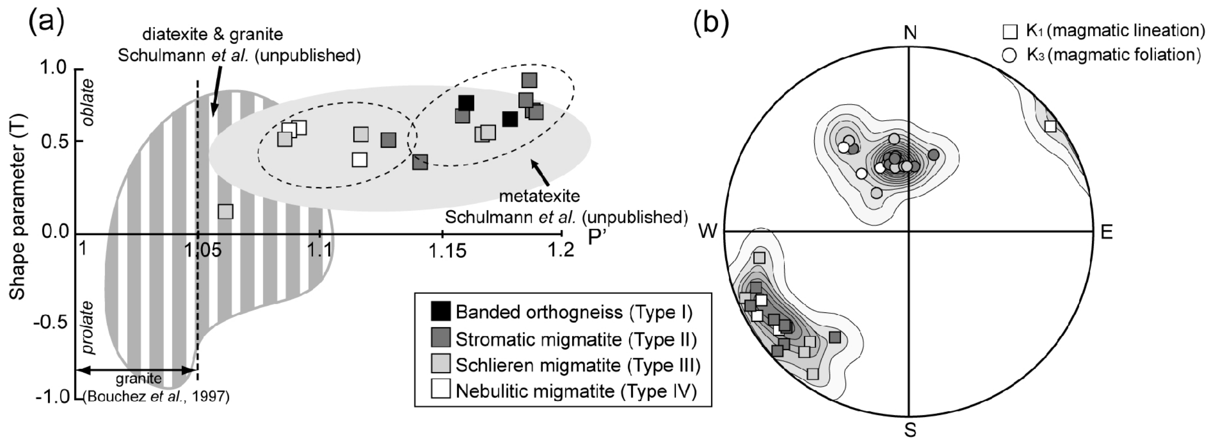


**Fig. 10:** *Plots to show the anisotropy of magnetic susceptibility (AMS). (a) P'-T plot, where the P' parameter represents the degree of magnetic anisotropy and T is a shape parameter that describes the shape of the ellipsoid of magnetic susceptibility. T can take either positive values (T > 0), characteristic for a planar fabric, or negative values (T < 0), typical for a linear fabric. Dashed ellipses show two distinct datasets. For comparison, data obtained by Schulmann et al. (unpublished) and Bouchez (1997) are shown. (b) Magnetic foliation (circles), plotted as the minimal susceptibility direction ($K_3$), perpendicular to the magnetic foliation, and magnetic lineation (squares), plotted as the maximal susceptibility direction ($K_1$).*

### *Lattice preferred orientation (LPO)*

To understand the deformation behaviour of individual phases, we measured and evaluated statistically the lattice preferred orientation (LPO) of aggregate grains (Pl, Kfs and Qtz) and grains apparently crystallized from melt (Pl, Kfs and Qtz) separately (Fig. 12 g, h). The LPO of quartz, plagioclase and K-feldspar were measured on a scanning electron microscope CamScan3200 in the Czech Geological Survey using the electron back-scattered diffraction technique (EBSD) and HKL technology (Adams *et al.*, 1993; Bascou *et al.,* 2001). Diffraction patterns were acquired at 20 kV accelerating voltage, 5 nA probe current and working distance of about 33 mm from the thin section prepared from the structural XZ plane. The procedure was carried out manually due to small differences in diffraction patterns. The chemistry and orientation of individual grains was controlled using a forescatter detector with combination of orientation and chemical contrast. Thus, each individual grain is represented by only one orientation measurement. The resulting pole figures are presented as lower hemisphere equal-area projections in which the trace of foliation is oriented along the equator and the stretching lineation is in the E–W direction.

Old quartz grains in ribbons of the Type I orthogneiss show c-axes distributed in weak sub-maxima arranged along weakly developed small circles close to the $S_1$ foliation trace. The most intense sub-maxima are developed close to the lineation direction. This type of c-axis pattern may indicate preferential prism <c> slip-system activity and dominantly coaxial deformation. The c-axes of large quartz grains in Type II, III and IV migmatites reveal strong maxima either parallel to the $S_2$ foliation pole or close to the centre of the diagram. These c-axis patterns indicate mainly activity of basal <a> or rhomb <a+c> slip-systems and less frequently prism <a> slip (Fig. 4a). Towards Type III and IV migmatites, the LPO of matrix quartz became less well developed, preserving activity of the same slip-systems as in the previous microstructural types (Fig. 11a). New quartz grains crystallized from melt in Type I orthogneiss and Type II migmatite show very weak LPO and nearly random distribution of all quartz axes (Fig. 11b). Whereas old grains show progressive weakening of the LPO from Type II to Type IV migmatite, the new and randomly crystallized grains tends to develop weak crystal preferred orientation during the same microstructural evolution from Type II to Type IV migmatite (Fig. 11). It is difficult to distinguish old from new quartz grains in the Type IV rock and therefore the LPO of quartz in this microstructure links LPO evolution between old and new grains in the final microstructural type.

K-feldspar and plagioclase commonly show weak lattice preferred orientation in all rock types regardless the origin of grains. K-feldspar shows crystallographic patterns which are compatible with dominant activity of the 1/2 [110](001) slip system (Willaime & Gandais, 1977; Willaime *et al.*, 1979) (Fig. 12a, c). Contribution of other slip systems as [100](010) (Fig.

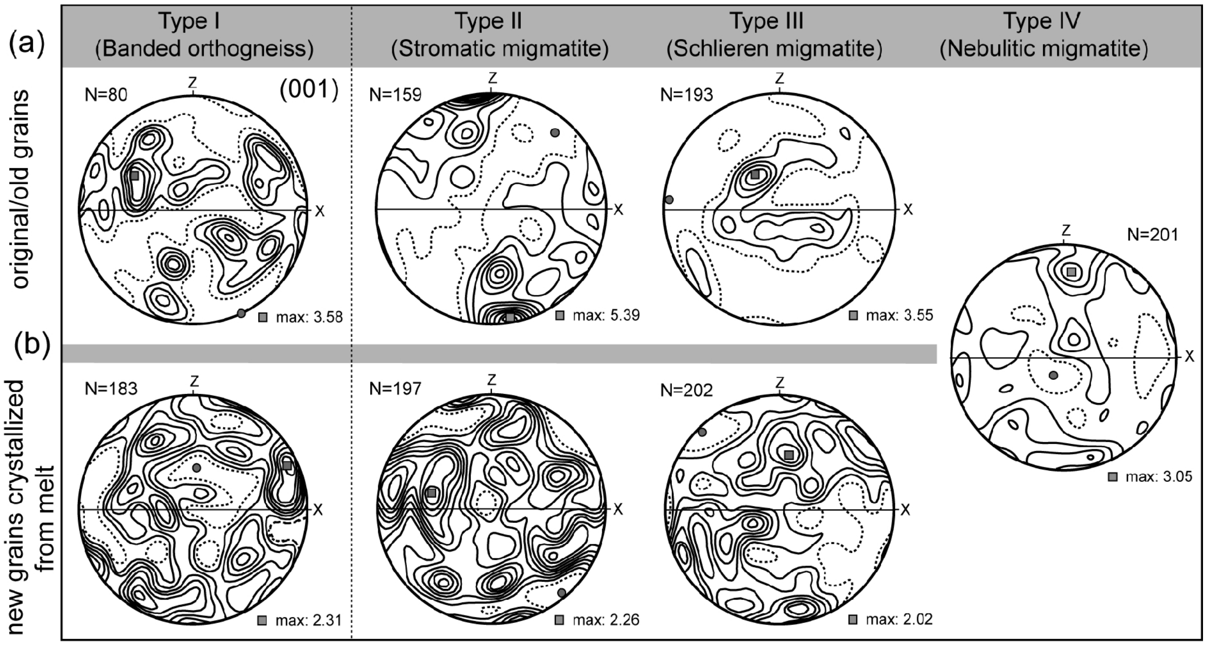


**Fig. 11:** *Characteristic c-axes preferred orientations of (a) old/relict quartz grains and (b) new quartz grains crystallized from areas of inferred former melt for all rock types. The c-axis patterns of old/relict quartz grains in Type I banded orthogneiss indicate prism <c> slip system activity whereas in Type II, III and IV migmatites basal <a> or rhomb <a+c> slip systems are dominant with minor prism <a> slip. New quartz grains inferred to have crystallized from melt in Type I banded orthogneiss to Type IV nebulitic migmatite show very weak LPO and nearly isotropic distribution of all quartz axes. Equal area projections, lower hemisphere, contoured at interval of 0.5 times uniform distribution. Foliation is horizontal and lineation is in this plane in the E-W direction. N is a number of measured grains. Maximum densities are marked on the bottom right of each pole figure. The dashed line represents the lowest contour level and the grey circle corresponds to the minimum density value.*

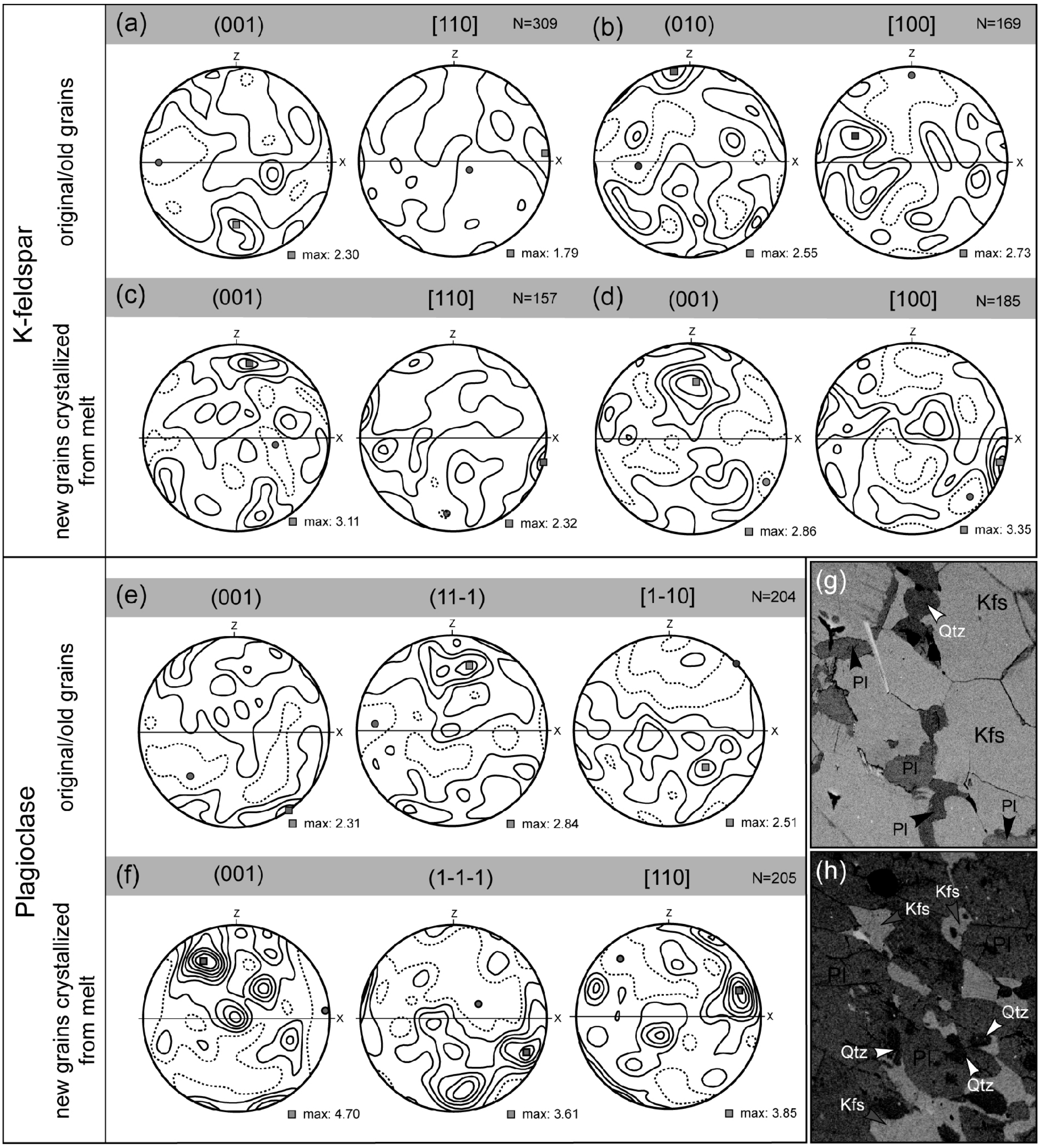


**Fig. 12:** *Characteristic LPO patterns of K-feldspar (a-d) and plagioclase (e-f). Both feldspars commonly show weak LPO in all rock types regardless of the origin of the grains. An exception is the strong LPO of new plagioclase grains in the Type I banded orthogneiss (f). K-feldspar usually shows activity of 1/2[110](001) (a, c; Type I), but also of [100](010) (b; Type IV) and [100](001) (d; Type IV) slip systems. Plagioclase reveals activity of secondary slip systems such as 1/2[1 1 0] on (001) and (11 1 ) or 1/2[110] on (001) and (111 ) (e, f; Type I). Equal area projections, lower hemisphere, contoured at intervals of 0.5 times uniform distribution. Foliation is horizontal and lineation is in this plane in the E-W direction. N is the number of measured grains. Maximum densities are marked on the bottom right of each pole figure. The dashed line represents the lowest contour level and the grey circle corresponds to the minimum density value. (f-g) BSE images depicting the microstructural appearance of examples of the measured phases (sample PH60/B). Original plagioclase (g) and K-feldspar (h) aggregates with newly crystallized quartz (white arrow), plagioclase (black arrows) and K-feldspar (grey arrows) are shown.*

12b) and [100](001) (Fig. 12d) also has been identified in both relict K-feldspar grains and in K-feldspar grains apparently crystallized from melt, respectively.

Distribution of the main lattice directions of plagioclase revealed slip parallel either to 1/2[110] on (001) and (111) planes (Fig. 12e) or to 1/2[110] on (001) and (111) planes for all types of rocks and both aggregate grains and plagioclase inferred to have crystallized from melt (Fig. 12e) (Olsen & Kohlstedt, 1984). The textures of plagioclase inferred to have crystallized from melt are commonly weak with exception of strong lattice preferred orientation of plagioclase in the Type I orthogneiss (Fig. 12f). Such slip-systems are supposed to be secondary and active if grains are in unsuitable ('hard') orientation to the dominant slip-system [100](010) (Kruse *et al.*, 2001).

## Discussion

This study presents a detailed microstructural and quantitative textural analysis of four types of migmatitic rocks identified in one of the largest (~ 5000 km$^2$) migmatitic complex of the eastern Variscan belt. We interpret the rock types to represent a textural sequence from banded orthogneiss via stromatic and schlieren migmatites to nebulitic migmatite. The possible mechanisms that could account for origin of this rock sequence involve: (i) genetically unrelated migmatites that have originated from distinct protoliths, (ii) variable degree of *in-situ* partial melting of a single protolith or different protoliths, and (iii) melt infiltration from an external source through solid rock in which banded orthogneiss and nebulitic migmatite represent genetically linked end members. These hypotheses are discussed further below.

### *Spatial relationships of individual migmatite types within the shear zone*

The structural sequence described in this work indicates an intimate relationship between Type I to III migmatites and nebulitic Type IV migmatite sheets that can be interpreted in terms of a shear zone, which was exploited by rising magma (Brown *et al.*, 1995; Collins & Sawyer, 1996; Brown & Solar, 1998b). We have shown that the $D_2$ flat fabrics that crosscut the steep foliation $S_1$ developed at high-temperature solid state conditions (Fig. 1). Tajčmanová *et al.* (2006) and Racek *et al.* (2006) described a similar sequence of superposed fabrics in lower crustal rocks several tens of kilometers to the north and south of the studied area, respectively. These authors proposed that the flat $D_2$ deformation fabrics originated due to thrusting of orogenic lower crust over middle crustal units along large scale retrograde shear zone. In agreement with these authors, we suggest that the $D_2$ fabrics developed in a thrust related crustal scale shear zone reported already by Urban (1992), Schulmann *et al.* (1994) and redefined later on by Schulmann *et al.* (2005). The main difference between other regions is in the degree of $D_2$ reworking, which is so high in the studied area that steep $D_1$ fabrics are preserved only as rare relics shown in Fig. 2.

Our structural observations are compatible with progressive transposition within the ductile shear zone ranging from Type I banded orthogneiss to highly reworked Type III schlieren migmatite. This interpretation is based on progressive folding of early steep orthogneiss fabric, development of isoclinal folds and complete fabric transposition and development of Type III migmatite in a ductile shear zone (Fig. 2; Turner & Weiss, 1963). In such a context, the elongated bodies of Type IV nebulitic migmatite can be seen as veins of isotropic granite penetrating parallel to the main $S_2$ mylonitic anisotropy (e.g. Cosgrove, 1997; Brown & Solar, 1998a). Alternatively, the Type IV nebulitic migmatites could be interpreted in terms of injected melt into hot country rocks (called also magma wedging, Weinberg & Searle, 1998) preventing magma freezing during $D_2$ shearing. Finally, the nebulitic migmatite can be also regarded as the most extreme end member of the structural sequence, i.e. completely disintegrated parental orthogneiss.

In summary, the Type I orthogneiss to Type III migmatite show intimate spatial relationships suggesting that they have originated from the same protolith and that they are genetically linked. However, the macroscopic observations alone cannot decide the origin of Type IV migmatite and further arguments are required.

### *Microstructural and petrological arguments for melt-rock interaction during exhumation*

We suggest, in agreement with Sawyer (1999, 2001), that the position and topology of new plagioclase, quartz and K-feldspar grains in Type I orthogneiss and Type II migmatite may be interpreted in terms of melt products crystallized along boundaries of the feldspars in individual aggregates (Fig. 5a-c). The main difference between Type I orthogneiss and Type II migmatite is a more albitic composition of plagioclase and a greater modal content of new phases in the latter. Type III and IV migmatites show development of highly corroded shapes of K-feldspar, plagioclase and biotite (Fig. 4c-f). This indicates that all rock types exhibit features compatible with presence of melt and its interaction with the solid rock. Additionally, the degree of melt-rock interaction is inferred to increase from Type I orthogneiss towards Type IV nebulitic migmatite (Fig. 4).

The structural sequence exhibits a distinct trend in modal composition of originally monomineralic layers that are progressively converted into polymineralic aggregates of granitic composition (Fig. 6). The compositional paths show evolutionary trends from Type I orthogneiss to Type III migmatite, interpreted to be associated with crystallization of melt, culminating in the Type IV migmatite, which has equal amounts of plagioclase, K-feldspar and quartz (Fig. 6).

Plagioclase shows systematic decrease of anorthite content for both original plagioclase grains ($An_{30}$ to $An_{25}$), their rims and inter-granular aggregates ($An_{20}$ to $An_{10}$) towards Type IV nebulitic migmatite. Both garnet and biotite exhibit systematically increasing $X_{Fe}$ towards Type IV migmatite (from 0.7 to 1.00 and from 0.4 to 0.9, respectively) coupled with decrease of Ti content in biotite (from 0.2 to 0.04 p.f.u.). The mineral compositional data suggest systematic equilibration of garnet, biotite and plagioclase compositions in the stability field of sillimanite with decreasing temperature. The full petrological data and *P–T* estimates for melt–rock interaction are presented in a companion paper (Hasalová *et al.*, 2008). Here, we quote the *P–T* estimates based on thermodynamical modeling using THERMOCALC (Powell *et al.*, 1998) to point out the decrease in temperature from 790–850°C at 7.5 kbar for Type I orthogneiss to 690–770°C at 4.5 kbar for Type IV nebulitic migmatite.

Taken together, the microstructural and petrological data show paradoxically an increasing degree of apparent melt–rock interaction coupled with decreasing equilibration temperature with textural evolution from Type I to Type IV rock type. The microstructural and modal composition data do not exclude either partial melting or infiltration of melt from an external source. However, the systematic modification of chemical composition of mineral phases across the migmatite sequence is in contradiction with the model of *in-situ* partial melting. Namely, as suggested by many field and experimental studies, the composition of plagioclase would be shifted towards more anorthitic contents and the $X_{Fe}$ of garnet and biotite would decrease during partial melting process (Le Breton & Thompson, 1988; Vielzeuf & Holloway, 1988; Gardien *et al.*, 1995; Greenfield *et al.*, 1998; Dallain *et al.*, 1999).

### *Interpretation of quantitative microstructural data*

Microstructural studies of partially molten rockhas revealed systematic changes in grain size, grain shape preferred orientation and spatial distribution of individual phases during increasing degree of partial melting (e.g. Vernon, 1976; McLellan 1983; Dallain *et al.*, 1999). Here we will compare these trends with our quantitative microstructural data and we will discuss the alternative origins that may result in the observed microstructural sequence.

### *Interpretation of crystal size distributions*

The most significant result of this study is the systematic decrease of average grain size (Fig. 7a) and systematic increase of a population density (nucleation rate) associated with possible decrease of growth rate for all feldspars from Type I orthogneiss to Type IV migmatite (Fig. 7b, c).

**Table 1:** *Representative data for the quantitative textural analysis.*

| | | Banded orthogneiss | | Stromatic migmatite | | Schlieren migmatite | | Nebulitic migmatite |
|---|---|---|---|---|---|---|---|---|
| | | Kfs domain | Pl domain | Kfs domain | Pl domain | Kfs domain | Pl domain | |
| **Grain size - Feret diameter (mm)** | | | | | | | | |
| Median | Kfs | 0.430 | 0.121 | 0.345 | 0.065 | 0.172 | 0.138 | 0.137 |
| | Pl | 0.134 | 0.224 | 0.086 | 0.225 | 0.094 | 0.119 | 0.110 |
| | Qtz | 0.079 | 0.076 | 0.071 | 0.079 | 0.070 | 0.076 | 0.074 |
| Q1 | Kfs | 0.120 | 0.065 | 0.194 | 0.042 | 0.103 | 0.082 | 0.085 |
| | Pl | 0.103 | 0.095 | 0.055 | 0.158 | 0.061 | 0.084 | 0.074 |
| | Qtz | 0.046 | 0.051 | 0.044 | 0.050 | 0.046 | 0.047 | 0.039 |
| Q3 | Kfs | 0.630 | 0.170 | 0.556 | 0.101 | 0.263 | 0.211 | 0.237 |
| | Pl | 0.257 | 0.373 | 0.161 | 0.350 | 0.172 | 0.164 | 0.160 |
| | Qtz | 0.105 | 0.114 | 0.119 | 0.127 | 0.105 | 0.121 | 0.127 |
| Q3 - Q1 | Kfs | 0.510 | 0.105 | 0.362 | 0.059 | 0.161 | 0.129 | 0.152 |
| | Pl | 0.154 | 0.278 | 0.107 | 0.192 | 0.111 | 0.080 | 0.086 |
| | Qtz | 0.059 | 0.063 | 0.075 | 0.077 | 0.060 | 0.074 | 0.089 |
| **Crystal size distribution (CSD)** | | | | | | | | |
| $N_0$ (mm-4) | Kfs | 0.0037 | — | 0.00487 | — | 0.053 | — | 0.2124 |
| | Pl | — | 0.0303 | — | 0.0733 | — | 0.06812 | 0.1857 |
| | Qtz | 1.008 | 2.334 | 1.6448 | 3.73 | 2.093 | 0.6585 | 2.286 |
| $G_t$ | Kfs | 0.347 | — | 0.286 | — | 0.148 | — | 0.1127 |
| | Pl | — | 0.15731 | — | 0.1269 | — | 0.11 | 0.0689 |
| | Qtz | 0.0736 | 0.0569 | 0.0669 | 0.0547 | 0.0644 | 0.0813 | 0.0623 |
| **Shape preferred orientation (SPO)** | | | | | | | | |
| Eigenvalue | Kfs | 1.48 | 1.42 | 1.42 | 1.32 | 1.21 | 1.13 | 1.15 |
| ratio | Pl | 1.17 | 1.42 | 1.1 | 1.23 | 1.21 | 1.14 | 1.13 |
| (Rg) | Qtz | 1.25 | 1.47 | 1 | 1.24 | 1.1 | 1.33 | 1.32 |
| Aspect ratio | Kfs | 1.66 | 1.69 | 1.6 | 1.5 | 1.59 | 1.6 | 1.55 |
| (median) | Pl | 1.51 | 1.6 | 1.59 | 1.44 | 1.65 | 1.5 | 1.61 |
| | Qtz | 1.5 | 1.5 | 1.46 | 1.5 | 1.5 | 1.5 | 1.49 |
| | Bt | 2.14 | 2.7 | 2 | 2.2 | 2.2 | 2.35 | 2.2 |
| **Grain boundary preferred orientation (GBPO)** | | | | | | | | |
| Eigenvalue | Kfs - Kfs | 1.34 | — | 1.25 | — | 1.06 | — | 1.5 |
| ratio | Kfs - Pl | 1.15 | 1.18 | 1.09 | 1.13 | 1.14 | 1.13 | 1.12 |
| (Rb) | Kfs - Qtz | 1.17 | — | 1.15 | — | 1.17 | — | 1.17 |
| | Pl - Pl | — | 1.18 | — | 1.15 | — | 1.15 | 1.36 |
| **Modal proportion (%)** | | | | | | | | |
| | Kfs | 70 - 80 | 10 | 70 - 80 | 5 | 50 | 20 - 25 | 30 |
| | Pl | 10 | 60 | 10 | 60 | 20 | 40 | 30 |
| | Qtz | 10 - 20 | 20 | 10 - 20 | 25 | 30 | 30 | 30 |
| | Bt | < 1 | < 10 | < 1 | ~ 10 | < 1 | < 10 | 10 |
| | Sill, Grt | 0 | < 1 | 0 | < 1 | 0 | < 1 | < 2 |

Results from migmatitic terrains show that the crystal size distribution associated with partial melting is characterized by production of coarse grained felsic mineral aggregates resulting from increase of temperature (e.g. Dougan, 1983; McLellan, 1983). This process is commonly followed by textural coarsening (Ashworth & McLellan, 1985; Dallain *et al.*, 1999; Berger & Roselle, 2001) explained by two competing approaches: the Lifshitz-Slyozov-Wagner (LSW) model (Lifshitz & Slyozov, 1961), and the communicating neighbor theory (CN of DeHoff, 1991). Higgins (1998) showed that textural coarsening results in progressive decrease of $N_0$ value and decrease of slope of the CSD curve; he interpreted this trend as a result of rapid undercooling during solidification of magma followed by reduced undercooling, suppression of nucleation and textural coarsening. However, our textural sequence exhibits the opposite trend in evolution of CSD curves, which is interpreted to indicate that *in-situ* partial melting and textural coarsening are not responsible for the origin of observed crystal size distributions.

The observed crystal size distribution trend may be explained by one of three different mechanisms: 1) solid state deformation under decreasing temperature and or increasing strain rate (Hickey & Bell, 1996; Azpiroz & Fernández, 2003; Lexa *et al.*, 2005), 2) different degree of reaction overstepping (Waters & Lovegrove, 2002; Moazzen & Modjarrad, 2005), and 3) different degree of undercooling (Marsh, 1988).

The grain size for dynamically recrystallized grains in a power-law creep regime is a function of differential stress (Twiss, 1977). Such grains are characterized by strong shape and lattice preferred orientation and commonly solid state differentiation (Baratoux *et al.*, 2005; Lexa *et al.*, 2005). However, this microstructural study does not reveal any features in quartz, plagioclase and K-feldspar of rock types II, III and IV which may indicate a dynamic recrystallization processes operating under decreasing temperature. Differences in the degree of reaction overstepping have been documented in contact aureoles, but may be rejected in this case due to the regional nature of the metamorphism. However, the role of different degrees of undercooling relating to an overall decrease in equilibration temperature cannot be excluded.

Our data indicate that the sequence of rock types reflects the progressive resorption of residual grains and crystallization of new grains from melt in inter-granular spaces. Moreover, the trend of CSD curves suggest a progressive increase of nucleation rate and decrease of growth rate from Type I orthogneiss to Type IV nebulitic migmatite. This trend could be explained by an increase in undercooling consistent with the decreasing equilibration temperature we report.

The CSD trend is compatible with crystallization of melt in a progressively exhuming and rapidly cooling system. This is in accordance with exceptionally high cooling rates up to several hundred degrees Celsius per million years estimated for nearby granulites by Tajčmanová *et al.*(2006).

### *Interpretation of spatial distributions of phases*

The quantitative analysis of spatial distributions of individual phases shows that the intensification of regular distribution (increasing amount of unlike contacts; Fig. 9) correlates with an increasing degree of host rock–melt equilibration. The process of melt crystallization leads to new mineral growth on the surfaces of residual grains . This is responsible for the increase of unlike grain boundaries, which commonly retain melt–solid geometries. Our case study shows that the development of a regular distribution of felsic phases is not related to solid state annealing, as supposed by some authors (Flinn, 1969; McLellan, 1983; Lexa *et al.*, 2005), but to the process of crystallization of melt, consistent with precipitation of the minor phase on triple points in granular polygonal aggregates to achieve lower total interfacial energy (Spry, 1969; Vernon, 1974). This process was documented by Dallain *et al.* (1999),who showed that the predominance of unlike contacts in polycrystalline aggregates originated through wetting of grain boundaries by fluids or melt, and subsequent precipitation of other phases on like–like contacts. However, we cannot exclude the possibility that a regular distribution reported from granulites and high-grade gneisses (Flinn, 1969; Kretz, 1994) results from solid state annealing of rocks where melt crystallized. Therefore, the regular distribution developed during melt crystallization may be inherited and perhaps further accentuated during later thermal and textural re-equilibration.

### *Origin of microstructural and compositional trends*

The sequence from Type I orthogneiss to Type IV migmatite exhibit continuous trends in all quantitative parameters (Table 1). The grain size decreases (Fig. 7a) and there is a progressive development of a regular distribution of all felsic phases (Fig. 9), which is linked with mineral compositional trends indicating temperature decrease. These clear evolutionary trends are incompatible with a process of partial melting of different protoliths. Partial melting of the same protolith may develop continuous trends, but these should show increase in grain size of individual felsic phases (Dallain *et al.*, 1999) and different mineral compositional evolution (e.g. Gardien *et al.*, 1995; Greenfield *et al.*, 1998). Additionally, we show that the degree of regular distribution for K-feldspar- and plagioclase-dominated aggregates evolves in the same manner throughout the microstructural sequence (Fig. 9). However, Dallain *et al.*, (1999) reported significantly more advanced regular distribution of plagioclase- compared to K-feldspar-rich aggregates in the microstructural sequence originated by partial melting. These authors proposed that this microstructural contrast originated due melting process preferentially operating in mica–plagioclase rich aggregates, whereas the K-feldspar-rich aggregates were more refractory. In the present case, Hasalová *et al*. (2007) report continuous trends in whole-rock geochemistry and mineral compositions for the sequence of rock types, but different Nd isotopic composition for the Type I orthogneiss compared with the rest of the sequence, which precludes of *in-situ* anatexis in a closed system.

### Melt infiltration model

The discrepancies between the evolutionary trends we report and generally accepted trends for anatectic terrains require an appropriate explanation that is consistent with the structural, quantitative microstructural and mineral compositional data. As a possible explanation, we introduce the concept of melt infiltration from an external source, where melt passes pervasively along grain boundaries through the whole rock volume and changes macroscopic (Fig. 2) and microscopic (Fig. 3) appearance of the rock. This process is characterized by resorption of old phases, nucleation of new phases along high energy like–like grain boundaries and modification of mineral and whole-rock compositions. These gradual changes are accompanied by grain size reduction (Fig. 7) and progressive disintegration of former aggregate (layered) distribution of original phases (Fig. 9). We suggest that the individual migmatite types represent different degrees of equilibration between the host rock and migrating melt. It should be emphasized, that all these processes occur along a retrograde path during exhumation of the Gföhl Unit. We are aware that a decrease of *P–T* conditions during melt infiltration is a fundamental and limiting factor for the model we propose.

The amount of melt and its connectivity are critical parameters controlling melt mobility and the rheological behaviour of melt-present rocks. In order to constrain these parameters we used both AMS and EBSD.Using AMS, we are able to distinguish between solid-state dominated deformation mechanisms in the melanosome and free rigid body particle rotation in the leucosome (e.g. Ferré *et al.*, 2003). On the other hand, using the EBSD technique enables us to distinguish deformation mechanisms in the solid framework and to constrain the mechanical role of melt during the deformation.

### *AMS fabric origin: solid framework or melt controlled deformation*

The AMS study shows that the magnetic anisotropy is dominated by biotite. The oblate shape of magnetic ellipsoid and high degree of anisotropy of Type I orthogneiss and Type II migmatite (Fig. 10a) are consistent with strong preferred orientation of biotite and the fact that biotite has a intrinsically oblate shape of the single-grain magnetic ellipsoid (Zapletal, 1990; Martín-Hernandez & Hirt, 2003). The Type III and IV migmatites reveal partly resorbed biotite flakes uniformly dispersed in the rock marked by slightly weaker degree of magnetic anisotropy and less oblate fabric ellipsoid compared to Types I and II migmatite (Fig. 10a). This contrasts with common granites and diatexites from other migmatitic terrains which show significantly lower values of degree of anisotropy and highly variable shapes of AMS ellipsoids (Fig. 10a; Bouchez, 1997; Ferré *et al.*, 2003).

Numerous natural studies supported by numerical modelling indicate that the magnetic susceptibility in viscously-flowing magmas is characterized by a very low degree of anisotropy, pulsatory fabrics and dominantly a plane strain AMS ellipsoid shape (Blumenfeld & Bouchez, 1988; Hrouda *et al.*, 1994; Arbaret *et al.*, 2000). A comparison of the AMS fabrics with those of diatexites and results of numerical models indicate that the intensity of the AMS fabric of Type III and IV migmatites does not originated from freely-rotated biotite in viscously flowing melt. On the contrary, we argue that the AMS fabric in all types of migmatites resembles fabrics usually acquired through solid state deformation of a load-bearing framework, similar to. melanosomes in migmatites (Ferré *et al.*, 2003) In order to understand the mechanisms responsible for development of such fabrics we discuss the grain scale deformation mechanisms and melt behaviour in individual rock types.

### *Deformation mechanisms*

Experimental studies of low melt fraction rocks deformed under high differential stress show that matrix minerals deform by grain boundary migration accommodated dislocation creep (Dell'Angelo *et al.*, 1987; Walte *et al.*, 2005). Strong shape and grain boundary preferred orientation of feldspars (Figs. 8 & 9) as well as LPO of residual quartz grains (Fig. 11a) in the Type I orthogneiss may be interpreted in terms of plastic deformation consistent with a dislocation creep deformation mechanisms (Rosenberg & Berger, 2001). However, the weak LPO of residual grains of both feldspars (Fig. 12a, e) in the Type I orthogneiss suggests a contribution of grain boundary sliding during the development of the microstructure. In other words, the Type I microstructure corresponds to a transient microstructure in terms of decreasing activity of dislocation creep and enhancement of diffusion controlled processes.

Decrease of SPO and GBPO and constantly weak LPO in feldspars of Type II migmatite (Figs. 8 & 9) may be interpreted as a result of melt enhanced diffusion creep (Garlick & Gromet, 2004). However, the large quartz grains reveal intense activity of basal <a> slip suggesting important plastic yielding of this mineral (Fig. 11a). Elongate pockets inferred to represent former melt oriented at a high angle to the stretching lineation in the Type I orthogneiss (Fig. 5a) and Type II migmatite indicate that the melt distribution was controlled by the deformation. This is supported by the strong LPO of interstitial plagioclase (Fig. 12f). Rosenberg & Riller (2000) reported that pockets within quartz aggregates inferred to have been former melt are oriented at highangle to the foliation plane, possibly close to $_1$. Melt distribution in our samples is similar to their results and also to experiments at high differential stresses (Dell'Angelo & Tullis, 1988) and high confining pressures. In these experiments, melt accumulated in pockets along faces of the grains sub-parallel to the main compressional stress direction $_1$ (Dell'Angelo & Tullis, 1988; Daines & Kohlstedt, 1997). Such a melt topology is also termed 'dynamic wetting' (Jin et al., 1994).

In Type III and IV migmatites both residual and new grains of K-feldspar and plagioclase exhibit low SPO, GBPO and LPO (Figs. 8, 9 & 12), indicating absence of dislocation creep, in contrast to quartz, which exhibits relatively strong crystallographic preferred orientation (Fig. 11a). The topology of former melt is poorly constrained in both Type III and IV migmatite but, the shape preferred orientation of the minor phases interpreted to have crystallized from melt shows a bimodal distribution sub-perpendicular and sub-parallel to the $S_2$ foliation. These observations are neither compatible with high differential stress nor low differential stress experiments, in which the melt occurs primarily in triple point junctions without any SPO (Dell'Angelo *et al.*, 1987; Gleason *et al.*, 1999). However, in some natural samples, former melt pockets are preferentially located along grain boundaries parallel to the foliation (John & Stünitz, 1998; Sawyer, 1999; Rosenberg & Berger, 2001), indicating that the orientation of melt pocket in nature is not always in agreement with experimental studies (Rosenberg, 2001). In our study, the melt pocket orientation sub-parallel to the foliation may indicate low differential stress and high fluid/melt pressure as suggested by Cosgrove (1997).

We conclude that during evolution from Type I banded orthogneiss to Type IV nebulitic migmatite melt wetted a majority of grain contacts. The AMS study and quartz microfabrics in Type II to IV migmatites suggest that the melt fraction did not exceed the critical amount to allow free relative movement of grains without interference, i.e., the melt fraction is below the critical threshold (e.g. RCMP of Arzi, 1978; RPT of Vigneresse et al., 1996). Rosenberg & Handy (2005) argued that melt fractions of only  = 0.07 (Melt Connectivity Threshold - MCT) will enable the formation of interconnected networks of melt under dynamic conditions which will lead to a substantial strength drop. These authors suggested that weakening at the MCT probably involves localized, inter- and intragranular microcracking, as well as limited rigid body rotation of grains, without an important contribution of dislocation creep and diffusion processes at grain boundaries. However, we do not observe any strain localization associated with brittle failure and therefore we suggest that the deformation has to be accommodated by mechanisms operating homogeneously across significant rocks volumes. Material science experiments (Mabuchi *et al.*, 1997) show that weakening due to melt-enhanced grain boundary sliding at low melt fraction is an efficient mechanism allowing homogeneous deformation. We suggest that deformation of both feldspars and quartz in the Type II to Type IV migmatites occurred by melt-enhanced grain boundary sliding with a contribution to the overall deformation by dislocation creep. These characteristics are compatible with granular flow as described by Paterson (2001) accompanied by melt-enhanced diffusion and/or direct melt flow.

## Conclusions

Based on a detail field and microstructural study, we distinguish four types of gneiss/migmatite in the Gföhl gneiss complex: (i) banded orthogneiss (Type I), with distinct layers of recrystallized plagioclase, K-feldspar and quartz separated by layers of biotite; (ii) stromatic migmatite (Type II), composed of plagioclase and K-feldspar aggregates with subordinate quartz and irregular quartz aggregates—the boundaries between individual aggregates are ill-defined and rather diffuse; (iii) schlieren migmatite (Type III), which consists of plagioclase–quartz and K-feldspar–quartz enriched domains with a foliation marked only by preferred orientation of biotite and sillimanite dispersed in the rock; and, (iv) nebulitic migmatite (Type IV), with no relicts of gneissosity. We demonstrate this is a continuous sequence developed by melt-present deformation, in which the Type I banded orthogneisses and Type IV nebulitic migmatites are end members.

The progressive disintegration of the banded microstructure and the development of nebulitic migmatite is characterized by several systematic textural changes. The grain size of all felsic phases continuously decrease whereas the population density of precipitated phases increases. The new phases preferentially nucleate along high-energy like–like boundaries, causing the development of a regular distribution of individual phases. Simultaneously, the modal proportions of felsic phases evolve towards a 'granite minimum' composition. Further, this evolutionary trend is accompanied by a decrease in grain shape preferred orientation (SPO) of all felsic phases. To explain these textural and compositional changes we introduce a model of melt infiltration from an external source in which melt is argued to pass pervasively along grain boundaries through the whole rock volume. It is suggest that the individual migmatite types represent different degrees of equilibration between the host rock and migrating melt during the retrograde metamorphic evolution.

The inferred melt topology in Type I orthogneiss exhibits elongated pockets of melt oriented at a high angle to the compositional banding, indicating that the melt distribution was controlled by deformation the solid framework. Here, the microstructure exhibits features compatible with a combination of dislocation creep and grain boundary sliding deformation mechanisms. The Type II–IV microstructures developed by granular flow accompanied by melt-enhanced diffusion and/or melt flow. However, the amount of melt present never exceeded a critical threshold during the deformation to allow free rotation of biotite grains.

The model of melt infiltration based on structural and microstructural observation is supported by thermodynamic (Hasalová *et al.*, 2008) and geochemical modelling (Hasalová *et al.*, 2007). Although our data seem to be consistent with such a model, there is still a number of issues to be resolved (e.g., time-scale of the process, the character of the melt and the grain-scale deformation mechanisms enabling pervasive flow of viscous melt). Nevertheless, our model has profound consequences for the petrogenesis of migmatites, the rheology of anatectic regions during syn-orogenic exhumation and melt transport in the crust.

## Acknowledgements

This work was financially supported by the Grant Agency of Czech Academy of Sciences (Grants No. IAA311140 and No. 205/04/2065) and by an internal CNRS funding (CGS/EOST). Visits by P. Hasalová to ULP Strasbourg were funded by the French Government Foundation (BGF). We gratefully acknowledge A. Langrová from the Institute of Geology at the Czech Academy of Sciences for operating the microprobe. We would also like to thank the reviewers C. Rosenberg, R. Weinberg and H. Stünitz for their constructive comments and suggestions for improving this paper, and the Journal editor M. Brown for his careful handling of the manuscript. R. Powell and M. Brown are thanked for helpful discussions.

## References

Adams, B.L., Wright, S.I. & Kunze, K., 1993. Orientation imaging: the emergence of a new microscopy. *Metallurgical Transactions* A, **24**, 819–831.

Arbaret, L., Fernandez, A., Ježek, J., Ildefonse, B., Launeau, P. & Diot, H., 2000.Analogue and numerical modeling of shape fabrics: application to strain and flow determination in magma. *Transactions of the Royal Society of Edinburgh: Earth Sciences*, **90**, 97–109.

Arzi, A. A., 1978. Critical phenomena in the rheology of partially melted rocks. *Tectonophysics*, **44**, 173–184.

Ashworth, J. R., 1976. Petrogenesis of migmatites in the Huntly-Portsoy area, north-east Scotland. *Mineralogical Magazine*, **40**, 661–682.

Ashworth, J. R., 1979. Comparative petrography of deformed and undeformed migmatites from the Grampian Highlands of Scotland. *Geological Magazine*, **116**, 445–456.

Ashworth, J. R. & McLellan, E. L., 1985. Textures. In: *Migmatites* (ed. Ashworth, J. R.), pp. 180–204, Blackie, Glasgow.

Azpiroz, M. D. & Fernández, C., 2003. Characterization of tectono-metamorphic events using crystal size distribution (CSD) diagrams. A case study from the Acebuches metabasites (SW Spain). *Journal of Structural Geology*, **25**, 935–947.

Bailey, E. H. & Stevens, R. H., 1960. Selecting straining of K-feldspar and plagioclase on rock lobes and thin sections. *American Mineralogist*, **45**, 1020–1025.

Baratoux, L., Schulmann, K., Ulrich, S. & Lexa, O., 2005. Contrasting microstructures and deformation mechanisms in metagabbro mylonites contemporaneously deformed under different temperatures (c. 650°C and c. 750°C). In: *Deformation Mechanisms, Rheology and Tectonics: from Minerals to Lithosphere*. (eds. Gapais, D., Brun, J. P., Cobbold, P. R.), *Geological Society Special Publications*, pp. 97–125, Geological Society of London, London, UK.

Barraud, J., Gardien, V., Allemand, P. & Grandjean, P., 2001. Analogue modelling of melt segregation and migration during deformation. *Physics and Chemistry of the Earth (A)*, **26**, 317–323.

Bascou, J., Barruol, G., Vauchez, A., Mainprice, D. & Egydio-Silva, M., 2001. EBSD-measured lattice-preferred orientations and seismic properties of eclogites. *Tectonophysics*, **342**, 61–80.

Berger, A. & Roselle, G., 2001. Crystallization processes in migmatites. *American Mineralogist*, **86**, 215–224.

Blumenfeld, P. & Bouchez, J.-L., 1988. Shear criteria and migmatite deformed in the magmatic and solid states. *Journal of Structural Geology*, **10**, 361–372.

Bouchez, J.-L., 1997. Granite is never isotropic: an introduction to AMS studies of granitic rocks. In: *Granite: from segregation of melt to emplacement fabrics* (eds. J.-L. Bouchez, D.H.W. Hutton & Stephens, W.E.), pp.95–112, Kluwer, Dortrecht.

Brown, M., 1994. The generation, segregation, ascent and emplacement of granite magma: The migmatite-to-crustally-derived granite connection in thickened orogens. *Earth-Science Reviews*, **36**, 83–130.

Brown, M., Averkin, Y., McLellan, E. L. & Sawyer, E. W., 1995. Melt segregation in migmatites. *Journal of Geophysical Research*, **100**, 15655–15679.

Brown, M. & Solar, G. S., 1998a. Granite ascent and emplacement during contractional deformation in convergent orogens. *Journal of Structural Geology*, **20**, 1365–1393.

Brown, M. & Solar, G. S., 1998b. Shear zone systems and melts: Feedback relations and self-organization in orogenic belts. *Journal of Structural Geology*, **20**, 211–227.

Brown, M. A., Brown, M., Carlson, W. D. & Denison, C., 1999. Topology of syntectonic melt-flow networks in the deep crust: Inferences from three-dimensional images of leucosome geometry in migmatites. *American Mineralogist*, **84**, 1793–1818.

Brown, M. & Rushmer, T., 2006. Evolution and Differentiation of the Continental Crust. Cambridge University Press, 553 pp.

Büsch, W., Schneider, G. & Mehnert, K. R., 1974. Initial melting at grain boundaries. Part II: Melting in rocks of granodioritic, quartz dioritic and tonalitic composition. *Neues Jahrbuch Für Mineralogie Monatshefte*, **8**, 345–370.

Carlson, W. D., 1989. The significance of intergranular diffusion to the mechanism and kinetics of porphyroblast crystallization. *Contributions to Mineralogy and Petrology*, **103**, 1–24.

Cashman, K. V. & Ferry, J. M., 1988. Crystal size distribution (CSD) in rocks and the kinetics and dynamics of crystallization; 3, Metamorphic crystallization. *Contributions to Mineralogy and Petrology*, **99**, 401–415.

Cashman, K. V. & Marsh, B. D., 1988. Crystal size distribution (CSD) in rocks and the kinetics and dynamics of crystallization; 2, Makaopulu lava lake. *Contributions to Mineralogy and Petrology*, **99**, 292–305.

Chandrasekhar, S., 1961. *Hydrodynamic and Hydromagnetic Stability.* Oxford University Press, London.

Cmíral, M., Fitz Gerald, J. D., Faul, U. H. & Green, D. H., 1998. A close look at dihedral angles and melt geometry in olivine-basalt aggregates: a TEM study. *Contributions to Mineralogy and Petrology*, **130**, 336–345.

Collins, W. J. & Sawyer, E. W., 1996. Pervasive granitoid magma transfer through the lower-middle crust during non-coaxial compressional deformation. *Journal of Metamorphic Geology*, **14**, 565–579.

Connolly, J. A. D., Holness, M. B., Rubie, D. C. & Rushmer, T., 1997. Reaction-induced microcracking: An experimental investigation of a mechanism for enhancing anatectic melts extraction. *Geology*, **25**, 591–594.

Cosgrove, J. W., 1997. The influence of mechanical anisotropy on the behaviour of the lower crust. *Tectonophysics*, **280**, 1–14.

Daines, M. J. & Kohlstedt, D. L., 1997. Influence of deformation on melt topology in peridotites. *Journal of Geophysical Research*, **102**, 10257–10271.

Dallain, C., Schulmann, K. & Ledru, P., 1999. Textural evolution in the transition from subsolidus annealing to melting process, Velay Dome, French Massif Central. *Journal of Metamorphic Geology*, **17**, 61–74.

DeHoff, R. T., 1991. A geometrically general theory of diffusion controlled coarsening. *Acta Metallica and Materialia*, **39**, 2349–2360.

Dell' Angelo, L. N. & Tullis, J., 1988. Experimental deformation of partially melted granitic aggregates. *Journal of Metamorphic Geology*, **6**, 495–515.

Dell' Angelo, L. N., Tullis, J. & Yund, R. A., 1987. Transition from dislocation creep to melt-enhanced diffusion creep in fine-grained granitic aggregates. *Tectonophysics*, **139**, 325–332.

DeVore, G. W., 1959. Role of minimum interfacial free energy in determining the macroscopic features of minerals assemblages. *Journal of Geology*, **67**, 211–227.

Dougan, T. W., 1983. Textural relations in melanosomes of selected specimens of migmatitic pelitic schists: implications for leucosome-generating process. *Contributions to Mineralogy and Petrology*, **83**, 82–98.

Dudek, A., Matějovská, O. & Suk, M., 1974. Gföhl orthogneiss in the Moldanubicum of Bohemia and Moravia. *Krystalinikum*, **10**, 67–78.

Ferré, E. C., Martín-Hernández, F., Teyssier, C. & Jackson, M., 2004. Paramagnetic and ferromagnetic anisotropy of magnetic susceptibility in migmatites: measurements in high and low fields and kinematic implications. *Geophysical Journal International*, **157**, 1119–1129.

Ferré, E. C., Teyssier, C., Jackson, M., Thill, J. W. & Rainey, E. S. G., 2003. Magnetic susceptibility anisotropy: A new petrofabric tool in migmatites. *Journal of Geophysical Research*, **108**.

Flinn, D., 1969. Grain contacts in crystalline rocks. *Lithos*, **2**, 361–370.

Friedl, G., Finger, F., Paquette, J., Quadt, A., McNaughton, N. & Fletcher, I., 2004. Pre-Variscan geological events in the Austrian part of the Bohemian Massif deduced from U-Pb zircon ages. *International Journal of Earth Sciences*, **93**, 802–823.

Fyfe, W. S., 1973. The granulite facies, partial melting and the Archaean crust. *Royal Society of London Philosophical Transactions, Series, A*, **273**, 457–461.

Gardien, V., Thompson, A. B., Grujic, D. & Ulmer, P., 1995. Experimental melting of biotite + plagioclase + quartz + muscovite assemblage and implications for crustal melting. *Journal of Geophysical Research*, **100**, 15581–15591.

Garlick, S. R. & Gromet, L. P., 2004. Diffusion creep and partial melting in high temperature mylonitic gneisses, Hope Valley shear zone, New England Appalachians, USA. *Journal of Metamorphic Geology*, **22**, 45–62.

Gleason, G. C., Bruce, V. & Green, H. W., 1999. Experimental investigation of melt topology in partially molten quartzo-feldspathic aggregates under hydrostatic and non-hydrostatic stress. *Journal of Metamorphic Geology*, **17**, 705–722.

Greenfield, J. E., Clarke, G. L. & White, R. W., 1998. A sequence of partial melting reactions at Mt. Stafford, central Australia. *Journal of Metamorphic Geology*, **16**, 363–378.

Hasalová, P., Janoušek, V., Schulmann, K., Štípská, P. & Erban, V., 2007. From orthogneiss to migmatite: geochemical assessment of the melt infiltration model in the Gföhl Unit (Moldanubian Zone, Bohemian Massif). *Lithos*

Hasalová, P., Štípská, P., Powell, R., Schulmann, K., Janoušek, V. & Lexa, O., 2008. Transforming mylonitic metagranite by open-system interactions during melt flow. *Journal of Metamorphic Geology.*

Hickey, K. A. & Bell, T. H., 1996. Syn-deformational grain growth: matrix coarsening during foliation development and regional metamorphism rather than by static annealing. *European Journal of Mineralogy*, **8**, 1351–1373.

Higgins, M. D., 1998. Origin of anorthosite by textural coarsening: quantitative measurements of a natural sequence of textural development. *Journal of Petrology*, **39**, 1307–1323.

Holub, F. V., Cocherie, A. & Rossi, P., 1997. Radiometric dating of granitic rocks from the Central Bohemian Plutonic Complex (Czech Republic): Constraints on the chronology of thermal and tectonic events along the Moldanubian-Barrandian boundary. *Earth and Planetary Sciences*, **325**, 19–26.

Hrouda, F., Jelínek, V. & Hrušková, L., 1990. A package of programs for statistical evaluation of magnetic anisotropy data using IBM-PC computers. *EOS, Transactions, American Geophysical Union*, **71**, 1289.

Hrouda, F., Melka, R. & Schulmann, K., 1994. Periodical changes in fabric intensity during simple shear deformation and its implications for magnetic susceptibility anisotropy of sedimentary and volcanic rocks. *Acta Universitatis Carolinae Geologica*, **38**, 37–56.

Jelínek, V., 1978. Statistical processing of anisotropy of magnetic susceptibility measured on groups of specimens. *Studia geophysica et geodaetica*, **22**, 50–62.

Jelínek, V., 1981. Characterization of magnetic fabric of rocks. *Tectonophysics*, **79**, 63–67.

Jin, Z., Green, H. W. & Zhou, Y., 1994. Melt topology in partially molten mantle peridotite during ductile deformation. *Nature*, **372**, 164–167.

John, B. E. & Stünitz, H., 1997. Evidence for magmatic fracturing and small-scale melt segregation during pluton emplacement. In: *Processes of Melt Segregation* (eds. Bouchez, J.-L. & Clemens, J.), pp. 55–74, Klewer Press, Amsterdam.

Jordan, P., 1988. The rheology of polymineralic rocks: An approach. *Geologische Rundschau*, **77**, 285–294.

Jurewicz, S. R. & Watson, E. B., 1984. Distribution of partial melt in a felsic system -the importance of surface energy. *Contributions to Mineralogy and Petrology*, **85**, 25–29.

Kim, C.-S. & Rohrer, G. S., 2004. Geometric and Crystallographic Characterization of WC Surfaces and Grain Boundaries in WC-Co Composites. *Interface Science*, **12**, 19–27.

Kretz, R., 1966. Grain-size distribution for certain metamorphic minerals in relation to nucleation and growth. *Journal of Geology*, **74**, 147–173.

Kretz, R., 1969. On the spatial distribution of crystals in rocks. *Lithos*, **2**, 39–66.

Kretz, R., 1994. *Metamorphic Crystallization*. Wiley, New York.

Kröner, A., Wendt, I., Liew, T. C., Compston, W., Todt, W., Fiala, J., Vaňková, V. & Vaněk, J., 1988. U-Pb zircon and Sm-Nd model ages of high grade Moldanubian metasediments, Bohemian Massif, Czechoslovakia. *Contributions to Mineralogy and Petrology*, **99**, 257–266.

Kruse, R. & Stünitz, H., 1999. Deformation mechanisms and phase distribution in mafic high-temperature mylonites from the Jotun Nappe, southern Norway. *Tectonophysics*, **303**, 223–249.

Kruse, R., Stünitz, H. & Kunze, A., 2001. Dynamic recrystallization processes in plagioclase porphyroclasts. *Journal of Structural Geology*, **24**, 587–589.

Lafeber, D., 1963. On the spatial distribution of fabric elements in rock and soil fabric. *Proceedings - Australia-New Zealand Conference on Soil Mechanics and Foundation Engineering*, 4th, Adelaide 11, 185–199.

Laporte, D., Rapaille, C. & Provost, A., 1997. Wetting angle, equilibrium melt geometry, and the permeability threshold of partially molten crustal protoliths. In: *Granite: from segregation of melt to emplacement fabrics.* (eds. Bouchez, J. L., Hutton, D. H. W., Stephens, W. E.), pp. 31–54, Kluwer, Dordrecht.

Laporte, D. & Watson, E. B., 1995. Experimental and theoretical constraints on melt distribution in crustal sources: the effect of crystalline anisotropy on melt interconnectivity. *Chemical Geology*, **124**, 161–184.

Le Breton, N. & Thompson, A. B., 1988. Fluid-absent (dehydration) melting of biotite in metapelites in the early stages of crustal anatexis. *Contributions to Mineralogy and Petrology*, **99**, 226–237.

Lexa, O., 2003. Numerical approaches in structural and microstructural analyses*, Unpublished PhD Thesis, Charles University, Prague.*

Lexa, O., Štípská, P., Schulmann, K., Baratoux, L. & Kröner, A., 2005. Contrasting textural record of two distinct metamorphic events of similar P–T conditions and different durations. *Journal of Metamorphic Geology*, **23**, 649–666.

Lifshitz, I. M. & Slyozov, V. V., 1961. The kinetics of precipitation from supersaturated solid solutions. *Journal of Physics and Chemistry of Solids*, **19**, 35–50.

Lister, J. R. & Kerr, R. C., 1991. Fluid-mechanical models of crack propagation and their application to magma-transport in dykes. *Journal of Geophysical Research*, **96**, 10049–10077.

Lucas, S. B. & St.Onge, M. R., 1995. Syn-tectonic magmatism and the development of compositional layering, Ungava Orogen (northern Quebec, Canada). *Journal of Structural Geology*, **17**, 475–491.

Mabuchi, M., Jeong, H. G., Hiraga, K., & Higashi, K., 1997. Partial melting at interfaces and grain boundaries for high-strain-rate superplastic materials. *Interface Science*, **4**, 357–368.

Marchildon, N. & Brown, M., 2001. Melt Segregation in late syn-tectonic anatectic migmatites: An example from the Onawa Contact Aureole, Maine, USA. *Physics and Chemistry of the Earth*, **26**, 225–229.

Marchildon, N. & Brown, M., 2002. Grain-scale melt distribution in two contact aureole rocks: implications for controls on melt localization and deformation. *Journal of Metamorphic Geology*, **20**, 381–396.

Marchildon, N. & Brown, M., 2003. Spatial distribution of melt-bearing structures in anatectic rocks from Southern Brittany, France: implications for melt transfer at grain-to orogen-scale. *Tectonophysics*, **364**, 215–235.

Marsh, B. D., 1988. Crystal size distribution (CSD) in rocks and the kinetics and dynamics of crystallization; 1, Theory. *Contributions to Mineralogy and Petrology*, **99**, 277–291.

Martín-Hernandéz, F. & Hirth, A.M., 2003. Paramagnetic anisotropy of magnetic susceptibility in biotite, muscovite and chlorite single crystals. *Tectonophysics*, **367**, 13–28.

Matějovská, O., 1974. Petrographic characteristic of gneiss series between Mohelno and Bítov, SW Moravia. MS Geofond, Prague (in Czech).

Matte, P., Maluski, H., Rajlich, P. & Franke, W., 1990. Terrane boundaries in the Bohemian Massif: Result of large-scale Variscan shearing. *Tectonophysics*, **177**, 151–170.

McKenzie, D., 1984. The generation and compaction of partially molten rock. *Journal of Petrology*, **25**, 713–765.

McLellan, E. L., 1983. Contrasting textures in metamorphic and anatectic migmatites - an example from the Scottish Caledonides. *Journal of Metamorphic Geology*, **1**, 241–262.

Mehnert, K. R., 1971. *Migmatites and the Origin of Granitic Rocks*. Elsevier, Amsterdam.

Mehnert, K. R., Büsch, W. & Schneider, G., 1973. Initial melting at grain boundary of quartz and feldspar in gneisses and granulites. *Neues Jahrbuch Für Mineralogie Monatshefte*, **4**, 165–183.

Moazzen, M. & Modjarrad, M., 2005. Contact metamorphism and crystal size distribution studies in the Shivar aureole, NW Iran. *Geological Journal*, **40**, 499–517.

Olsen, T. S. & Kohlstedt, D. L. 1984. Analysis of dislocations in some naturally deformed plagioclase feldspars. *Physics of the Earth and Planetary Interiors*, **11**, 153–160.

Panozzo, R., 1983. The two-dimensional analysis of shape fabric using projections of lines in a plane. *Tectonophysics*, **95**, 279–295. Paterson, M. S., 2001. A granular flow theory for the deformation of partially molten rock. *Tectonophysics*, **335**, 51–61.

Peterson, T. D., 1996. A refined technique for measuring crystal size distributions in thin section. *Contributions to Mineralogy and Petrology*, **124**, 395–405.

Petford, N., 1995. Segregation of tonalitic-trondhjemitic melts in the continental crust: the mantle connection. *Journal of Geophysical Research*, **100**, 15735–15743.

Powell, R., Holland, T. & Worley, B., 1998. Calculating phase diagrams involving solid solutions via non-linear equations, with examples using THERMOCALC. *Journal of Metamorphic Geology,* **16**, 577–588.

Racek, M., Štípská, P., Pitra, P., Schulmann, K. & Lexa, O., 2006. Metamorphic record of burial and exhumation of orogenic lower and middle crust: a new tectonothermal model for the Drosendorf window (Bohemian Massif, Austria). *Mineralogy and Petrology,* **86**, 221–251.

Ramberg, H., 1981. *Gravity, deformation and the Earth's crust in theory, experiments and geological applications*. Academic Press, London.

Randolph, A. D. & Larson, M. A., 1971. *Theory of Particle Processes*. Academic Press, New York.

Rosenberg, C., 2001. Deformation of partially molten granite: a review and comparison of experimental and natural case studies. *International Journal of Earth Sciences*, **90**, 60–76.

Rosenberg, C. & Berger, A., 2001. Syntectonic melt pathways in granitic gneisses, and melt-induced transitions in deformation mechanisms. *Physics and Chemistry of the Earth (A)*, **26**, 287–293.

Rosenberg, C. & Handy, M. R., 2001. Mechanisms and orientation of melt segregation paths during pure shearing of a partially molten rock analogue (norcamphor-benzamide). *Journal of Structural Geology*, **23**, 1917–1932.

Rosenberg, C. L. & Handy, M. R., 2000. Syntectonic melt pathways during simple shearing of a partially molten rock analogue (norcamphor-benzamide). *Journal of Geophysical Research*, **105**, 3135–3149.

Rosenberg, C. L. & Riller, U., 2000. Partial-melt topology in statically and dynamically recrystallized granite. *Geology*, **28**, 7–10.

Sakai, T. & Jonas, J. J., 1984. Dynamic recrystallization: mechanical and microstructural consideration. *Acta Metallurgica*, **32**, 198–209.

Sawyer, E. W., 1994. Melt segregation in the continental crust. *Geology*, **22**, 1019–1022.

Sawyer, E. W., 1998. Formation and evolution of granite magmas during crustal reworking: the significance of diatexites. *Journal of Petrology*, **39**, 1147–1167.

Sawyer, E. W., 1999. Criteria for the recognition of partial melting. *Physics and Chemistry of the Earth*, **24**, 269–279.

Sawyer, E. W., 2001. Melt segregation in the continental crust: distribution and movement of melt in anatectic rocks. *Journal of Metamorphic Geology*, **19**, 291–309.

Schulmann, K., Kröner, A., Hegner, E., Wendt, I., Konopásek, J., Lexa, O. & Štípská, P., 2005. Chronological constraints on the pre-orogenic history, burial and exhumation of deep-seated rocks along the eastern margin of the Variscan orogen, Bohemian Massif, Czech Republic. *American Journal of Science*, **305**, 407–448.

Schulmann, K., Melka, R., Lobkowicz, M., Ledru, P., Lardeaux, J. M. & Autran, A., 1994. Contrasting styles of deformation during progressive nappe stacking at the southeastern margin of the Bohemian Massif (Thaya Dome). *Journal of Structural Geology*, **16**, 355–370.

Seng, H., 1936. Die Migmatitfrage und der Mechanismus parakristalliner Prägung. *Geologische Rundschau*, **27**, 471–492.

Spry, A. H., 1969. Metamorphic textures. *Pergamon Press*, Oxford.

Štípská, P., Schulmann, K. & Kröner, A., 2004. Vertical extrusion and middle crustal spreading of omphacite granulite: a model of syn-convergent exhumation (Bohemian Massif, Czech Republic). *Journal of Metamorphic Geology*, **22**, 179–198.

Stünitz, H., 1998. Syndeformational recrystallization - dynamic or compositionally induced? *Contributions to Mineralogy and Petrology*, **131**, 219–236.

Tajčmanová, L., Konopásek, J. & Schulmann, K., 2006. Thermal evolution of the orogenic lower crust during exhumation within a thickened Moldanubian root of the Variscan belt of Central Europe. *Journal of Metamorphic Geology*, **24**, 119–134.

Tanner, D. C., 1999. The scale-invariant nature of migmatite from the Oberpfalz, NE Bavaria and its significance for melt transport. *Tectonophysics*, **302**, 297–305.

Turner, F. J. & Weiss, L., 1963. *Structural Analysis of Metamorphic Tectonites*. McGraw Hill, New York.

Twiss, R. J., 1977. Theory and applicability of a recrystallized grain size paleopiezometer. *Pure and Applied Geophysics*, **115**, 227–244.

Urban, M., 1992. Kinematics of the Variscan thrusting in the Eastern Moldanubicum (Bohemian Massif, Czechoslovakia): evidence from the Náměšt granulite massif. *Tectonophysics*, **201**, 371–391.

van Breemen, O., Aftalion, M., Bowes, D. R., Dudek, A., Mísař, Z., Povondra, P. & Vrána, S., 1982. Geochronological studies of the Bohemian Massif, Czechoslovakia, and their significance in the evolution of Central Europe. *Transactions of the Royal Society of Edinburgh, Earth Sciences*, **73**, 89–108.

Vanderhaeghe, O., 1999. Pervasive melt migration from migmatites to leucogranite in the Shuswap metamorphic core complex, Canada: control of regional deformation. *Tectonophysics*, **312**, 35–55.

Vernon, R. H., 1974. Controls of mylonitic compositional layering during non-cataclastic ductile deformation. *Geological Magazine*, **111**, 121–123.

Vernon, R. H., 1976. *Metamorphic Processes: Reactions and Microstructure Development*. Wiley, New York.

Vernon, R. H. & Paterson, S. R., 2001. Axial-surface leucosomes in anatectic migmatites. *Tectonophysics*, **335**, 183–192.

Vielzeuf, D. & Holloway, J. R., 1988. Experimental determination of the fluid-absent melting relations in the pelitic system-consequences for crustal differentiation. *Contributions to Mineralogy and Petrology*, **98**, 257–276.

Vigneresse, J.-L., Barbey, P., Cuney, M., 1996. Rheological transitions during partial melting and crystallization with application to felsic magma segregation and transfer. *Journal of Petrology*, **37**, 1579–1600.

Walte, N. P., Bons, P. D. & Passchier, C. W., 2005. Deformation of melt-bearing systems—insight from in situ grain-scale analogue experiments. *Journal of Structural Geology*, **27**, 1666–1679.

Walte, N. P., Bons, P. D., Passchier, C. W. & Koehn, D., 2003. Disequilibrium melt distribution during static recrystallization. *Geology*, **31**, 1009–1012.

Waters, D. J. & Lovegrove, D. P., 2002. Assessing the extent of disequilibrium and overstepping of prograde metamorphic reactions in metapelites from the Bushveld aureole. *Journal of Metamorphic Geology*, **20**, 135–149.

Weinberg, R. F. & Searle, M. P., 1998. The Pangong Injection Complex, Indian Karakoram: A case of pervasive granite flow through hot viscous crust. *Journal of Geological Society*, **155**, 883–891.

Wickham, S. M., 1987. The segregation and emplacement of granitic magmas. *Journal of the Geological Society of London*, **144**, 281–297.

Willaime, C. & Gandais, M., 1977. Electron microscope study of plastic defects in experimentally deformed alkali feldspars. *Bulletin de la Societe Francaise de Mineralogie et de Cristallographie*, **100**, 263–271.

Willaime, C., Christie J. M. & Kovacs M.-P., 1979. Experimental deformation of K-feldspar single crystals. *Bulletin de Mineralogie*, **102**, 168–177.

Zapletal, K., 1990. Low-field susceptibility anisotropy of some biotite crystals. Physics of the *Earth and Planetary Interiors*, **63**, 85–97.

Závada, P., Schulmann, K., Konopásek, J., Ulrich, S. and Lexa O., in press. Extreme ductility of feldspar aggregates – melt enhanced grain boundary sliding (GBS) and creep failure: rheological implications for felsic lower crust. *Journal of Geophysical Research*.

# CHAPTER II:

## Transforming mylonitic metagranite by open-system interactions during melt flow

Accepted to Journal of Metamorphic Geology

# Transforming mylonitic metagranite by open-system interactions during melt flow

*Pavlína Hasalová [1,2] , Pavla Štípská [2], Roger Powell [3], Karel Schulmann [2],*

*Vojtěch Janoušek [1,4] and Ondrej Lexa [1,2]*

[1] Institute of Petrology and Structural Geology, Charles University, Albertov 6, 128 43, Pragu , Czech Republic

[2] Université Louis Pasteur, CGS/EOST, UMR 7517, 1 Rue Blessig, Strasbourg, France

[3] Schoolof Earth Sciences, University of Melbourne, Victoria 3010, Australia

[4] Czech Geological Survey, Klárov 3, 118 21 Prague 1, Czech Republic

## Abstract

Gneisses and migmatites of the Gföhl unit (Moldanubian Zone, Bohemian Massif) range from banded mylonitic orthogneiss with recrystallized monomineralic bands, through stromatic (metatexite) and schlieren (inhomogeneous diatexite) migmatite, to isotropic nebulite (homogeneous diatexite). This sequence was classically attributed to increasing degree of anatexis. Under the microscope, the evolution is characterised by progressive destruction of the monomineralic banding that characterises the original mylonitic orthogneiss. Throughout, the mineral assemblage is biotite–K-feldspar–plagioclase–quartz ± garnet ± sillimanite, but the mineral compositions exhibit systematic changes with progressive disintegration of the layering. From banded orthogneiss to nebulite, the garnet composition changes systematically, $Alm_{75\quad 94}Prp_{17\quad 0.8}Grs_{2.5\quad 1.2}Sps_{2\quad 11}$ and $X_{Fe}$ = 0.45    0.99, and for biotite, $X_{Fe}$ = 0.80    1. This is consistent with a decrease in equilibration temperature and pressure of 790°C and 8.5–6 kbar, to 690°C and 5–4 kbar. There is also a systematic change of whole-rock composition, marked by an increase in $SiO_2$ (71    77 wt. %) and $X_{Fe}$ (0.62    0.85) and by a decrease in $Al_2O_3$ (16    13 wt. %) and CaO (1.50    0.43 wt. %). Assuming that the rocks started with the same composition, these systematic changes indicate open-system behaviour. The predicted consequences of various open-system processes are assessed using thermodynamic modelling. The observed variations are interpreted to be a consequence of melt flow through, and interaction with the rocks, and, in order to change the rock composition sufficiently, a large volume of melt must have been involved.

**Keywords:** infiltration migmatite, melt transport, metasomatism by melt, metatexite–diatexite, thermodynamic modelling

## Introduction

In the most frequently-used descriptive classification scheme, migmatites form a continuum from stromatite to nebulite (e.g. Mehnert, 1971), or from metatexite to diatexite if interpretation of origin is taken into account (e.g. Brown, 1973). Stromatite and metatexite exhibit migmatitic banding that was produced by metamorphic differentiation, mainly associated with partial melting, while nebulite and diatexite do not show continuous migmatitic banding. The textural transition from stromatite to nebulite is commonly interpreted to be the result of increasing degree of partial melting, whereby the solid matrix loses its cohesion and becomes melt-supported. When such a process is demonstrated or when such an interpretation is accepted, the textural varieties are referred to as metatexite and diatexite, respectively (Sawyer, 1998; Milord *et al.*, 2001). Estimated melt contents in diatexites deduced from field studies vary between 20 and 40 mol. % (e.g. Sawyer, 1998; Milord *et al.*, 2001, White *et al.*, 2003), which is consistent with the experimentally determined 'solid to liquid' transition (Arzi 1978; Wickham, 1987; Vigneresse *et al.*, 1996). In felsic rocks, such an amount of melt may only be attained at upper amphibolite facies conditions if melt or $H_2O$ are introduced, or if the temperature reached granulite-facies conditions (e.g. White *et al.*, 2005 and references therein). However, it has been shown that the destruction of pre-migmatite or migmatite banding may also occur at lower melt fractions (McLellan, 1983; Sawyer 1994, 1996; Dallain *et al.*, 1999). These authors suggest that solid state annealing in conjunction with incipient anatexis can result in apparent "granite-like" texture. Hence, apparently, several distinct processes may lead to the formation of nebulites and not all nebulites may be interpreted as diatexites.

When melt is present in a rock, the melt can move, and therefore such metamorphism may be a closed or an open-system process. In a generally-accepted scheme, called here the '*melt loss*' model, the melt is thought to form or collect for example around porphyroblasts, parallel to the foliation or in dilatant structures. With increasing melt production, a mesoscale interconnected network develops, capable of allowing the draining of melt (Marchildon & Brown, 2003). Given the commonly-observed lack of re-hydration reactions on cooling (Powell & Downes 1990; Brown, 2001; White & Powell, 2002), most migmatites have lost melt and such systems are considered as open with respect to melt loss.

The second open-system model considers '*melt redistribution*' involving the existence of rock volumes from which melt is lost and volumes into which melt is introduced (Marchildon & Brown, 2001; Milord *et al.*, 2001). The third open-system model may be called '*transformation by melt*' and relates to melt movement through rocks that causes chemical changes of the protolith (e.g. Mehnert, 1971, p.285). This model was largely abandoned several decades ago for crustal rocks, although such a mechanism has been invoked in recent studies concerned with metasomatic processes in the mantle, being referred to as reactive porous melt flow (e.g. Nielson & Wilshire, 1993; Van der Wal & Bodinier, 1996; Kelemen *et al.*, 1997; Reiners, 1998).

The first model is the most generally accepted one, and arises from studies that have been carried out almost exclusively on metasedimentary rocks (Barbey *et al.*, 1996; Fitzsimons, 1996; Greenfield *et al.*, 1996, 1998; Milord *et al.*, 2001; Milord & Sawyer, 2003). However, granitic orthogneiss is another abundant crustal lithology capable of producing granitic melt, but with some exceptions (e.g. Sawyer & Barnes, 1988; Hand & Dirks, 1992; Sawyer, 1998; Dallain *et al.*, 1999), they have not been the focus of studies of anatexis and melt transport. Processes that operate at subsolidus conditions on a prograde path in orthogneiss are dominated by textural modifications, involving various recrystallization mechanisms, rather than changes that affect the stable mineral assemblage. Recrystallization leads to the formation of augen and ribbons of recrystallized aggregates of plagioclase, K-feldspar, quartz and micas, and may result in monomineralic bands (Gapais, 1989; Schulmann *et al.*, 1996; Závada *et. al.*, in press). In studying the melting process, the lack of prograde changes in stable mineral assemblage in a granitic orthogneiss may be taken as an advantage because, in most cases, they begin to melt with mineralogy identical to their protolith, similar from one granitic orthogneiss to another, e.g. with quartz–plagioclase–K-feldspar ± biotite ± muscovite. The rock structure, commonly characterized by monomineralic recrystallized bands and augen of felsic minerals, starts to disintegrate progressively in the presence of melt (Dallain *et al.*, 1999). Such disintegration of K-feldspar, plagioclase and quartz bands cannot be studied in metasediments where such monomineralic banding of felsic minerals does not occur. It may also be expected that a deformed granitic orthogneiss starts to melt with whole-rock chemistry more or less unchanged from that of the protolith granite. Therefore, geochemical and mineralogical changes may be interpreted to result mainly from the melting process.

Textural variations between banded mylonite orthogneiss, stromatic and nebulitic migmatites are observed within the Gföhl orthogneiss complex in the Bohemian Massif, and have been considered as reflecting increasing degree of anatexis (Dudek *et al.*, 1974; Matějovská, 1974). However, Hasalová *et al.* (2008) studied the Gföhl gneiss using microstructural analysis and interpreted the variations to originate from a single protolith by progressive disintegration of banded mylonite orthogneiss by interaction with infiltrating melt. In this model, melt passes through and interacts with a rock volume and changes its macroscopic and microscopic appearance. Consequently, the individual migmatite types represent different degrees of interaction with melt. Hasalová *et al.* (2007) studied whole-rock major-element, trace-element and Sr–Nd isotopic data and concluded that the systematic variations reflect open-system behaviour during transformation from banded orthogneiss into nebulitic migmatite. However these approaches could not, for example, determine *P–T* conditions of equilibration and could not quantify the volume of melt involved.

In the first part of the current paper, the variations in mineral chemistry of the four rock types are used to determine the *P–T* conditions of equilibration of the Gföhl migmatites, based on mineral equilibria modelling. These *P–T* conditions are interpreted to reflect an exhumation path along which equilibration of orthogneiss occurred while melt was still present, the equilibration becoming progressively localized between rock volumes that became melt-absent with decreasing temperature. In the second part, forward modelling is used to discuss possible open-system processes that may have operated in the rocks in order to assess the conclusion of Hasalová *et al.* (2008) that melt infiltration must be the main process involved in the rock transformations. The mineral equilibria and rock chemistry consequences of melt infiltration are then considered in detail.

## Geological setting and previous studies

The area studied is situated at the eastern extremity of the Gföhl Unit (Moldanubian Zone, Bohemian Massif), one of the largest Variscan migmatite terrains in Europe (Fig.1). This terrain is formed mainly of high-grade felsic gneisses and migmatites (the so-called Gföhl gneiss) showing a range of varieties from banded orthogneiss without macroscopic signs of melting through to isotropic nebulitic migmatite. The gneisses and migmatites include large bodies of high-pressure felsic granulite, eclogite and peridotite (for review see Schulmann *et al.* 2005; Fig. 1).

The structural succession in the area studied approximately 10 km north of Znojmo (Fig. 1) is defined by vertical $S_1$ structures that are locally preserved in low strain domains of a flat $S_2$ foliation (Fig. 2) that is connected with the development of a large crustal-scale shear zone (Urban *et al.*, 1992; Hasalová *et al.*, 2008). The transition from the $S_1$ to the $S_2$ fabric is marked by centimetre to meter scale open to isoclinal folds with NE–SW oriented axes and sub-horizontal axial planes. This structural evolution has been explained in terms of vertical extrusion of orogenic lower crust and its lateral spreading at mid-crustal levels (Štípská *et al.*, 2004; Schulmann *et al.*, 2005; Franěk *et al.*, 2006; Racek *et al.*, 2006). This exhumation was accompanied by a profound textural modification of rocks that is the focus of the present study.

The conditions of retrogression in the proximity of the area studied were determined to be 770–720°C and 4.5–4 kbar for the HP granulites (Tajčmanová *et al.*, 2006). The metamorphism is dated at ca. 340–323 Ma (van Breemen *et al.*, 1982).

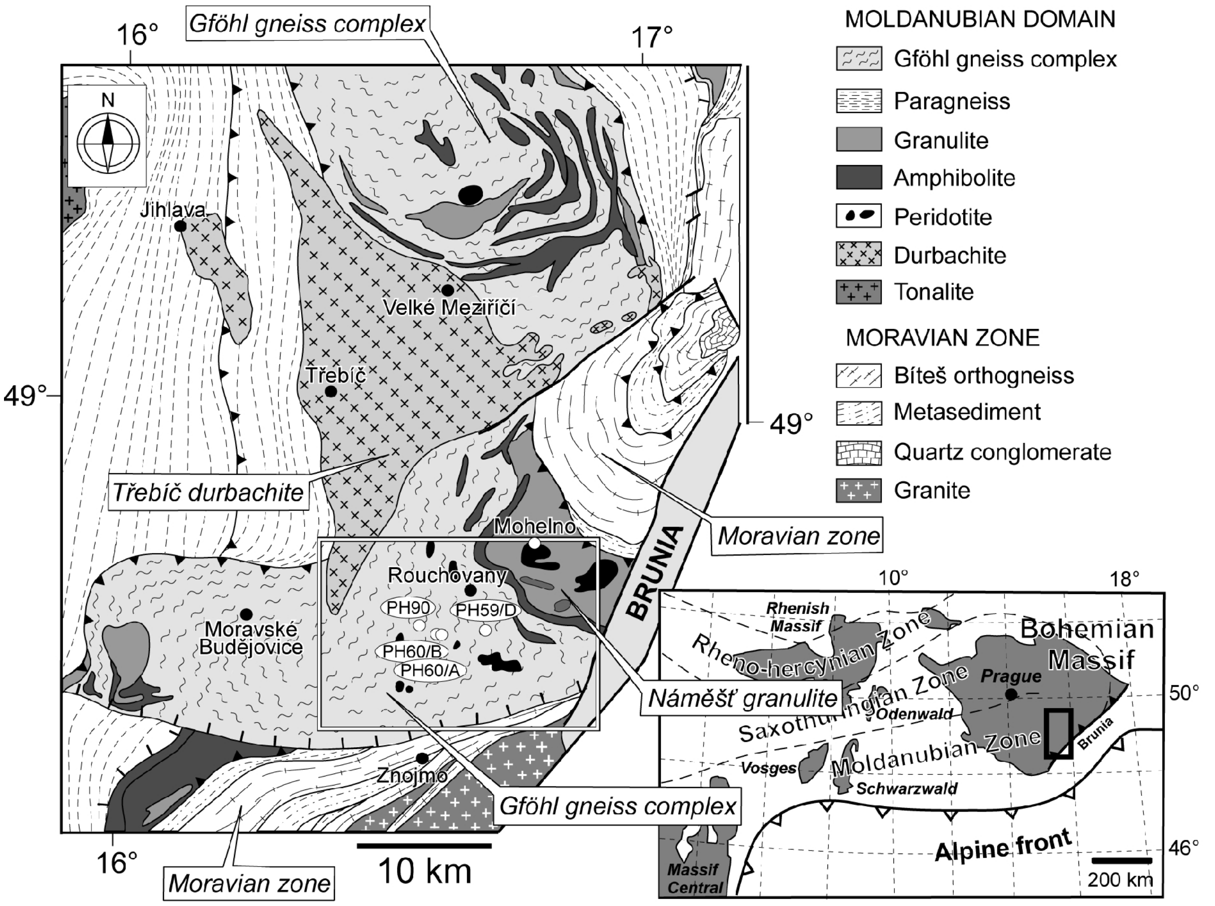


**Fig.1:** *Geological map of the eastern part of the Bohemian Massif (the area studied is outlined). Location of four characteristic samples used in this study is shown. The lower right inset displays the general location of the Bohemian Massif within the European Variscides.*

Hasalová *et al.* (2008) established a continuous structural succession for the Gföhl orthogneiss (Fig. 2), in four 30 km long NW–SE profiles across the Gföhl orthogneiss complex. The rocks in the succession have been classified in terms of the descriptive scheme of Mehnert (1971), as used by Matějovská (1974) in this area, as follows: banded orthogneiss (Type I), stromatic migmatite (Type II), schlieren migmatite (Type III) and nebulitic migmatite (Type IV).

The migmatite variations are identified both on outcrop and regional scales. The banded orthogneiss (Type I) is relatively rare, the size of individual occurrences ranging from centimetre to outcrop-scale relicts commonly surrounded by an anastomosing network of Type II migmatites. The Type II and III migmatites are the most common, having diffuse and gradational contacts between them. The nebulitic migmatite (Type IV) is rare, forming irregular or elongated bodies, several centimetres to several meters across, with relatively sharp boundaries towards Type III migmatite that surrounds them (Fig. 2).

The banded orthogneiss (Type I) (Fig. 2a), characterized by the presence of monomineralic layers of plagioclase, K-feldspar, quartz and biotite, is folded and reworked by the $D_2$ deformation. This $S_1$ compositional banding is locally preserved in elongated relict domains (Fig. 2) that are surrounded by a tightly folded $S_1$ fabric. The $S_1$ fabric is commonly transposed into the new $S_2$ foliation and the resulting fabric is characterized by banded structure with polymineralic K-feldspar- and plagioclase-rich domains resembling stromatic migmatite (Type II, Fig. 2b). The stromatic migmatite gradually passes into more isotropic rock resembling schlieren migmatite (Type III, Fig. 2c) that still contains rootless folds modifying the relicts of the $S_1$ fabric. This rock type alternates with irregular bodies or elongated lenses of felsic nebulitic migmatite (Type IV, Fig. 2d). The field observations suggest that the Type I banded orthogneiss is progressively transformed into Type II and III migmatites. Whether the Type IV is transformed from Type III cannot be assessed from field observations, because of the lack of $S_1$ structures in Type IV and the relatively sharp boundaries between Type III and IV.

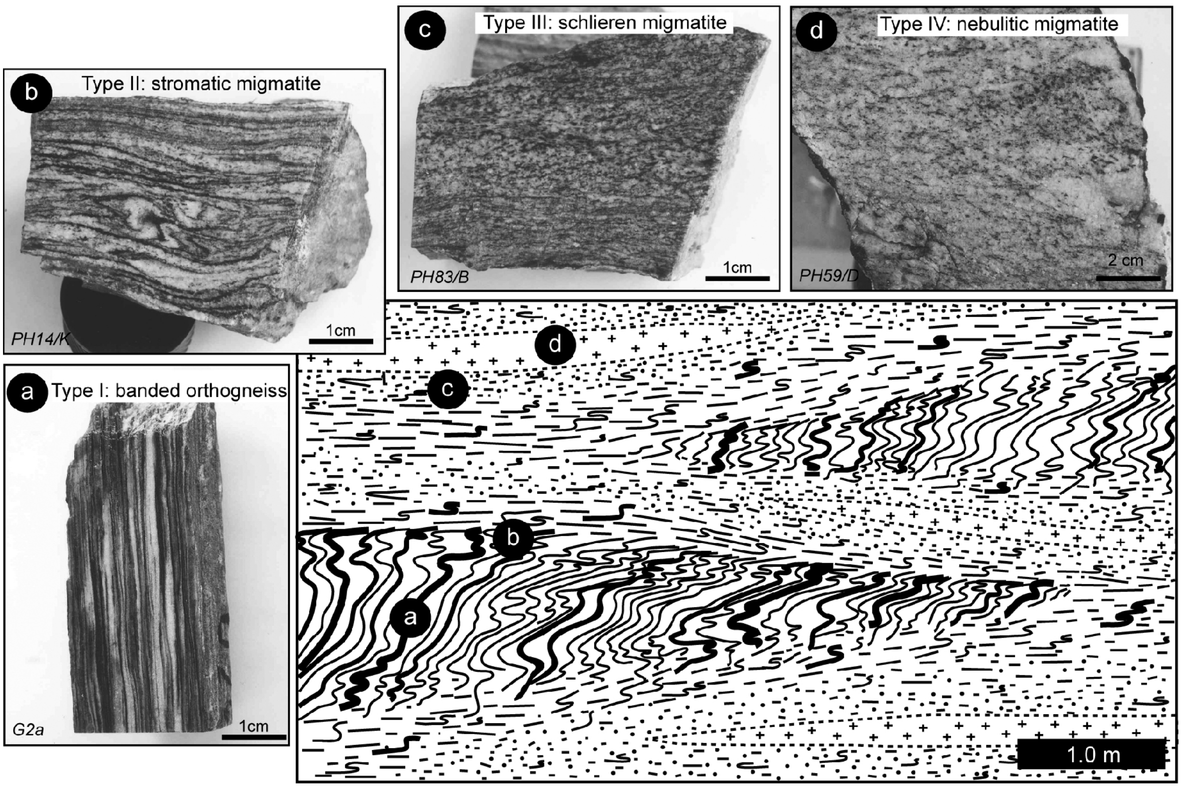


**Fig. 2:** *Individual gneiss and migmatite types, and a sketch of the outcrop relationships (modified after Hasalová et al., 2008). (a) Banded orthogneiss with $S_1$ monomineralic layering, (b) stromatic migmatite in folded and transposed $S_1$ foliation by $S_2$ fabric, (c) schlieren migmatite surrounds stromatic migmatite in $S_2$ foliation, (d) macroscopically isotropic nebulitic migmatite forms elongated lenses that are inferred to be interconnected in the $S_2$ foliation.*

## Petrology, mineral and whole-rock chemistry

### *Analytical procedures and abbreviations*

Minerals were analysed using the scanning electron microscope CamScan S4 with attached Link ISIS 300 EDX microanalytical system at Charles University in Prague, Czech Republic, in point beam mode at 20 kV and 10 nA, and using the Cameca SX100 at the Geological Institute of the Czech Academy of Sciences in point beam mode at 15 kV and 10 nA. Representative mineral analyses are summarized in Tables 1–4. Whole-rock major-element analyses (Table were carried out on the ICP-MS at the University Louis Pasteur in Strasbourg. The mineral abbreviations used are: mu = muscovite, qtz = quartz, g = garnet, bi = biotite, ky = kyanite, sill = sillimanite, and = andalusite, pl = plagioclase, cd = cordierite, liq = liquid; ilm = ilmenite; ru = rutile; Alm = Fe/(Ca + Fe + Mg + Mn), Prp = Mg/(Ca + Fe + Mg + Mn), Grs = Ca/(Ca + Fe + Mg + Mn), Sps = Mn/(Ca + Fe + Mg + Mn), $X_{Fe}$ = Fe/(Fe + Mg), An = Ca/(Ca + Na + K), Ab = Na/(Ca + Na + K), Or = K/(Ca + Na + K). The isopleths notations used are: $x$(g) = Fe/(Fe + Mg), $z$(g) = Ca/(Ca + Fe + Mg + Mn), $m$(g) = Mn/(Ca + Fe + Mg + Mn), $x$(bi) = Fe/(Fe + Mg), $ca$(pl) = Ca/(Ca + Na).

### *Microstructures and mineralogy*

The mineral assemblage in all rock types is biotite, K-feldspar, plagioclase and quartz; all the migmatite types commonly also contain garnet and sillimanite. Kyanite was not found in thin section, but was identified rarely in mineral concentrates. Apatite, monazite, zircon, xenotime, ilmenite and rutile are present as accessory phases.

#### *Microstructure of felsic phases*

The most obvious difference in microstructures between the individual migmatite types involves the different distribution of K-feldspar, plagioclase and quartz that ranges from monomineralic recrystallized bands to an isotropic distribution, and also involves a different amount and distribution of interstitial felsic phases.

The banded orthogneiss (Type I) shows alternation of monomineralic bands of recrystallized K-feldspar, quartz and plagioclase separated by discrete bands rich in biotite, garnet and sillimanite (Figs. 2a & 3a). Some feldspar boundaries in K-feldspar and plagioclase bands are coated by small interstitial plagioclase, quartz and K-feldspar grains (arrows in Figs 3a & 4a). The stromatic migmatite (Type II) is composed of plagioclase-rich, K-feldspar-rich

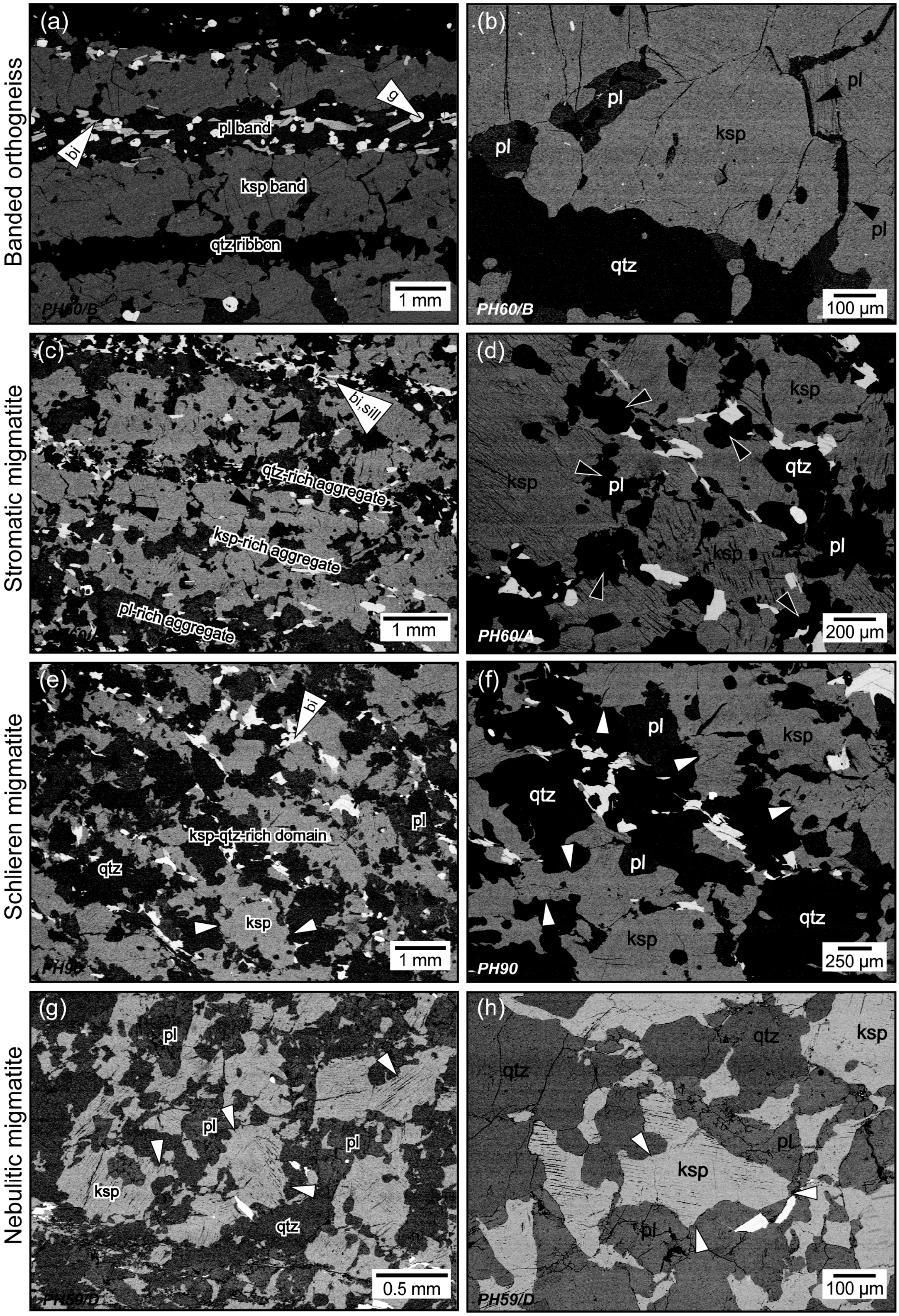
Banded orthogneiss
(a)
g
bi
pl band
ksp band
qtz ribbon
1 mm
PH60/B
(b)
pl
pl
ksp
pl
pl
qtz
100 µm
PH60/B
Stromatic migmatite
(c)
bi,sill
qtz-rich aggregate
ksp-rich aggregate
pl-rich aggregate
1 mm
(d)
ksp
ksp
pl
qtz
ksp
pl
200 µm
PH60/A
Schlieren migmatite
(e)
bi
pl
ksp-qtz-rich domain
qtz
ksp
1 mm
(f)
pl
ksp
qtz
pl
qtz
ksp
250 µm
PH90
Nebulitic migmatite
(g)
pl
pl
pl
ksp
qtz
0.5 mm
(h)
qtz
ksp
qtz
pl
ksp
pl
100 µm
PH59/D

and quartz-rich aggregates (Fig. 3b). The limits between individual aggregates are ill-defined and commonly traced only by biotite-sillimanite-rich layers. The interstitial quartz and feldspar grains coat the majority of feldspar boundaries (arrows in Fig. 3b). In the schlieren migmatite (Type III), plagioclase–quartz-rich and K-feldspar–quartz-rich domains are present (Fig. 3c). Most of the large feldspar grains show cuspate boundaries that are completely coated by interstitial feldspar and quartz (arrows in Fig. 3c). The Type IV (nebulitic migmatite) is isotropic, without banding, resembling the characteristic texture of diatexites (Figs 2d & 3d). The microstructure of this migmatite shows cuspate shapes of large feldspars and quartz grains and high proportion of interstitial grains along feldspar boundaries (Fig. 3d).

According to Sawyer (1999, 2001), interstitial grains as observed in the migmatites are interpreted as having crystallized from a granitic melt, and the cuspate shapes of feldspars as a result of their dissolution in the presence of melt. The progressively higher proportion of interstitial grains and more cuspate form of feldspar towards the Type III and IV migmatites is interpreted according to Mehnert (1971) and Sawyer (1999) to result from an increasing degree of melt–rock interaction involving dissolution and precipitation. The microstructural evolution of the Type I orthogneiss to Type IV migmatites are interpreted to result from the progressive disintegration of monomineralic banding of a single mylonitic orthogneiss in the presence of melt.

### *Microstructural position of biotite, garnet and sillimanite*

Whereas biotite is found in all thin sections, garnet and sillimanite are present in most of them. These minerals display different textural appearance and position in four rock types. In Type I orthogneiss and Type II migmatite, small idiomorphic garnet is typically arranged into aggregates or appears as individual grains that are commonly associated with biotite and sillimanite along or within the plagioclase bands (Fig. 4b, c). In Type III and IV migmatites the garnet is atoll-shaped and randomly distributed in the matrix; garnet also tends to be bigger and the proportion lower than in Type I and II (Fig. 4d). Biotite defines the foliation in all the migmatite types. In rock Type I and II biotite appears as large elongated flakes in layers separating felsic bands (Figs. 2a & 4c) and in Type III and IV migmatites it is dissipated in the

**Fig. 3:** *Textural features of the Types I-IV (SEM backscatter images). (a–b) Type I: Alternation of monomineralic bands of recrystallized K-feldspar, quartz and plagioclase separated by discrete bands rich in biotite, garnet and sillimanite. Some K-feldspar grains are traced by interstitial plagioclase and quartz (black arrows). (c–d) Type II: Plagioclase-rich, K-feldspar-rich and quartz-rich aggregates. Interstitial feldspars and quartz coat most of the feldspar boundaries (black arrows). (e–f) Type III: Alternation of plagioclase–K-feldspar-rich and K-feldspar–quartz-rich domains. Large irregular K-feldspar grains with highly lobate boundaries (white arrows) are embayed in plagioclase, K-feldspar and quartz. (g-h) Type IV: Isotropic structure with large feldspars with highly lobate shapes (white arrows), note the different scale.*

matrix, commonly exhibiting highly corroded shapes (Fig. 4e). Sillimanite is in all the migmatite types associated with biotite, and also defines the foliation (Fig. 4c), although in Type III and IV migmatites it also may occur in aggregates and nodules that are up to 5 cm in size (Fig. 4f).

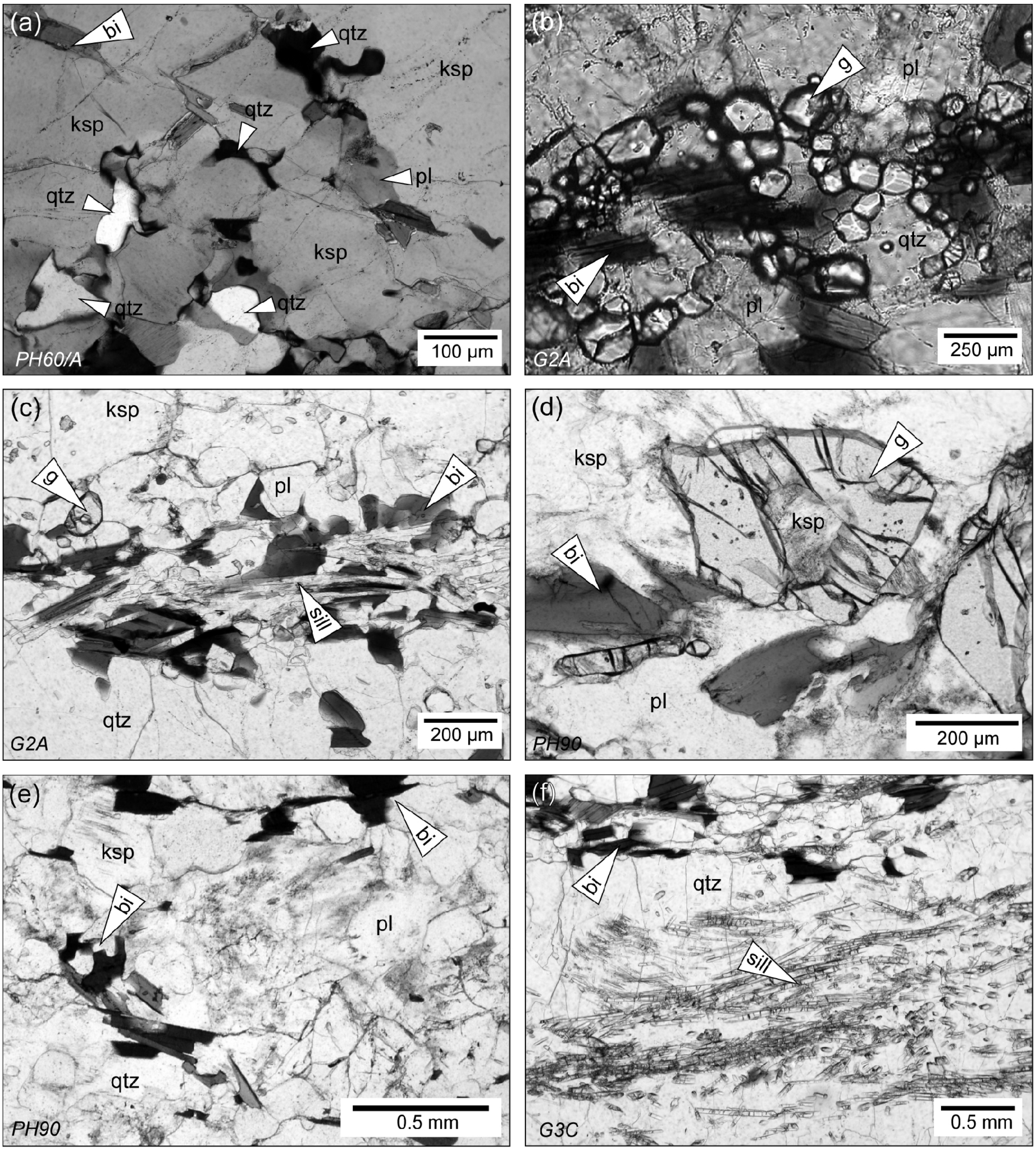


**Fig.4:** *Photomicrographs showing typical textures and mineral assemblages. (a) K-feldspar with highly cuspate interstitial plagioclase and quartz (example from Type II). (b) Small idiomorphic garnet associated with biotite along the boundary of plagioclase band (in Type I & II). (c) Biotite is locally associated with fibrolitic sillimanite (Type I). (d) Large atoll-shaped garnet with biotite in felsic matrix (in Type III & IV). (e) K-feldspar-quartz-rich domain with random distribution of biotite. Biotite preferred orientation emphasizes the foliation (Type III). (f) Large sillimanite nodules parallel to the foliation (in Types III and IV).*

## Mineral chemistry

### Garnet

Garnet in all rock types is rich in almandine with minor pyrope, spessartine and grossular and does not exhibit compositional zoning. In Type I orthogneiss it has the lowest $X_{Fe}$ of rock types ($Alm_{73–81}Prp_{15–21}Sps_{2–3}Grs_{2–3.5}$, $X_{Fe}$ = 0.77–0.85; Figs. 5 & 6a). Garnet in Type II migmatite has higher almandine and spessartine and lower pyrope contents ($Alm_{78–84}Prp_{8–15}Sps_{4–7}Grs_{2–2.5}$, $X_{Fe}$ = 0.84–0.91). In Type III and IV migmatites the garnet composition is $Alm_{84–86}Prp_{2–3}Sps_{9–13}Grs_{1.7–2}$, $X_{Fe}$ = 0.96–0.97 and $Alm_{91–94}Prp_{0–2}Sps_{4–15}Grs_{1.2–2}$, $X_{Fe}$ = 0.99–1.0, respectively. Consequently, garnet displays systematic changes that involve

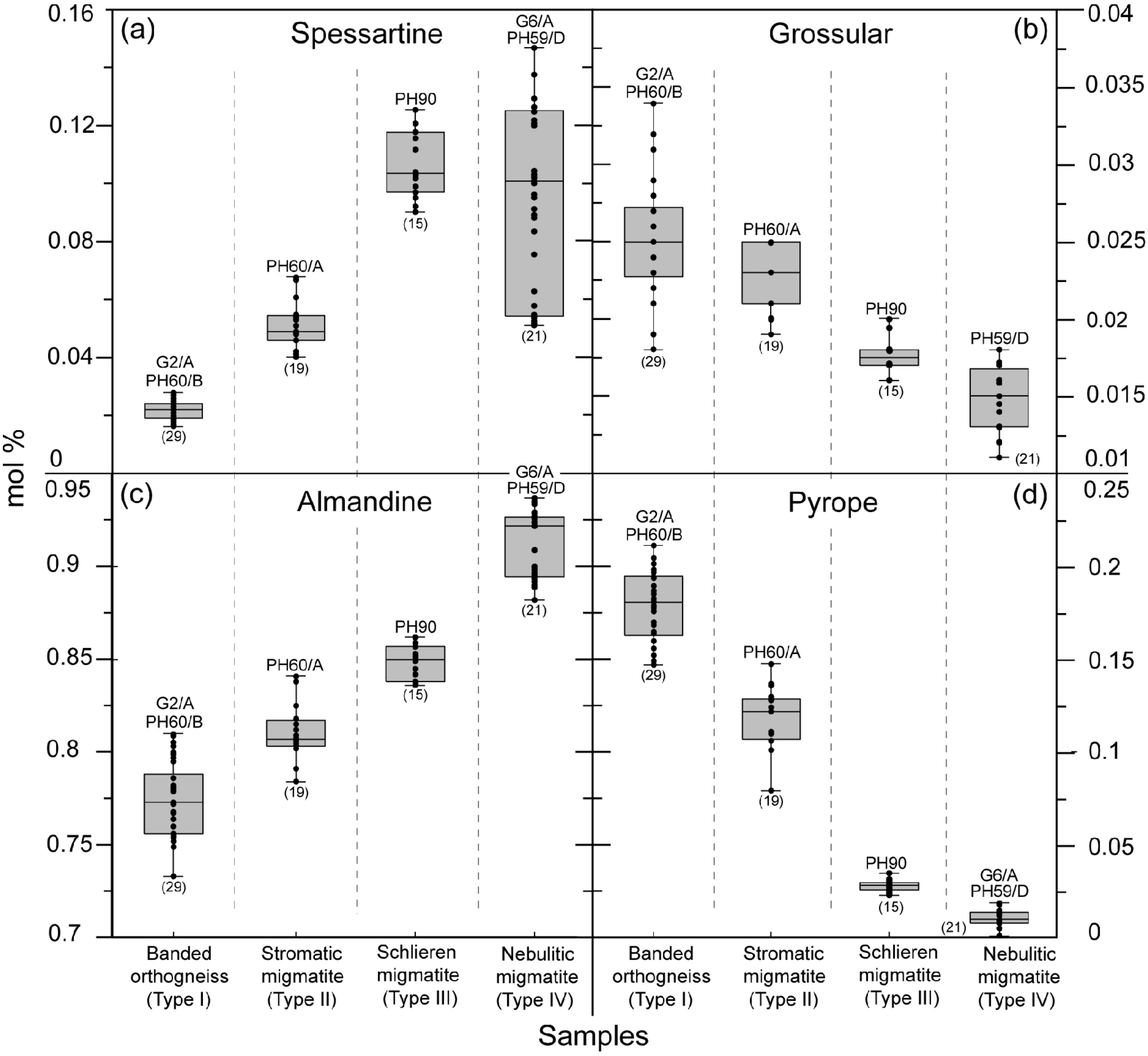


**Fig. 5:** *Garnet composition trends of (a) spessartine, (b) grossular, (c) almandine, (d) pyrope. The data are summarized in box-plots of individual component content (mol. %) vs. rock type. Individual boxes show median and 1st and 3rd quartile of the component content. The whiskers represent a statistical estimate of the data range, where outliers are not plotted. The number of analyses is marked.*

progressive increase in content of almandine (73   91 mol. %) and spessartine (2   13 mol. %), and increase in $X_{Fe}$ (0.77   1.0 mol. %) that are accompanied by a decrease in pyrope (15   0 mol. %) and grossular (3.5   1.2 mol. %) (Figs. 5 & 6a, Tables 1 & 4).

### *Biotite*

Within each type, biotite does not display significant chemical variation. In the Type I orthogneiss biotite has $X_{Fe}$ = 0.45, Ti = 0.18–0.27 pfu and $Al^{VI}$ = 0.36–0.80 pfu. Towards Type IV migmatite $X_{Fe}$ and $Al^{VI}$ exhibit systematically higher values ($X_{Fe}$ = 0.57, $Al^{VI}$ = 0.44–0.53 pfu in Type II; $X_{Fe}$ = 0.78, $Al^{VI}$ = 0.60–0.76 pfu in Type III and $X_{Fe}$ = 0.92, $Al^{VI}$ = 0.85–1.05 pfu in Type IV) while the amount of Ti decreases (Ti = 0.20–0.28 pfu in Type II; Ti = 0.16–0.20 pfu in Type III; Ti = 0.01–0.04 pfu in Type IV) (Fig. 6b, Tables 1 & 4).

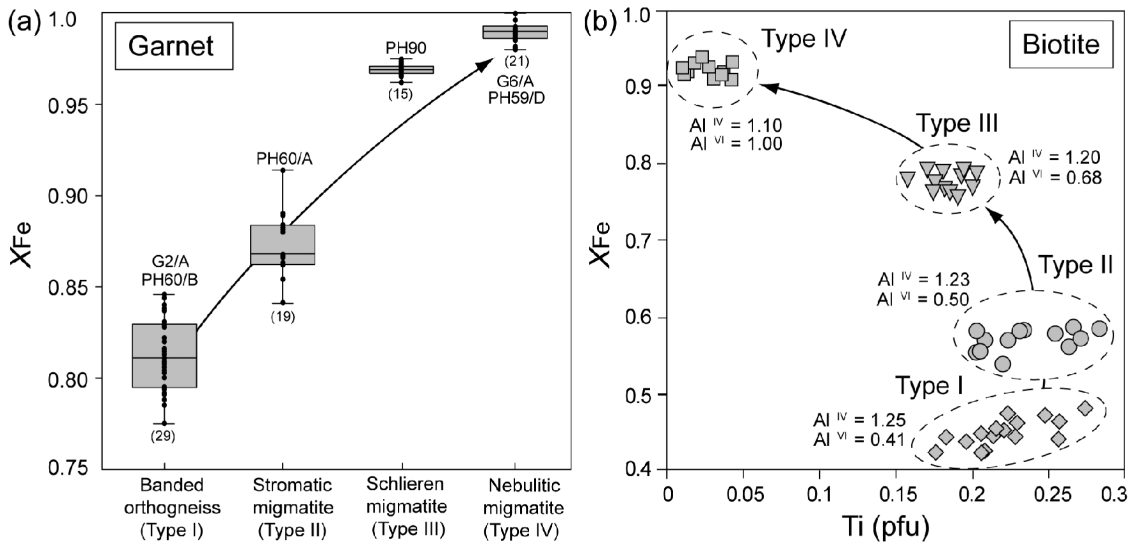


**Fig. 6:** *(a) Garnet $X_{Fe}$ plotted in a form of box-plot diagram ($X_{Fe}$ vs. rock type). For details see the caption for Fig. 4. (b) Compositional changes of biotite.*

### *K-feldspar*

K-feldspar composition does not vary significantly, except for barium and higher albite contents in cores of large highly cuspate K-feldspar grains that commonly show preferentially-oriented exsolved albite. In both the K-feldspar and plagioclase aggregates the composition is $Or_{79–95}$ $Ab_{5–8}$ $An_{0–1}$ (Tables 3 & 4). Barium shows progressively lower contents from Type I orthogneiss to Type IV migmatite (Ba = 0.06–0.20 pfu for Type I; 0.02–0.08 for Type II: 0.00–0.05 for Type III and 0.00–0.02 for Type IV).

*Table 1: Representative analyses of garnet and biotite.*

| | **Banded orthogneiss (Type I)** | | **Stromatic migmatite (Type II)** | | **Schlieren migmatite (Type III)** | | **Nebulitic migmatite (Type IV)** | |
|---|---|---|---|---|---|---|---|---|
| Sample | G2A | | PH60/A | | PH90 | G3c | PH59/D | |
| Mineral | g | bi | g | bi | g | bi | g | bi |
| Wt.% oxide | | | | | | | | |
| $SiO_2$ | 37.75 | 35.98 | 36.92 | 36.14 | 36.03 | 35.00 | 36.68 | 36.18 |
| $TiO_2$ | 0.00 | 3.85 | 0.00 | 3.96 | 0.00 | 2.99 | 0.00 | 0.17 |
| $Al_2O_3$ | 21.50 | 17.97 | 21.20 | 18.66 | 20.43 | 19.52 | 21.15 | 22.38 |
| FeO | 34.57 | 17.78 | 35.77 | 19.96 | 36.88 | 24.49 | 40.14 | 27.14 |
| MnO | 1.13 | 0.00 | 2.64 | 0.00 | 4.97 | 0.00 | 1.89 | 0.00 |
| MgO | 4.26 | 11.03 | 2.63 | 8.01 | 0.67 | 4.20 | 0.41 | 1.34 |
| CaO | 1.12 | 0.00 | 0.72 | 0.12 | 0.58 | 0.24 | 0.41 | 0.00 |
| $Na_2O$ | 0.00 | 0.00 | 0.00 | 0.00 | 0.04 | 0.00 | 0.00 | 0.00 |
| $K_2O$ | 0.00 | 9.66 | 0.00 | 9.31 | 0.02 | 9.75 | 0.00 | 9.39 |
| Total | 100.33 | 96.28 | 99.88 | 96.17 | 99.62 | 96.18 | 100.68 | 96.61 |
| Cations/Charges | 8/24 | 8/24 | 8/24 | 8/24 | 8/24 | 8/24 | 8/24 | 8/24 |
| Si | 3.00 | 2.78 | 2.99 | 2.84 | 2.98 | 2.81 | 3.00 | 2.91 |
| Ti | 0.00 | 0.22 | 0.00 | 0.23 | 0.00 | 0.18 | 0.00 | 0.01 |
| Al | 2.02 | 1.63 | 2.02 | 1.73 | 1.99 | 1.85 | 2.04 | 2.12 |
| $Fe^{3+}$ | 0.00 | 0.00 | 0.00 | 0.00 | 0.07 | 0.00 | 0.00 | 0.00 |
| $Fe^{2+}$ | 2.30 | 1.15 | 2.42 | 1.31 | 2.48 | 1.64 | 2.75 | 1.83 |
| Mn | 0.08 | 0.00 | 0.18 | 0.00 | 0.35 | 0.00 | 0.13 | 0.00 |
| Mg | 0.51 | 1.27 | 0.32 | 0.94 | 0.08 | 0.50 | 0.05 | 0.16 |
| Ca | 0.10 | 0.00 | 0.06 | 0.01 | 0.05 | 0.02 | 0.04 | 0.00 |
| Na | 0.00 | 0.00 | 0.00 | 0.00 | 0.01 | 0.00 | 0.00 | 0.00 |
| K | 0.00 | 0.95 | 0.00 | 0.93 | 0.00 | 1.00 | 0.00 | 0.96 |
| Total | 8.00 | 8.00 | 8.00 | 8.00 | 8.00 | 8.00 | 8.00 | 8.00 |
| $X_{Fe}$ | 0.82 | 0.47 | 0.88 | 0.58 | 0.97 | 0.77 | 0.98 | 0.92 |
| Alm | 0.77 | | 0.81 | | 0.84 | | 0.93 | |
| Prp | 0.17 | | 0.11 | | 0.03 | | 0.02 | |
| Grs | 0.03 | | 0.02 | | 0.02 | | 0.01 | |
| Sps | 0.03 | | 0.06 | | 0.11 | | 0.04 | |

$X_{Fe}$ = Fe/(Fe+Mg); *Alm* = Fe/(Fe+Mg+Ca+Mn); *Prp* = Mg/ (Fe+Mg+Ca+Mn); *Grs* = Ca/ (Fe+Mg+Ca+Mn); *Sps* = Mn/ (Fe+ Mg+Ca+Mn)

### *Plagioclase*

Plagioclase composition within each of the individual rock types varies according to the microstructural position (Fig. 7 & Table 2), with less sodic plagioclase ($An_{15–30}$) forming the matrix and small interstitial grains or films and rims of larger grains being more albitic ($An_{0–15}$). Interstitial grains or thin films trace K-feldspar boundaries in the K-feldspar aggregates, whereas albitic rims occur on more calcic plagioclase grains in plagioclase aggregates (Fig. 7).

The most anorthite-rich plagioclase occurs in the plagioclase domains in the Type I orthogneiss. It exhibits homogeneous oligoclase cores ($An_{19–28}$) and more sodic ($An_{5–22}$), clear 2–10 m thick rims at the boundaries with K-feldspar (Fig. 7). Simultaneously with progressively thicker albite rims on plagioclase grains from Type I orthogneiss to Type IV migmatite, both the plagioclase grains and their rims become more sodic (the variation in compositions from core to rim is: Type II – $An_{11–26}$ $An_{1–18}$; Type III – $An_{11–17}$ $An_{0–13}$; Type IV – $An_{5–10}$ $An_{0–5}$) (Tables 2 & 4). The orthoclase component of plagioclase remains nearly constant at 1–2 mol. % (Table 2).

Small interstitial plagioclase grains and films in the K-feldspar aggregates (Figs. 3a & 7) are generally more sodic than the grains in the plagioclase aggregates. The anorthite content of this interstitial plagioclase decreases in a fashion similar to the trend in the plagioclase aggregates, but with lower anorthite contents (Type I – $An_{12–17}Ab_{75–91}Or_{0–1}$; Type II – $An_{4–8}Ab_{91–95}Or_{0–1}$; Type III – $An_{2–5}Ab_{95–99}Or_{0–1}$; Type IV – $An_{0–3}Ab_{98–100}Or_{0–1}$) (Fig. 7).

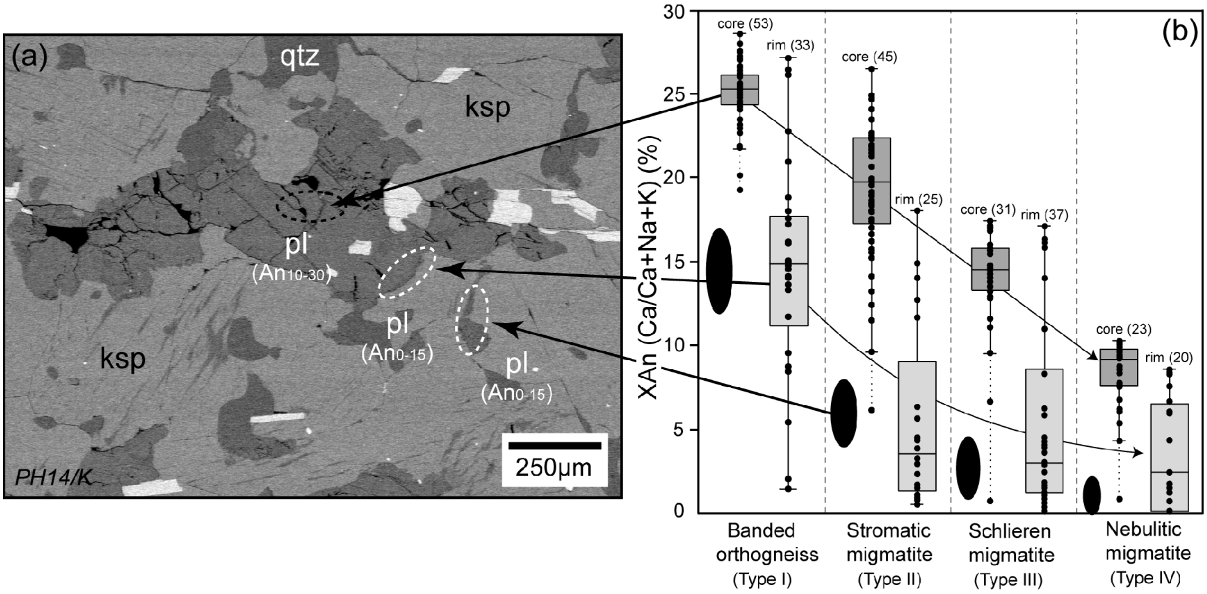


**Fig. 7:** *Plagioclase composition with respect to its microstructural position. (a) SEM backscatter image shows typical microstructural varieties of plagioclase (example from Type II migmatite). Large plagioclase from plagioclase aggregates (black dashed circle), interstitial plagioclase tracing the K-feldspar boundaries or rims of large plagioclase (white dashed circles). (b) Composition of texturally different plagioclase. In each rock type cores are more anorthite-rich than adherent rims and interstitial plagioclase (shown as black ellipses). From Type I to IV, each plagioclase microstructural type displays enrichment in sodium. The compositional data are summarized in box-plots of anorthite content (mol. %) vs. rock type (for detail see caption for Fig. 4, the outliers are plotted), with number of analyses in brackets.*

### *Whole-rock chemistry*

Representative whole-rock chemical analyses are given for the four rock types in Table 5. The whole suite is slightly peraluminous (A/CNK = 1.1–1.2) and broadly granitic in composition ($SiO_2$ = 68–78 wt. %). There is a tendency to smooth, systematic changes in many geochemical parameters from Type I orthogneiss to Type IV migmatite. After an initial dramatic drop (from Type I to Type III), the concentrations of most of the major-element oxides ($Al_2O_3$, $TiO_2$, $FeO_t$, MgO and CaO) level off at $SiO_2$ of 73–74 wt. % and do not change significantly thereafter

(Type IV migmatite). Alkalis ($Na_2O$ and $K_2O$) and $P_2O_5$ are rather scattered or show a feeble tendency to increase from the Type I orthogneiss to the Type IV migmatite. The $X_{Fe}$ increases towards the nebulitic migmatite (Table 5). Additional detailed information on the whole-rock geochemistry is given in Hasalová *et al.* (2007).

The whole-rock compositions and mineral chemistries are related for higher variance mineral assemblages, whereas the mineral compositions reflect *P–T* conditions in lower variance mineral assemblages. The rock and mineral compositions are plotted in the $Al_2O_3$–FeO–MgO compositional diagram where tie triangles of sillimanite-biotite-garnet plot at progressively higher $X_{Fe}$ values from Type I orthogneiss to Type IV migmatite, corresponding to the rock compositional changes (Fig. 8). However, the assemblage garnet–sillimanite–biotite–K-feldspar–quartz–plagioclase–ilmenite–rutile–melt is trivariant in the NCKFMASHTO system and quadrivariant in the more complete MnNCKFMASHTO system. Therefore, the observed changes in $X_{Fe}$ of the minerals in the four rock types are most likely to reflect also changes in *P–T* conditions (as established in the pseudosection modelling below).

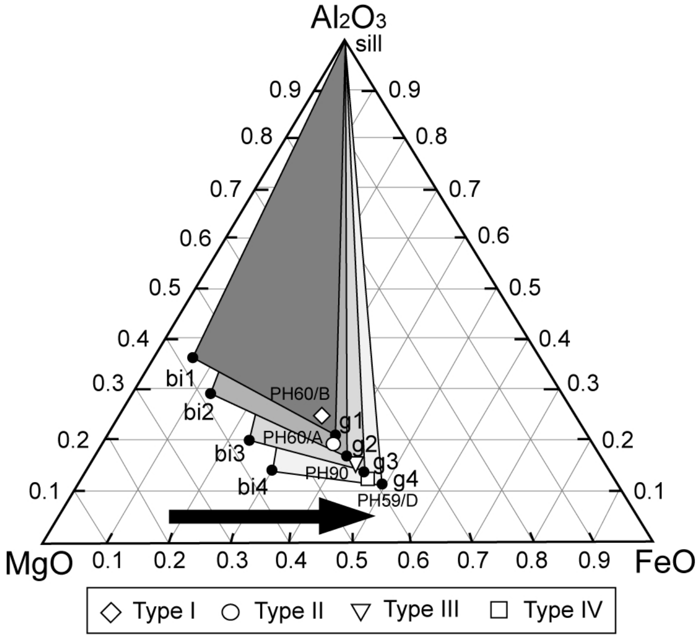


**Fig. 8:** *$Al_2O_3$–FeO–MgO compositional diagram. Type I orthogneiss to Type IV migmatite mineral compositions (black symbols, mol. %) and whole-rock analyses (opens symbols, mol. %) plot at progressively higher $X_{Fe}$ values.*

The progressive shift of rock compositions to higher $X_{Fe}$ values could be explained by originally-different protoliths. However as progressive evolution from Type I orthogneiss to Type IV migmatite is suggested in the field, the rocks are considered to have originally the same protolith and variations of the whole-rock chemistry are ascribed to open-system processes during metamorphism.

*Table 2: Representative analyses of plagioclase.*

| | Banded orthogneiss (Type I) | | | | | | Stromatic migmatite (Type II) | | | | | |
|---|---|---|---|---|---|---|---|---|---|---|---|---|
| Sample | PH60/B | | PH60/B | | PH60/B | | PH14/K | PH60/A | PH60/A | | PH14/K | PH60/A |
| Position | pl core | | pl rim | | pl film | | pl core | | pl rim | | pl film | |
| Wt. % oxide | | | | | | | | | | | | |
| $SiO_2$ | 61.70 | 61.24 | 66.12 | 66.49 | 67.48 | 66.39 | 63.41 | 66.94 | 63.21 | 64.65 | 64.57 | 67.24 |
| $Al_2O_3$ | 24.12 | 24.18 | 20.99 | 20.81 | 20.16 | 21.20 | 22.54 | 20.58 | 23.81 | 22.78 | 22.61 | 20.27 |
| CaO | 5.29 | 5.88 | 3.05 | 1.88 | 2.83 | 3.25 | 3.94 | 0.80 | 3.72 | 2.55 | 2.78 | 1.07 |
| $Na_2O$ | 8.59 | 8.65 | 9.81 | 10.79 | 9.63 | 9.46 | 9.63 | 10.93 | 9.00 | 9.42 | 10.03 | 11.50 |
| $K_2O$ | 0.43 | 0.17 | 0.10 | 0.17 | 0.12 | 0.08 | 0.19 | 0.14 | 0.51 | 0.83 | 0.17 | 0.10 |
| Total | 100.12 | 100.11 | 100.07 | 100.14 | 100.22 | 100.37 | 99.75 | 99.48 | 100.25 | 100.23 | 100.16 | 100.18 |
| Cations/Charges | 5/16 | 5/16 | 5/16 | 5/16 | 5/16 | 5/16 | 5/16 | 5/16 | 5/16 | 5/16 | 5/16 | 5/16 |
| Si | 2.73 | 2.71 | 2.91 | 2.91 | 2.98 | 2.93 | 2.80 | 2.95 | 2.79 | 2.85 | 2.84 | 2.93 |
| Al | 1.26 | 1.26 | 1.09 | 1.07 | 1.05 | 1.10 | 1.17 | 1.07 | 1.24 | 1.18 | 1.17 | 1.04 |
| Ca | 0.25 | 0.28 | 0.14 | 0.09 | 0.13 | 0.15 | 0.19 | 0.04 | 0.18 | 0.12 | 0.13 | 0.05 |
| Na | 0.74 | 0.74 | 0.84 | 0.92 | 0.83 | 0.81 | 0.83 | 0.93 | 0.77 | 0.80 | 0.85 | 0.97 |
| K | 0.02 | 0.01 | 0.01 | 0.01 | 0.01 | 0.00 | 0.01 | 0.01 | 0.03 | 0.05 | 0.01 | 0.01 |
| Total | 5.00 | 5.00 | 5.00 | 5.00 | 5.00 | 5.00 | 5.00 | 5.00 | 5.00 | 5.00 | 5.00 | 5.00 |
| Endmembers | | | | | | | | | | | | |
| Ab | 0.73 | 0.72 | 0.85 | 0.90 | 0.85 | 0.84 | 0.81 | 0.95 | 0.79 | 0.83 | 0.86 | 0.95 |
| An | 0.25 | 0.27 | 0.15 | 0.09 | 0.14 | 0.16 | 0.18 | 0.04 | 0.18 | 0.12 | 0.13 | 0.05 |
| Or | 0.02 | 0.01 | 0.01 | 0.01 | 0.01 | 0.00 | 0.01 | 0.01 | 0.03 | 0.05 | 0.01 | 0.01 |

| | Schlieren migmatite (Type III) | | | | | | Nebulitic migmatite (Type IV) | | | | | |
|---|---|---|---|---|---|---|---|---|---|---|---|---|
| Sample | PH90 | | PH90 | | PH90 | | PH59/D | | PH59/D | | PH59/D | |
| Position | pl core | | pl rim | | pl film | | pl core | | pl rim | | pl film | |
| Wt. % oxide | | | | | | | | | | | | |
| $SiO_2$ | 65.04 | 64.89 | 68.19 | 67.64 | 67.73 | 67.98 | 65.97 | 65.57 | 67.79 | 66.70 | 67.39 | 67.50 |
| $Al_2O_3$ | 21.11 | 21.62 | 19.51 | 19.41 | 19.65 | 19.51 | 21.51 | 21.59 | 19.90 | 22.39 | 20.28 | 20.25 |
| CaO | 2.53 | 2.86 | 0.29 | 0.42 | 0.67 | 0.35 | 2.07 | 1.70 | 0.28 | 0.00 | 0.20 | 0.35 |
| $Na_2O$ | 10.53 | 10.23 | 11.87 | 11.86 | 11.73 | 11.73 | 10.46 | 11.03 | 11.86 | 10.81 | 11.76 | 11.89 |
| $K_2O$ | 0.15 | 0.20 | 0.15 | 0.10 | 0.09 | 0.17 | 0.14 | 0.30 | 0.02 | 0.22 | 0.11 | 0.05 |
| Total | 99.36 | 99.80 | 100.01 | 99.43 | 99.87 | 99.74 | 100.15 | 100.19 | 99.86 | 100.12 | 99.75 | 100.03 |
| Cations/Charges | 5/16 | 5/16 | 5/16 | 5/16 | 5/16 | 5/16 | 5/16 | 5/16 | 5/16 | 5/16 | 5/16 | 5/16 |
| Si | 2.87 | 2.87 | 2.97 | 2.96 | 2.96 | 2.97 | 2.89 | 2.86 | 2.96 | 2.92 | 2.94 | 2.94 |
| Al | 1.10 | 1.10 | 1.00 | 1.00 | 1.01 | 1.01 | 1.11 | 1.11 | 1.02 | 1.15 | 1.04 | 1.04 |
| Ca | 0.12 | 0.11 | 0.01 | 0.02 | 0.03 | 0.02 | 0.10 | 0.08 | 0.01 | 0.00 | 0.01 | 0.02 |
| Na | 0.90 | 0.89 | 1.00 | 1.01 | 0.99 | 0.99 | 0.89 | 0.93 | 1.00 | 0.92 | 1.00 | 1.00 |
| K | 0.01 | 0.02 | 0.01 | 0.01 | 0.01 | 0.01 | 0.01 | 0.02 | 0.00 | 0.01 | 0.01 | 0.00 |
| Total | 5.00 | 5.00 | 5.00 | 5.00 | 5.00 | 5.00 | 5.00 | 5.00 | 5.00 | 5.00 | 5.00 | 5.00 |
| Endmembers | | | | | | | | | | | | |
| Ab | 0.88 | 0.87 | 0.98 | 0.98 | 0.96 | 0.97 | 0.89 | 0.91 | 0.99 | 0.99 | 0.98 | 0.98 |
| An | 0.12 | 0.11 | 0.01 | 0.02 | 0.03 | 0.02 | 0.10 | 0.08 | 0.01 | 0.00 | 0.01 | 0.02 |
| Or | 0.01 | 0.02 | 0.01 | 0.01 | 0.00 | 0.01 | 0.01 | 0.02 | 0.00 | 0.01 | 0.01 | 0.00 |

*An* = Ca/(Ca + Na + K); *Ab* = Na/(Ca + Na + K); *Or* = K/(Ca + Na + K)

*Table 3: Representative analyses of K-feldspar.*

| | Banded orthogneiss (Type I) | | Stromatic migmatite (Type II) | | Schlieren migmatite (Type III) | | Nebulitic migmatite (Type IV) | |
|---|---|---|---|---|---|---|---|---|
| Sample | PH60/B | PH60/B | PH14/K | PH14/K | PH90 | PH90 | PH59/C | PH59/C |
| Wt.% oxide | | | | | | | | |
| $SiO_2$ | 64.69 | 64.36 | 64.37 | 64.50 | 64.51 | 64.89 | 63.97 | 64.19 |
| $Al_2O_3$ | 18.41 | 18.26 | 18.55 | 18.70 | 18.38 | 18.38 | 18.98 | 18.79 |
| FeO | 0.00 | 0.00 | 0.10 | 0.09 | 0.10 | 0.09 | 0.00 | 0.00 |
| CaO | 0.05 | 0.06 | 0.04 | 0.05 | 0.01 | 0.05 | 0.05 | 0.01 |
| $Na_2O$ | 2.24 | 1.35 | 1.56 | 2.15 | 1.41 | 1.55 | 1.22 | 1.41 |
| $K_2O$ | 13.96 | 15.37 | 15.04 | 14.16 | 15.18 | 15.11 | 15.65 | 15.22 |
| BaO | 0.39 | 0.40 | 0.13 | 0.10 | 0.08 | 0.07 | 0.00 | 0.02 |
| Total | 99.73 | 99.79 | 99.78 | 99.74 | 99.67 | 100.15 | 99.86 | 99.62 |
| Cations/Charges | 5/16 | 5/16 | 5/16 | 5/16 | 5/16 | 5/16 | 5/16 | 5/16 |
| Si | 2.97 | 2.97 | 2.97 | 2.96 | 2.98 | 2.98 | 2.94 | 2.96 |
| Al | 0.99 | 1.00 | 1.01 | 1.01 | 1.00 | 0.99 | 1.03 | 1.02 |
| Ca | 0.00 | 0.00 | 0.00 | 0.00 | 0.00 | 0.00 | 0.00 | 0.00 |
| Na | 0.12 | 0.20 | 0.14 | 0.19 | 0.13 | 0.14 | 0.11 | 0.13 |
| K | 0.90 | 0.82 | 0.88 | 0.83 | 0.89 | 0.88 | 0.92 | 0.89 |
| Ba | 0.01 | 0.01 | 0.00 | 0.00 | 0.00 | 0.00 | 0.00 | 0.00 |
| Total | 5.00 | 5.00 | 5.00 | 5.00 | 5.00 | 5.00 | 5.00 | 5.00 |
| Endmembers | | | | | | | | |
| Ab | 0.12 | 0.19 | 0.14 | 0.19 | 0.12 | 0.13 | 0.10 | 0.12 |
| An | 0.00 | 0.00 | 0.00 | 0.00 | 0.00 | 0.00 | 0.00 | 0.00 |
| Or | 0.88 | 0.80 | 0.86 | 0.81 | 0.88 | 0.86 | 0.89 | 0.88 |

*An* = Ca/(Ca + Na + K); *Ab* = Na/(Ca + Na + K); *Or* = K/(Ca + Na + K)

## Pseudosection modelling

The aim of this section is to assess the ability of various closed- and open-system processes to account for the observed mineral and whole-rock chemistry variations and to estimate the amount of melt involved and/or produced. In order to achieve this, the *P–T* conditions of equilibration for each migmatite type are estimated. Then the likely rock composition and mineral assemblage of the granite protolith is estimated to allow the forward modelling of the processes.

### Calculation methods

The calculations were performed using THERMOCALC 3.25 (Powell *et al.,* 1998; 2005 upgrade) and the internally-consistent thermodynamic dataset 5.5 (Holland & Powell, 1998; November 2003 upgrade). The pseudosections for the four rock types were calculated in the system MnO–$Na_2O$–CaO–$K_2O$–FeO–MgO–$Al_2O_3$–$SiO_2$–$H_2O$–$TiO_2$–O (MnNCKFMASHTO). The rock compositions were used with the molar amounts of these oxides normalized to 100% (Table 5). The amount of $H_2O$ to include in the rock compositions was chosen after construction of *T–M*($H_2O$) sections, in order to explain the observed mineral assemblage and chemistry of the minerals.

*Table 4: Summary of important changes in mineral chemistry throughout the studied sequence.*

| | **Banded orthogneiss (Type I)** | **Stromatic migmatite (Type II)** | **Schlieren migmatite (Type III)** | **Nebulitic migmatite (Type IV)** |
|---|---|---|---|---|
| *Garnet* | | | | |
| $X_{Fe}$ | 0.77–0.85 (0.81) | 0.84–0.91 (0.87) | 0.96–0.97 (0.97) | 0.98–1.00 (0.99) |
| Alm | 0.73–0.81 (0.77) | 0.78–0.84 (0.81) | 0.84–0.86 (0.85) | 0.91–0.94 (0.93) |
| Prp | 0.15–0.21 (0.18) | 0.08–0.15 (0.12) | 0.02–0.03 (0.03) | 0.00–0.02 (0.01) |
| Sps | 0.02–0.03 (0.02) | 0.04–0.07 (0.05) | 0.09–0.13 (0.11) | 0.04–0.07 (0.05) |
| Grs | 0.02–0.03 (0.02) | 0.02–0.03 (0.02) | 0.01–0.02 (0.02) | 0.01–0.02 (0.02) |
| *Biotite* | | | | |
| $X_{Fe}$ | 0.42–0.48 (0.45) | 0.55–0.59 (0.57) | 0.77–0.79 (0.78) | 0.91–0.94 (0.92) |
| Ti (p.f.u) | 0.18–0.27 (0.22) | 0.20–0.28 (0.23) | 0.16–0.20 (0.19) | 0.01–0.04 (0.02) |
| $Al^{IV}$ (p.f.u) | 1.06–1.33 (1.25) | 1.18–1.30 (1.23) | 1.18–1.20 (1.20) | 1.08–1.16 (1.10) |
| $Al^{VI}$ (p.f.u) | 0.36–0.80 (0.42) | 0.44–0.53 (0.50) | 0.60–0.76 (0.68) | 0.85–1.05 (1.00) |
| *Plagioclase* | | | | |
| An (pl core) | 0.19–0.28 (0.25) | 0.11–0.26 (0.19) | 0.11–0.17 (0.14) | 0.05–0.10 (0.08) |
| An (pl rim) | 0.05–0.22 (0.14) | 0.01–0.18 (0.06) | 0.00–0.13 (0.05) | 0.00–0.10 (0.03) |
| *K-feldspar* | | | | |
| Ba (p.f.u) | 0.06–0.20 (0.13) | 0.02–0.08 (0.04) | 0.00–0.05 (0.02) | 0.00–0.02 (0.00) |
| Or | 0.79–0.90 (0.85) | 0.81–0.94 (0.88) | 0.79–0.93 (0.88) | 0.86–0.95 (0.89) |

$X_{Fe}$ = Fe/(Fe+ Mg); *An* = Ca/(Ca+Na+K); *Or* = K/(Ca+Na+K). Shown are the ranges and average values (in brackets).

In the absence of activity-composition models for all minerals in the MnNCKFMASHTO system, for some minerals a choice had to be made between activity-composition models that involve Mn and models that involve $Fe^{3+}$ and Ti. Garnet stability at low temperature depends largely on Mn, therefore the Mn-bearing activity-composition model (THERMOCALC documentation, Powell & Holland, 2004) was preferred to the $Fe^{3+}$-bearing model (White *et al.*, 2007) as the solubility of $Fe^{3+}$ in garnet is small. A consequence of garnet being the only Mn-bearing mineral is that it is stable in the whole range of modelled *P-T* conditions, but this is likely to be realistic in the range of *P–T* conditions of interest. For biotite, the activity-composition model that includes Ti-$Fe^{3+}$ substitution (White *et al.*, 2007) was chosen for calculations rather than a Mn-bearing activity-composition model, as Mn incorporation in biotite is minor but Ti and $Fe^{3+}$ influence considerably the stability of biotite. The activity-composition relationship for ilmenite is from White *et al.* (2000), for melt is from White *et al.* (2007), for the feldspars is from Holland & Powell (2003) and for paragonite–muscovite is from Coggon & Holland (2002).

Modelling of the likely protolith composition and modelling of closed-system melting was also done in the MnNCKFMASHTO system. Modelling of the open-system processes involving melt loss, melt gain and simulation of the equilibration of the rock with infiltrating melt was done in the NCKFMASH system, because the available activity-composition model for melt does not include Ti, $Fe^{3+}$ and Mn. The activity-composition relationships used are as follows: for melt, from White *et al.* (2007); for the feldspars, from Holland & Powell (2003); for paragonite-muscovite, from Coggon & Holland (2002); and, for other NCKFMASH phases, from White *et al.* (2001).

*Tab. 5: Whole-rock compositions*

| | Whole-rock compositions (ICP-MS) | | | | Whole-rock compositions from modelling | | |
|---|---|---|---|---|---|---|---|
| Rock type | **Banded orthogneiss (Type I)** | **Stromatic migmatite (Type II)** | **Schlieren migmatite (Type III)** | **Nebulitic migmatite (Type IV)** | **reconstructed mu-bi granite** | **melt loss composition after 11mol. % of melt loss in a closed system (820°C/9kbar)** | **melt loss compositions after 40mol. % of melt loss in H2O saturated system (800°C/9kbar)** |
| Sample | PH 60/B | PH 60/A | PH89/C | PH 59/D | | | |
| Wt. % | | | | | | | |
| $SiO_2$ | 69.90 | 71.40 | 72.30 | 77.10 | 69.57 | 69.21 | 67.62 |
| $TiO_2$ | 0.45 | 0.36 | 0.20 | 0.10 | 0.46 | 0.51 | 0.71 |
| $Al_2O_3$ | 15.40 | 15.20 | 12.70 | 12.70 | 16.02 | 16.06 | 16.26 |
| $Fe_2O_3$* | 3.25 | 2.59 | 1.76 | 1.68 | 2.91 | 3.13 | 4.14 |
| MnO | 0.04 | 0.03 | 0.03 | 0.03 | 0.07 | 0.07 | 0.10 |
| MgO | 1.04 | 0.74 | 0.27 | 0.15 | 0.98 | 1.06 | 1.43 |
| CaO | 1.50 | 1.42 | 0.69 | 0.43 | 1.74 | 1.84 | 2.23 |
| $Na_2O$ | 2.87 | 3.08 | 2.43 | 2.79 | 2.90 | 2.81 | 2.50 |
| $K_2O$ | 4.98 | 4.99 | 5.86 | 5.21 | 5.35 | 5.31 | 4.99 |
| $P_2O_5$ | 0.18 | 0.21 | 0.24 | 0.23 | — | — | — |
| Total | 99.61 | 100.02 | 96.48 | 100.42 | 100.00 | 100.00 | 99.99 |
| A/CNK | 1.20 | 1.17 | 1.10 | 1.15 | 1.17 | 1.17 | 1.20 |
| $X_{Fe}$ | 0.61 | 0.64 | 0.77 | 0.85 | 0.63 | 0.62 | 0.62 |

* Total iron as $Fe_2O_3$

### *P-T conditions of last equilibration*

In determining the conditions of last equilibration, it is assumed that the assemblage tends to continuously equilibrate until it becomes fluid or melt absent (Guiraud *et al.*, 2001; Powell *et al.,* 2005; Štípská & Powell, 2005). For migmatites, this is likely to correspond to the *P–T* conditions on the retrograde path where the rock becomes melt-poor, or possibly when it crosses the solidus. As the position of the solidus in a *P–T* pseudosection depends largely on the amount of $H_2O$ present in the rock, the amount of $H_2O$ that should be used in the calculation of a *P–T* pseudosection must be evaluated using a $T$–$M(H_2O)$ pseudosection.

The $T$–$M(H_2O)$ calculations are shown only for the Type I orthogneiss (Fig. 9). The observed assemblage is g–sill–bi–pl–ksp–qtz–ru–ilm, with garnet $X_{Fe}$ = 0.70–0.84, biotite $X_{Fe}$ =

0.42–0.58 and spessartine in garnet of 1–4 mol. %, therefore a section at 7 kbar in the stability field of sillimanite was chosen for modelling.

The major features of the diagram involve the assemblage g–sill–bi–liq–pl–ksp–qtz–ru–ilm at high temperature and high $M(H_2O)$, the liquid-out line that appears at low $M(H_2O)$ at high temperature and the muscovite-in line at around 715°C for $M(H_2O)$ higher than about 1.54 mol. %. From the point of view of a cooling path for a hypothetical rock at intermediate $M(H_2O)$ (arrow A, Fig. 9), there is a molar increase of biotite coupled with molar decrease of garnet, muscovite becomes stable just before sillimanite-out is crossed at 715°C. Such a rock would have a preserved assemblage of g–bi–liq–mu–pl–ksp–qtz–ru. This does not correspond to the observed mineral assemblage. For a rock at intermediate $M(H_2O)$ (black arrow B, Fig. 9), the molar proportions of garnet and melt decrease in favour of biotite until the liquid-out line is reached and muscovite appears. Such a rock would have a preserved assemblage g–sill–bi–mu–pl–ksp–qtz–ru–ilm (along the gray arrow B, Fig. 9) that, again, does not correspond to the observed assemblage.

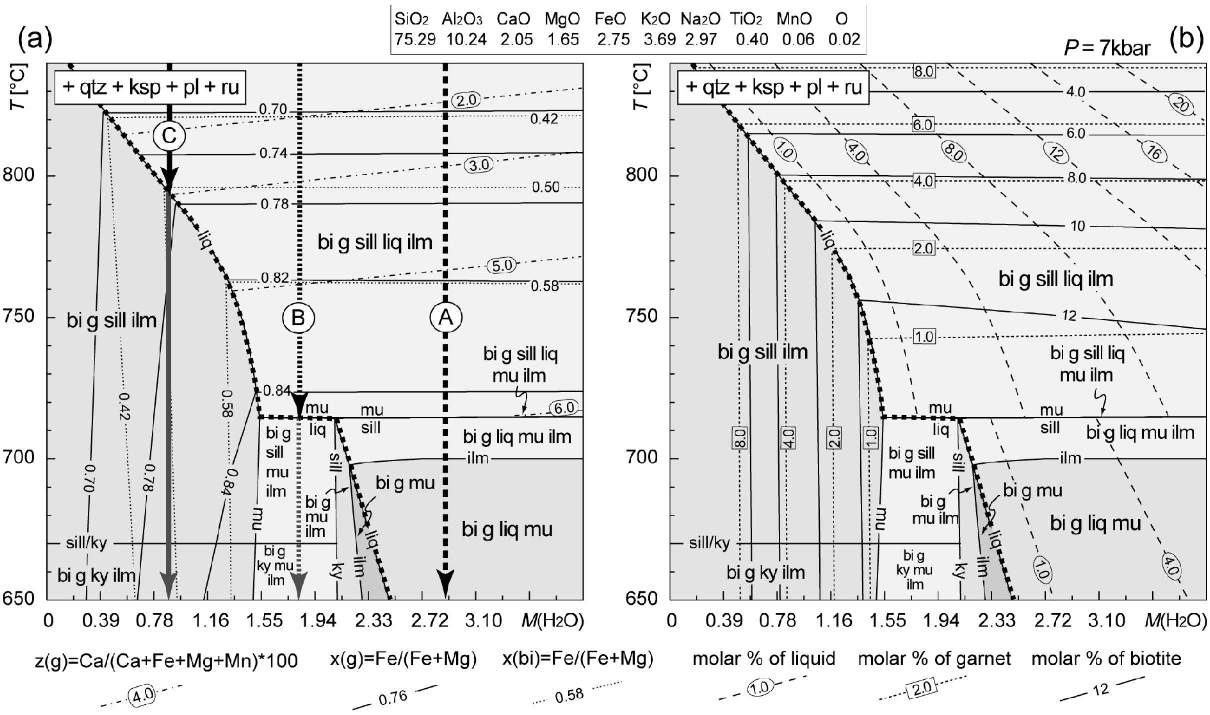


Fig. 9: *T-M($H_2O$) pseudosection for Type I orthogneiss at 7 kbar contoured for (a) x(g), z(g), x(bi) and (b) molar proportions of liquid, garnet and biotite. Three cooling paths at different proportions of $H_2O$ are discussed in the text.*

For a rock at low $M(H_2O)$, (black arrow C, Fig. 9), the molar proportions of garnet and melt decrease in favour of biotite, associated with important changes in *x*(g), *m*(g) and *x*(bi), until the liquid-out line is reached. Here the mineral assemblage g–sill–bi–pl–ksp–qtz–ru–ilm is likely to be the preserved one, and this does correspond to the mineral assemblage observed in the rocks. The calculated mineral compositions are $x$(g) = 0.77, $x$(bi) = 0.5 and $m$(g) = 0.03 (compare Type I, $X_{Fe}$ of the garnet = 0.77–0.85, $X_{Fe}$ of the biotite = 0.45 and sps in garnet of 2–3 mol. %). For arrow C, $M(H_2O)$ = 0.88, and therefore this amount of $M(H_2O)$ is used for the construction of a $P$–$T$ pseudosection for Type I orthogneiss. In this way, the amount of $H_2O$ necessary to preserve the assemblage and mineral chemistry was determined for construction of pseudosections for the whole-rock chemistry of Type II, III and IV migmatites.

The major features and topology of $H_2O$-undersaturated pseudosections for Types I-IV (Figs. 10 & 11) are similar, but with the exact position of fields and curves varying in $P$–$T$ space dependent on the $X_{Fe}$ of the rock and on $M(H_2O)$. They show a steeply-inclined solidus at progressively lower temperature. The muscovite-in line is temperature sensitive and steep at suprasolidus conditions and pressure sensitive at subsolidus conditions. Cordierite-bearing assemblages are restricted to the low pressure part of the pseudosections and the biotite upper temperature limit decreases from 850°C for Type I orthogneiss to 780°C for Type IV migmatite.

The transition from g–sill–bi–liq–pl–ksp–qtz–ru–ilm into g–sill–bi–pl–ksp–qtz–ru–ilm at the solidus occurs on pseudosections on cooling at progressively lower temperature between 800–790°C, 770–750°C, 720–710°C and 690–680°C for Type I orthogneiss to Type IV migmatite. Conditions of this transition are also limited by the muscovite-in line from the high-pressure side and by the cordierite-in line from the low-pressure side. These correspond to 9–5.3 kbar, 8.6–4.8 kbar, 6.6–4 kbar and 5.2–4 kbar, and can be considered to be $P$ windows through which mineral assemblage preservation is likely to have occurred, indicated by grey arrows.

The $P$–$T$ conditions of equilibration can be further refined by comparing the observed chemistry of garnet, and biotite and garnet modal proportions, with chemical variables and molar proportions calculated in pseudosections (Figs. 10 & 11). From the point of view of decreasing $P$–$T$ conditions, in the field of g–sill–bi–liq–pl–ksp–qtz–ru–ilm the molar proportions of garnet and melt decrease in favour of biotite and the molar proportion of garnet is progressively lower at the liquid-out line for the Types I–IV. This is in accordance with the observed decrease of modal proportion of garnet from the Type I orthogneiss to the Type IV migmatite. In the diagrams, during the continuous reaction involving g–sill–bi–liq–pl–ksp–qtz–ru–ilm, the $x$(g) and $x$(bi) increase until the solidus is crossed (Figs. 10 & 11), where the continuous reaction is stopped as biotite loses its source of $H_2O$. On further cooling, the only reaction that operates is exchange of Fe–Mg between garnet and biotite.

Regarding the spacing of $x$(g) and $x$(bi) isopleths in the g–sill–bi–pl–ksp–qtz–ru–ilm and g–sill–bi–liq–pl–ksp–qtz–ru–ilm fields, the Fe–Mg exchange is much less efficient in

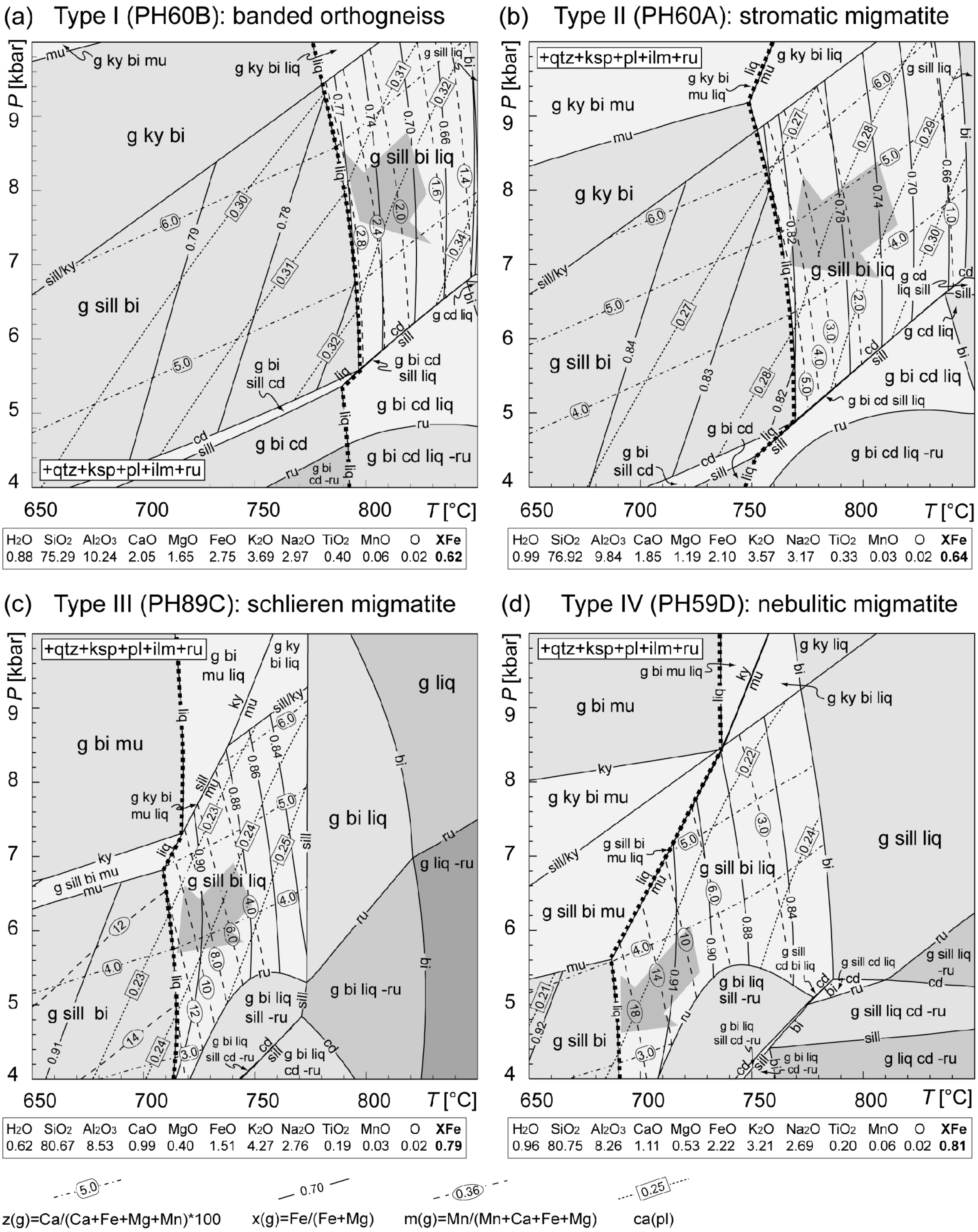


(a) Type I (PH60B)

| $H_2O$ | $SiO_2$ | $Al_2O_3$ | CaO | MgO | FeO | $K_2O$ | $Na_2O$ | $TiO_2$ | MnO | O | XFe |
|---|---|---|---|---|---|---|---|---|---|---|---|
| 0.88 | 75.29 | 10.24 | 2.05 | 1.65 | 2.75 | 3.69 | 2.97 | 0.40 | 0.06 | 0.02 | **0.62** |

(b) Type II (PH60A)

| $H_2O$ | $SiO_2$ | $Al_2O_3$ | CaO | MgO | FeO | $K_2O$ | $Na_2O$ | $TiO_2$ | MnO | O | XFe |
|---|---|---|---|---|---|---|---|---|---|---|---|
| 0.99 | 76.92 | 9.84 | 1.85 | 1.19 | 2.10 | 3.57 | 3.17 | 0.33 | 0.03 | 0.02 | **0.64** |

(c) Type III (PH89C)

| $H_2O$ | $SiO_2$ | $Al_2O_3$ | CaO | MgO | FeO | $K_2O$ | $Na_2O$ | $TiO_2$ | MnO | O | XFe |
|---|---|---|---|---|---|---|---|---|---|---|---|
| 0.62 | 80.67 | 8.53 | 0.99 | 0.40 | 1.51 | 4.27 | 2.76 | 0.19 | 0.03 | 0.02 | **0.79** |

(d) Type IV (PH59D)

| $H_2O$ | $SiO_2$ | $Al_2O_3$ | CaO | MgO | FeO | $K_2O$ | $Na_2O$ | $TiO_2$ | MnO | O | XFe |
|---|---|---|---|---|---|---|---|---|---|---|---|
| 0.96 | 80.75 | 8.26 | 1.11 | 0.53 | 2.22 | 3.21 | 2.69 | 0.20 | 0.06 | 0.02 | **0.81** |

**Fig. 10:** *$H_2O$-undersaturated MnNCKFMASHTO P–T pseudosections for the rock compositions of (a) banded orthogneiss (Type I), (b) stromatic migmatite (Type II), (c) schlieren migmatite (Type III) and (d) nebulitic migmatite (Type IV). For the $H_2O$ content used, see text. Solidus is underlined by a dashed line and isopleths of x(g), z(g), x(bi), m(g) and ca(pl) are shown.*

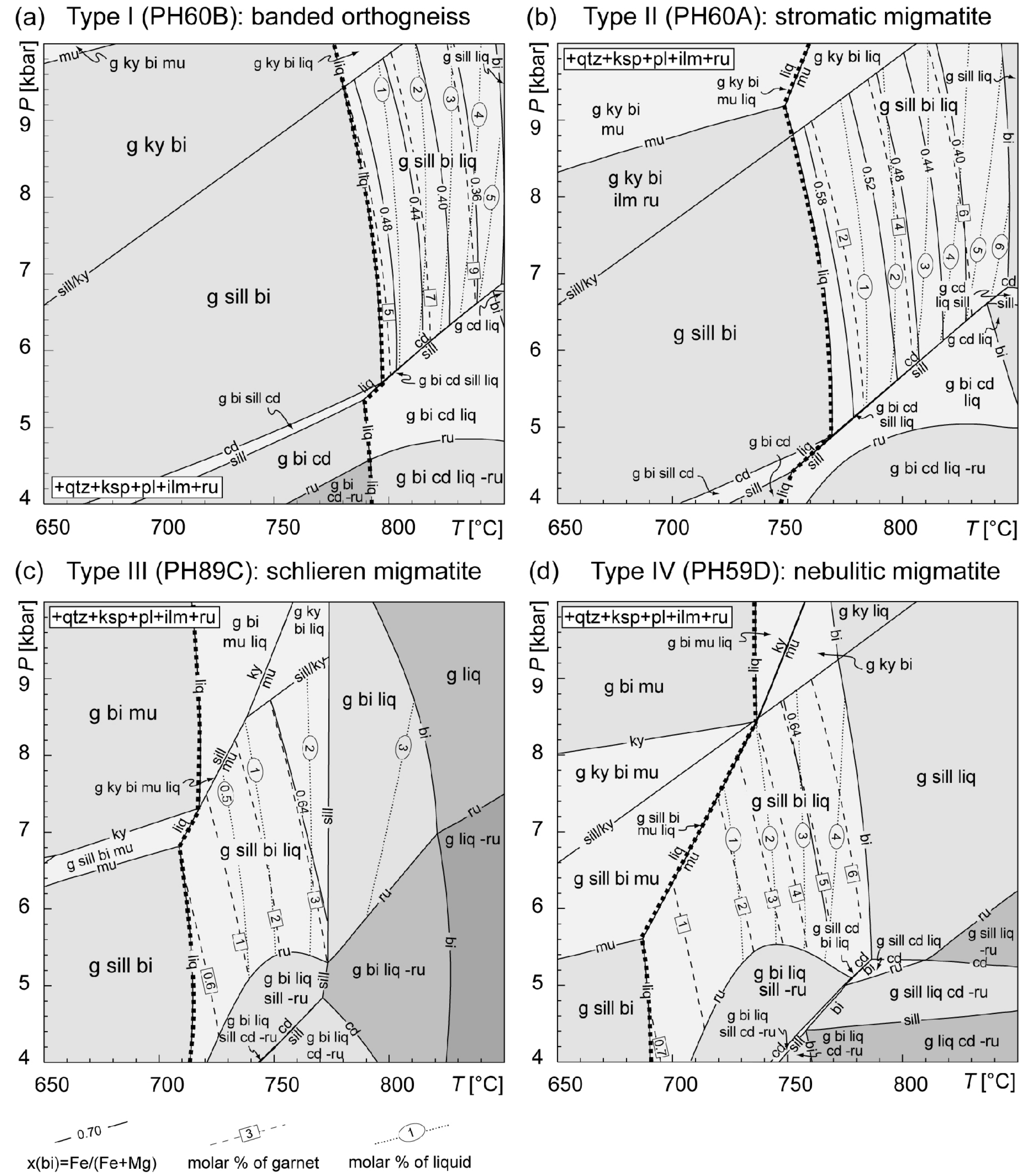


**Fig. 11:** *P–T pseudosections of Types I–IV (same as in Fig. 10) contoured for molar proportions of liquid and garnet.*

changing garnet and biotite chemistry than is the continuous reaction in the presence of melt. Therefore, the observed decrease in $X_{\mathrm{Fe}}$ of garnet and biotite in Types I to IV is attributed to the decreasing temperature of last melt crystallization. The isopleths of $z$(g) are pressure sensitive and decrease in the field of g–sill–bi–liq–pl–ksp–qtz–ru–ilm from 6.5 to 3 kbar with decreasing pressure. Therefore, the decreasing grossular content in garnet from the Type I orthogneiss to the Type IV migmatite is interpreted as reflecting the decreasing pressure of last melt crystallization in the rocks (Fig. 10 & Table 4).

Based on the pseudosection modelling, the mineral assemblage and mineral chemistry of Type I orthogneiss to Type IV migmatite is interpreted to record the last re-equilibration in the presence of melt that occurred along an exhumation path. The equilibration *P–T* conditions in the pseudosections for Types I, II, III and IV are therefore inferred to be 790°C and 9–5 kbar, 760°C and 8.5–4.5 kbar, 710°C and 6.5–4 kbar and 690°C and 5–3 kbar, respectively. Because the calculations were performed in the relatively complete MnNCKFMASHTO system, these *P–T* conditions are likely to be realistic.

### *P-T path before the last equilibration*

Because it is likely that open-system processes have operated during metamorphism, the bulk-rock composition of each rock type is not likely to correspond to an original protolith composition. For this reason, the *P–T* evolution before the last equilibration cannot be evaluated from pseudosections calculated for observed bulk-rock compositions. The general *P–T* evolution may be constrained, however, because the presence of kyanite in mineral concentrates suggests that the *P–T* evolution was likely to have involved decompression from the kyanite stability field.

## Forward modelling of open-system processes

Prior to considering melt infiltration, the melt amount that it might be possible to produce by various processes is modelled in order to assess whether the change from banded, metatexite-like structure, into isotropic, diatexite-like structure may be caused by loss of coherence due to high melt production in the rocks themselves. The amount of melt is modelled for (1) temperature increase for an appropriate protolith composition (closed-system model) and (2) $H_2O$ introduction (fluid infiltration model). Also examined are processes that may alter the rock composition, including melt loss and its influence on the resulting whole-rock composition. Reaction sequences, and the evolution of mineral proportions and mineral compositions of the assemblages are discussed for the various cases in the context of the observed trends in Types I to IV. Before these calculations can be undertaken the protolith is reconstructed using the composition of Type I orthogneiss, the least modified rock composition available.

### *Reconstruction of the protolith*

The likely protolith is reconstructed in order to estimate the maximum amount of melt that such protolith would produce along a prograde path (can a diatexite be formed?) and in order to examine compositional trends of phases with increasing degree of melting (do they correspond to observed compositional trends?). The least modified rock is Type I banded orthogneiss that contains sillimanite and kyanite. However it is likely that the original granitic protolith before metamorphism and mylonitization did not involve aluminosilicate, but that aluminosilicate was a product of muscovite-breakdown melting along the prograde path. In order to preserve the aluminosilicate from reaction at the solidus during the retrograde path, some melt must have been lost (Brown, 2002; White & Powell, 2002), and such melt loss is likely to occur after muscovite dehydration melting (White & Powell, 2002). The chemistry of the melt to be introduced is taken from a point located on a prograde path after muscovite-breakdown melting in the g–ky–bi–liq–pl–ksp–qtz–ru–ilm field and conditions of 11.5 kbar and 790°C were chosen, but the results are insensitive to this *P*-*T* choice. It is necessary to add 7 mol. % of melt in order to obtain a kyanite-absent assemblage on the prograde path prior to muscovite breakdown. An upper limit of melt addition, only slightly larger than 7 mol. %, results in $H_2O$ saturation at the solidus. The pseudosection for the composition of the Type I rock with 7 mol. % of reintegrated melt is presented in Fig. 12a, b.

### *Melting of the protolith in a closed-system and with melt loss*

The pseudosection in Fig. 12a is used to estimate the maximum amount of melt that a biotite-muscovite protolith with the starting assemblage g–bi–mu–pl–ksp–qtz–ru–ilm would produce along a prograde path in order to discuss whether the degree of closed-system melting is sufficient to form a diatexite. This pseudosection is also used for examination of compositional trends of phases with increasing degree of melting and on the retrograde path (Fig. 12b), and to infer the whole-rock compositional trends caused by melt loss.

The major prediction from the pseudosection from the point of view of a simple prograde heating path (Fig. 12a, path A) are: the appearance of first liquid at 650°C, disappearance of muscovite associated with the appearance of kyanite at 745°C (Fig. 12a, b), and, the kyanite/sillimanite transformation at 755°C. A similar evolution occurs along path B, involving an increase in *P* and *T* followed by decompression, with kyanite formed on the prograde path, then being transformed into sillimanite on decompression (Fig. 12 a, b).

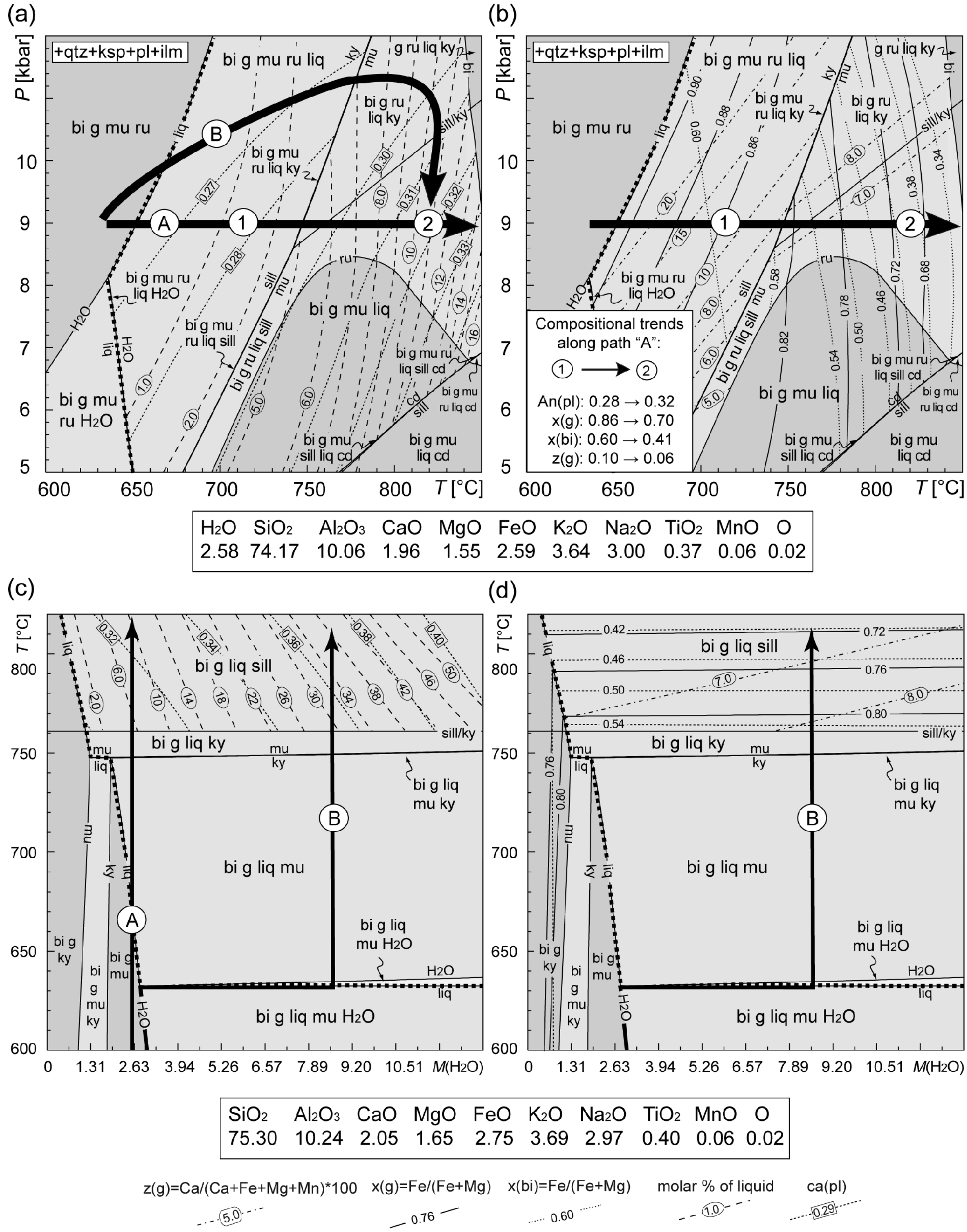


| $H_2O$ | $SiO_2$ | $Al_2O_3$ | CaO | MgO | FeO | $K_2O$ | $Na_2O$ | $TiO_2$ | MnO | O |
|---|---|---|---|---|---|---|---|---|---|---|
| 2.58 | 74.17 | 10.06 | 1.96 | 1.55 | 2.59 | 3.64 | 3.00 | 0.37 | 0.06 | 0.02 |

| $SiO_2$ | $Al_2O_3$ | CaO | MgO | FeO | $K_2O$ | $Na_2O$ | $TiO_2$ | MnO | O |
|---|---|---|---|---|---|---|---|---|---|
| 75.30 | 10.24 | 2.05 | 1.65 | 2.75 | 3.69 | 2.97 | 0.40 | 0.06 | 0.02 |

**Fig. 12:** *Reconstruction of the granite protolith and forward modelling of closed system melting and $H_2O$ infiltration. Pseudosections calculated for the bi-mu granite, reconstructed by adding 7 mol. % of melt into the rock composition of the Type I. (a, b) P–T pseudosections contoured for x(g), z(g), x(bi), ca(pl) and molar % of liquid. Closed system model is discussed for two prograde paths A and B. Inset shows calculated mineral compositions along path A. Rock composition after melt loss at 820°C and 9 kbar is shown in Table 5. (c, d) T–M($H_2O$) pseudosection. Path A illustrates closed system melting of bi-mu granite and path B $H_2O$ infiltration at the solidus. Melt proportion and mineralogical changes are discussed in the text, the rock composition after melt loss at 800°C is listed in Table 5.*

The melt amount is controlled by the *P–T* path and the $H_2O$ content in the micas. The amount of melt produced before muscovite dehydration melting is around 2 mol. % and then the amount of melt increases over a small interval by 3 mol. %, when muscovite-breakdown melting connected with the appearance of kyanite occurs at 740–750°C. The dehydration of biotite continues up to 850°C and the total amount of melt reaches 12–15 mol. % by the point at which all the biotite is consumed. The amount of melt does not increase significantly on decompression, so the degree of melting is controlled only by heating on the prograde path. The mineral chemistry changes involve increasing anorthite content of plagioclase, decreasing $X_{Fe}$ of garnet and biotite (Fig. 12a, b) and decreasing grossular content in garnet (Fig. 12b). In addition to the increasing amount of melt, the phase changes involve disappearance of muscovite, appearance of kyanite and sillimanite, increasing molar content of garnet and decreasing molar content of biotite. On a retrograde path garnet and sillimanite are consumed by continuous reactions producing biotite and muscovite, respectively. When the hypothetical rock becomes melt absent the stable assemblage is g–bi–mu–pl–ksp–qtz–ru–ilm.

These predictions are now discussed in terms of evolutionary trends observed in the migmatites. If the protolith was biotite–muscovite granite that was by deformation and metamorphism converted into a bi–mu orthogneiss, then the first melt has been produced at 650°C and the fertility of the rock was controlled by dehydration melting of biotite and muscovite. The amount of melt produced at peak (800–850°C) may have reached up to 12–15 mol. %. If the protolith was a bi–ky(sill) orthogneiss, then the maximum melt production in the biotite stability field would have been only 5 mol. % (Fig. 11a). Thus the amount of melt in both cases is not likely to be sufficient to produce a melt-supported structure required for diatexite formation, but may be sufficient to allow melt-assisted granular flow (at around 7 vol. %: Rosenberg & Handy, 2005).

Additionally, modal, and especially the compositional evolution of minerals (e.g. $X_{Fe}$ of garnet and biotite and anorthite content in plagioclase) from Type I orthogneiss to Type IV nebulite do not fit the evolution on the prograde path in the pseudosection (Table 4). In order to preserve the observed assemblage g–sill–bi–pl–ksp–qtz–ru–ilm, some melt must have been lost before retrogression. The melt loss alters the rock composition, but the whole-rock composition after melt loss (calculated at 820°C and 9 kbar, point 2 in Fig. 12 a, b) shows $X_{Fe}$ = 0.62, $SiO_2$ = 69.21, $Al_2O_3$ = 16.06, CaO = 1.74 and $Na_2O$ = 2.90, which are changes that are opposite to the trend observed from Type I orthogneiss to Type IV migmatite ($X_{Fe}$ 0.62 0.85, $SiO_2$ 69.90 77.10, $Al_2O_3$ 15.40 12.70, CaO 1.50 0.43) (Table 5). Therefore, the whole-rock compositional changes from Type I orthogneiss to Type IV migmatite cannot be explained by melt loss in a closed-system melting model.

### *$H_2O$ infiltration model*

The amount of melt necessary to form a diatexite may be obtained if $H_2O$ is introduced from an external source, for example from associated dehydrating metasediments at near-solidus conditions (White *et al.*, 2005). Therefore, we assess the possibility that the Type I orthogneiss to Type IV migmatite evolution can result from addition of external $H_2O$ using a $T$–$M$($H_2O$) pseudosection. For the path A in Fig. 12c the melting of a mu–bi-bearing protolith is controlled only by mica-breakdown melting, and the path corresponds to path A in the $P$–$T$ pseudosection in Fig. 12a. To the right side may be shown paths with additional $H_2O$. For example in path B, a bi–mu-bearing protolith is dehydrating until the $H_2O$ saturated solidus is reached at 630°C and at these conditions additional $H_2O$ is introduced (Fig. 12c, d). The melt production is then controlled by the $P$–$T$ path and the amount of $H_2O$ introduced, and for path B it may reach 38 mol. % of melt at 810°C (Fig. 12c). The augmented degree of melting due to the addition of $H_2O$ along the prograde path has little influence on the molar content of garnet and biotite, although both become more magnesian (see horizontal $x$(g) and $x$(bi) isopleths in Fig. 12d), but influences more significantly the composition of plagioclase and the grossular content in garnet, plotted as $ca$(pl) and $z$(g) isopleths (Fig. 12c, d). If the high amount of melt produced along path B is accompanied by subsequent melt loss, the whole-rock composition is altered and for melt loss at 800°C shows $X_{Fe}$ = 0.62, $SiO_2$ = 67.62, $Al_2O_3$ = 16.26, CaO = 2.23 and $Na_2O$ = 2.50 (Table 5).

The transformation of Type I mylonitic orthogneiss into Type IV nebulitic migmatite might be explained by increased degree of melting due to $H_2O$ influx. However, the decrease in anorthite content of plagioclase and the increasing $X_{Fe}$ of biotite and garnet would remain unexplained. Also the model, even if it is accompanied by melt loss (into $X_{Fe}$ = 0.62, $SiO_2$ = 67.62, $Al_2O_3$ = 16.26, CaO = 2.23; Table 5) cannot account for the observed whole-rock trends (see Table 5).

### *Melt infiltration model*

In this section a model in which melt moves through and equilibrates with a rock is assessed, to evaluate the change of rock composition that such a continuing equilibration with infiltrating melt produces. The infiltrating melt may have been lost from similar protoliths at any point on the *P–T* path, moving up through the rock pile, or it can be of foreign derivation, for example from granulitic migmatites outside the Gföhl orthogneiss migmatite body. This melt then equilibrates with the rock and leaves it with slightly different composition, the rock also changing composition. Additionally, the infiltration may occur during exhumation, corresponding to the implied decreasing equilibration *P–T* conditions from Type I orthogneiss to Type IV migmatite, and therefore the equilibration of the melt with the rock may also be complicated by decompression and cooling. As the processes involved may be complex, the modelling is undertaken for simplified situations. It will be assumed that the rock had time to equilibrate during the melt infiltration.

### *Estimation of melt composition*

The modelling is done in the NCKFMASH subsystem as noted above. For this, the *P–T* conditions used for calculations are displaced to slightly lower temperature to be approximately equivalent to the calculations in MnNCKFMASHTO (740°C at 7–5 kbar, 720°C at 6.5–5 kbar, 690°C at 5–4 kbar and 670–660°C at 5–3 kbar for Types I, II, III and IV, respectively, using Fig. 13).

*Table 6: Melt compositions*

| | $T$ (°C) | $P$ (kbar) | An(pl) | | $H_2O$ | $SiO_2$ | $Al_2O_3$ | CaO | MgO | FeO | $K_2O$ | $Na_2O$ | $x$(g) | $z$(g) | $x$(bi) |
|---|---|---|---|---|---|---|---|---|---|---|---|---|---|---|---|
| **melt I** (PH60/B) | 740 | 6.50 | 0.15 | (mol.%) | 23.02 | 62.74 | 7.32 | 0.21 | 0.10 | 0.24 | 2.71 | 3.66 | 0.77 | 0.03 | 0.47 |
| | | | | (wt.%) | 7.61 | 69.22 | 13.71 | 0.22 | 0.07 | 0.32 | 4.69 | 4.17 | | | |
| **melt II** (PH60/A) | 720 | 5.50 | 0.07 | (mol.%) | 22.76 | 63.17 | 7.26 | 0.09 | 0.09 | 0.28 | 2.57 | 3.78 | 0.82 | 0.02 | 0.55 |
| | | | | (wt.%) | 7.52 | 69.63 | 13.58 | 0.09 | 0.07 | 0.37 | 4.44 | 4.30 | | | |
| **melt III** (PH90) | 690 | 4.50 | 0.04 | (mol.%) | 23.27 | 63.21 | 6.97 | 0.09 | 0.05 | 0.23 | 2.51 | 3.68 | 0.90 | 0.01 | 0.72 |
| | | | | (wt.%) | 7.74 | 70.12 | 13.13 | 0.09 | 0.04 | 0.31 | 4.37 | 4.21 | | | |
| **melt IV** (PH59/D) | 660 | 3.50 | 0.02 | (mol.%) | 23.64 | 63.49 | 6.72 | 0.02 | 0.01 | 0.16 | 2.46 | 3.50 | 0.98 | 0.01 | 0.94 |
| | | | | (wt.%) | 7.90 | 70.81 | 12.72 | 0.02 | 0.01 | 0.21 | 4.30 | 4.03 | | | |

There is no direct evidence for the composition of the melt present during metamorphism, apart from the mineral compositions preserved in the rocks. Assuming that the infiltrating melt tends to be in equilibrium with the minerals (at least with their rim compositions) and that this equilibrium evolves as temperature decreases, the composition of the percolating melt can be estimated from the preserved assemblages and their mineral chemistry.

From the phase rule it follows that a melt composition that is in equilibrium with garnet–sillimanite–biotite–plagioclase–K-feldspar–quartz in the NCKFMASH system can be calculated if three variables are fixed. In the following calculations pressure, temperature and anorthite content of plagioclase are fixed (Table 6). For example, the melt composition that is in

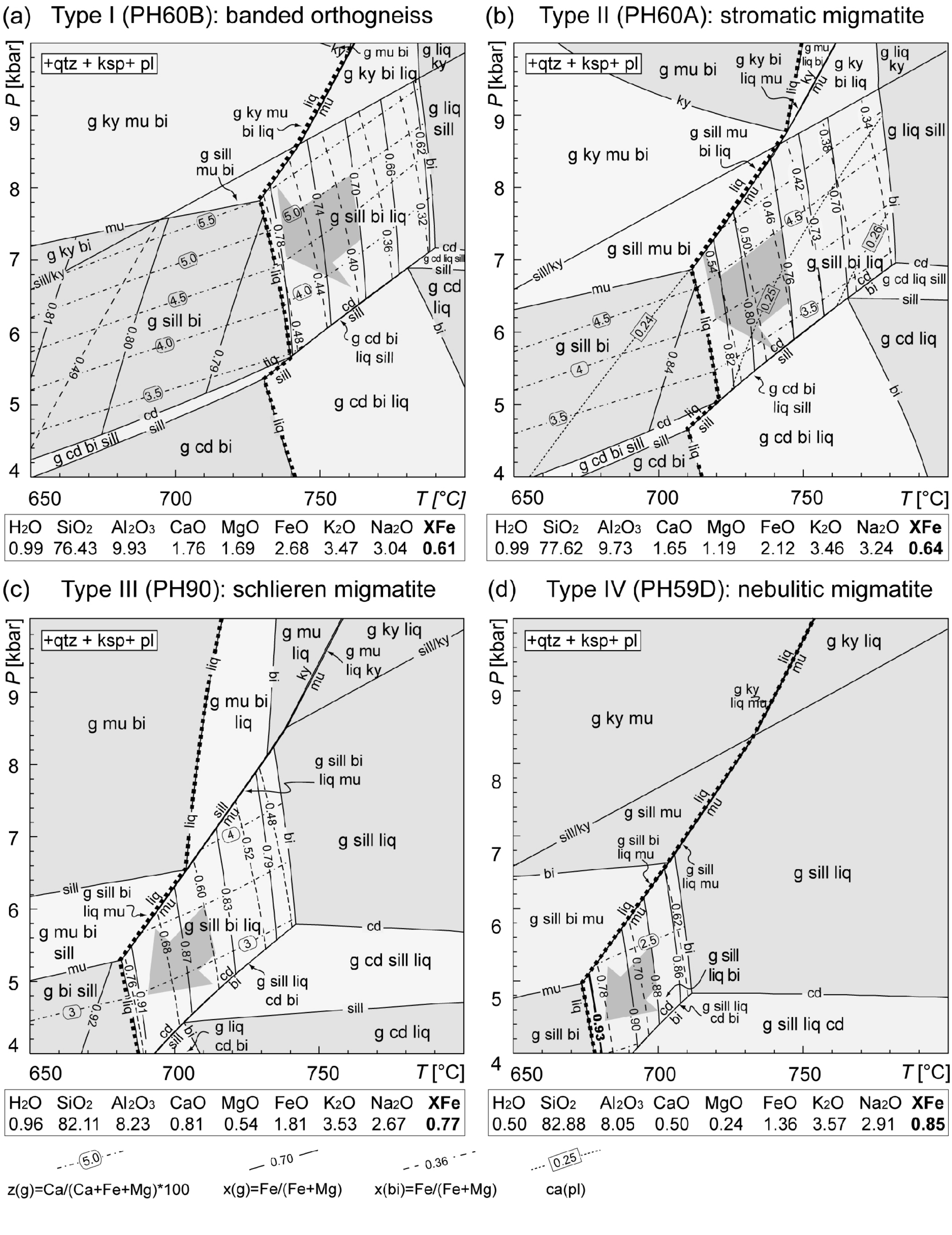


**Fig. 13:** *$H_2O$-undersaturated NCKFMASH P–T pseudosections for the whole-rock composition of (a) Type I, (b) Type II, (c) Type III and (d) Type IV, contoured for x(g), z(g), x(bi), and ca(pl). Solidus is shown as a dashed line.*

equilibrium with 15 mol. % anorthite content in plagioclase at 6.5 kbar and 740°C in a rock with the assemblage garnet–sillimanite–biotite–liquid–plagioclase–K-feldspar–quartz is $H_2O$ = 23.02, $SiO_2$ = 62.74, $Al_2O_3$ = 7.32, CaO = 0.21, MgO = 0.10, FeO = 0.24, $K_2O$ = 2.71, $Na_2O$ = 3.66 (in mol. %), which is taken to approximate the melt composition in equilibrium with the rim compositions of the minerals in the Type I orthogneiss (Table 6). In the same way melt compositions were calculated for decreasing *P–T* conditions at 5.5 kbar and 720°C and 4.5 kbar and 690°C and 3.5 kbar and 660°C, in equilibrium with $X_{An}$ = 0.07, 0.04 and 0.02, that are taken to approximate the melt compositions in equilibrium with rim compositions of the phases in Type II, III and IV migmatites, respectively (Table 6). The choice of fixed variables was assessed by comparing the calculated garnet and biotite compositions with observed values in the rocks.

### *Equilibration with infiltrating melt*

Modelling the equilibration of host rock with infiltrating melt is presented for a model situation in which the rock is kept at fixed *P–T* conditions (6.5 kbar, 740°C) and equilibrates with infiltrating melt of fixed composition (melt II, III or IV in Table 6) (Fig. 14a). The starting composition is that of the Type I orthogneiss (sample PH60/B) in which the mineral assemblage is g–sill–bi–liq–pl–ksp–qtz. Melt infiltration is simulated in cycles, each consisting of addition of 10 mol. % of melt, equilibration, and melt loss, as schematically presented in the *T–X* section (Fig. 14b), where *X* links the rock to the melt composition. Following equilibration of infiltrating melt with the host minerals, a new rock composition named solids $_{(1)}$ is calculated for the modified mineral compositions. The equilibrated melt leaves the rock to be replaced with 10 mol. % of new melt of the same composition as the first infiltrating batch. Following equilibration of solids $_{(1)}$ and melt, a new rock composition is calculated named solids $_{(2)}$, and so on. These 'metasomatic' runs are repeated and the changes of major oxides in the evolving rock composition for infiltration by melt composition III are reported in Figs. 14c–f. The procedure was also undertaken for melt of compositions II and IV, shown in the insets in Fig. 14c–f.

The rock composition that equilibrates with melts II, III and IV shows similar trends of increasing $SiO_2$, decreasing CaO and $Al_2O_3$, constant $Na_2O$ and decreasing $K_2O$, irrespective of the melt composition used (Fig. 14). The $X_{Fe}$ ratio increases only slightly (0.60–0.67, not shown). In order to change the whole-rock composition as indicated by the arrows in Fig. 14 by melt II, III and IV it was necessary to produce 60, 60, and 40 runs, respectively. Similar trends were obtained for simulations where the rock changes *P–T* conditions and equilibrates with

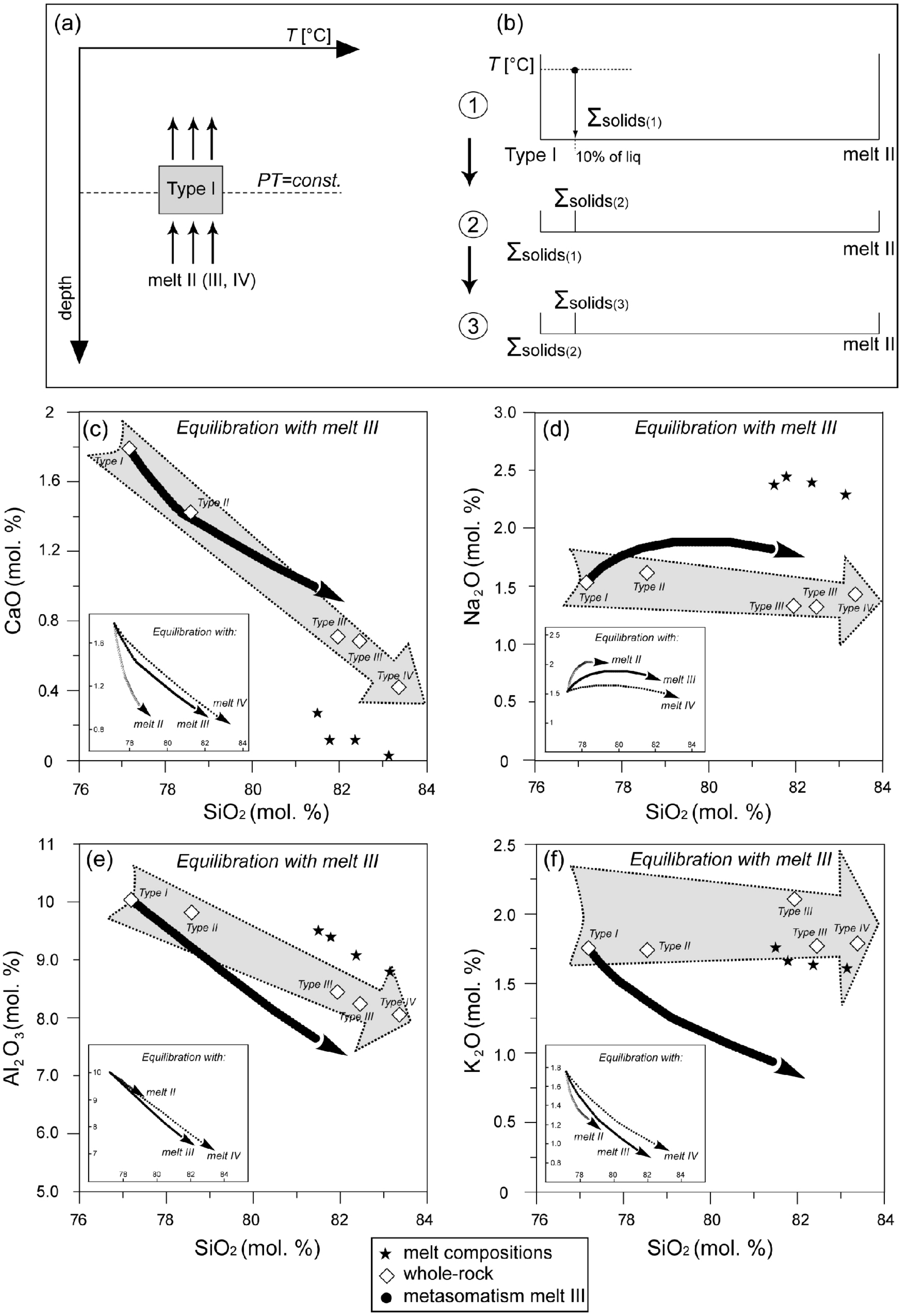


**Fig. 14:** *Model of the melt infiltration. (a) Sketch of the rock at fixed P–T conditions equilibrating with infiltrating melt; (b) Modelling steps of rock equilibration with melt in the T-X section. For explanation see text. (c-f) Major oxides changes in the infiltration model compared with Type I to IV rock composition (white diamonds) and calculated melt compositions (black stars, compositions from Table 6). The lower left insets show compositional variations for infiltration by melt composition II, III and IV. For details see text.*

melt of fixed composition, and where the rock changes *P–T* conditions and equilibrates with melt that changes composition (from melt II, to melt III to melt IV, not shown).

The trends obtained for the major oxides $SiO_2$, CaO, $Al_2O_3$ and, to a lesser extent, $Na_2O$ are very similar to the trends in Types I–IV (large arrow in Fig. 14 c–f), with best fits for equilibration with melt III and IV. In the model, the rock composition may change significantly by equilibration with infiltrating melt and that this process may explain major chemical trends in Types I–IV. However, with the calculated melt compositions the trends of the Types I–IV in $K_2O$ and $X_{Fe}$ are not well reproduced. The most likely explanation for this is that the melt compositions used do not correspond to the melt infiltrating, the necessary approximation having been made that they correspond to the melt already in equilibrium with the rocks (see above). The trends may indicate that the melts infiltrating the rocks have a somewhat different K/(Na+K) than those used in the modelling. Given the low FeO and MgO contents in haplogranitic melts (White *et al.*, 2001, 2007), modification of $X_{Fe}$ is inevitably limited. Arbitrarily increasing these contents does allow the observed trends to be reproduced.

### *Melt redistribution*

In the melt redistribution model (Marchildon & Brown, 2001, Milord *et al.*, 2001), the resulting composition of the rock should lie between the protolith and melt composition. The whole-rock compositions of the Type I–IV do not lie exactly on the line between Type I and calculated melt compositions (stars in Fig. 14c–f) but follow similar trends. An important consequence of interpreting the observed trends as a result of melt redistribution is that the Type II to IV migmatites gained a significant and progressively increasing proportion of melt. The melt loss from Type I orthogneiss or from a theoretical mu-bi granite protolith (calculated to be a maximum of 15 mol. % of melt for a closed system, Fig. 12a) is clearly not enough to change significantly the chemistry of Type II to IV migmatites. However, some contribution of melt gain on the rock chemistry changes cannot be excluded, but it is likely to be of minor importance.

### *Destruction of monomineralic banding*

An aspect of the evolution of the rocks, as seen progressively in Type I orthogneiss to Type III migmatite, is the destruction of the monomineralic banding. Accepting that infiltrating melt is largely responsible for the evolution from Type I to Type IV, the response of the original monomineralic layers to melt infiltration is investigated. In this, the original monomineralic layers of recrystallized plagioclase and K-feldspar are considered as equilibration volumes. In a reduced NCKASH system, the assemblage liquid–plagioclase–K-feldspar–quartz–sillimanite is divariant if $a(H_2O)$ is fixed. An albite–anorthite–K-feldspar compatibility diagram then can be calculated for any point in *P–T* space if sillimanite and quartz are in excess (Fig. 15). A diagram is calculated for 740°C and 6.5 kbar with $a(H_2O)$ = 0.75, chosen such that the plagioclase in equilibrium with K-feldspar and the infiltrating melt is $An_{20}$. This divariant assemblage liq–ksp–pl appears as a tie triangle involving K-feldspar with $Ab_{29}$. The tie lines in the trivariant fields of pl–ksp and pl–liq join the coexisting compositions, on the left side a quadrivariant field of plagioclase is located and at the bottom a quadrivariant field of liquid. The composition of the plagioclase layer which has higher anorthite content than this occurs outside the divariant assemblage liq–pl–ksp. A plagioclase layer infiltrated by melt is therefore drawn towards the liquid composition along the black arrow. As there exists a miscibility gap in the feldspars, the vector is decomposed, and plagioclase composition is drawn to anorthite 20 mol. % (white arrow), at the same time K-feldspar crystallizes in the layer. In such a way the composition of the original plagioclase layer (Fig. 15, circle 1) is shifted into the pl–ksp trivariant field. Equilibration with melt pulls the composition to the pl–ksp tie line forming one edge of the liq–pl–ksp divariant (Fig. 15, circle 2). A similar process occurs in the K-feldspar layer (not shown in Fig.15).

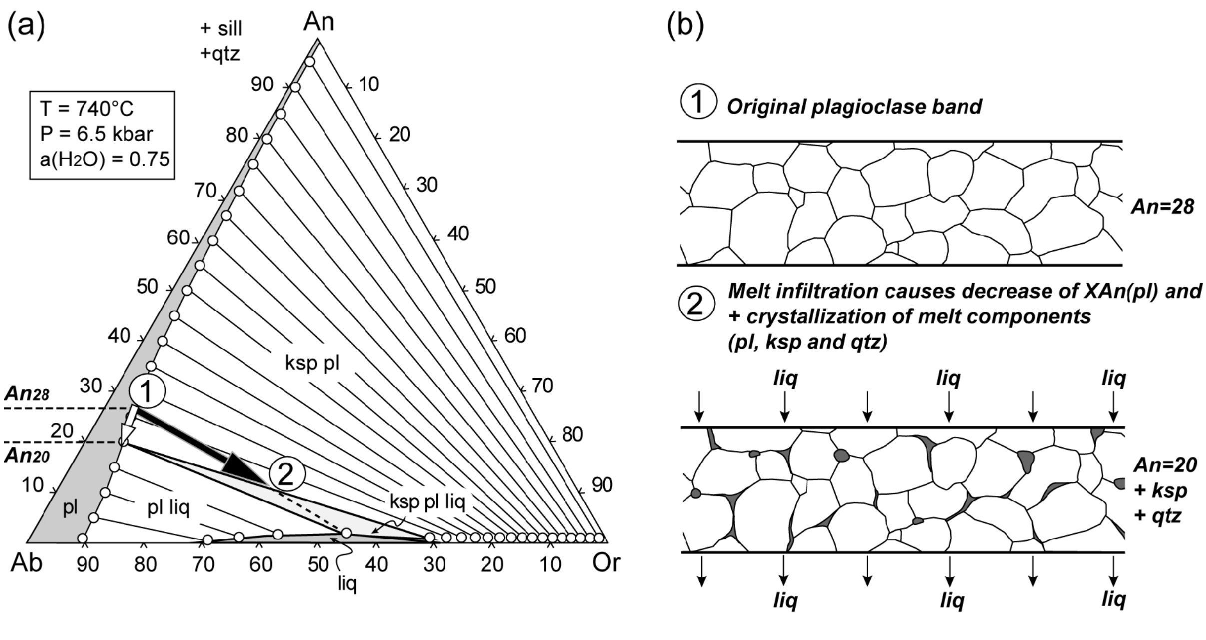


**Fig. 15:** *(a) Ab–An–Or compatibility diagram calculated for 740°C, 6.5 kbar and a($H_2O$) = 0.75. For details see text. (b) Schematic sketch illustrating the disintegration of monomineralic banding.*

## Conclusions

In the Gföhl gneiss, eastern Bohemian Massif, a sequence of felsic orthogneiss migmatites shows macroscopic features typical of evolution from metatexites to diatexites. They are divided into four stages that involve a progressive evolution of a banded mylonitic orthogneiss (Type I) through stromatite migmatite (Type II) and schlieren migmatite (Type III) into nebulitic migmatite (Type IV). The transformation of the rocks occurred during superposition of a flat $D_2$ deformation on a steep $S_1$ foliation, and microscopically it is characterized by progressive destruction of monomineralic banding and its replacement by a random microstructure typical of diatexites (Hasalová *et al.*, 2008).

The rocks contain the assemblage g–sill–bi–liq–pl–ksp–qtz–ru–ilm. The mineral composition trends of banded orthogneiss changing into nebulitic migmatite involve mainly increase in $X_{Fe}$ of garnet and biotite, and decrease of grossular content in garnet. These variations reflect decreasing temperature and pressure conditions of equilibration in the presence of melt, according to pseudosection modelling in MnNCKFMASHTO system (Figs. 10 & 11).

The major-element whole-rock compositional changes involve mainly increase in $SiO_2$ and $X_{Fe}$ and decrease in CaO and $Al_2O_3$ (Table 5). These appear to be inconsistent with closed-system melting or by an $H_2O$-infiltration model accompanied by melt loss. However, they are largely compatible with rock equilibration with an infiltrating melt. The open-system simulation was undertaken at essentially constant volume. Otherwise, the rock composition changes requiring infiltration by a large quantity of melt would result in an unacceptable increase in rock volume, although a small (less than 10 mol. %) final accumulation of melt in Type IV nebulitic migmatite is implied by the microstructural results of Hasalová *et al.* (2008).

The textural and whole-rock chemical changes from banded orthogneiss to nebulitic migmatite are attributed to an increasing volume of melt that infiltrated through and interacted with the parental banded orthogneiss. The *P–T* path suggests that the melt infiltration proceeded at progressively lower *P–T* conditions for Type I to IV (Fig. 16), which implies that melt flow changed from pervasive to channelized during exhumation (Fig. 16) corresponding to the observed relationships between the four rock types in the field (Fig. 2).

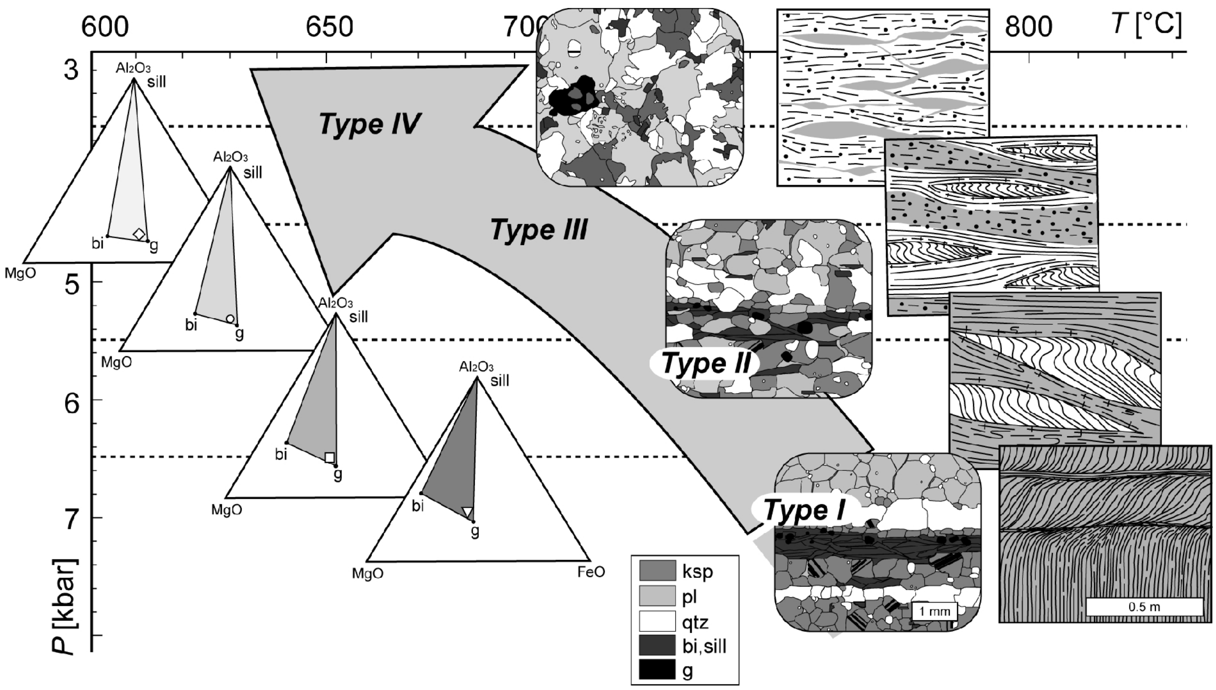


**Fig. 16:** *Exhumation P–T path deduced from four migmatite types in the Gföhl orthogneiss complex. Shown are mineral and rock chemistry changes, microstructures of bending disintegration and a schematic model of melt distribution (shaded areas) within the complex during exhumation.*

## Acknowledgements

This work was financially supported by the Grant Agency of the Czech Academy of Science (No. IAA311140), the Czech National Grant Agency (No. 205/05/2187) and the French National Agency (No. 06-1148784 to K. Schulmann). Visits by P. Hasalová to ULP Strasbourg were funded by the French Government Foundation (BGF). A. Langrová from the Geological Institute of the Czech Academy of Sciences and J. Haloda from the Czech Geological Survey are thanked for operating the microprobe. RP acknowledges the support of ARC DP0451770. Richard White is thanked for suggestions concerning how to model the melt infiltration. We would also like to thank R. White, R. Weinberg and P. Barbey for their constructive reviews and the journal editor M. Brown for all his editorial work on the manuscript.

## References

Arzi, A. A., 1978. Critical phenomena in the rheology of partially melted rocks. *Tectonophysics*, **44**, 173–184.

Barbey, P., Brouand, M., Le Fort, P. & Pęcher, A., 1996. Granite-migmatite genetic link: the example of the Manaslu granite and Tibetan Slab migmatites in central Nepal. *Lithos*, **38**, 63–79.

Brown, M., 1973. The definition of metatexites, diatexites and migmatite. *Proceedings of the Geologist's Association*, **84**, 371–382.

Brown, M., 2001. Crustal melting and granite magmatism: key issues. *Physics and Chemistry of the Earth*, **26**, 201–212.

Brown, M., 2002. Retrograde processes in migmatites and granulites revised. *Journal of Metamorphic Geology*, **20**, 25–40.

Coggon, R. & Holland, T., 2002. Mixing properties of phengitic micas and revised garnet-phengite thermobarometers. *Journal of Metamorphic Geology*, **20**, 683–696.

Dallain, C., Schulmann, K. & Ledru, P., 1999. Textural evolution in the transition from subsolidus annealing to melting process, Velay Dome, French Massif Central. *Journal of Metamorphic Geology*, **17**, 61–74.

Dudek, A., Matějovská, O. & Suk, M., 1974. Gföhl orthogneiss in the Moldanubicum of Bohemia and Moravia. *Krystalinikum*, **10**, 67–78.

Fitzsimons, I. C. W., 1996. Metapelitic migmatites from Brattstrand Bluffs, East Antarctica-metamorphism, melting and exhumation of the mid crust. *Journal of Petrology*, **37**, 395–414.

Franěk, J., Schulmann, K. & Lexa, O., 2006. Kinematic and rheological model of exhumation of high pressure granulites in the Variscan orogenic root: example of the Blanský les granulite, Bohemian Massif, Czech Republic. *Mineralogy and Petrology*, **86**, 253–276.

Gapais, D., 1989. Shear structures within deformed granites; mechanical and thermal indicators. *Geology*, **17**, 1144–1147.

Greenfield, J. E., Clarke, G. L., Bland, M. & Clark, D. J., 1996. In-situ migmatite and hybrid diatexite at Mt Stafford, central Australia. *Journal of Metamorphic Geology*, **14**, 413–426.

Greenfield, J. E., Clarke, G. L. & White, R. W., 1998. A sequence of partial melting reactions at Mt. Stafford, central Australia. *Journal of Metamorphic Geology*, **16**, 363–378.

Guiraud M., Powell R., Rebay G., 2001. $H_2O$ in metamorphism and unexpected behaviour in the preservation of metamorphic mineral assemblages. *Journal of Metamorphic Geology*, **19**, 445–454.

Hand, M. & Dirks, P. H. G. M., 1992. The influence of deformation on the formation of axial-planar leucosomes and the segregation of small melt bodies within the migmatitic Napperby Gneiss, central Australia. *Journal of Structural Geology*, **14,** 591– 604.

Hasalová, P., Janoušek, V., Schulmann, K., Štípská, P. & Erban, V., 2007. From orthogneiss to migmatite: geochemical assessment of the melt infiltration model in the Gföhl Unit (Moldanubian Zone, Bohemian Massif). *Lithos*.

Hasalová, P., Schulmann, K., Lexa, O., Štípská, P., Hrouda, F., Ulrich, S., Haloda, J. & Týcová, P., 2008. Origin of migmatites by deformation enhanced melt infiltration of orthogneiss: a new model based on quantitative microstructural analysis. *Journal of Metamorphic Geology*.

Holland, T. & Powell, R., 2003. Activity-composition relations for phases in petrological calculations: an asymmetric multicomponent formulation. *Contributions to Mineralogy and Petrology*, **145**, 492–501.

Holland, T. J. B. & Powell, R., 1998. An internally consistent thermodynamic dataset for phases of petrological interest. *Journal of Metamorphic Geology*, **16**, 309–343.

Kelemen, P. B., Hirth, G., Shimizu, N., Spiegelman, M. & Dick, H. J. B., 1997. A review of melt migration processes in the adiabatically upwelling mantle beneath oceanic spreading ridges. *Philosophical Transactions of the Royal Society of London Series A: Mathematical Physical and Engineering Sciences*, **355**, 283–318.

Marchildon, N. & Brown, M., 2001. Melt segregation in late syn-tectonic anatectic migmatites: an example from the Onawa contact aureole, Maine, USA. *Physics and Chemistry of the Earth*, **26**, 225–229.

Marchildon, N. & Brown, M., 2003. Spatial distribution of melt-bearing structures in anatectic rocks from Southern Brittany, France: implications for melt transfer at grain- to orogen-scale. *Tectonophysics*, **364**, 215–235.

Matějovská, O., 1974. Petrographic characteristic of gneiss series between Mohelno and Bítov, SW Moravia. *MS Geofond*, Prague (in Czech).

McLellan, E. L., 1983. Contrasting textures in metamorphic and anatectic migmatites - an example from the Scottish Caledonides. *Journal of Metamorphic Geology*, **1**, 241–262.

Mehnert, K. R., 1971. *Migmatites and the Origin of Granitic Rocks*. Elsevier, Amsterdam.

Milord, I., Sawyer, E. W. & Brown, M., 2001. Formation of diatexite migmatite and granite magma during anatexis of semi-pelitic metasedimentary rocks: an example from St. Malo, France. *Journal of Petrology*, **42**, 487–505.

Milord, I. & Sawyer, E. W., 2003. Schlieren formation in diatexite migmatite: examples from the St Malo migmatite terrane, France. *Journal of Metamorphic Geology*, **21**, 347–362.

Nielson, J. E. & Wilshire, H. G., 1993. Magma transport and metasomatism in the mantle: a critical review of current geochemical models. *American Mineralogist*, **78**, 1117–1134.

Powell, R. & Downes, J., 1990. Garnet porphyroblast-bearing leucosomes in metapelites: mechanisms, phase diagrams, and an example from Broken Hill, Australia. In: *High temperature metamorphism and crustal anatexis.* (eds. Ashworth, J. R. & Brown, M.), pp. 105–123.Unwin Hyman, London, UK.

Powell, R., Holland, T. & Worley, B., 1998. Calculating phase diagrams involving solid solutions via non- linear equations, with examples using THERMOCALC. *Journal of Metamorphic Geology*, **16**, 577–588.

Powell, R. & Holland, T., 2004. Course notes for ‘‘THERMOCALC workshop 2004: calculating metamorphic phase equilibria’’ (ETH Zurich). (CD-ROM).

Racek, M., Štípská, P., Pitra, P., Schulmann, K. & Lexa, O., 2006. Metamorphic record of burial and exhumation of orogenic lower and middle crust: a new tectonothermal model for the Drosendorf window (Bohemian Massif, Austria). *Mineralogy and Petrology*, **86**, 221–251.

Reiners, P. W., 1998. Reactive melt transport in the mantle and geochemical signatures of mantle-derived magmas. *Journal of Petrology*, **39**, 1039–1061.

Rosenberg, C.L. & Handy, M. R., 2005. Experimental deformation of partially melted granite revisited: implications for the continental crust. *Journal of Metamorphic Geology,* **23**, 19–28.

Sawyer E. W. & Barnes S.-J. 1988 Temporal and compositional differences between subsolidus and anatectic migmatite leucosomes from the Quetico metasedimentary belt, Canada. *Journal of Metamorphic Geology,* **6**, 437–450

Sawyer, E. W., 1994. Melt segregation in the continental crust. *Geology*, **22**, 1019–1022.

Sawyer, E. W., 1996. Melt segregation and magma flow in migmatites: implications for the generation of granite magmas. *Transactions for the Royal Society of Edinburgh: Earth Sciences*, **87**, 85–94.

Sawyer, E. W., 1998. Formation and evolution of granite magmas during crustal reworking: the significance of diatexites. *Journal of Petrology*, **39**, 1147–1167.

Sawyer, E. W., 1999. Criteria for the recognition of partial melting. *Physics and Chemistry of the Earth*, **24**, 269–279.

Sawyer, E. W., 2001. Melt segregation in the continental crust: distribution and movement of melt in anatectic rocks. *Journal of Metamorphic Geology*, **19**, 291–309.

Schulmann, K., Kröner, A., Hegner, E., Wendt, I., Konopásek, J., Lexa, O. & Štípská, P., 2005. Chronological constraints on the pre-orogenic history, burial and exhumation of deep-seated rocks along the eastern margin of the Variscan orogen, Bohemian Massif, Czech Republic. *American Journal of Science*, **305**, 407–448.

Schulmann, K., Mlčoch, B. & Melka, R., 1996. High-temperature microstructures and rheology of deformed granite, Erzgebirge, Bohemian Massif. *Journal of Structural Geology*, **18**, 719–733.

Štípská, P. & Powell, R., 2005. Does ternary feldspar constrain the metamorphic conditions of high-grade meta-igneous rocks? Evidence from orthopyroxene granulites, Bohemian Massif. *Journal of Metamorphic Geology*, **23**, 627–647.

Štípská, P., Schulmann, K. & Kröner, A., 2004. Vertical extrusion and middle crustal spreading of omphacite granulite: a model of syn-convergent exhumation (Bohemian Massif, Czech Republic). *Journal of Metamorphic Geology*, **22**, 179–198.

Tajčmanová, L., Konopásek, J. & Schulmann, K., 2006. Thermal evolution of the orogenic lower crust during exhumation within a thickened Moldanubian root of the Variscan belt of Central Europe. *Journal of Metamorphic Geology*, **24**, 119–134.

Urban, M., 1992. Kinematics of the Variscan thrusting in the Eastern Moldanubicum (Bohemian Massif, Czechoslovakia): evidence from the Náměš granulite massif. *Tectonophysics*, **201**, 371–391.

van Breemen, O., Aftalion, M., Bowes, D. R., Dudek, A., Mísař, Z., Povondra, P. & Vrána, S., 1982. Geochronological studies of the Bohemian Massif, Czechoslovakia, and their significance in the evolution of Central Europe. *Transactions of the Royal Society of Edinburgh: Earth Sciences*, **73**, 89–108.

Van der Wal, D. & Bodinier, J.-L., 1996. Origin of the recrystallization front in the Ronda peridotite by km-scale pervasive porous melt flow. *Contributions to Mineralogy and Petrology*, **122**, 387–405.

Vigneresse, J.-L., Barbey, P. & Cuney, M., 1996. Rheological transitions during partial melting and crystallization with application to felsic magma segregation and transfer. *Journal of Petrology*, **37**, 1579–1600.

White, R. W., Powell, R., Holland, T. J. B. & Worley, B. A., 2000. The effect of $TiO_2$ and $Fe_2O_3$ on metapelitic assemblages at greenschist and amphibolite facies conditions: mineral equilibria calculations in the system $K_2O$–$FeO$–$MgO$–$Al_2O_3$–$SiO_2$–$H_2O$–$TiO_2$–$Fe_2O_3$. *Journal of Metamorphic Geology*, **18**, 497–511.

White, R. W. & Powell, R., 2002. Melt loss and the preservation of granulite facies mineral assemblages. *Journal of Metamorphic Geology*, **20**, 621–632.

White, R. W., Powell, R. & Clarke, G. L., 2003. Prograde metamorphic assemblage evolution during partial melting of metasedimentary rocks at low pressures: migmatites from Mt Stafford, Central Australia. *Journal of Petrology*, **44**, 1937–1960.

White, R. W., Pomroy, N.E. & Powell, R., 2005. An in situ metatexite-diatexite transition in upper amphibolite facies rocks from Broken Hill, Australia. *Journal of Metamorphic Geology*, **23**, 579–602.

White, R. W., Powell, R. & Holland, T.J.B., 2007. Progress relating to calculation of partial melting equilibria for metapelites. *Journal of Metamorphic Geology*. In print.

White, R. W., Powell, R. & Holland, T. J. B., 2001. Calculation of partial melting equilibria in the system $Na_2O$-CaO-$K_2O$-FeO-MgO-$Al_2O_3$-$SiO_2$-$H_2O$ (NCKFMASH). *Journal of Metamorphic Geology*, **19**,139–153.

Wickham, S. M., 1987. Crustal anatexis and granite petrogenesis during low-pressure regional metamorphism: The Trois Seigneurs Massif, Pyrenees, France. *Journal of Petrology*, **28**, 127–169.

Závada, P., Schulmann, K., Konopásek, J., Ulrich, S. and Lexa O., in press. Extreme ductility of feldspar aggregates – melt enhanced grain boundary sliding (GBS) and creep failure: rheological implications for felsic lower crust. *Journal of Geophysical Research*.

# CHAPTER III:

## From orthogneiss to migmatite: geochemical assessment of the melt infiltration model in the Gföhl Unit (Moldanubian Zone, Bohemian Massif)

Accepted to Lithos

# From orthogneiss to migmatite: geochemical assessment of the melt infiltration model in the Gföhl Unit (Moldanubian Zone, Bohemian Massif)

*Pavlína Hasalová [1, 2], Vojtěch Janoušek [3, 1], Karel Schulmann [2],*

*Pavla Štípská [2] and Vojtěch Erban [3]*

[1] Institute of Petrology and Structural Geology, Charles University, Albertov 6, 128 43 Prague 2, Czech Republic

[2] Université Louis Pasteur, CGS/EOST, UMR 7517, 1 rue Blessig, Strasbourg 67084, France

[3] Czech Geological Survey, Klárov 3, 118 21 Prague 1, Czech Republic

## Abstract

The Gföhl Unit is the largest migmatite terrain of the Variscan orogenic root domain in Europe. Its genesis has been until now attributed to variable degrees of *in-situ* partial melting. In the Rokytná Complex (Gföhl Unit, Czech Republic) there is a well-preserved sequence documenting the entire migmatitization process on both outcrop and regional scales. The sequence starts with (i) banded orthogneiss with distinctly separated monomineralic layers, continuing through (ii) migmatitic mylonitic gneiss, (iii) schlieren migmatite characterised by disappearance of monomineralic layering and finally to (iv) felsic nebulitic migmatite with no relics of the original banding.

While each type of migmatite shows a distinct whole-rock geochemical and Sr-Nd isotopic fingerprint, the whole sequence evolves along regular, more or less smooth trends for most of the elements. Possible mechanisms which could account for such a variation are that the individual migmatite types (i) are genetically unrelated, (ii) originated by equilibrium melting of a single protolith, (iii) formed by disequilibrium melting (with or without a small-scale melt movement) or (iv) were generated by melt infiltration from external source. The first scenario is not in agreement with the field observations and chemistry of the orthogneisses/migmatites. Neither of the remaining hypotheses can be ruled out convincingly solely on whole-rock geochemical grounds. However in light of previously obtained structural, petrologic and microstructural data, this sequence can be interpreted as a result of a process in which the banded orthogneiss was pervasively, along grain boundaries, penetrated by felsic melt derived from an external source.

In terms of this melt infiltration model the individual migmatites can be explained by different degrees of equilibration between the bulk rock and the passing melt. The melt infiltration can be modelled as an open-system process, characterised by changes of the total mass/volume and accompanied by gains/losses in many of the major- and trace elements. The modelling of the mass balance resulted in identification of a component added by a heterogeneous nucleation of feldspars, quartz and apatite from the passing melt. This is in line with the observed presence of new albitic plagioclase, K-feldspar and quartz coatings as well as resorption of relict feldspars. At the most advanced stages (schlieren and nebulitic migmatites) the whole-rock trace-element geochemical variations document an increasing role for fractional crystallization of the K-feldspar and minor plagioclase, with accessory amounts of monazite, zircon and apatite.

The penetrating melt was probably (leuco-) granitic, poor in mafic components, Rb rich, with low Sr, Ba, LREE, Zr, U and Th contents. It probably originated by partial melting of micaceous quartzo-feldspathic rocks.

If true and the studied migmatites indeed originated by a progressive melt infiltration into a single protolith resembling the banded orthogneiss, this until now underappreciated process would have profound implications regarding rheology and chemical development of anatectic regions in collisional orogens.

**Keywords:** melt infiltration, porous flow, migmatites, whole-rock geochemistry, mass balance, Bohemian Massif (Gföhl Unit)

## Introduction

The melt extraction from lower crustal rocks and its further transport to higher crustal levels are key issues of granite petrogenesis. Generally the melt fraction produced during anatexis is rather small; it is originally concentrated mainly at grain boundaries and along microfractures (Rushmer, 1995; Sawyer, 2000; Guernina & Sawyer, 2003). The mechanism of the melt segregation is still a controversial issue. It may be drained from the grain boundaries to melt-assisted sites, networks of leucosome-filled structures or dykes (see Lister & Kerr, 1991; Petford *et al.*, 1994 for review) responsible for its further transport. The other, arguably more popular model involves pervasive flow through a porous space or fracture network (McKenzie, 1984; Wickham, 1987; Weinberg, 1999) and is strongly controlled by the permeability of the system.

Regardless of its exact mechanism, the segregation will be governed by the melt density and viscosity, which in turn reflect its composition, volatile contents and temperature (Brown *et al.,* 1995; Petford *et al.*, 2000). Important factor is also the thermal and mechanical state of the crust surrounding the melting zone (Weinberg & Searle, 1998). The efficiency of the melt extraction can be further boosted by active deformation in the source (McKenzie, 1984). At the grain scale, the transport is controlled mainly by the melt geometry (wetting angle) (von Bargen & Wolf, 1986) and its amount (Rushmer, 1995; Vigneresse *et al.*, 1996). The grain-scale movement is possible as soon as the melt forms an interconnected network. Even when the wetting angle is low (von Bargen & Wolf, 1986) an important prerequisite for the operation of pervasive porous flow is the lower solidus temperature of the country rock compared to that of the penetrating melt.

The other passionately discussed problem is the further transport of the granitic melts. As an alternative to dyking (Petford *et al.*, 1994; 2000), mesoscale pervasive magma migration, either channelized using the country-rock anisotropies (Collins & Sawyer, 1996; Weinberg &

Searle, 1998; Brown & Solar, 1999; Vanderhaeghe, 1999; Weinberg, 1999; Leitch & Weinberg, 2002; Olsen *et al.*, 2004), or penetrative through the whole rock volume (Hasalová *et al.*, 2008a,b) has been proposed for hot low-viscosity crustal rocks. For the latter model, the deformation is essential.

The whole-rock compositions of the migmatitic rocks, and the trace elements with radiogenic isotopes in particular, can be useful in constraining the nature of the source, residual mineralogy, as well as degree, mechanism and timescales of the crustal melting (see Whittington & Treloar, 2002 for review). For instance the water-saturated or dehydratation melting driven by decomposition of individual hydrous phases (muscovite, biotite or amphibole) will each leave its own geochemical imprint. Moreover, the chemistry of the melt will be substantially different depending whether its bulk equilibrated with the restite (batch melting) or the extraction was in small increments with no mutual homogenization (fractional melting). Apart from these two models for the equilibrium melting, variable degrees of disequilibria seem commonplace. The disequilibrium melting takes over especially in collisional orogens, when the melt extraction was accelerated by deformation or the accessory phases were shielded by major phases in the source not participating in the melting reaction (e.g. Watt & Harley, 1993; Nabelek & Glascock, 1995; Bea, 1996; Harris & Ayres, 1998). Last but not least, the protolith is often not exposed, and thus its exact nature and composition are unknown.

The ideal elements for modelling of partial melting are those residing in the main rock-forming minerals. This is the case of LILE, whose main reservoirs are feldspars and micas (e.g. Harris & Inger, 1992). On the other hand, several trace elements are incompatible in the main rock-forming minerals but form essential structural components (ESC) in accessory phases (Hanson & Langmuir, 1978). The dissolution of such an accessory mineral at the contact with the melt will continue until either the appropriate saturation level is reached or the source is exhausted (Watson & Harrison, 1984). The saturation models are defined for the main accessories of interest in granitic magmas, zircon (Watson & Harrison, 1983), apatite (Harrison & Watson, 1984) and monazite (Montel, 1993). In reality, the dissolution of the accessory minerals is governed by a number of factors, including the temperature, melt composition, crystal size, the water activity in the magma, diffusivity, absolute solubility of the ESC coupled with the degree of the melt undersaturation and its distribution within the rock volume.

Taken together, balancing the element fluxes during partial melting is not an easy task, as the granitic melts can result from a complex interplay of a number of processes, operative on various scales (e.g. Barbey *et al.*, 1996). For open systems, a promising approach are mass transfer calculations, which take into account the changes in the total mass or volume of the system concerned (Grant, 1986; Olsen & Grant, 1991).

The Gföhl Unit of the Moldanubian Zone, Czech Republic, offers an exceptional opportunity to study the origin of migmatitic rocks, because it is possible to observe the spatial and structural relationships between the migmatites with different proportion of melt directly in the field. This means that one is able, for rocks with the same orthogneiss protolith and increasing degrees of migmatization, to investigate gradual changes in modal proportions of the rock-forming minerals, their chemistry, microstructures and whole-rock geochemical signature.

The present contribution aims to describe the major- and trace-element as well as Sr-Nd isotopic whole-rock geochemical variation in the individual gneiss and migmatite types in this unit. This, together with information on field relations, petrography and textures is used to evaluate the possible genetic hypotheses. Using the mass transfer calculations and other arguments we test the feasibility of the possible genetic scenarios. Included among them is the newly defined melt infiltration model (Hasalová *et al.*, 2008a, b), in whose terms the various types of the Gföhl gneisses and migmatites were interpreted by a process in which the banded orthogneiss was pervasively, along grain boundaries, penetrated by felsic melt derived from an external source. Such a melt infiltration model would have potentially large consequences for generation of granitic magmas and crustal rheology in collisional orogens.

## Regional setting

The Moldanubian Zone represents the orogenic root domain of the Bohemian Massif, which developed during the Variscan collision in the Devonian to Carboniferous times (Fig. 1a) (Matte *et al.*, 1990; Dallmeyer *et al.*, 1995; Schulmann *et al.*, 2005 and references therein). At its eastern extremity, the Moldanubian rocks were thrust over the Cadomian Brunia basement along a so-called Moldanubian Thrust. The associated deformation produced a crustal-scale shear zone in the basement (the Moravian Zone, MZ), which crops out as three NE-SW trending tectonic windows (Suess, 1912; Urban, 1992; Schulmann *et al.*, 1994; Fritz *et al.*, 1996) (Fig. 1b).

The Moldanubian Zone is a tectonic assemblage of medium- to high-grade metamorphic rocks, intruded by numerous large, mostly Carboniferous plutons (Finger *et al.*, 1997). The Moldanubian sequence has been subdivided into mainly metasedimentary and gneissic middle-crustal rocks of Proterozoic and Lower Palaeozoic protolith ages assigned to the Drosendorf Unit by some authors (e.g. Tollmann, 1982; Franke, 2000) and the structurally upper and higher grade Gföhl Unit (Fuchs & Matura, 1976; Petrakakis, 1997 and references therein). The middle crustal rock assemblage consists of the Monotonous Series (mainly migmatitic Grt–Bt–Sil paragneiss with minor orthogneiss and amphibolite) and the Varied Series (paragneiss with intercalations of amphibolite, calc-silicate gneiss, marble, quartzite and graphite schist).

The Gföhl Unit is dominated by high-grade felsic gneiss and migmatite and layered migmatitic amphibolites. It also includes a high-pressure felsic Grt–Ky–Kfs granulite, which encloses bodies of garnet and spinel peridotites, pyroxenites and eclogites (Carswell, 1991;

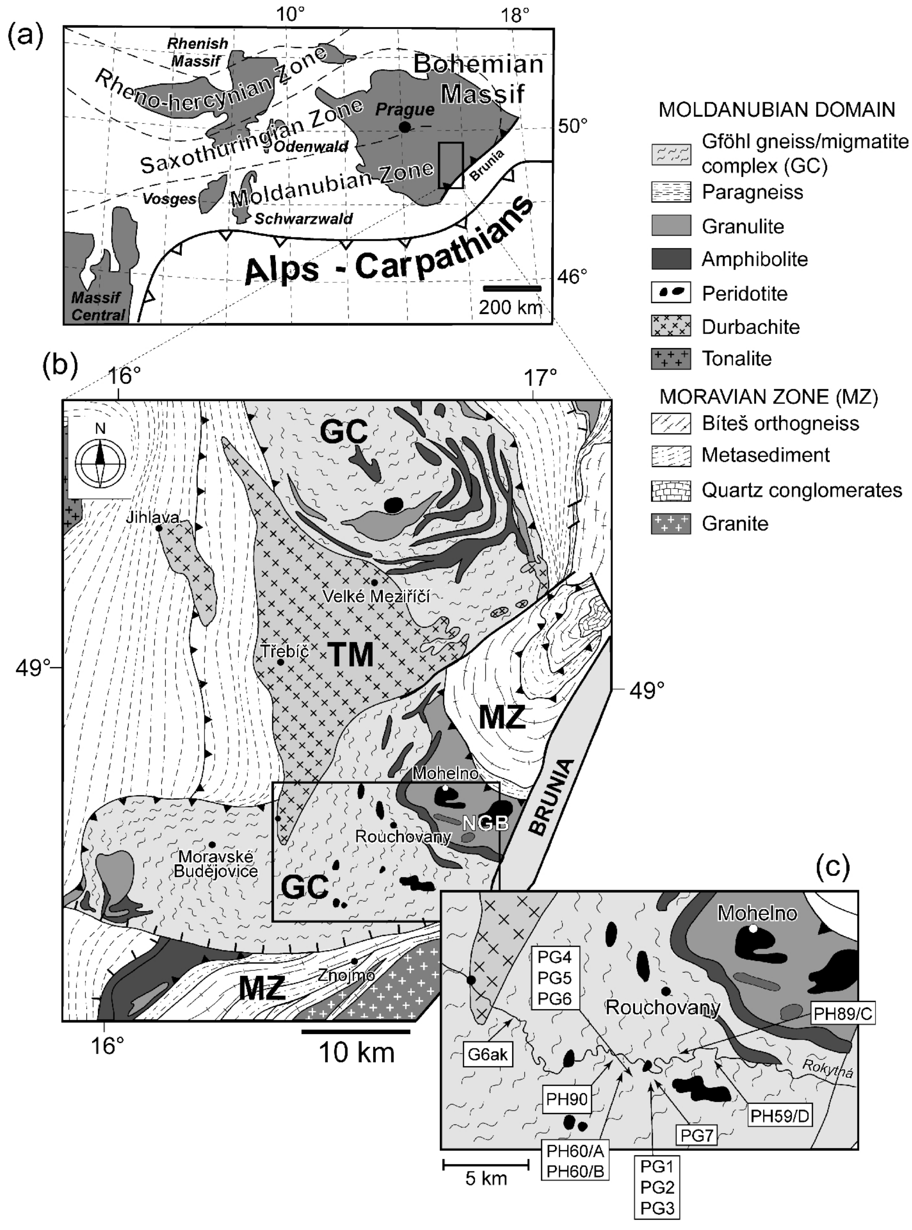


**Fig 1:** *(a) Location of the Gföhl Unit in the context of the Central European Variscides. (b) Geological map of the eastern part of the Bohemian Massif with location of the studied area (outlined).(c) Schematic map of the Rokytná Complex, showing the distribution of whole-rock samples collected in the course of this work.*

O'Brien & Carswell, 1993; Medaris *et al.*, 1995). The exhumation of high-grade rocks and their juxtaposition to the middle crust within the orogenic root has been recently attributed to vertical extrusion of orogenic lower crust followed by horizontal channelized spreading at middle crustal levels, associated with retrogression and widespread melting (Schulmann *et al.*, 2005; Tajčmanová *et al.*, 2006).

The Gföhl gneiss and migmatite vary from banded orthogneiss without signs of melting towards migmatite with isotropic (nebulitic) structure without traces of earlier fabrics. The protolith is considered to be granitic (Dudek *et al.*, 1974; Matějovská, 1975). The U-Pb SHRIMP dating showed that the protolith was Early Palaeozoic (488 ± 6 Ma: Friedl *et al.*, 2004). The age of Variscan metamorphism of the Gföhl gneiss has been estimated at 341 ± 4 and 337 ± 3 Ma (conventional U-Pb ages for zircon and monazite, respectively: van Breemen *et al.*, 1982) in Moravia and at 340 ± 10 Ma (SHRIMP ages of outer growth zones of zircons: Friedl *et al.*, 1998) together with 339.9 ± 0.9 Ma (U–Pb monazite: Friedl *et al.*, 1994) in Austria.

The Gföhl gneisses and HP felsic granulites show in many places intimate mutual association (Dudek *et al.*, 1974; O'Brien & Rötzler, 2003), which led some workers to propose that the gneisses may represent retrogressed granulites (Cooke & O'Brien, 2001). The peak conditions in the granulite bodies, estimated by many workers at 1000°C and >15 kbar (see O'Brien, 2006 for review), have been recently constrained by others to c. 800–900°C and 18 kbar (Medaris Jr. *et al.*, 1998; Štípská & Powell, 2005; Tajčmanová *et al.*, 2006). The peak pressure estimates have been interpreted as metamorphic conditions of the vertical extrusional fabric at *c.* 340 Ma (Schulmann *et al.*, 2005). The estimated pressure of re-equilibration associated with flat fabric that originated during the lateral spreading varies from 10 kbar (Štípská *et al.*, 2004), through 7 kbar (Racek *et al.*, 2006) to 4.0 kbar (Tajčmanová *et al.*, 2006), at temperatures between 700 and 800°C. In Austria the metamorphic conditions of the Gföhl gneiss and migmatite were estimated at 750°C and *c.* 7 kbar (Petrakakis, 1986a, 1986b), and nearly identical values were obtained by Owen & Dostal (1996) from western Moravia.

## Field relations and migmatite occurrence

The studied area (Fig. 1b, c), the so-called **Rokytná Complex** (Svoboda *et al.*, 1966), is situated at the eastern extremity of the Gföhl Unit close to its contact with the Moravian Zone. It is bound by the rocks of the Moravian Zone (MZ) in the East, by the Náměš granulite body (NGB) in the North and by the Třebíč durbachite Massif (TM) in the West (Fig. 1b). The main rock types in the Rokytná Complex are high-grade orthogneisses and migmatites, enclosing minor bodies of amphibolites, granulites and paragneisses (Matějovská, 1975). The migmatites of the Rokytná Complex are texturally highly variable. In order to refer to individual rock types, the current paper employs migmatite terminology of Mehnert (1971), based on their macroscopic appearance.

Two major deformation events were recorded in this gneiss-migmatite complex (Urban, 1992; Schulmann *et al.*, 1994; Hasalová *et al.*, 2008a). The $D_1$ event most likely corresponded to early stages of lower crust exhumation, triggered by shortening of the thickened orogenic

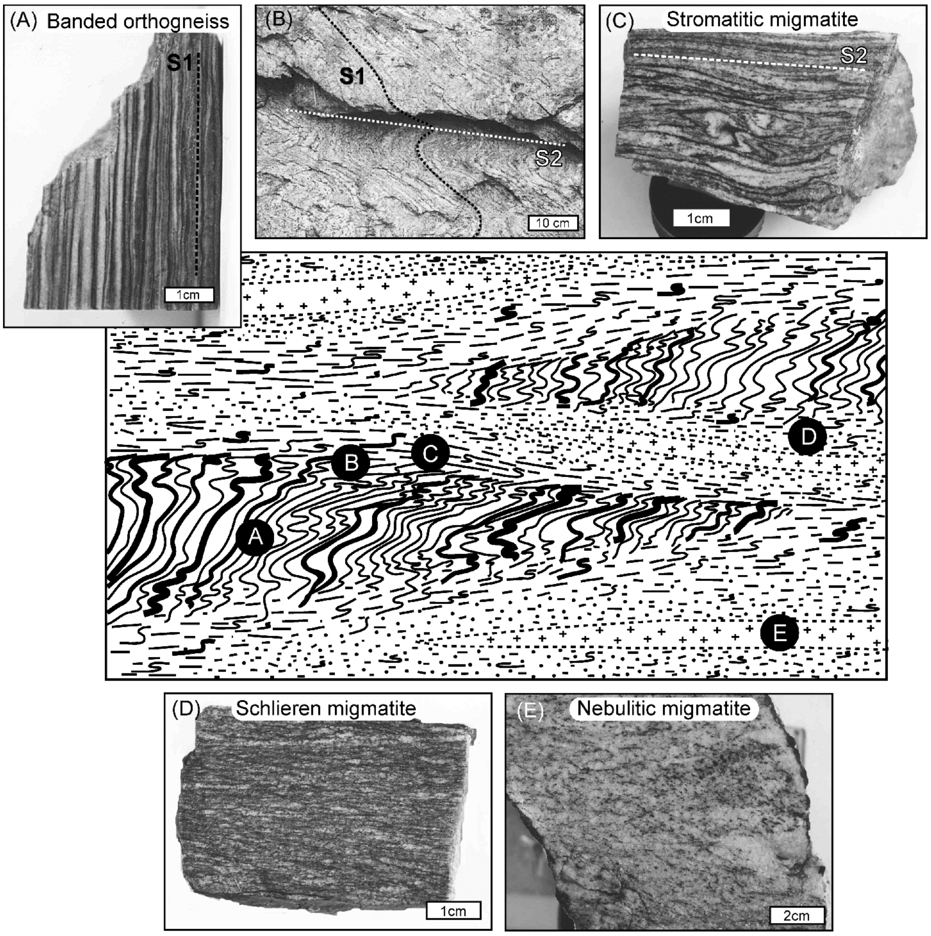


**Fig. 2**: *Sketch showing the individual gneiss and migmatite types and their relationships within an outcrop (the width of the figure is 5 m; modified after Hasalová et al, 2008a). Banded orthogneiss with distinct $S_1$ compositional layering (a) is folded and transposed (b) to the stromatitic migmatite (c) that passes gradually to the schlieren migmatite (d) and finally to the completely isotropic nebulitic migmatite with no relics of gneissosity (e). Shown are typical macrophotographs of each rock type.*

root (Schulmann *et al.*, 2005). The $D_2$ shearing has been attributed to horizontal spreading of lower crust at mid-crustal levels (e.g. Tajčmanová *et al.*, 2006).

The deformation phase $D_1$ resulted in formation of steep, west dipping solid-state foliation $S_1$, represented by compositional layering in the *banded orthogneiss* (Fig. 2a). The $D_2$ deformation led to development of a large crustal-scale shear zone and was associated with reworking and folding of $S_1$compositional layering that is locally preserved in elongated relict domains (Fig. 2). These relict domains with gently folded $S_1$ fabric are surrounded by highly deformed zones with tightly folded $S_1$ fabric. Locally the $S_1$ fabric is completely transposed into the new $S_2$ foliation dipping gently to the SW. The resulting composite $S_{1-2}$ fabric is characterized by banded structure with polymineralic K-feldspar- and plagioclase-rich domains resembling *stromatitic migmatite* (Fig. 2c). Detailed field study revealed that, with increasing degree of deformation, the stromatitic migmatite gradually passes into more isotropic *schlieren migmatite* (Fig. 2d) still containing rootless folds modifying the relics of the $S_1$ fabric. This rock type is alternating with irregular bodies or elongated lenses of felsic fine-grained *nebulitic migmatite* (Fig. 2e).

Such migmatite variations, which have originated through intense $D_2$ deformation superimposed on early steep anisotropy, can be identified both on the outcrop and the regional scales. In the studied area, stromatitic migmatites generally prevail over schlieren migmatites; the banded orthogneisses and nebulitic migmatites are subordinate. Macroscopically visible melt accumulations or granitic veins parallel to $S_2$ and tensional gashes perpendicular to $S_2$ are locally present.

### *Definition of individual rock types*

Hasalová *et al.* (2008a) showed the intimate relationship between different migmatite types suggesting that they all originated from the same protolith and that the banded orthogneiss and nebulitic migmatite can be considered as end-members of a continuous structural evolution.

All the studied samples contain stable mineral assemblage Pl + Kfs + Qtz + Bt ± Grt ± Sill; common accessory phases are apatite, monazite, zircon and xenotime. The modal proportion of feldspars remains in all rock types nearly the same, only the quartz shows a marked increase. On the other hand, the biotite and garnet contents decrease towards the nebulitic migmatite (Table 1).

*The banded orthogneiss* is characterized by monomineralic banding, defined by recrystallized K-feldspar, plagioclase aggregates and quartz bands, alternating with layers rich in biotite, garnet, sillimanite and apatite.

*The stromatitic migmatite* is marked by the onset of disintegration of the original monomineral banding and is composed of plagioclase and K-feldspar aggregates with subordinate quartz. These aggregates are rimmed by biotite locally overgrown by fibrolitic sillimanite.

*The schlieren migmatite* is made of K-feldspar-quartz-rich and plagioclase-quartz-rich aggregates. The original banding is distinguishable only from the modal content of the mineral phase dominant in these feldspar aggregates.

*The nebulitic migmatite* represents the most isotropic rock type, completely lacking relics of the original gneissosity. The migmatite occurs as irregular flat bodies or elongated lenses.

### Mineral chemistry and microstructures

The banded orthogneiss always contains two chemically and microstructurally distinct **plagioclase** populations (Table 1 & Fig. 3a-d): (i) well-equilibrated grains with straight boundaries in plagioclase aggregates ($An_{25–30}$ and (ii) newly grown plagioclase ($An_{10–20}$) forming interstitial grains or thin films coating the K-feldspar or plagioclase grains. In the stromatitic migmatite, the degree of albite coating increases and both the newly formed grains ($An_{4–10}$) and the relict grains ($An_{15–25}$) are more sodic (Table 1). In the schlieren migmatite large, corroded relict grains ($An_{7–15}$) are resorbed by new interstitial plagioclase ($An_{1–5}$) (Fig. 3c). This results, in the nebulitic migmatite, in complete overgrowths of small cuspate plagioclase ($An_{0–4}$) accompanied by K-feldspar and quartz on residual, strongly irregular plagioclase ($An_{5–10}$) grains. The newly-grown albitic plagioclase is, in agreement with Sawyer (1999, 2001) interpreted as having crystallized from the former melt.

*Table 1: Evolution of mineral chemistry and mineral proportions in the studied sequence*

| | **Banded orthogneiss** | **Stromatitic migmatite** | **Schlieren migmatite** | **Nebulitic migmatite** |
|---|---|---|---|---|
| XFe (Grt) | 0.75–0.85 | 0.85–0.91 | 0.96–0.97 | 0.98–1.00 |
| XFe (Bt) | 0.43–0.50 | 0.55–0.59 | 0.76–0.79 | 0.91–0.93 |
| An (Pl relict) | 0.25–0.30 | 0.15–0.25 | 0.07–0.15 | 0.05–0.10 |
| An (Pl new) | 0.10–0.20 | 0.04–0.10 | 0.01–0.05 | 0.00–0.04 |
| Or (Kfs) | 0.80–0.95 | 0.80–0.95 | 0.80–0.95 | 0.80–0.95 |
| Ti (Bt) (p.f.u.) | 0.20–0.30 | 0.20–0.25 | 0.18–0.20 | 0.02–0.05 |
| Mineral proportions (wt. %) | | | | |
| Kfs | 19–34 (27) | 28–31 (30) | 28–31 (27) | 29–34 (37) |
| Plg | 26–32 (30) | 28–35 (30) | 24–29 (27) | 21–28 (26) |
| Qtz | 25–32 (28) | 26–33 (31) | 33–36 (35) | 32–43 (37) |
| Bt | 5–15 (10) | 4–9 (7) | 6–9 (7) | 6–7 (6) |
| Grt | 5–6 (5) | 4–2 (2) | <2 | <1 |
| $R^2$ | 0.33–0.82 | 0.31–0.60 | 0.25–0.53 | 0.20–0.90 |

*Grt* garnet; *Bt* biotite; *Pl* plagioclase; *Kfs* K-feldspar; *Qtz* quartz; *XFe* = $Fe_{(tot)}/(Fe_{(tot)} + Mg)$; *An* anorthite = Ca/(Ca+Na+K); *Or* orthoclase = K/(Ca+Na+K). Mineral proportions were obtained by the constrained least-squares method (Albarède, 1999); shown are the ranges and (in brackets) average values; $R^2$ = goodness of fit (see text for details)

Composition of **K-feldspar** is rather uniform (Table 1), however its microstructure evolves (Fig. 3). In the banded orthogneiss, recrystallized K-feldspar grains form almost monomineral bands (Fig. 3a). In the stromatitic migmatite, the K-feldspar bands start to be disintegrated with individual grains having slightly lobate boundaries traced by interstitial quartz and plagioclase. The schlieren migmatite shows K-feldspar relics that are highly irregular and surrounded by myrmekite and newly-grown interstitial quartz, plagioclase and K-feldspar (Fig. 3c). The degree of K-feldspar corrosion is highest in the nebulitic migmatite, where the residual grains are completely overgrown by cuspate plagioclase, accompanied by new K-feldspar and quartz (Fig. 3b).

**Quartz** occurs as recrystallized ribbons or interstitial grains and inclusions in the feldspar aggregates in the banded orthogneiss. Stromatitic, schlieren and nebulitic migmatite show gradual disappearance of the former quartz ribbons. Instead the quartz forms irregular polycrystalline aggregates with lobate grain boundaries or interstitial grains at feldspar boundaries, where it participates in resorption of the relict feldspar.

**Biotite** evolves texturally from elongated flakes in layers separating the feldspar-rich aggregates (banded orthogneiss) to grains dispersed in plagioclase-rich aggregates (stromatitic migmatite) or in the matrix composed of plagioclase, quartz and K-feldspar (schlieren and nebulitic migmatites). Cuspate biotite shapes, developed mostly in the nebulitic migmatite, were interpreted by Mehnert *et al.* (1973) and Büsch *et al.* (1974) as resulting from the reaction with the melt. The biotite chemistry evolves continuously, in the sequence from the banded orthogneiss to nebulitic migmatite, towards more Fe-rich and Ti-poor compositions (Table 1). Biotite is locally overgrown by fibrolitic **sillimanite**.

**Garnet** is unzoned almandine, with remarkable systematic increase in $X_{Fe}$ from the banded orthogneiss to nebulitic migmatite (Table 1). Garnet in banded orthogneiss and stromatitic migmatite occurs as small idiomorphic grains along plagioclase and biotite layers. In schlieren and nebulitic migmatite, rare large atoll-shaped garnet appears in the matrix.

The most abundant among **accessory minerals** is apatite; characteristic but less common are monazite, zircon and xenotime. The Th content in monazite is continuously increasing towards the nebulitic migmatite, documenting an increasing brabantite substitution (Fig. 4 & Table 2). Monazite in the nebulitic migmatites is characterised by the highest contents of Th (up to 24 wt. % $ThO_2$), with elevated U (< 4 wt. % $UO_2$), Ca (up to 6 wt. % CaO) and Y (< 2.2wt. % $Y_2O_3$).

Hasalová *et al.* (2008a) assessed and quantified the microstructural changes from banded orthogneiss to nebulitic migmatite, finding out that the grain size of all felsic phases

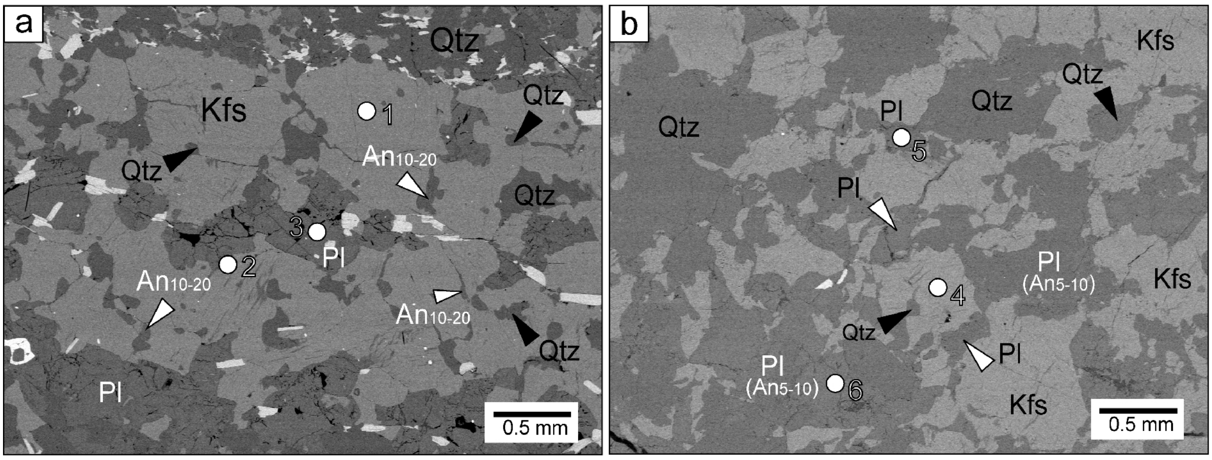


| | Banded orthogneiss | | | Stromatitic migmatite | | | Schlieren migmatite | | | Nebulitic migmatite | | |
|---|---|---|---|---|---|---|---|---|---|---|---|---|
| Mineral | Kfs | Pl | Pl | Kfs | Pl | Pl | Kfs | Pl | Pl | Kfs | Pl | Pl |
| Position | core | rim/films | core | core | rim/films | core | core | rim/films | core | core | rim/films | core |
| Wt. % | (1) | (2) | (3) | | | | (7) | (8) | (9) | (4) | (5) | (6) |
| $SiO_2$ | 64.69 | 67.48 | 61.70 | 64.37 | 67.24 | 63.68 | 64.51 | 67.64 | 65.04 | 63.97 | 67.79 | 65.42 |
| $Al_2O_3$ | 18.41 | 20.16 | 24.12 | 18.55 | 20.27 | 22.55 | 18.38 | 19.41 | 21.11 | 18.98 | 19.90 | 21.69 |
| CaO | 0.05 | 2.83 | 5.29 | 0.04 | 1.07 | 3.90 | 0.01 | 0.42 | 2.53 | 0.05 | 0.28 | 1.93 |
| $Na_2O$ | 2.24 | 9.63 | 8.59 | 1.56 | 11.50 | 9.76 | 1.41 | 11.86 | 10.53 | 1.22 | 11.86 | 10.97 |
| $K_2O$ | 13.96 | 0.12 | 0.43 | 15.04 | 0.10 | 0.23 | 15.18 | 0.10 | 0.15 | 15.65 | 0.02 | 0.18 |
| BaO | 0.39 | 0.00 | 0.00 | 0.13 | 0.00 | 0.00 | 0.08 | 0.00 | 0.00 | 0.00 | 0.00 | 0.00 |
| Total | 99.73 | 100.22 | 100.12 | 99.68 | 100.18 | 100.12 | 99.57 | 99.43 | 99.36 | 99.86 | 99.86 | 100.19 |

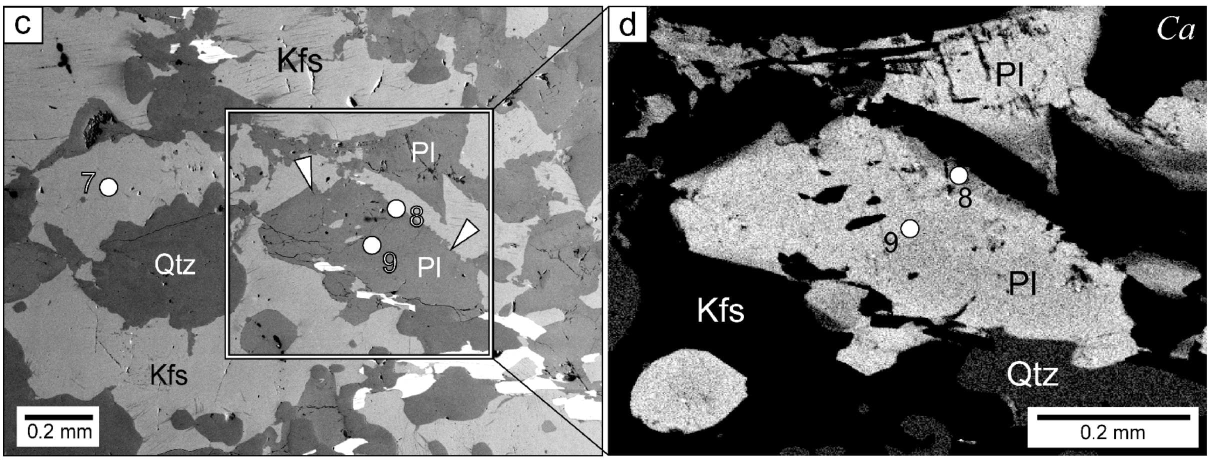


**Fig. 3:** *Microscopic appearance and composition of feldspars in studied samples. (a-c) BSE images showing presence of melt and important changes in the feldspar textures within the studied sequence. (a) Typical microstructure of banded orthogneisses and stromatitic migmatites: recrystallized feldspar aggregate with numerous quartz (black arrows) and plagioclase (white arrows) interstitial grains/ films tracing the K-feldspar boundaries (sample PH60/B). Relict plagioclase ($An_{24–30}$) is rimmed by more albitic plagioclase ($An_{10–20}$) and K-feldspar grains are traced by thin plagioclase ($An_{10–20}$) films (white arrows).This albitic plagioclase represents a component crystallized from the partialmelt. (b) Typical appearance of schlieren and nebulitic migmatites featuring irregularly shaped feldspar and quartz grains. New interstitial plagioclase (white arrows), K-feldspar and quartz (black arrows) grains are tracing most of the feldspar boundaries. These newly crystallized feldspar and quartz resorb relict feldspar grains, causing their highly irregular shapes (sample PH59/C). (c) Detail of the irregular lobate K-feldspar grain completely embayed with newly crystallized quartz and plagioclase. Relict plagioclase grains are also surrounded by new albitic plagioclase (white arrows) (sample PH90). (d) Compositional map of the Ca distribution. It shows that a less sodic plagioclase is overgrown by albitic plagioclase crystallized from the melt (sample PH90). The feldspar compositions are summarized in the table. Note a continuous decrease in the $Na_2O$ contents in each of the relict and newly-crystallized plagioclases throughout the studied sequence.*

*Table 2: Representative microprobe analyses of monazite in individual rock types*

| | Banded orthogneiss | | Stromatitic migmatite | | Schlieren migmatite | | Nebulitic migmatite | |
|---|---|---|---|---|---|---|---|---|
| Sample | PH60/B | PH60/B | PH14/N | PH14/N | PH63/C | PH63/C | PH59/D | PH59/D |
| Wt. % | | | | | | | | |
| $P_2O_5$ | 29.97 | 30.40 | 28.87 | 29.24 | 29.83 | 30.18 | 29.62 | 28.86 |
| $SiO_2$ | 0.31 | 0.14 | 0.55 | 0.52 | 0.54 | 0.49 | 0.77 | 0.91 |
| $ThO_2$ | 4.04 | 2.59 | 8.53 | 8.85 | 10.08 | 8.53 | 22.01 | 24.10 |
| $U_2O_3$ | 0.71 | 0.85 | 1.50 | 0.78 | 0.94 | 0.59 | 1.68 | 3.65 |
| $La_2O_3$ | 13.42 | 13.04 | 10.87 | 11.24 | 10.01 | 10.39 | 8.00 | 6.82 |
| $Ce_2O_3$ | 33.41 | 32.49 | 27.70 | 27.84 | 27.78 | 28.61 | 22.19 | 18.64 |
| $Pr_2O_3$ | 3.08 | 3.00 | 2.51 | 2.80 | 2.90 | 2.65 | 2.16 | 1.68 |
| $Nd_2O_3$ | 10.95 | 11.55 | 9.39 | 9.25 | 9.27 | 9.11 | 5.16 | 4.42 |
| $Sm_2O_3$ | 1.16 | 1.45 | 1.24 | 1.38 | 1.31 | 1.57 | 1.03 | 0.42 |
| $Gd_2O_3$ | 1.20 | 1.61 | 1.17 | 1.11 | 1.38 | 1.26 | 0.83 | 0.56 |
| $Y_2O_3$ | 0.75 | 1.60 | 4.40 | 4.00 | 3.95 | 3.93 | 2.24 | 1.80 |
| $Al_2O_3$ | 0.03 | 0.02 | 0.01 | 0.00 | 0.00 | 0.00 | 0.01 | 0.00 |
| CaO | 0.91 | 0.84 | 1.81 | 1.86 | 2.13 | 1.73 | 4.83 | 6.03 |
| SrO | 0.00 | 0.00 | 0.00 | 0.00 | 0.00 | 0.00 | 0.00 | 0.01 |
| Total | 99.91 | 99.57 | 98.54 | 98.88 | 100.11 | 99.02 | 100.52 | 97.90 |
| P | 1.002 | 0.992 | 0.969 | 0.974 | 0.982 | 0.978 | 0.971 | 0.969 |
| Si | 0.006 | 0.012 | 0.022 | 0.021 | 0.016 | 0.021 | 0.030 | 0.036 |
| ∑ (P→Si) | 1.008 | 1.005 | 0.991 | 0.994 | 0.998 | 0.999 | 1.001 | 1.005 |
| Th | 0.023 | 0.036 | 0.077 | 0.079 | 0.072 | 0.089 | 0.194 | 0.218 |
| U | 0.008 | 0.006 | 0.014 | 0.007 | 0.005 | 0.008 | 0.015 | 0.033 |
| La | 0.187 | 0.194 | 0.159 | 0.163 | 0.161 | 0.143 | 0.114 | 0.100 |
| Ce | 0.463 | 0.478 | 0.402 | 0.401 | 0.427 | 0.394 | 0.315 | 0.271 |
| Pr | 0.043 | 0.044 | 0.036 | 0.040 | 0.037 | 0.041 | 0.030 | 0.024 |
| Nd | 0.161 | 0.153 | 0.133 | 0.130 | 0.129 | 0.128 | 0.071 | 0.063 |
| Sm | 0.019 | 0.016 | 0.017 | 0.019 | 0.017 | 0.017 | 0.014 | 0.006 |
| Gd | 0.021 | 0.016 | 0.015 | 0.015 | 0.017 | 0.018 | 0.011 | 0.007 |
| Y | 0.033 | 0.016 | 0.093 | 0.084 | 0.075 | 0.081 | 0.046 | 0.038 |
| Al | 0.001 | 0.001 | 0.001 | 0.000 | 0.000 | 0.000 | 0.000 | 0.000 |
| Ca | 0.035 | 0.038 | 0.077 | 0.079 | 0.070 | 0.088 | 0.200 | 0.256 |
| Sr | 0.000 | 0.000 | 0.000 | 0.000 | 0.000 | 0.000 | 0.000 | 0.000 |
| ∑ (Th→Sr) | 0.993 | 0.997 | 1.023 | 1.016 | 1.009 | 1.008 | 1.011 | 1.016 |
| Total | 2.000 | 2.000 | 2.010 | 2.010 | 2.010 | 2.010 | 2.010 | 2.020 |
| End-members | | | | | | | | |
| Huttonite | 0.56 | 1.23 | 2.15 | 2.03 | 1.58 | 2.06 | 2.93 | 3.57 |
| Monazite | 87.95 | 88.83 | 73.07 | 74.11 | 76.41 | 71.77 | 53.88 | 45.62 |
| Xenotime | 5.43 | 3.11 | 10.57 | 9.66 | 9.07 | 9.82 | 5.62 | 4.47 |
| Brabantite | 6.05 | 6.83 | 14.22 | 14.19 | 12.95 | 16.35 | 37.57 | 46.34 |

Huttonite = $ThSiO_4$; monazite = (La–Sm)$PO_4$; xenotime = (Y,Gd–Lu)$PO_4$;
brabantite = (Th, Ca, U, Pb)$(PO_4)_2$

decreases continuously in the studied sequence. Resulting grain size distribution was interpreted to result from increasing nucleation rate and decreasing growth rate in the textural sequence. This is in accord with resorption of old/relict minerals and crystallization of new minerals from melt along the feldspar boundaries. For further details on mineralogy and microstructures in the migmatite sequence the reader is referred to this publication.

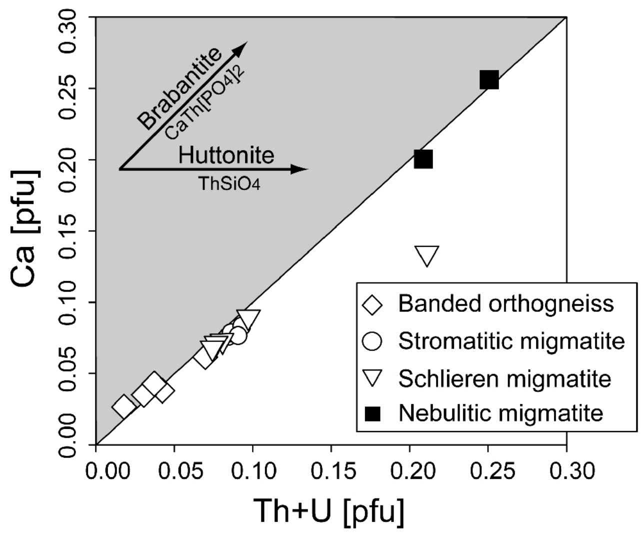


**Fig. 4:** *Monazite compositions from the four studied rock types. Binary plot Th + U vs. Ca (pfu) demonstrates the importance of brabantite substitution, Ca(Th, U) REE-2 and only a minor role for the huttonite substitution, (Th, U) Si $REE_{-1}P_{-1}$*

## Whole-rock geochemistry

### *Major elements*

The studied samples are all broadly granitic in composition, as demonstrated for instance by the Q'-ANOR diagram of Streckeisen & Le Maître (1979) based on the CIPW normative mineralogy (Fig. 5). Whereas the banded orthogneisses and stromatitic migmatites correspond mostly to granite, schlieren migmatites straddle the boundary of the alkali feldspar granite domain occupied by the nebulitic migmatites.

Analogously, each of the groups shows a rather restricted range of major-element compositions. However there is a tendency for systematic changes in the whole migmatite sequence (Fig. 6 & Table 3). Thus the banded orthogneiss is the least siliceous ($SiO_2$ = 68.09–72.93 wt. %) and richest in most other oxides ($TiO_2$ = 0.29–0.56, $Al_2O_3$ = 11.50–15.40, $FeO_t$ = 1.98–3.39, MgO = 0.32–1.04, CaO = 0.95–1.66). Convex downward trends with an initial sharp decrease and an inflection point at $SiO_2$ *c.* 73–74 % are characteristic

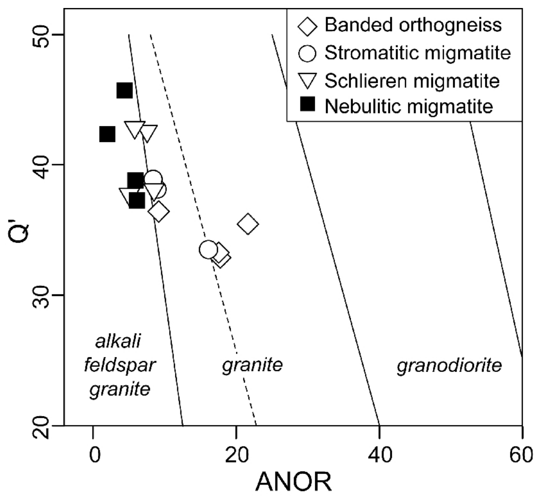


**Fig. 5:** *Enlarged part of the Q'–ANOR classification for studied orthogneiss and migmatite samples (after Streckeisen and Le Maître, 1979; based on the CIPW norm). Banded orthogneiss and stromatitic migmatite correspond to granite. Schlieren migmatite straddle the boundary of the alkali feldspar granite domain, nebulitic migmatite falls purely into the alkali feldspar granite field.*

also of the mafic components $TiO_2$, $FeO_t$, MgO and CaO. The compositional ranges observed in the most siliceous nebulitic migmatite are $SiO_2$ = 73.8–78.10, $TiO_2$ = 0.10–0.19, FeOt = 1.41–1.75, MgO = 0.15–0.30 and CaO = 0.95–1.66. On the other hand, the alkalis and $P_2O_5$ fail to define clear, non-scattered trends. All the studied samples are peraluminous; the values of the Shand's index A/CNK (molar $Al_2O_3/(CaO + Na_2O + K_2O)$, Table 3), decrease from 1.13–1.20 in the banded orthogneiss to 1.09–1.16 in the nebulitic migmatite.

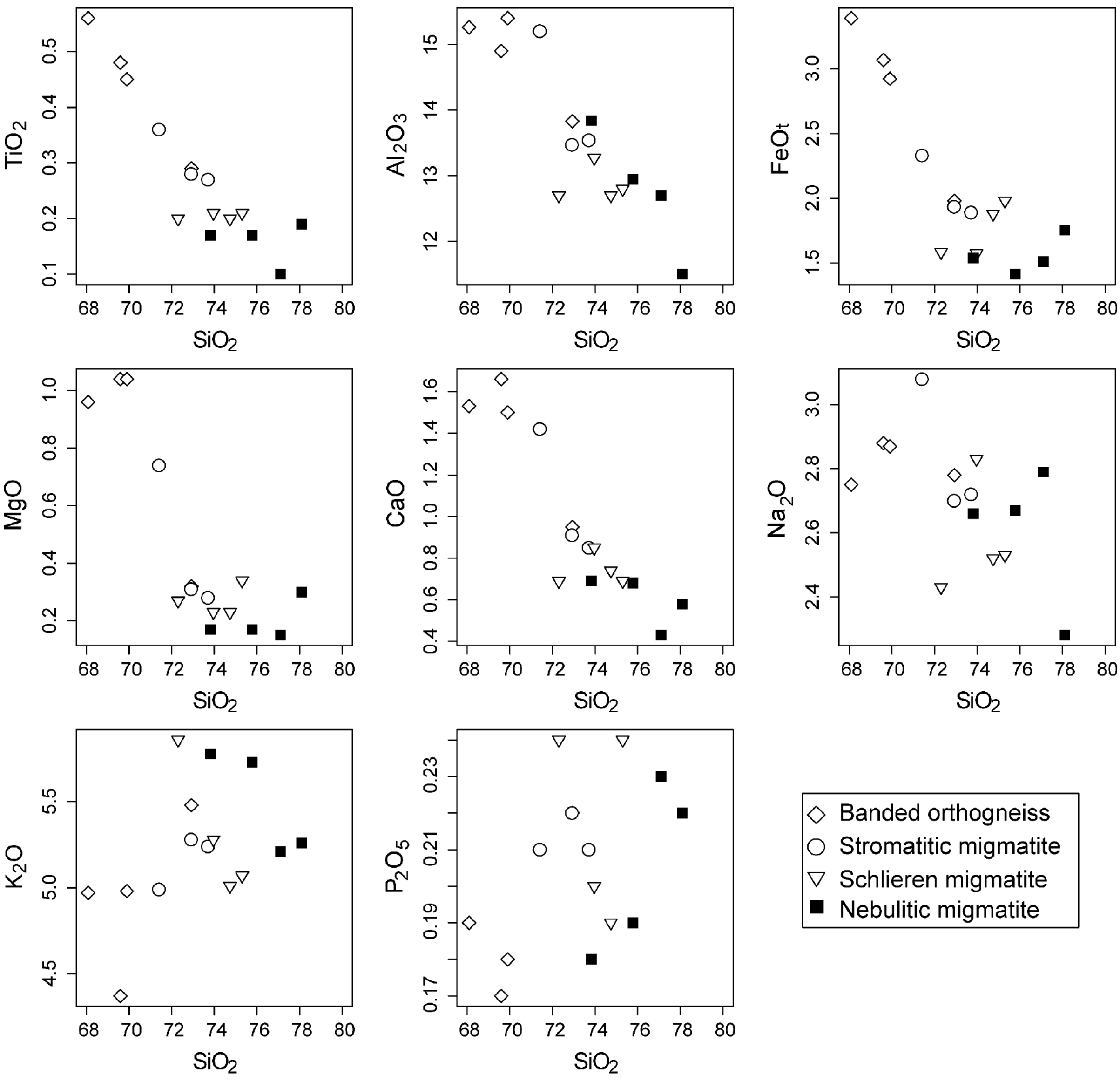


**Fig. 6:** *Harker plots showing the major-element evolution from the banded orthogneiss to the nebulitic migmatite (wt. %). Note that some of the oxides show remarkable horizontal shifts at the end of the sequence, i.e. in the more siliceous schlieren and nebulitic migmatites. This is ascribed to an increasing role for the fractional crystallization. See text for explanation.*

## Trace elements

### Overall variation

While some of the trace elements show a more or less monotonous decrease with increasing silica (Ba, La, Eu and Zr) the trends for the others are more complicated (Fig. 7 & Table 4). The comparisons of trace-element concentrations between individual samples and their groups are facilitated by spiderplots normalized to the average composition of the Earth‘s upper crust (Taylor & McLennan, 1985) (Fig. 8). The banded orthogneiss is characterised by having concentrations comparable with the upper crustal averages. Notable is only a slight (up to *c.*

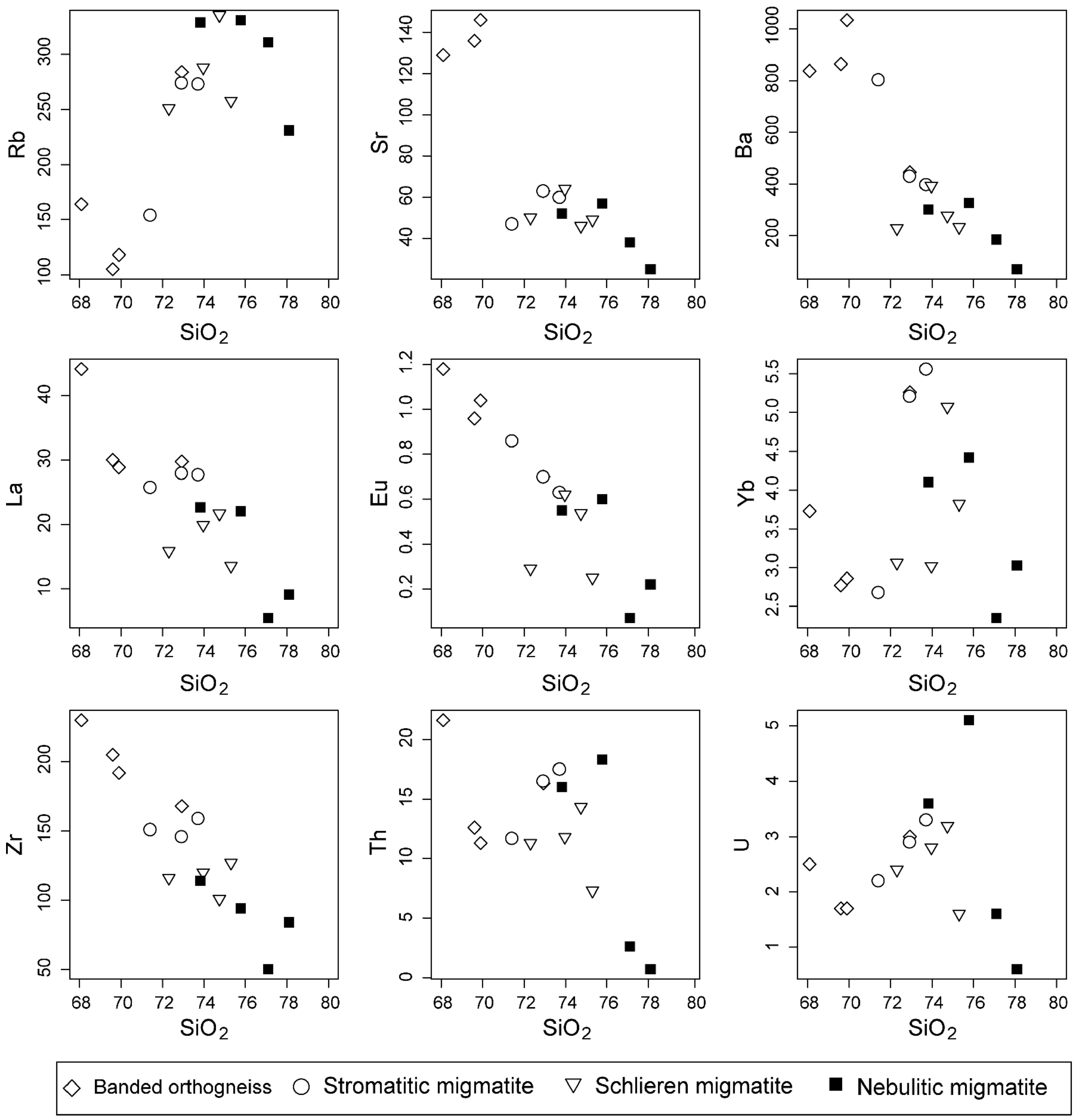


**Fig. 7**: *Selected binary plots of $SiO_2$ vs. trace elements (typical LILE, REE and HFSE, in ppm). Some of the trace elements (Ba, La, Eu and Zr) show a more or less continuous decrease throughout the studied sequence, the trends for the others are more complicated..*

2.5×) enrichment in the HREE, and remarkable troughs for Nb (0.3–0.5), Sr (0.18–0.42), Tb (0.40–0.54) and a less apparent one for Ti (0.48–0.93). The character of distribution patterns for other rock types is generally similar; however many of the trace elements show large variations and an overall tendency do decrease, especially in the more siliceous schlieren and nebulitic migmatites. The troughs for Sr, Tb and Ti progressively deepen. Later in the sequence conspicuous negative Ba, Th and, lesser, U, La, Ce, Nd, Sm, Zr and Hf anomalies also appear.

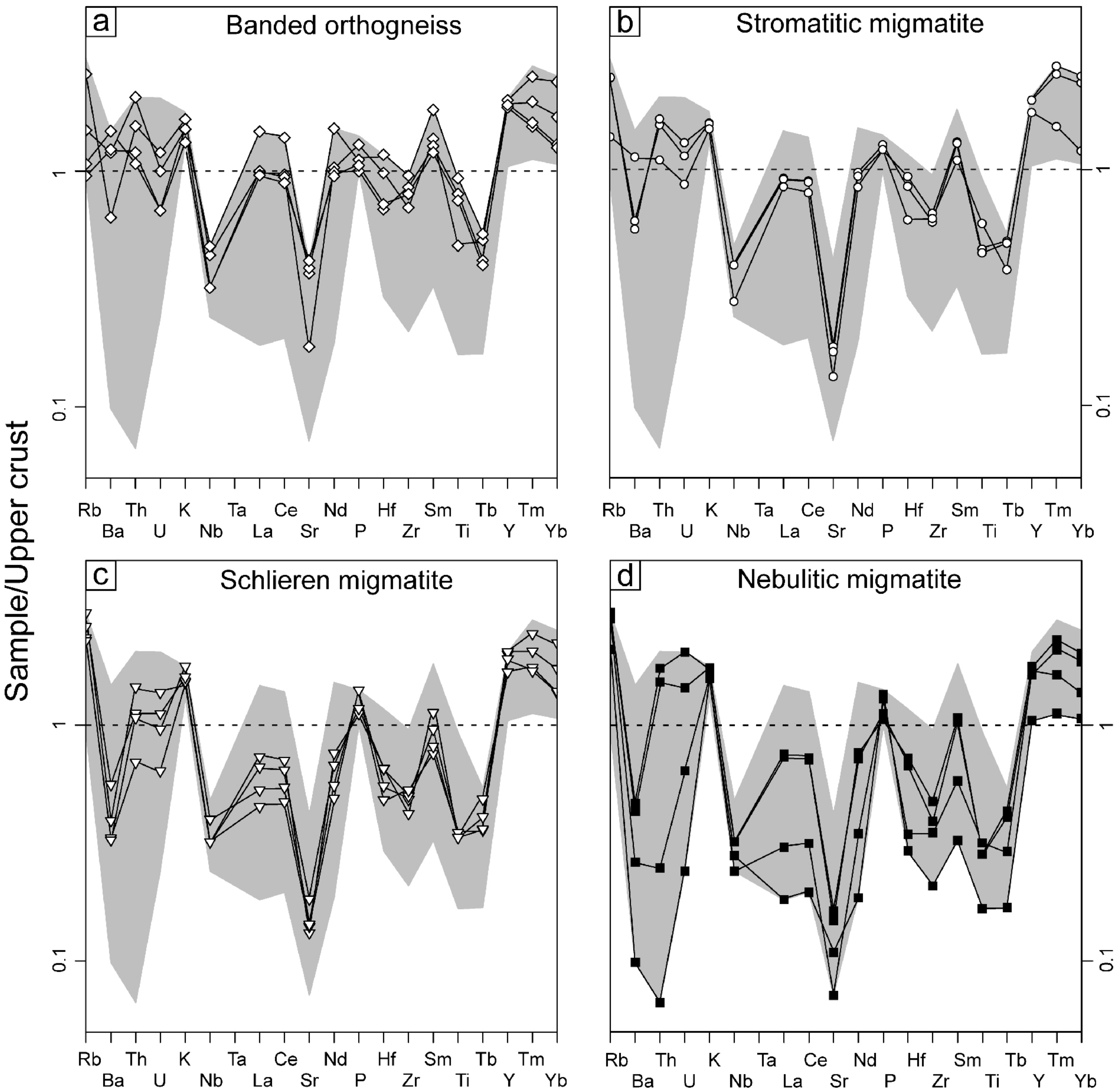


**Fig. 8:** *Spider plots normalized to the composition of the average upper crust (Taylor & McLennan, 1985). The overall shape of the individual patterns for all rock types is similar. Broad ranges in compatible elements for the schlieren and nebulitic migmatites are interpreted as being due to the K-feldspar dominated fractional crystallization. Shaded field corresponds to the total variation in the whole dataset.*

### LILE

There is a marked Cs depletion in all samples from the Rokytná Complex. Without exception, the Rb/Cs ratios (Table 4) are significantly higher than in the average continental crust (Rb/Cs = 30; Taylor & McLennan, 1985 or 23; Wedepohl, 1995). The Rb/Cs ratios fall into a broad interval between 40 and 183, with the ratios increasing systematically in the sequence from the banded orthogneiss to nebulitic migmatite. On the other hand, the available analyses yield K/Rb ratios of 126–350 typical of ordinary crustal rocks (i.e. ranging between *c.* 120 and 500: Shaw, 1968; Rudnick *et al.*, 1985) (Table 4). Therefore there is no evidence to support a notable Rb depletion.

### REE

Like most major and other trace elements, the total REE contents also drop sharply in the sequence from banded orthogneiss to nebulitic migmatite, spanning a broad range ( REE 36–220 ppm, Table 4). At the same time the chondrite-normalized (Boynton, 1984) patterns (Fig. 9a-d) feature a strong progressive depletion in LREE and MREE; the HREE decrease is retarded. Thus a marked drop in $La_N/Yb_N$ ratios (from 7.98 to 1.57; see also Fig. 9e) is accompanied with a rotation in the LREE segment ($La_N/Sm_N$ 3.39 to 2.19; Fig. 9f). With rising degree of fractionation (expressed, for instance, by $SiO_2$ contents) there is an increase in the magnitude of the negative europium anomaly (Eu/Eu* dropping from 0.62 to 0.15). Banded orthogneiss, stromatitic and schlieren migmatites are fairly homogeneous in terms of their total REE contents and distributions. However, generally subparallel patterns for the samples of the nebulitic migmatite vary much in LREE and HREE contents, as they do in the magnitude of their negative Eu anomalies.

The REE patterns show a gradually developing M-type (or concave) lanthanide tetrad effect (Masuda *et al.*, 1987). Its magnitude expressed as a parameter $TE_{1-3}$ (Irber, 1999) ranges from negligible/none (banded orthogneiss, $TE_{1-3}$ = 0.98–1.01, Table 4), through noticeable in stromatitic migmatite (1.02–1.04), schlieren migmatite (1.05–1.10) to pronounced in the nebulitic migmatite (1.04–1.17). In addition, the $TE_{1-3}$ values correlate positively with some variables expressing fluid/melt or crystal/melt fractionation, such as Rb/Cs (Fig. 9g) and Eu/Eu* (Fig. 9h).

Most of the workers nowadays agree that the occurrence of M-type lanthanide tetrad effect is connected to fluorine-rich environments, being caused by melt/fluid (Irber, 1999; Monecke *et al.*, 2002; Zhao *et al.*, 2002) or melt/melt (Veksler *et al.*, 2005) fractionation. However, the fluorine contents are constantly low (0.10–0.13) regardless the migmatite type

(Table 3) and thus this element does not seem to play a major role. In our case the reason for the formation of the tetrad effect remains enigmatic.

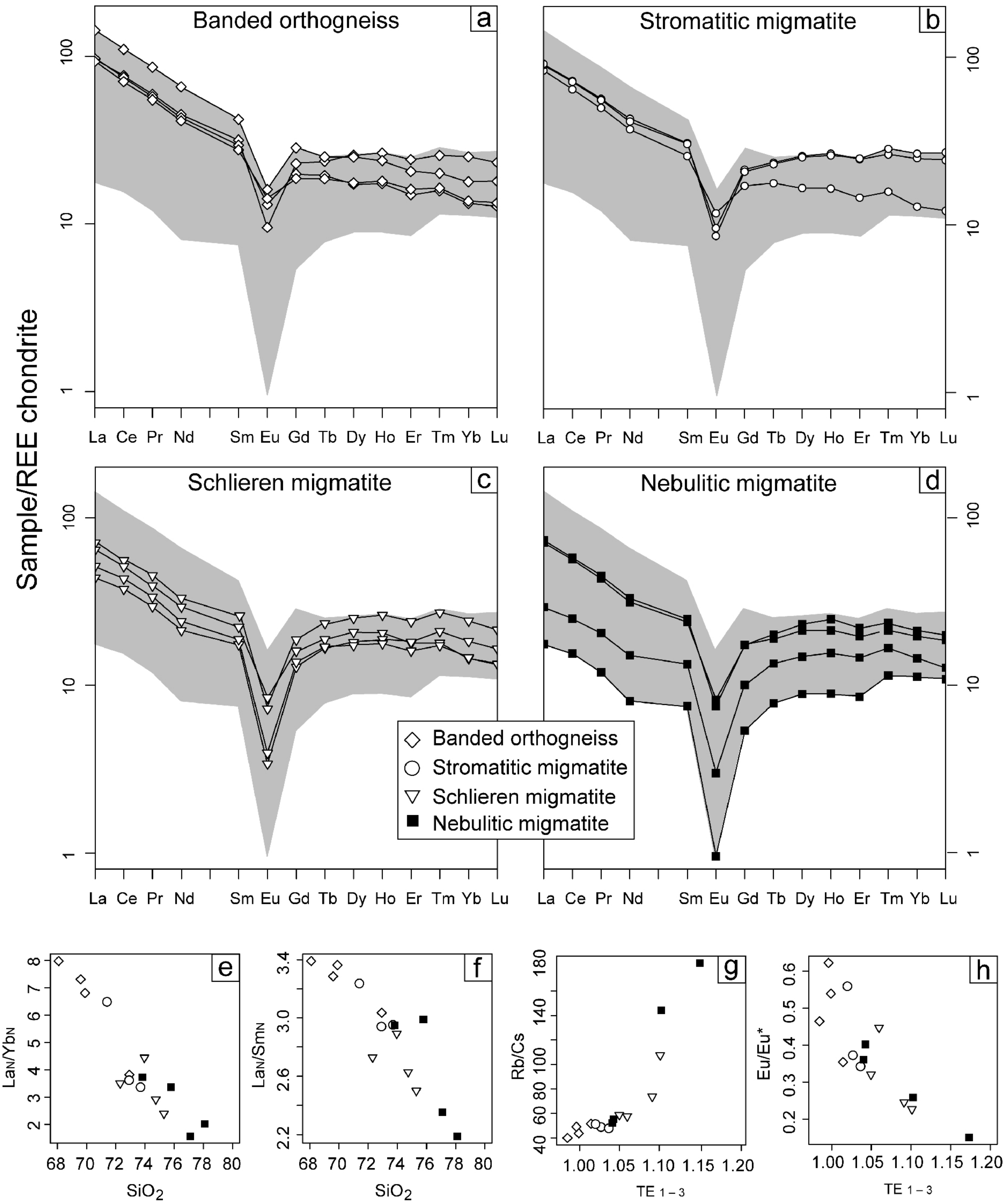


**Fig. 9:** *(a-d) Chondrite-normalized (Boynton, 1984) REE patterns for the studied samples. The REE contents drop sharply in the sequence from banded orthogneisses to nebulitic migmatite, spanning a broad range. Magnitude of the negative Eu anomaly increases with degree of fractionation. Shaded field corresponds to the total variation in the whole dataset. (e-f) Binary plots of $SiO_2$ versus $La_N/Yb_N$ and $La_N/Sm_N$ characterising the shape of the normalized REE patterns. (g-h) Binary plots exhibiting the magnitude of the tetrad effect (expressed as a parameter $TE_{1-3}$: Irber, 1999) versus Rb/Cs and Eu/Eu*. The $TE_{1-3}$ values correlate positively with Rb/Cs (g) and negatively with the Eu/Eu* (h) ratios.*

### *Zircon and monazite saturation temperatures*

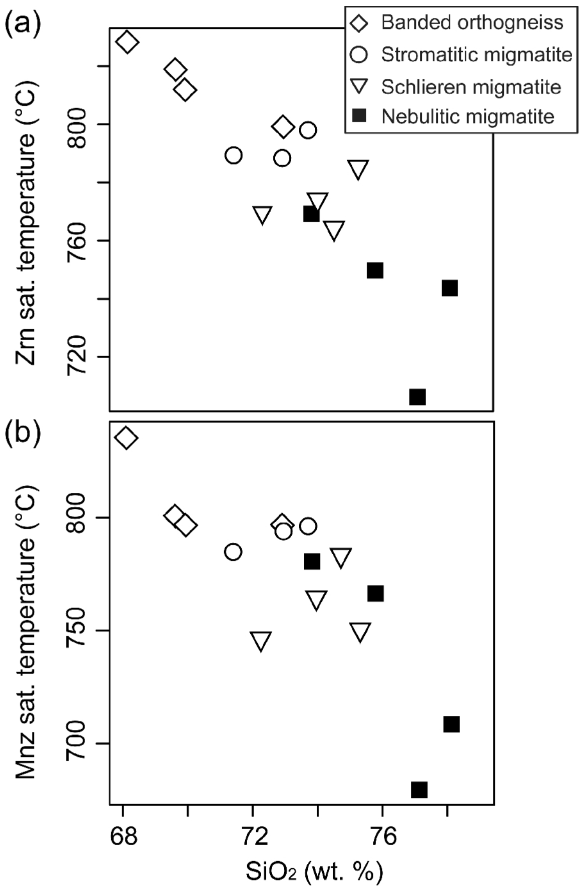


**Fig. 10:** *Calculated saturation temperatures for (a) zircon (Watson & Harrison, 1983) and (b) monazite (Montel, 1993) plotted against $SiO_2$. The both sets of the saturation temperatures decrease continuously in the morphologic migmatite sequence.*

The calculated zircon saturation temperatures (Watson & Harrison, 1983; Hanchar & Watson, 2003) range from *c.* 830°C to 710°C (Table 3), and decrease monotonously in the structural sequence from banded orthogneiss to nebulitic migmatite (Fig. 10). The same trend is seen for the monazite saturation temperatures (Montel, 1993) spanning a comparable interval (*c.* 800°C to 680°C, Table 3).

### *Radiogenic isotopes*

Whole-rock Sr–Nd isotopic ratios for the four main varieties of the Rokytná gneisses and migmatites, age-corrected to 340 Ma, are presented in the Table 5 and Fig. 11.

The two most basic banded orthogneisses (PG7 and PH60B) show an identical, most negative value of -6.7. The rest of the data set seems to contain Nd significantly more radiogenic ( = -5.6 to -5.2). Altogether the data correspond to fairly uniform two-stage Nd depleted-mantle model ages ($T_{Nd}^{DM}$ = 1.46–1.58 Ga). There are, however, more pronounced differences in the Sr isotopic compositions (Fig. 11a). The Sr isotopic ratios correlate positively with silica spanning the broad range from 0.7153 for the most basic orthogneiss PG7 to 0.7332 and 0.7347 in the most siliceous nebulites PG1 and PG3 (Fig. 11b).

The Sr–Nd data for the Rokytná Complex resemble the previously published analyses from the Austrian outcrops of the Gföhl gneiss Frank *et al.* (1990), as a part of their extensive study concerned with Rb-Sr whole-rock and thin slab dating, obtained a comparably broad range of Sr isotopic compositions ($^{87}Sr/^{86}Sr_{340}$ = 0.7192–0.7412). The only three Sr–Nd isotopic

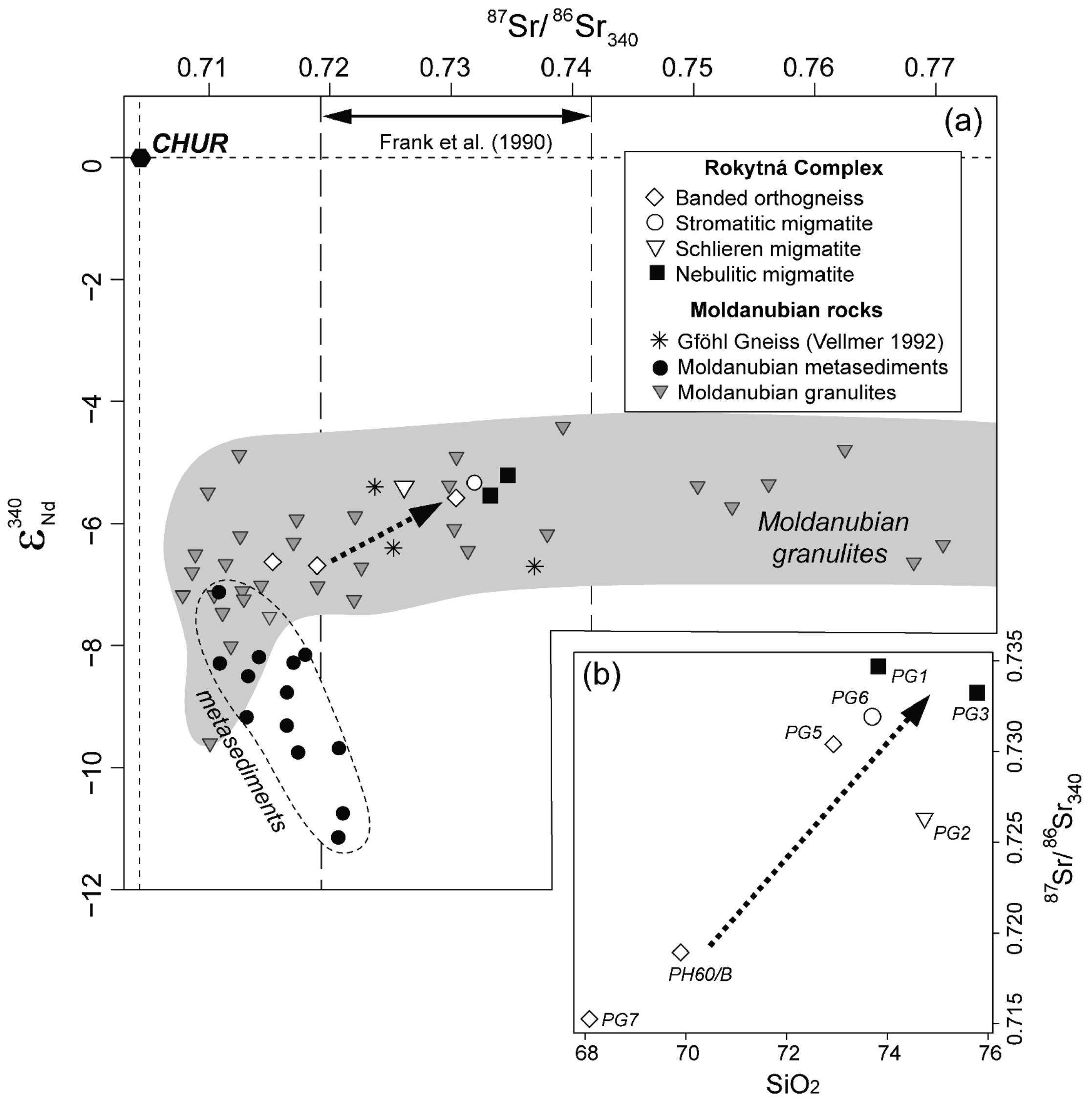


**Fig. 11:** *Sr–Nd isotopic compositions of the Gföhl gneisses and migmatites. (a) $^{87}Sr/^{86}Sr_{340}$ vs. $^{340}_{Nd}$ diagram. Selected rock types from the Moldanubian Zone of the Bohemian Massif are shown for comparison: metasediments (black circles) (Janoušek et al. 1995 and unpublished data), mostly felsic granulites (gray field) (Vellmer, 1992; Valbracht et al.1994; Becker et al.1999; Janoušek et al. 2004) and Gföhl gneisses (black asterisks) (Vellmer, 1992). The labelled range corresponds to the Sr isotopic analyses of the Gföhl gneisses from Frank et al. (1990). The samples from Rokytná Complex (this study) form a positive trend deep within the field of the Moldanubian granulites, far from the metasedimentary rocks. (b) Binary plot $SiO_2$ vs. $^{87}Sr/^{86}Sr_{340}$ for the analysed gneiss/migmatite samples shows a positive correlation. Dashed arrow denotes a tentative evolution of the individual rock types interpreted as being due to the melt infiltration into the banded gneiss (essentially a binary mixing). Closed-system fractional crystallization would result in horizontal shifts in this diagram.*

pairs for Gföhl gneisses were reported by Vellmer (1992): $^{87}Sr/^{86}Sr_{340}$ = 0.7237–0.7367 and = -5.4 to -6.7 ($T^{DM}_{Nd}$ = 1.47–1.55 Ga).

The $^{87}Sr/^{86}Sr_{340}$ - $^{340}_{Nd}$ plot (Fig. 11a) shows clearly that the Sr–Nd isotopic compositions of the Rokytná gneisses fall within the compositional range of the typical Moldanubian granulites (Vellmer 1992; Valbracht *et al.* 1994; Becker *et al.* 1999; Janoušek *et al.* 2004). However they differ from the Czech Moldanubian metasediments (paragneisses and kinzigites; Janoušek *et al.* 1995 and unpublished data), which have epsilon Nd values significantly lower than the gneisses described in the present work (Fig. 11a).

*Table 3: Major-element compositions (ICP-MS) and saturation temperature estimates for zircon (Zrn) and monazite (Mnz)*

| | Banded orthogneiss | | | | Stromatitic migmatite | | |
|---|---|---|---|---|---|---|---|
| Sample | G2A | PH60/B | PG5 | PG7 | PH60/A | PG4 | PG6 |
| Wt. % | | | | | | | |
| $SiO_2$ | 69.60 | 69.90 | 72.93 | 68.09 | 71.40 | 72.91 | 73.70 |
| $TiO_2$ | 0.48 | 0.45 | 0.29 | 0.56 | 0.36 | 0.28 | 0.27 |
| $Al_2O_3$ | 14.90 | 15.40 | 13.83 | 15.26 | 15.20 | 13.47 | 13.54 |
| $Fe_2O_3$ | 3.41 | 3.25 | 2.20 | 3.77 | 2.59 | 2.15 | 2.10 |
| MnO | 0.04 | 0.04 | 0.03 | 0.05 | 0.03 | 0.03 | 0.03 |
| MgO | 1.04 | 1.04 | 0.32 | 0.96 | 0.74 | 0.31 | 0.28 |
| CaO | 1.66 | 1.50 | 0.95 | 1.53 | 1.42 | 0.91 | 0.85 |
| $Na_2O$ | 2.88 | 2.87 | 2.78 | 2.75 | 3.08 | 2.70 | 2.72 |
| $K_2O$ | 4.37 | 4.98 | 5.48 | 4.97 | 4.99 | 5.28 | 5.24 |
| $P_2O_5$ | 0.17 | 0.18 | 0.22 | 0.19 | 0.21 | 0.22 | 0.21 |
| F | —— | —— | 0.11 | 0.08 | —— | 0.10 | 0.10 |
| Total | 99.22 | 100.21 | 99.53 | 98.71 | 100.66 | 98.83 | 99.53 |
| A/CNK | 1.19 | 1.20 | 1.13 | 1.20 | 1.16 | 1.14 | 1.16 |
| $K_2O/Na_2O$ | 1.5 | 1.7 | 2.0 | 1.8 | 1.6 | 2.0 | 1.9 |
| $CaO/Na_2O$ | 0.6 | 0.5 | 0.3 | 0.6 | 0.5 | 0.3 | 0.3 |
| $Al_2O_3/TiO_2$ | 31.2 | 34.3 | 48.4 | 27.1 | 41.9 | 48.7 | 51.0 |
| $FeO_{tot}$[1]$+MgO+TiO_2$ | 4.6 | 4.4 | 2.6 | 4.9 | 3.4 | 2.5 | 2.4 |
| (°C) | | | | | | | |
| Zrn sat. | 819 | 812 | 799 | 828 | 789 | 789 | 798 |
| Mnz sat. | 801 | 797 | 796 | 836 | 785 | 794 | 796 |

| | Schlieren migmatite | | | | Nebulitic migmatite | | | |
|---|---|---|---|---|---|---|---|---|
| Sample | PH89/C | PH90 | PG2 | PH14/D | PH59/D | G 6ak | PG1 | PG3 |
| Wt. % | | | | | | | | |
| $SiO_2$ | 72.30 | 75.30 | 74.74 | 73.96 | 77.10 | 78.10 | 73.82 | 75.78 |
| $TiO_2$ | 0.20 | 0.21 | 0.20 | 0.21 | 0.10 | 0.19 | 0.17 | 0.17 |
| $Al_2O_3$ | 12.70 | 12.80 | 12.70 | 13.27 | 12.70 | 11.50 | 13.84 | 12.95 |
| $Fe_2O_3$ | 1.76 | 2.20 | 2.09 | 1.75 | 1.68 | 1.95 | 1.71 | 1.57 |
| MnO | 0.03 | 0.03 | 0.03 | 0.02 | 0.03 | 0.03 | 0.03 | 0.02 |
| MgO | 0.27 | 0.34 | 0.23 | 0.23 | 0.15 | 0.30 | 0.17 | 0.17 |
| CaO | 0.69 | 0.69 | 0.74 | 0.85 | 0.43 | 0.58 | 0.69 | 0.68 |
| $Na_2O$ | 2.43 | 2.53 | 2.52 | 2.83 | 2.79 | 2.28 | 2.66 | 2.67 |
| $K_2O$ | 5.86 | 5.07 | 5.01 | 5.28 | 5.21 | 5.26 | 5.78 | 5.73 |
| P2O5 | 0.24 | 0.24 | 0.19 | 0.20 | 0.23 | 0.22 | 0.18 | 0.19 |
| F | —— | —— | 0.13 | 0.10 | —— | —— | 0.12 | 0.11 |
| Total | 97.10 | 100.20 | 98.93 | 99.98 | 101.16 | 100.98 | 99.59 | 100.42 |
| A/CNK | 1.10 | 1.17 | 1.16 | 1.11 | 1.15 | 1.10 | 1.16 | 1.09 |
| $K_2O/Na_2O$ | 2.4 | 2.0 | 2.0 | 1.9 | 1.9 | 2.3 | 2.2 | 2.1 |
| $CaO/Na_2O$ | 0.3 | 0.3 | 0.3 | 0.3 | 0.2 | 0.3 | 0.3 | 0.3 |
| $Al_2O_3/TiO_2$ | 62.3 | 61.8 | 62.1 | 63.7 | 130.9 | 60.2 | 80.1 | 77.4 |
| $FeO_{tot}$[1]$+MgO+TiO_2$ | 2.1 | 2.5 | 2.3 | 2.0 | 1.8 | 2.2 | 1.9 | 1.8 |
| (°C) | | | | | | | | |
| Zrn sat. | 766 | 781 | 761 | 770 | 706 | 744 | 770 | 750 |
| Mnz sat. | 743 | 747 | 782 | 761 | 679 | 708 | 780 | 766 |

[1] Total iron as FeO

*Table 4: Trace-element compositions (ICP-MS)*

| | **Banded orthogneiss** | | | | **Stromatitic migmatite** | | | **Schlieren migmatite** | | | | **Nebulitic migmatite** | | | |
|---|---|---|---|---|---|---|---|---|---|---|---|---|---|---|---|
| Sample p.p.m. | G2A | PH60/B | PG5 | PG7 | PH60/A | PG4 | PG6 | PH89/C | PH90 | PG2 | PH14/D | PH59/D | G 6ak | PG1 | PG3 |
| Rb | 105 | 118 | 284 | 164 | 154 | 274 | 273 | 251 | 258 | 337 | 288 | 311 | 231 | 329 | 331 |
| Sr | 136 | 146 | 63 | 129 | 130 | 63 | 60 | 49 | 50 | 46 | 64 | 25 | 38 | 52 | 57 |
| Ba | 865 | 1035 | 445 | 838 | 226 | 430 | 397 | 232 | 228 | 276 | 392 | 69 | 184 | 301 | 326 |
| Cs | 2.4 | 2.4 | 5.5 | 4.1 | 3.0 | 5.6 | 5.7 | 3.4 | 2.4 | 5.8 | 5.0 | 1.7 | 1.6 | 6.3 | 6.0 |
| Th | 12.6 | 11.3 | 16.3 | 21.6 | 11.7 | 16.5 | 17.5 | 11.3 | 7.3 | 14.1 | 11.8 | 2.6 | 0.7 | 16.0 | 18.3 |
| U | 1.7 | 1.7 | 3.0 | 2.5 | 2.2 | 2.9 | 3.3 | 2.4 | 1.6 | 3.2 | 2.8 | 1.6 | 0.6 | 3.6 | 5.1 |
| Pb | 21 | 23 | 29 | 29 | 23 | 31 | 27 | 13 | 11 | 41 | 27 | 9 | 9 | 48 | 35 |
| Cr | 38 | 43 | 13 | 35 | 21 | 11 | 11 | 13 | 24 | 10 | 10 | 13 | 28 | 11 | 34 |
| V | 46 | 46 | 16 | 49 | 27 | 17 | 16 | 4 | 6 | 12 | 12 | 5 | < 2 [1] | 10 | 9 |
| Sc | 8 | 8 | 4 | 9 | 3 | 4 | 4 | 3 | 4 | 3 | 3 | 4 | 4 | 3 | 3 |
| Zn | 68 | 61 | 21 | 45 | 53 | 22 | 17 | 39 | 54 | 20 | 14 | 65 | 35 | 14 | 446 |
| Zr | 205 | 192 | 168 | 230 | 172 | 146 | 159 | 127 | 116 | 101 | 120 | 84 | 50 | 114 | 94 |
| Hf | 4.0 | 4.2 | 5.7 | 6.8 | 3.6 | 5.0 | 5.5 | 3.2 | 2.8 | 3.8 | 3.8 | 1.7 | 2.0 | 4.2 | 3.9 |
| Nb | 8.1 | 7.7 | 10.6 | 12.3 | 7.2 | 9.6 | 10.0 | 9.9 | 8.1 | 8.6 | 8.0 | 6.8 | 5.5 | 7.5 | 8.5 |
| Ta | 1.9 | 2.0 | 0.8 | 1.0 | 2.5 | 0.7 | 0.8 | 3.7 | 3.1 | 0.6 | 0.7 | 3.0 | 2.0 | 0.6 | 0.8 |
| K/Rb | 345.5 | 350.3 | 160.2 | 251.6 | 269.0 | 160.0 | 159.3 | 193.8 | 163.1 | 123.4 | 152.2 | 139.1 | 189.0 | 145.8 | 143.7 |
| Rb/Sr | 0.8 | 0.8 | 4.5 | 1.3 | 1.2 | 4.4 | 4.5 | 5.1 | 5.2 | 7.3 | 4.5 | 12.5 | 6.1 | 6.3 | 5.8 |
| Rb/Cs | 43.4 | 48.7 | 51.2 | 40.0 | 50.7 | 49.3 | 48.2 | 74.9 | 106.4 | 57.7 | 57.7 | 182.0 | 144.4 | 52.6 | 54.9 |
| Rb/Ba | 0.1 | 0.1 | 0.6 | 0.2 | 0.7 | 0.6 | 0.7 | 1.1 | 1.1 | 1.2 | 0.7 | 4.5 | 1.3 | 1.1 | 1.0 |
| La | 30.0 | 28.9 | 29.8 | 44.1 | 25.8 | 28.0 | 27.7 | 15.9 | 13.6 | 21.6 | 19.9 | 5.5 | 9.1 | 22.7 | 22.1 |
| Ce | 60.4 | 57.1 | 61.8 | 88.7 | 51.8 | 58.2 | 57.5 | 34.9 | 30.3 | 45.4 | 41.3 | 12.5 | 20.2 | 46.6 | 45.4 |
| Pr | 7.0 | 6.7 | 7.2 | 10.5 | 6.1 | 6.9 | 6.8 | 4.1 | 3.6 | 5.5 | 4.8 | 1.5 | 2.5 | 5.5 | 5.3 |
| Nd | 25.8 | 24.7 | 26.9 | 39.4 | 22.3 | 25.7 | 24.8 | 14.4 | 12.8 | 19.9 | 17.6 | 4.8 | 9.0 | 19.8 | 18.7 |
| Sm | 5.7 | 5.4 | 6.2 | 8.2 | 5.0 | 6.0 | 5.9 | 3.7 | 3.4 | 5.2 | 4.3 | 1.5 | 2.6 | 4.8 | 4.6 |
| Eu | 0.96 | 1.04 | 0.70 | 1.18 | 0.86 | 0.70 | 0.63 | 0.29 | 0.25 | 0.53 | 0.62 | 0.07 | 0.22 | 0.55 | 0.60 |
| Gd | 5.1 | 4.8 | 5.9 | 7.4 | 4.4 | 5.5 | 5.4 | 3.6 | 3.3 | 4.9 | 4.1 | 1.4 | 2.6 | 4.5 | 4.5 |
| Tb | 0.92 | 0.88 | 1.12 | 1.19 | 0.84 | 1.11 | 1.09 | 0.80 | 0.79 | 1.08 | 0.89 | 0.37 | 0.64 | 0.90 | 0.95 |
| Dy | 5.5 | 5.7 | 8.3 | 8.1 | 5.3 | 8.3 | 8.1 | 5.6 | 5.8 | 8.4 | 6.7 | 2.9 | 4.8 | 6.9 | 7.5 |
| Ho | 1.25 | 1.29 | 1.90 | 1.71 | 1.18 | 1.91 | 1.86 | 1.27 | 1.35 | 2.0 | 1.47 | 0.64 | 1.12 | 1.53 | 1.78 |
| Er | 3.1 | 3.4 | 5.1 | 4.3 | 3.0 | 5.2 | 5.2 | 3.4 | 3.8 | 5.4 | 3.7 | 1.8 | 3.1 | 4.1 | 4.6 |
| Tm | 0.51 | 0.53 | 0.83 | 0.65 | 0.51 | 0.85 | 0.92 | 0.56 | 0.68 | 0.85 | 0.58 | 0.37 | 0.54 | 0.69 | 0.76 |
| Yb | 2.8 | 2.9 | 5.3 | 3.7 | 2.7 | 5.2 | 5.6 | 3.1 | 3.8 | 5.1 | 3.0 | 2.3 | 3.0 | 4.1 | 4.4 |
| Lu | 0.41 | 0.43 | 0.75 | 0.58 | 0.39 | 0.78 | 0.87 | 0.43 | 0.53 | 0.69 | 0.43 | 0.35 | 0.41 | 0.60 | 0.64 |
| Y | 41.0 | 42.0 | 44.1 | 42.3 | 46.0 | 43.7 | 43.9 | 45.0 | 42.0 | 44.4 | 37.3 | 38.0 | 23.0 | 35.6 | 39.1 |
| Sum REE | 149.6 | 143.7 | 161.8 | 219.8 | 130.1 | 154.2 | 152.4 | 91.9 | 83.9 | 126.6 | 109.5 | 35.9 | 59.8 | 123.2 | 121.9 |
| $La_N/Yb_N$ | 7.31 | 6.81 | 3.82 | 7.98 | 6.49 | 3.62 | 3.36 | 3.50 | 2.39 | 2.85 | 4.44 | 1.57 | 2.02 | 3.73 | 3.36 |
| $La_N/Sm_N$ | 3.29 | 3.36 | 3.04 | 3.39 | 3.24 | 2.94 | 2.95 | 2.73 | 2.50 | 2.62 | 2.89 | 2.35 | 2.19 | 2.95 | 2.99 |
| Eu/Eu* | 0.54 | 0.62 | 0.35 | 0.46 | 0.56 | 0.37 | 0.34 | 0.25 | 0.23 | 0.32 | 0.45 | 0.15 | 0.26 | 0.36 | 0.40 |
| $TE_{1-3}$ | 1.00 | 1.00 | 1.01 | 0.98 | 1.02 | 1.03 | 1.04 | 1.09 | 1.10 | 1.05 | 1.06 | 1.17 | 1.10 | 1.04 | 1.04 |

[1] values given as < mean that the concentration is below the respective detection limit

*Table 5: Sr-Nd isotopic data for gneisses/migmatites from the Rokytná Complex*

| Sample | Rock type | Rb (ppm) | Sr (ppm) | $^{87}Rb/^{86}Sr$ | $^{87}Sr/^{86}Sr$ [1] | $(^{87}Sr/^{86}Sr)_i$ [2] |
|---|---|---|---|---|---|---|
| PG7 | Banded orthogneiss | 163.6 | 129.4 | 3.669 | 0.733034 (9) | 0.715275 |
| PH60/B | Banded orthogneiss | 117.7 | 146.0 | 2.337 | 0.730249 (14) | 0.718936 |
| PG5 | Banded orthogneiss | 283.7 | 63.3 | 13.074 | 0.793691 (18) | 0.730418 |
| PG6 | Stromatitic migmatite | 273.2 | 60.3 | 13.215 | 0.795889 (19) | 0.731933 |
| PG2 | Schlieren migmatite | 337.4 | 46.3 | 21.329 | 0.829370 (18) | 0.726143 |
| PG1 | Nebulitic migmatite | 329.4 | 52.4 | 18.400 | 0.823759 (9) | 0.734707 |
| PG3 | Nebulitic migmatite | 331.0 | 57.4 | 16.873 | 0.814908 (14) | 0.733248 |

| Sample | Sm (ppm) | Nd (ppm) | $^{147}Sm/^{144}Nd$ | $^{143}Nd/^{144}Nd$ [1] | $(^{143}Nd/^{144}Nd)_i$ [2] | $\varepsilon^i_{Nd}$ [2] | $T^{Nd}_{CHUR}$ (Ga) | $T^{Nd}_{DM}$ [3] (Ga) |
|---|---|---|---|---|---|---|---|---|
| PG7 | 8.19 | 39.43 | 0.1255 | 0.512134 (8) | 0.511855 | -6.7 | 1.08 | 1.58 |
| PG7 [4] | 8.19 | 39.43 | 0.1255 | 0.512140 (8) | 0.511861 | -6.6 | 1.07 | 1.57 |
| PH60/B | 5.40 | 24.74 | 0.1318 | 0.512151 (9) | 0.511858 | -6.7 | 1.15 | 1.58 |
| PG5 | 6.17 | 26.89 | 0.1387 | 0.512223 (9) | 0.511914 | -5.6 | 1.09 | 1.49 |
| PG6 | 5.91 | 24.79 | 0.1441 | 0.512248 (7) | 0.511927 | -5.3 | 1.13 | 1.47 |
| PG2 | 5.19 | 19.90 | 0.1573 | 0.512269 (6) | 0.511919 | -5.5 | 1.43 | 1.48 |
| PG1 | 4.83 | 19.80 | 0.1473 | 0.512261 (9) | 0.511933 | -5.2 | 1.16 | 1.46 |
| PG3 | 4.64 | 18.74 | 0.1498 | 0.512250 (9) | 0.511916 | -5.5 | 1.26 | 1.49 |

[1] values in parentheses are errors on the last decimal place (2SE).
[2] isotopic ratios with subscript “i” were all age corrected to 340 Ma.
[3] two-stage Nd model ages calculated after Liew and Hofmann (1988).
[4] duplicated mesurement (including sample decomposition and column separation)

## Discussion

Among the Gföhl gneisses and migmatites, several macroscopically distinct types can be distinguished. As shown by Hasalová *et al.* (2008a), they apparently form a continuous structural sequence related to a disintegration of the parental orthogneiss. This distinctly banded rock is gradually transposed to stromatitic and schlieren migmatites. The migmatites are characterised by abundance of feldspar- and quartz-rich aggregates, presumably formed by fragmentation of the original banding. Eventually, the monomineralic layering vanishes and schlieren migmatite develops into isotropic nebulitic migmatite with no relics of gneissic morphology. At the first glance, this sequence resembles evolution of migmatite types described in classical works (e.g. Mehnert, 1971; Brown, 1973).

### Genesis of the Gföhl migmatites

Partial melting of rocks with a broadly granitic composition is the generally accepted explanation for the petrogenesis of the Gföhl migmatites (Dudek *et al.*, 1974; Matějovská, 1975). Even though such a conclusion is generally in line with the results presented in the current paper, the exact cause for the chemical variability observed in the Gföhl migmatites was never seriously discussed. The possible mechanisms involve: (i) tectonic or intrusive juxtaposition of genetically unrelated migmatites that have originated from distinct protoliths, (ii) equilibrium melting of a single metagranitic protolith, (iii) disequilibrium melting (with or without a small-scale melt movement) and (iv) infiltration of a melt derived from an external source into the parental orthogneiss. These hypotheses are evaluated below.

#### *Distinct protoliths to each of the migmatite types*

The first and arguably the most unrealistic is a model in which each of the migmatite types had its own, genetically unrelated protolith and their juxtaposition was purely accidental. This possibility can be first of all ruled out because of the observed gradual transposition of the $S_1$ banded gneisses into the $S_2$ stromatitic and schlieren migmatites (Hasalová *et al.*, 2008a). These authors pointed out that the structural data are compatible with progressive deformation within a ductile shear zone resulting in generation of a continuous spectrum of variably deformed rock types ranging from pristine banded orthogneiss to the most affected schlieren migmatite. This interpretation is based on observed progressive folding of early steep orthogneiss fabric, in more advanced stages with development of isoclinal folds, leading eventually to complete fabric transposition and formation of schlieren migmatite. At the first glimpse, the elongated bodies of nebulitic migmatite can be viewed either as veins of isotropic granite penetrating parallel to the main $S_2$ mylonitic anisotropy (e.g. Brown & Solar, 1998) or as tectonically expelled granitic liquid injected into country rocks, which were hot thus preventing freezing (Weinberg & Searle, 1998). However, the nebulitic migmatite can be also regarded as the most extreme end-member of the structural sequence, i.e. completely disintegrated parental orthogneiss. This possibility is strongly supported by the microstructures, mineral chemistry

(Table 1) and whole-rock geochemical parameters (Figs 6–9) including the Sr-Nd isotopic compositions (Fig. 11 & Table 5) which change continuously from the banded orthogneiss to the nebulitic migmatite. Additionally, the overall resemblance in the trace-element distribution patterns and only gradual changes in the elemental concentrations (Figs 8–9) together with the monotonously decreasing zircon/monazite saturation temperatures (Fig. 10) argue against significant differences in the protoliths. In other words, the available data for four studied orthogneiss and migmatite types suggest that they all have to have originated from the same protolith.

### *Equilibrium melting*

The equilibrium melting model rests upon an assumption that the anatexis was slow enough for the full equilibration between the solid residue and the in situ partial melt to be achieved. In the closed-system, equilibrium melting model, followed by homogenization of the individual melt batches, one would not expect any variations in their radiogenic isotope compositions (e.g. Briquet & Lancelot, 1979). However, the Sr-Nd isotope data in the Rokytná Complex display considerable variability and regular changes with independent geochemical parameters (see for instance the linear trend in the $SiO_2$ - $^{87}Sr/^{86}Sr_i$ plot: Fig. 11b). This may reflect the source isotopic heterogeneity, perhaps due to in situ $^{87}Sr$ growth in the pre-Variscan protolith to the Gföhl gneisses (Frank *et al.*, 1990). Such an isotopic heterogeneity is frequently observed on grain to meter scale in many high-grade metamorphic terrains and anatectic granites worldwide (e.g. Barbero *et al.*, 1995).

Even though the variation in radiogenic isotope compositions does not preclude small-scale equilibria, the evolution of mineral compositions (Table 1) provides an independent argument disproving the equilibrium melting hypothesis. Assuming a closed-system, equilibrium melting along a prograde path, the $X_{Fe}$ in garnet and biotite should decrease in accord with the decreasing modal proportion of garnet. In addition, the plagioclase should exhibit an increase in anorthite component with increasing degrees of melting. Such a compositional evolution was reported in a number of field and experimental studies (e.g. Vielzeuf & Holloway, 1988; Gardien *et al.*, 1995; Dallain *et al.*, 1999). However the compositional changes in the Rokytná Complex are just opposite, the $X_{Fe}$ in garnet and biotite increase and the basicity of plagioclase drops (Table 1). This evolution is thus incompatible with a hypothesis invoking increasing degrees of melting in a closed system.

Another possible argument is the strong textural and chemical disequilibrium between the rims and cores of the plagioclase crystals, demonstrating that it were apparently only their rims that have been in equilibrium with the melt (Fig. 3). However, because of the commonly slow diffusion of major and trace elements in the plagioclase (e.g. Blundy & Shimizu, 1991), this observation can not exclude the in situ partial melting completely.

On this basis, the equilibrium melting hypothesis can be discounted as the main process responsible for the origin of the studied sequence, leaving the disequilibrium partial melting and open-system interactions as the only viable alternatives.

### *Disequilibrium melting*

There is a growing evidence experimental (e.g. Johannes 1980; Hammouda *et al.*, 1996; Knesel & Davidson 1996, 2002) as well as from field observations and whole-rock geochemistry (e.g. Sawyer, 1991; Barbero *et al.*, 1995; Bea, 1996; Harris & Ayres, 1998) indicating that the equilibrium between the melt and the solid residue does not have to be always attained in course of the crustal anatexis.

Firstly, the disequilibrium may occur when some accessory phases have remained armoured by main rock-forming minerals that have not participated in the melting reaction(s) (e.g. Watson & Harrison, 1984; Watt & Harley 1993; Nabelek & Glascock, 1995; Bea, 1996). However in the high-grade metamorphic rocks, the great majority of the accessory mineral grains is thought be located at newly-formed (or migrated) grain boundaries of the main rock-forming minerals and thus probably in contact with the partial melt (Watson *et al.,* 1989). In lower-grade rocks, the accessories are mostly included in biotite and/or hornblende that in course of the dehydratation melting would release them (Clemens, 2003).

The more common cause of disequilibrium is rapid melt production, extraction and segregation, not allowing enough time for the diffusional equilibration between the residual minerals and the melt. In normal granitic magmas derived by dehydratation crustal melting, the dissolution of zircon is assumed to be fast enough for the equilibrium to be attained (Harrison & Watson 1983; Watson 1996). However, achievement of equilibrium is less likely in the case of monazite and apatite, whose dissolution is controlled mainly by sluggish LREE and phosphorus diffusion (Harrison & Watson, 1984; Rapp & Watson, 1986). Swift extraction of low- to moderate melt fractions can be promoted by a feedback mechanism between increasing melt production and deformation or shear-enhanced compaction, as was demonstrated for instance in the Himalayas (D'Lemos *et al.*, 1992; Rutter & Neumann, 1995; Ayres *et al.*, 1997). Muscovite dehydratation melting can as well cause high dilatation strain that may further boost melt segregation (Rushmer 1996; 2001).

Disequilibrium melting may have a profound influence on the radiogenic isotopic composition of granitic magmas. Their Sr isotopic signature is controlled mainly by the main rock-forming minerals in the source (principally the balance between feldspars with low Rb/Sr and micas with high Rb/Sr, and thus also high $^{87}Sr/^{86}Sr$ isotopic ratios). Consequently, the melts produced by disequilibrium dehydratation melting involving muscovite and/or biotite will tend to have a more radiogenic Sr than their source. On the other hand, the bulk of the Nd in the felsic magmas will be controlled mainly by monazite and apatite, and thus the Nd isotope ratios will be governed by dissolution kinetics of these minerals. As shown by modelling of Zeng *et al.* (2005), these two phases ought to show a contrasting behaviour. The apatite with high Sm/Nd ratio will develop, with time, a more radiogenic Nd. Thus the progressive dissolution of apatite will yield melts with Nd isotopic signature increasingly more radiogenic (higher epsilon Nd values) than the source. Monazite, which has relatively low Sm/Nd, will have an opposite effect.

Disequilibrium melting model can explain the observed variation in the $^{87}Sr/^{86}Sr_{340}$- as well as $SiO_2$ - $^{87}Sr/^{86}Sr_{340}$ plots (Fig. 11a, b). The trends may theoretically argue for an increasing role of biotite dehydratation melting and apatite dissolution in the more siliceous samples. Two disequilibrium melting scenarios can be distinguished, one without, and one involving melt movement.

If there was ***no melt movement*** the differences in the amount of melt should directly reflect the primary variations in the protolith fertility, starting from nearly zero in the most basic of the banded orthogneisses. This would imply that the more acid portions with presumably higher melt contents would correspond to more fertile protoliths. In the context of dehydratation melting model, they would have to contain more micas compared to their more basic (and more refractory) counterparts. This is unlikely in a co-genetic granitic suite of comparable silica range. More importantly, the obtained zircon and monazite saturation temperatures are mutually comparable and reasonably high for biotite dehydratation melting to be a feasible melting mechanism. This seems to indicate that there was enough time for equilibrium between the residual zircon/monazite and the liquid to be established.

The whole-rock geochemical data can also be used to prove or disprove whether the melts could have originated from protoliths resembling the banded orthogneiss. From the composition of the least siliceous nebulitic migmatite follows that the anatectic melt had to have been granitic, poor in most major- and minor-element oxides ($TiO_2$, MgO, CaO) albeit rather Fe- and K-rich (FeOt~ 1.6 %; $K_2O/Na_2O$ = 1.9–2.3) (Table 3 & Fig. 6). As shown by Sylvester (1998), the $CaO/Na_2O$ ratios in peraluminous magmas are controlled mostly by the plagioclase/clay ratio of the source. This enables the distinction between granites generated from plagioclase-poor (pelitic; low $CaO/Na_2O$) and plagioclase-rich (psammitic; high $CaO/Na_2O$) sources. The Rokytná migmatites are characterized by intermediate $CaO/Na_2O$ (0.15–0.26) and high $Al_2O_3/TiO_2$ (61–127) ratios. The nebulitic migmatites are relatively rich in Rb (231–331 ppm), as well as extremely poor in Ba (69–326 ppm) and Sr (25–57 ppm), translating to relatively high Rb/Sr (5.8–9.2) and Rb/Ba (1.0–3.4) ratios. This, together with the presence of marked negative Eu anomalies, are compatible with generation via rather low-degree, dehydratation melting of muscovite–biotite-rich quartzo-feldspathic lithologies (Harris & Inger, 1992; Barbarin, 1996; Sylvester 1998 and references therein). Thus the chemistry of the nebulitic migmatite does not seem to match in situ melts of the rocks similar to the banded orthogneiss.

The more plausible is the possibility that the melt was ***drained out on distances not exceeding the outcrop scale*** If the melt extraction was rapid, there would not be enough time for its full equilibration. Nowadays, the most accepted model for melt migration (low to moderate melt fraction) involves movement through the network of interconnected pores, driven by deformation. Ultimately the deformation results in pervasive melt migration utilizing the main rock anisotropies such as foliation planes, fold hinges and boudin necks as suggested by many field studies (e.g. Collins & Sawyer, 1996; Weinberg, 1996; Brown & Solar, 1999). Additionally, shear-enhanced compaction would drive melt into a network of melt-filled vein-like leucosomes. Porous flow through such a vein network would transfer the melt rapidly to the higher structural levels (Rutter & Neumann, 1995).

In this scenario one would expect, at least a rudimentary preservation of the melt flow network throughout the area affected. However no such structures have been observed in the field. Moreover, the distribution of migmatites in the studied region is not homogenous; there exist large regions that are formed by products of advanced migmatization (schlieren and nebulitic migmatites) that are however distributed rather randomly and definitely not structurally above the other two migmatite types as should be anticipated. On this basis, a small (outcrop) scale melt movement can be probably ruled out.

Additionally, we have calculated (using the whole-rock and mineral chemistries) the composition of a melt that would be in equilibrium with the stable mineral assemblage of the banded orthogneiss (Pl–Kfs–Qtz–Sil–Grt–Bt) at 6.5 kbar and 740–760°C. The calculations were performed using THERMOCALC 3.25 (Powell *et al.*, 1998) and the internally-consistent thermodynamic dataset 5.5 (Holland & Powell, 1998) in the $Na_2O–CaO–K_2O–FeO–MgO–Al_2O_3–SiO_2–H_2O$ (NCKFMASH) system. The obtained melt is granitic ($SiO_2$ = 68.3–69.3 wt. %; alkali feldspar granite in CIPW-based Q‘-ANOR plot of Streckeisen & Le Maître, 1979), slightly peraluminous (A/CNK ~ 1.1), CaO poor (0.32–0.41 %) and alkali rich ($K_2O$+$Na_2O$ = 8.8–8.9 wt. %), with prevalence of potassium over sodium ($K_2O/Na_2O$ ~ 1.35). Simple comparison with the composition of nebulitic migmatite reveals that the modelled melt has clearly too low SiO, CaO, MgO (0.07–0.09 %), $FeO_t$ (0.27–0.33%), and exceedingly high alkalis ($Na_2O$ = 3.7–3.8% and $K_2O$ = 5.1%) (cf. Fig. 6). Even in this case, the nebulitic migmatites seem to be too different to represent rocks dominated by partial melts of the banded orthogneisses.

An alternative would be that the nebulitic migmatites represent diatexites that left behind some of their residue. In spite of its macroscopic appearance, the nebulitic migmatite probably never contained higher amounts of melt, regardless the fact that considerable melt volume had to have passed through the system to account for all the observed variations. Hasalová *et al.* (2008a) presented the AMS (anisotropy of magnetic susceptibility) data on biotite that show strong degree of anisotropy of magnetic susceptibility even in the nebulitic migmatite. This is in contrast with AMS data from other migmatitic terrains (e.g. Ferré *et al.*, 2004) and with results of numerical modelling (e.g. Blumenfeld & Bouchez, 1988) that both yielded significantly lower values of degree of magnetic anisotropy in diatexites. The high degree of AMS in the Rokytná Complex thus documents predominance of solid-state deformation with only minor contribution from melt. The system had to have been still matrix and not melt supported, precluding free rotation of biotite in viscously flowing melt.

### *Melt infiltration from an external source*

By *“melt infiltration”* we mean a process , whereby melt derived from an external source passes pervasively, i.e. along grain boundaries, the whole rock volume. In this model, the textural and geochemical variations can be interpreted by different degrees of equilibration between the bulk rock and the passing melt. Melt infiltration is a well known process from studies concerned with metasomatism in the Earth’s mantle and contact aureoles around igneous intrusions. In the mantle, melt infiltration, loosely termed reactive flow, corresponds to grain-scale porous flow along high porosity dissolution channels (e.g. McKenzie, 1989; Van der Wal & Bodinier, 1996; Kelemen *et al.*, 1997; Reiners, 1998). The effects of reactive flow can be identified due to highly contrasting modal and chemical composition of the peridotite and the percolating basaltic melt (Godard *et al.*, 1995). The large difference in viscosities between the melt and host rock is the reason why the porous flow in the mantle, albeit slow, does not require deformation to occur. Even though this mechanism has been invoked to explain the transport of basaltic magma in the

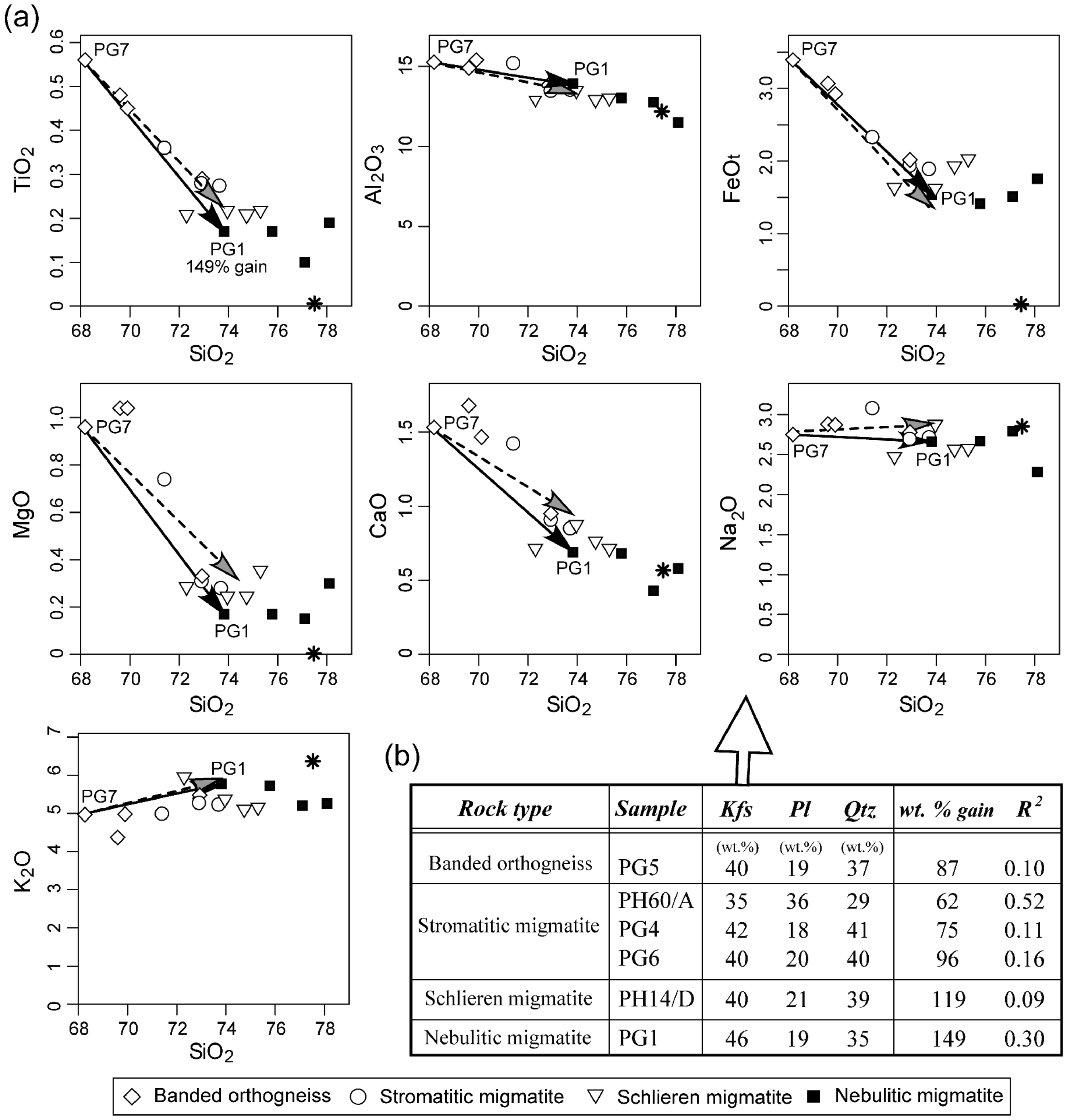


| *Rock type* | *Sample* | *Kfs* (wt.%) | *Pl* (wt.%) | *Qtz* (wt.%) | *wt. % gain* | $R^2$ |
|---|---|---|---|---|---|---|
| Banded orthogneiss | PG5 | 40 | 19 | 37 | 87 | 0.10 |
| Stromatitic migmatite | PH60/A | 35 | 36 | 29 | 62 | 0.52 |
| | PG4 | 42 | 18 | 41 | 75 | 0.11 |
| | PG6 | 40 | 20 | 40 | 96 | 0.16 |
| Schlieren migmatite | PH14/D | 40 | 21 | 39 | 119 | 0.09 |
| Nebulitic migmatite | PG1 | 46 | 19 | 35 | 149 | 0.30 |

**Fig. 12:** *(a) Modelling of chemical effects connected with the leucogranitic melt infiltration into the Rokytná Complex. As the melt passes through the system, K-feldspar, plagioclase and quartz crystallize/overgrow the corresponding phases in the matrix. The model treated various rock samples as mixtures of the banded orthogneiss and the crystallizing minerals from the melt. The compositions of the latter are listed in the table forming a part of the Fig. 3; as the starting material has been chosen the least evolved banded orthogneiss (PG7). Solid black arrows represent the tie line between the real compositions of the banded orthogneiss (PG7) and the nebulitic migmatite (PG1). The dashed arrows represent the outcome of the modelling. Note the good correspondence of the real and modelled trends. The stars portray the best-fit solution for the assemblage added. The results indicate that the whole compositional spectrum from the banded orthogneisses to the least siliceous nebulitic migmatites could have been produced by addition of up to c. 150 wt. % of the both feldspars and quartz combined (if the original rock is taken as 100 %, i.e. corresponding to a relative gain of 60 %). (b) Summary of the modelling for various migmatite pairs. Presented are proportions of the minerals (Kfs, Pl, Qtz) added into the system, total percentages of these newly crystallized phases (protolith gneiss PG7 = 100 %) and sum of squared residuals ($R^2$) indicating the goodness of the fit.*

mantle (Kelemen *et al.*, 1997 and references therein), many workers still tend to prefer fracture-controlled melt flow (e.g. Spiegelman & Kenyon, 1992; Harte *et al.*, 1993).

However, pervasive melt infiltration is even further from being generally accepted for melt transport mechanism in the crust. Melt percolation from/along grain boundaries has until now been reserved only for the scale of several centimetres (e.g. Sawyer, 2001) and it has been considered only rarely as a serious possibility for large-scale melt transport in the crust (Hasalová *et al.*, 2008a, b).

The main problem consists in the fact that this process is considered too sluggish to be efficient. McKenzie (1984) showed that the pervasive porous flow in crustal rocks would be possible only in a matrix which is able to compact, in other words they concluded that such a flow is essentially a deformation-driven process. This could have been the case in the Rokytná Complex, where a large, crustal-scale shear zone played an important role in its exhumation.

During the penetration by externally-derived melt, the rock complex would clearly display open-system behaviour, with components having been lost to, or introduced from, the passing melt of unknown volume. The whole-rock composition would then represent a net result of the changing system mass/volume, the contributions from newly precipitated minerals as well as the mass balance of geochemical species exchanged with the melt/fluid phase.

We have attempted to model the process as an addition of K-feldspar, plagioclase and quartz crystallized from the melt passing through the banded orthogneiss. The exact composition of the pristine orthogneiss is unknown; therefore we have opted for the presumably least influenced sample PG7. The mineral compositions employed were those of the newly formed rims overgrowing the relict mineral grains in the matrix (Fig. 3). A graphical representation of the modelling approach is shown in Figure 12a. The whole compositional spectrum from the banded orthogneiss to the least siliceous nebulitic migmatite can be explained by a relative gain up to 60% of K-feldspar, plagioclase and quartz. The proportion of the three minerals changes from roughly balanced to a strong prevalence of K-feldspar (~40%) and quartz (~40%) over plagioclase (~20%).

Additionally, for assessment of the mass balance in individual major- and trace-elements during the orthogneiss transformation was used the approach of Gresens (1967) in the form of isocon plots (Grant, 1986; 2005) (Fig. 13a). The results of individual isocon analyses were pulled together into binary plots of an immobile element vs. relative gains/losses (%) of individual elements (Fig. 13b). The most appropriate choice of immobile components seem high-field strength elements Zr, Hf, La, Sm, Nb and Th, as follows from examination of

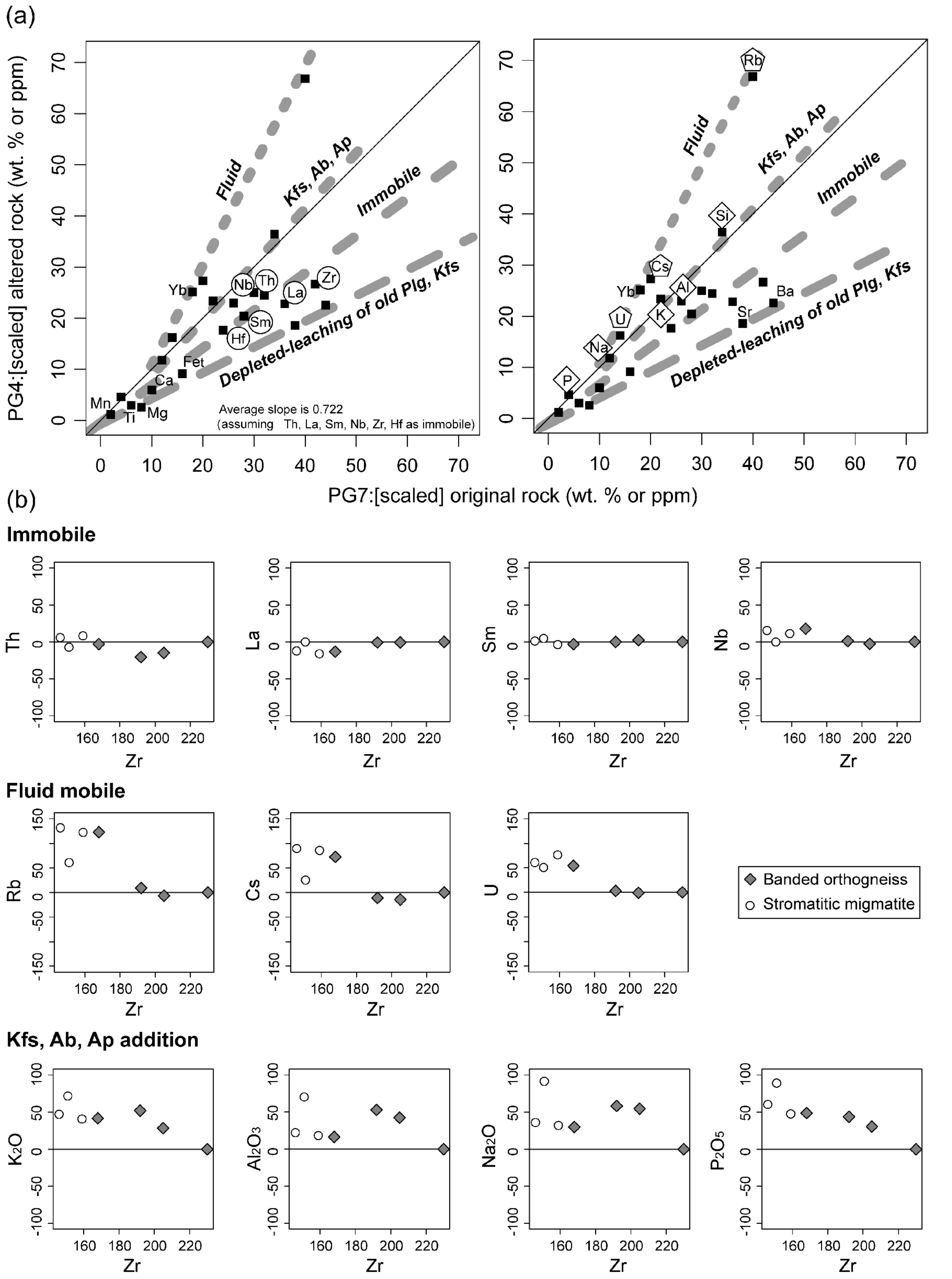


**Fig. 13:** *Mass balance calculations of individual major- and trace-elements (after Gresens, 1967) (a) Typical isocon plot (Grant, 1986; 2005) for transformation of banded orthogneiss (PG7) into schlieren migmatite (PG4). The slope of the isocon has been obtained taking the presumably immobile elements Zr, Hf, La, Sm, Nb and Th (circled) into consideration. The sample plot with highlighted elements that are interpreted as having been added to the system due to growth of new mineral phases (Pl, Kfs, Ap) and brought by hydrous fluid (Rb, Cs and U). (b) Plots of Zr vs. relative gains/losses (%: Grant, 2005) of individual elements. As a starting material was taken the least evolved orthogneiss (PG 7) with the highest Zr contents. This element has been chosen as it varies greatly, decreases monotonously (see also Fig. 7) and seems immobile in course of the progressive breakdown of the orthogneiss matrix.*

isocon plots as well as the ordered ratios of concentrations of individual elements in the 'altered' and 'original'rocks (Grant, 2005).

Slopes of the isocons fitted to these HFS elements are lower than unity in all cases, pointing to an increase in the overall mass of the system (an increase in volume if changes in density were negligible) (e.g. Fig. 13a). Many of the elements show coherent behaviour, with three groups emerging (Fig. 13b): (1) immobile elements that have been used in the construction of the isocons, oscillating around zero (e.g. Th, La, Sm and Nb), (2) hydrous fluid-mobile trace elements (LILE) showing extreme relative enrichments (Rb, Cs and U), and (3) significantly less affected major and minor elements Si, Al, K, Na and P. In accordance with the previous modelling (Fig. 12), the behaviour of the elements in the latter group (Si, Al, K, Na and P), can be interpreted as precipitation of new albitic plagioclase, K-feldspar, quartz and apatite. Variable but less pronounced depletion in Ca, Sr and Ba may point to instability and partial replacement of the original K-feldspar and more calcic plagioclase. This would explain the origin of the observed albitic plagioclase and K-feldspar overgrowths/films formed on older feldspars generation of the matrix (Fig. 3).

Taken together, both modelling approaches seem to support the model of melt infiltration, which is in accord with the major- and trace-element variation and Sr–Nd isotopic data indicating open-system behaviour.

### *The possible role for fractional crystallization*

While some major elements display consistent trends over the whole silica range, the others feature remarkable horizontal shifts at the end of the sequence, i.e. in the more siliceous schlieren and nebulitic migmatites (Fig. 6). In addition, the spider plots (Fig. 8) show large ranges for compatible elements in these two migmatite types, with the contents decreasing rapidly in the most silica-rich samples. This seems to indicate that there was an additional process involved.

Theoretically such a differentiation to more siliceous compositions could have been driven by the restite unmixing (Chappell *et al.*, 1988; Barbero & Villaseca, 1992; Chappell, 1996; Williamson *et al.*, 1997). However this does not agree with the observed limited variations in the ferromagnesian components, nearly constant A/CNK and sharp decrease in feldspar-compatible elements, such as Ba, Sr and Eu. Moreover this scenario would require separation of large volumes of refractory garnet-bearing residua, whose occurrence is unknown from the Gföhl Unit.

The major- and trace-element signatures of the most siliceous samples of the nebulitic migmatite are remarkably similar to felsic, strongly fractionated granites. The broad variation

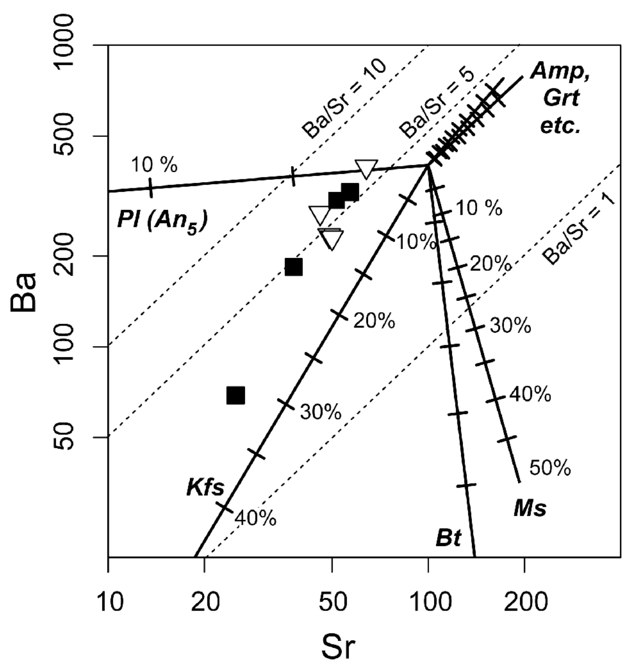


**Fig. 14:** *Fractional crystallization modelling for schlieren and nebulitic migmatites. The results are plotted in Sr vs. Ba diagram (ppm). The diagram is in logarithmic co-ordinates in order to transform the exponential fractional crystallization trends into linear ones.Labelled vectors correspond to up to 50% fractional crystallization of the main rock-forming minerals. The starting point was chosen arbitrarily and the vectors can be shifted freely. Trace-element distribution coefficients are from Hanson (1978; Kfs, Amp, Rb in Pl), Icenhower & London(1995; Bt and Ms) and Blundy & Shimizu(1991; Sr in Pl, assuming 750 °C, $An_5$). The whole compositional spectrum forthe nebulitic migmatite can be reproduced by reasonable degree of fractionation of an assemblage dominated by K-feldspar, with minor plagioclase and biotite.*

and progressive decrease in Ba, Sr, Eu, LREE, Th (Figs 6 & 7) and, to some extent, Pb (not shown) seem to bear a testimony to fractional crystallization, a process very efficient in removing compatible elements from an evolving magma. This mechanism is expected to have operated already during the ascent and, more importantly, at the terminal stages of the melt infiltration process.

This hypothesis is corroborated for instance by the binary plot involving Sr and Ba (Fig. 14). The diagram demonstrates that the entire compositional spectrum of the schlieren and nebulitic migmatites can be modelled by reasonable amounts of K-feldspar > albitic plagioclase and biotite fractionation.

In addition, some role for the accessory minerals is evident. The sharp decrease in LREE and Th with increasing silica (Figs 7 & 8) points to monazite removal (Fig. 4), a phenomenon common in relatively LREE-poor granitic melts (Villaseca *et al.,* 2003). Lastly, the drop in MREE can be accounted for by apatite fractionation.

### *P–T conditions of the orthogneiss-melt interaction*

In order to understand better the mechanism of the migmatization, information on the *P–T* conditions is essential. Some constraints are provided by the saturation thermometry on accessory minerals. In slightly peraluminous, calcium-poor leucogranites the most important will be zircon (Watson & Harrison, 1983) and monazite (Montel, 1993).

Given that the amount of melt present in the banded orthogneiss was limited, the whole-rock geochemistry can be used as a proxy to assess the concentrations of many elements in its Early Palaeozoic protolith. Even though inherited Precambrian components are by no means rare in the Gföhl gneiss zircons, at least in Austria (Friedl *et al.*, 2004), their proportion by volume is small. Consequently, their influence on the Zr budget and thus the calculated Zr saturation temperatures should be negligible. Then the zircon (*c.* 815 ± 24°C, median ±2 ) and monazite (*c.* 800 ± 38°C) saturation temperatures yield the upper constraints on the liquidus temperature of the magma parental to the granitic protolith (e.g. Hanchar & Watson, 2003; Miller *et al.*, 2003; Janoušek, 2006). This agrees with the coincidence of the two independent saturation temperatures derived from both accessory minerals.

On the other hand, the nebulitic migmatite may provide information on the maximum liquidus temperature of the Variscan anatectic melt. The temperature is near 740°C, derived from zircon (747 ± 53°C) and monazite (740 ± 90°C). If the melt infiltration has indeed taken place, the apparent gradual decrease in zircon and monazite saturation temperatures in the whole rock sequence (Fig. 10) may be an artefact, resulting from mixing of two dissimilar components.

The second approach, using the THERMOCALC calculations, was adopted by Hasalová *et al.* (2008b). These authors calculated equilibration temperature of the banded orthogneiss, stromatitic, schlieren and nebulitic migmatites to be 790–850°C at 7.5 kbar, 760–820°C at 6.5 kbar, 715–770°C at 5.5 kbar and 690–750°C at 4.5 kbar, respectively. Moreover, the *P–T* calculations clearly show that the infiltrating melt equilibrated with the host rock on the retrograde branch of the *P–T* path.

### Broader implications for the petrogenesis of felsic migmatites

Several authors have recently proposed a new mechanism for transport of felsic magma through hot, mid-crustal rocks, termed pervasive flow (Weinberg, 1999; Olsen *et al.*, 2004). In this model, foliation-parallel veins/sheets of granitic composition invade hot country rocks, whose low viscosity inhibits hydrofracturing and dyking (Weinberg & Searle, 1998). Additionally, their high temperature (higher than the solidus of the invading melt) enables the magma to migrate upwards without crystallizing. This process should result eventually in a formation of up to several km thick injection complexes, common in hot crustal terraines (Weinberg, 1999; Leitch & Weinberg, 2002). Hasalová *et al.* (2008a, b) argued that the large-scale pervasive flow does not require formation of channelized pathways but can also occur penetratively, along grain boundaries. These authors presented microstructural observations indicating that the porous flow commonly described in mantle rocks (McKenzie, 1984; Reiners, 1998) can in fact play a significant role in the crust as well.

The model of pervasive flow still contains several aspects that remain to be clarified. Firstly, its physical background is still poorly understood. So far there are only several theoretical papers (Leitch & Weinberg, 2002; Olsen *et al.*, 2004), accompanied by works providing field and petrographic evidence from a handful of terrains world-wide (e.g. Collins & Sawyer, 1996; Weinberg & Searle, 1998; Vanderhaeghe, 1999).

A key problem is the expected involvement of small volumes of penetrating acid melt, which should theoretically have high viscosities. The process of reactive porous flow is very slow even for mantle-derived melts (tens to hundreds centimetres per year; McKenzie, 1984) and is likely to be even more so in the crust. This would make the system vulnerable to freezing, and subsequently render the long-distance melt percolation impossible.

These problems can be possibly less important for volatile-rich melts, as water, F and B dramatically decrease the viscosity of granitic melts (Dingwell *et al.*, 1996; Giordano *et al.*, 2004; Whittington *et al.*, 2004). This was probably not the case in the Rokytná Complex, as the whole-rock fluorine contents are uniformly low (Table 1) and tourmaline, the main boron host, is absent. However, the pervasive melt migration, even at small volumes, can occur as soon as a sufficient porosity is created. This is associated with dilatation related either to cavitation process, known well from the material science (Čadek, 1988), in conjunction with melt underpressure or to grain-scale hydrofracturing related to melt overpressure and high differential stress (Závada *et al.*, in press). The most straightforward scenario in our case seems that the pervasive porous flow was a deformation-driven process associated with diffusion creep deformation mechanism. It could have been connected to a crustal-scale shear zone, described in many previous works (e.g. Schulmann *et al.*, 2005; Racek *et al.*, 2006; Tajčmanová *et al.*, 2006).

Generally speaking, we have not found in course of the current research any arguments invalidating the melt infiltration model. In fact the whole-rock geochemistry may provide important constraints on the nature and source of the protolith, the penetrating melt and the overall mass balance. However, the crucial point that ought to be stressed here is that the whole-rock geochemical data by themselves, even though not contradicting the melt infiltration model, do not provide an unequivocal proof for its operation. They cannot rule out completely some common scenarios, such as disequilibrium melting with small-scale melt movement or in situ equilibrium melting, in which the individual small melt batches failed to homogenize with each other, still reflecting the geochemical/isotopic variation of their protolith. In order to disprove the other genetic possibilities microstructural, petrological and field data are essential.

In this context the reader is referred to complementary work providing the necessary additional information (Hasalová *et al.*, 2008a, b).

## Conclusions

Four types of gneisses and migmatites (banded orthogneiss, stromatitic, schlieren and nebulitic migmatites) were defined previously in the RokytnáComplex (Gföhl Unit, Bohemian Massif). While each of the types shows a distinct geochemical and Sr-Nd isotopic fingerprint, the whole sequence evolves along regular, more or less smooth trends for most of the elements. This evolution of the RokytnáComplex has been interpreted by (Hasalová *et al.*, 2008a, b) as a result of melt infiltration. The melt infiltration has been defined as a process in which the banded orthogneiss was pervasively, along grain boundaries, penetrated by felsic melt derived from an external source. In this context the individual migmatite types can be explained by different degrees of equilibration between the bulk rock and the passing melt.

The current study is in agreement with this model, however the available whole-rock geochemical data alone are not unequivocal and need to be supported by field, microstructural and petrological observations. Nevertheless, the major- and trace-element as ell as Sr-Nd isotopic compositions yield some important constraints concerning the nature of the protolith, the composition and possible source of the penetrating melt and the overall mass balance.

If true, the melt infiltration can be modelled as an open-system process, characterised by changes of the total mass/volume, accompanied by gains/losses in many of the major- and trace-elements. The numerical modelling of the mass balance resulted in identification of a component added by a heterogeneous nucleation of feldspars, quartz and apatite from the passing melt. This is in accord with presence of new albitic plagioclase, K-feldspar and quartz coatings as well as resorption of relict feldspars. At the most advanced stages, the chemical variations in the schlieren and nebulitic migmatites require an increasing role for fractional crystallization of the K-feldspar and plagioclase, with accessory amounts of Th-rich monazite ±apatite.

In general, the melt infiltration model may potentially explain the origin some of the felsic migmatites in other high-grade metamorphic terrains. If proven widespread, the process would have profound implications for chemical development of large crustal segments overlaying anatectic regions and the melt transport therein. Melt infiltration would also strongly influence the rheology of large crustal domains, with potential consequences for deformation mechanism in collisional orogens. Clearly, much more work remains to be done before it could be truly established and well understood.

## Acknowledgements

This work was financially supported by the Grant Agency of the Czech Academy of Sciences (Grant No. IAA311140), the Czech Grant Agency (No. 205/04/2065), the French National Agency (No. 06-1148784) and an internal CNRS funding (CGS/EOST). Stays of P. Hasalová at ULP Strasbourg were founded by the French Government Foundation (BGF). Our sincere thanks are due to R. Boutin, who has performed timely and precise ICP-MS analyses at ULP Strasbourg and to J. Míková with P. Denková from the Czech Geological Survey for the assistance in the isotopic laboratory. We gratefully acknowledge A. Langrová from the Institute of Geology at the Czech Academy of Sciences for operating the electron microprobe. Last but not least, the quality of this paper benefited from careful editorial handling by Carlo Dietl, as well as helpful reviews by Peter Nabelek and Malcolm Roberts.

## Appendix 1: analytical techniques

Four samples of each rock type were taken in order to document the compositional variation on both the outcrop as well as regional scale (Fig. 1c). Minerals were analysed using the Cameca SX100 electron microprobe at the Czech Academy of Sciences in point beam mode at 15 kV and 10 nA. Representative analyses are summarized in the Table 2.

Following a lithium tetraborate fusion, major-element oxides and trace elements were determined by ICP MS VG PQ 2+ at the Centre de Géochimie de la Surface, Université Louis Pasteur, Strasbourg. The obtained results are listed in Tables 3 & 4. Fluorine was measured by an ion selective electrode in the laboratories of the Czech Geological Survey in Prague (Table 3). Data management, recalculation, plotting and statistical evaluation of the whole-rock geochemical data were facilitated using *GCDkit* (Janoušek *et al.*, 2006).

For the isotopic study, samples were dissolved using a combined HF-HCl-HNO3attack. Strontium was isolated by exchange chromatography techniques on PP columns with Sr.spec Eichrom resin and bulk REE were isolated on PP columns filled with TRU.spec Eichrom resin (Pin *et al.*, 1994). The Nd was further separated on PP columns with Ln.spec Eichrom resin (Pin & Zalduegui, 1997). Isotopic analyses were performed on Finnigan MAT 262 thermal ionization mass spectrometer in dynamic mode using a double Re filament assembly (CGS). The $^{143}Nd/^{144}Nd$ ratios were corrected for mass fractionation to $^{146}Nd/^{144}Nd = 0.7219$, $^{87}Sr/^{86}Sr$ ratios assuming $^{86}Sr/^{88}Sr = 0.1194$. External reproducibility is given by results of repeat analyses of the La Jolla ($^{143}Nd/^{144}Nd = 0.511852 \pm 14$ (2 ; n = 23)) and NBS 987 ($^{87}Sr/^{86}Sr = 0.710247 \pm 26$ (2 ; n = 25)) isotopic standards. The Rb, Sr, Sm and Nd concentrations were obtained by ICP-MS.

The decay constants applied to age-correct the isotopic ratios are from Steiger & Jäger (1977) (Sr) and Lugmair & Marti (1978) (Nd). The $^{i}_{Nd}$ values and single-stage CHUR Nd model ages were obtained using Bulk Earth parameters of Jacobsen & Wasserburg (1980), the two-stage Depleted Mantle Nd model ages ($T^{DM}_{Nd}$) were calculated after Liew & Hofmann (1988). The Sr–Nd isotopic data for studied migmatites are listed in Table 5.

## References

Albaréde, F., 1995. Introduction to Geochemical Modeling. Cambridge University Press, Cambridge.

Ayres, M., Harris, N. & Vance, D., 1997. Possible constraints on anatectic melt residence times from accessory mineral dissolution rates: an example from Himalayan leucogranites. *Mineralogical Magazine*, **61**, 29–36.

Barbarin, B., 1996. Genesis of the two main types of peraluminous granitoids. *Geology*, **24**, 295–298.

Barbey, P., Brouand, M., Le Fort, P. & Pecher, A., 1996. Granite-migmatite genetic link: the example of the Manaslu granite and Tibetan Slab migmatites in central Nepal. *Lithos*, **38**, 63–79.

Barbero, L. & Villaseca, C., 1992. The Layos Granite, Hercynian Complex of Toledo (Spain): an example of paraautochthonus restite-rich granite in a granulitic area. *Transactions for the Royal Society of Edinburgh: Earth Sciences*, **83**, 127–138.

Barbero, L., Villaseca, C., Rogers, G. & Brown, P.E., 1995. Geochemical and isotopic disequilibrium in crustal melting: An insight from the anatectic granitoids from Toledo, Spain. *Journal of Geophyical Research*, **100**, 15745–15765.

Bea, F., 1996. Controls on the trace element composition of crustal melts. *Transactions for the Royal Society of Edinburgh: Earth Sciences*, **87**, 33-41.

Becker, H., Wenzel, T. &Volker, F., 1999. Geochemistry of glimmerite veins in peridotites from Lower Austria –implications for the origin of K-rich magmas in collision zones. *Journal of Petrology*, **40**, 315-338.

Blumenfeld, P. & Bouchez, J.-L., 1988. Shear criteria and migmatite deformed in the magmatic and solid states. *Journal of Structural Geology*, **10**, 361–372.

Blundy, J.D. & Shimizu, N., 1991. Trace element evidence for plagioclase recycling in calc-alkaline magmas. *Earth and Planetary Science Letters*, **102**, 178–197.

Boynton, W.V., 1984. Cosmochemistry of the rare earth elements: meteorite studies. In: P. Henderson (Editor), Rare Earth Element Geochemistry. Elsevier, Amsterdam, pp. 63–114.

Briquet, L. & Lancelot, J., 1979. Rb–Sr systematics and crustal contamination trends for calc-alkaline igneous rocks. *Earth and Planetary Science Letters*, **43**, 385-396.

Brown, M., 1973. The definition of Metatexites, Diatexites and Migmatites. *Proceedings of the Geologist's Association*, **84**, 371–382.

Brown, M. & Solar, G. S., 1998. Granite ascent and emplacement during contractional deformation in convergent orogens. *Journal of Structural Geology*, **20**, 1365–1393.

Brown, M. & Solar, G.S., 1999. The mechanism of ascent and emplacement of granite magma during transpression: a syntectonic granite paradigm. *Tectonophysics*, **312**, 1–33.

Brown, M., Averkin, Y.A., McLellan, E.L. & Sawyer, E.W., 1995. Melt segregation in migmatites. *Journal of Geophyical Research*, **100**, 15655–15679.

Büsch, W., Schneider, G. & Mehnert, K. R., 1974. Initial melting at grain boundaries. Part II: Melting in rocks of granodioritic, quartz dioritic and tonalitic composition. *Neues Jahrbuch Für Mineralogie Monatshefte*, **8**, 345–370.

Čadek, J., 1988. Creep in Metallic Materials. Elsevier, Amsterdam.

Carswell, D.A., 1991. Variscan high P–T metamorphism and uplift history in the Moldanubian Zone of the Bohemian Massif in Lower Austria. *European Journal of Mineralogy*, **3**, 323–342.

Chappell, B.W., 1996. Magma mixing and the production of compositional variation within granite suites: Evidence from the granites of southeastern Australia. *Journal of Petrology*, **37**, 449–470.

Chappell, B.W., White, A.J.R. & Wyborn, D., 1987. The importance of residual source material (restite) in granite petrogenesis.*Journal of Petrology*, **28**, 571–604.

Clemens, J.D., 2003. S-type granitic magmas –petrogenetic issues, models and evidence. Earth-Science Reviews, **61**, 1–18.

Collins, W.J. & Sawyer, E.W., 1996. Pervasive granitoid magma transfer through the lower-middle crust during non-coaxial compressional deformation. *Journal of Metamorphic Geology*, **14**, 565–579.

Cooke, R.A. & O'Brien, P.J., 2001. Resolving the relationship between high P–T rocks and gneisses in collisional terranes: an example from the Gföhl gneiss–granulite association in the Moldanubian Zone, Austria. *Lithos*, **58**, 33–54.

Dallain, C., Schulmann, K. &Ledru, P., 1999. Textural evolution in the transition from subsolidus annealing to melting process, Velay Dome, French Massif Central. *Journal of Metamorphic Geology*, **17**, 61–74.

D'Lemos, R.S., Brown, M. & Strachan, R.A., 1992. Granite magma generation, ascent and emplacement within a transpressional orogen. *Journal of Geological Society, London*, **149**, 487–490.

Dallmeyer, R.D., Franke, W. & Weber, K. 1995. Pre-Permian Geology of Central and Eastern Europe. Springer, Berlin.

Dingwell, D.B., Hess, K.U. & Knoche, R., 1996. Granite and granitic pegmatite melts: Volumes and viscosities. *Transactions for the Royal Society of Edinburgh: Earth Sciences*, **87**, 65–72.

Dudek, A., Matějovská, O. & Suk, M., 1974. Gföhl orthogneiss in the Moldanubicum of Bohemia and Moravia. *Krystalinikum*, **10**, 67–78.

Ferré, E. C., Martín-Hernández, F., Teyssier, C. & Jackson, M., 2004. Paramagnetic and ferromagnetic anisotropy of magnetic susceptibility in migmatites: measurements in high and low fields and kinematic implications. *Geophysical Journal International*, **157**, 1119–1129.

Finger, F., Roberts, M.P., Haunschmid, B., Schermaier, A. & Steyrer, H.P., 1997. Variscan granitoids of Central Europe: their typology, potential sources and tectonothermal relations. *Mineralogy and Petrology*, **61**, 67–96.

Frank, W., Hammer, S., Popp, F., Scharbert, S. & Thöni, M., 1990. Isotopengeologische Neuergebnisse zur Entwicklungsgeschichte der Böhmischen Masse. *Österreichische Beiträge zu Meteorologie und Geophysik*, **3**, 185-228.

Franke, W., 2000. The mid-European segment of the Variscides: tectonostratigraphic units, terrane boundaries and plate tectonic evolution. In: W. Franke, V. Haak, O. Oncken, and D. Tanner (Editors), Orogenic Processes: Quantification and Modelling in the Variscan Belt. *Geological Society Special Publication,* **179**, London, pp. 35–61.

Friedl, G., von Quadt, A. & Finger, F., 1994. 340 Ma U/Pb-Monazitalter aus dem niederösterreichischen Moldanubikum und ihre geologische Bedeutung. *Terra Nostra*, **94**, 43–46.

Friedl, G., McNaughton, N.J., Fletcher, A. & Finger, F., 1998. New SHRIMP-zircon ages for orthogneisses from the south-eastern part of the Bohemian Massif (Lower Austria). *Acta Universitatis Carolinae, Geologica*, **42**, 251–252.

Friedl, G., Finger, F., Paquette, J.L., von Quadt, A., McNaughton, N.J. & Fletcher, I.R., 2004. Pre-Variscan geological events in the Austrian part of the Bohemian Massif deduced from U/Pb zircon ages. *Geologische Rundschau*, **93**, 802–823.

Fritz, H., Dallmeyer, R.D. & Neubauer, F., 1996. Thick-skinned versus thin-skinned thrusting: Rheology controlled thrust propagation in the Variscan collisional belt (the southeastern Bohemian Massif, Czech Republic-Austria). *Tectonics*, **15**, 1389–1413.

Fuchs, G. & Matura, A., 1976. Zur Geologie des Kristallins der südlichen Böhmischen Masse. *Jahrbuch der Geologischen Bundesanstalt Wien*, **119**, 1–43.

Gardien, V., Thompson, A. B., Grujic, D. & Ulmer, P., 1995. Experimental melting of biotite + plagioclase + quartz + muscovite assemblage and implications for crustal melting. *Journal of Geophysical Researc*h, **100**, 15581–15591.

Giordano, D., Romano, D.B., Dingwell, D.B., Poe, B. & Behrens, H., 2004. The combined effects of water and fluorine on the viscosity of silicic magmas. *Geochimica et Cosmochimica Acta*, **68**, 5159–5168.

Godard, M., Bodinier, J.-L. & Vasseur, G. 1995. Effects of mineralogical reactions on trace element redistributions in mantle rocks during percolation processes: a chromatographic approach, *Earth and Planetary Science Letters*, **133**, 449-461.

Grant, J.A., 1986. The isocon diagram –a simple solution to Gresens equation for metasomatic alteration. *Economic Geology*, **81**, 1976–1982.

Grant, J.A., 2005. Isocon analysis: A brief review of the method and applications. *Physics and Chemistry of the Earth (A)* **30**, 997–1004.

Gresens, R.L., 1967. Composition–volume relationships of metasomatism. *Chemical Geology*, **2**, 47–55.

Guernina, S. & Sawyer, E.W., 2003. Large-scale melt-depletion in granulite terranes: an example from the Archean Ashuanipi Subprovince of Quebec. *Journal of Metamorphic Geology*, **21**, 181–201.

Hammouda, T., Pichavant, M. & Chaussidon, M., 1996. Isotopic equilibration during partial melting: an experimental test of the behaviour of Sr. *Earth and Planetary Science Letters,* **144**, 109–121.

Hanchar, J.M. & Watson, E.B., 2003. Zircon saturation thermometry. In: J.M. Hanchar and P.W.O. Hoskin (Eds.), Zircon. Reviews in Mineralogy and Geochemistry.. *Mineralogical Society of America and Geochemical Society*, Washington, **53**, pp. 89–112.

Hanson, G.N., 1978. The application of trace elements to the petrogenesis of igneous rocks of granitic composition. *Earth and Planetary Science Letters*, **38**, 26–43.

Hanson, G.N. & Langmuir, C.H., 1978. Modelling of major elements in mantle-melt systems using trace element approaches. *Geochimica et Cosmochimica Acta*, **42**, 725–741.

Harris, N. & Ayres, M., 1998. The implications of Sr-isotope disequilibrium for rates of prograde metamorphism and melt extraction in anatectic terrains. In: P. Treloar and P.J. O'Brien (Eds.), What Drives Metamorphism and Metamorphic Reactions? *Geological Society London, Special Publication*, **138**, London, pp. 171–182.

Harris, N.B.W. & Inger, S., 1992. Trace element modelling of pelite-derived granites. *Contributions to Mineralogy and Petrology*, **110**, 46–56.

Harrison, T.M. & Watson, E.B., 1983. Kinetics of zircon dissolution and zirconium diffusion in granitic melts of variable water content. *Contributions to Mineralogy and Petrology*, **84**, 66–72.

Harrison, T.M. & Watson, E.B., 1984. The behavior of apatite during crustal anatexis: equilibrium and kinetic considerations. *Geochimica et Cosmochimica Acta*, **48**, 1467–1477.

Harte, B., Hunter, R.H. & Kinny, P.D., 1993. Melting and melt movement in the Earth. *Philosophical Transactions of Royal Society London A*, **342**, 1–21.

Hasalová, P., Schulmann, K., Lexa, O., Štípská, P., Hrouda, F., Ulrich, S., Haloda, J., Týcová, P., 2008a. Origin of migmatites by deformation enhanced melt infiltration of orthogneiss: a new model based on quantitative microstructural analysis. *Journal of Metamorphic Geology*.

Hasalová, P., Štípská, P., Powell, R., Schulmann, K., Janoušek, V., Lexa, O., 2008b. Transforming mylonitic metagranite by open-system interactions during melt flow. *Journal of Metamorphic Geology*.

Holland, T.J.B. & Powell, R., 1998. An internally consistent thermodynamic data set for phases of petrological interest. *Journal of Metamorphic Geology*, **16**, 309–343.

Icenhower, J. & London, D., 1995. An experimental study of element partitioning among biotite, muscovite and coexisting peraluminous silicic melt at 200 MPa ($H_2O$). *American Mineralogist*, **80**, 1229–1251.

Irber, W., 1999. The lanthanide tetrad effect and its correlation with K/Rb, Eu/Eu*, Sr/Eu, Y/Ho, and Zr/Hf of evolving peraluminous granite suites. *Geochimica et Cosmochimica Acta*, **63**, 489–508.

Jacobsen, S.B. & Wasserburg, G.J., 1980. Sm–Nd evolution of chondrites. *Earth and Planetary Science Letters*, **50**, 139-155.

Janoušek, V., 2006. Saturnin, R language script for application of accessory-mineral saturation models in igneous geochemistry. *Geologica Carpathica*, **57**, 131–142.

Janoušek, V., Rogers, G. & Bowes, D.R., 1995. Sr-Nd isotopic constraints on the petrogenesis of the Central Bohemian Pluton, Czech Republic. *Geologische Rundschau*, **84**, 520–534.

Janoušek, V., Finger, F., Roberts, M.P., Frýda, J., Pin, C. & Dolejš, D., 2004. Deciphering petrogenesis of deeply buried granites: whole-rock geochemical constraints on the origin of largely undepleted felsic granulites from the Moldanubian Zone of the Bohemian Massif. *Transactions for the Royal Society of Edinburgh: Earth Sciences*, **95**, 141–159.

Janoušek, V., Farrow, C.M. & Erban, V., 2006. Interpretation of whole-rock geochemical data in igneous geochemistry: introducing Geochemical Data Toolkit (GCDkit). *Journal of Petrology*, **47**, 1255–1259.

Johannes W., 1980. Metastable melting in the granite system Qz-Or-Ab-An-H2O. *Contributions to Mineralogy and Petrology*, **72**, 73–80.

Kelemen, P.B., Hirth, G., Shimizu, N., Spiegelman, M. & Dick, H.J.B., 1997. A review of melt migration processes in the adiabatically upwelling mantle beneath oceanic spreading ridges. *Philosophical Transactions of Royal Society London A*, **355**, 283–318.

Knesel, K.M. & Davidson, J.P., 1996. Isotopic disequilibrium during melting of granite and implications for crustal contamination of magmas. *Geology*, **24**, 243–246.

Knesel, K.M. & Davidson, J.P., 2002. Insights into collisional magmatism from isotopic fingerprints of melting reactions. *Science*, **296**, 2206–2208.

Leitch, A.M. & Weinberg, R.F., 2002. Modelling granite migration by mesoscale pervasive flow. *Earth and Planetary Science Letters*, **200**, 131–146.

Liew, T.C. & Hofmann, A.W., 1988. Precambrian crustal components, plutonic associations, plate environment of the Hercynian Fold Belt of Central Europe: indications from a Nd and Sr isotopic study. *Contributions to Mineralogy and Petrology*, **98**, 129-138.

Lister, J.R. & Kerr, R.C., 1991. Fluid-mechanical models of crack propagation and their application to magma transport in dykes. *Journal of Geophysical Research*, **96**, 10049–10077.

Lugmair, G.W. & Marti, K., 1978. Lunar initial $^{143}$Nd/$^{144}$Nd: differential evolution line of the lunar crust and mantle. *Earth and Planetary Science Letters*, **39**, 349-357.

Masuda, A., Kawakami, O., Dohmoto, Y. & Takenaka, T., 1987. Lanthanide tetrad effects in nature: two mutually opposite types, W and M. *Geochemical Journal*, 119–124.

Matějovská, O., 1975. The Moldanubian gneiss series of south-western Moravia and its relation to granulites. *Věstník Ústředního Ústavu Geologického*, **50**, 345–351.

Matte, P., Maluski, H., Rajlich, P. & Franke, W., 1990. Terrane boundaries in the Bohemian Massif: result of large-scale Variscan shearing. *Tectonophysics*, **177**, 151–170.

McKenzie, D., 1984. The generation and compaction of partially molten rock. *Journal of Petrology*, **25**, 713–765.

McKenzie, D., 1989. Some remarks on the movement of small melt fractions in the mantle. *Earth and Planetary Science Letters*, **95**, 53–72.

Medaris Jr., L.G., Jelínek, E. & Mísař, Z., 1995. Czech eclogites: Terrane settings and implications for Variscan tectonic evolution of the Bohemian Massif. *European Journal of Mineralogy*, **7**, 7–28.

Medaris Jr., L.G., Fournelle, J.H., Ghent, E.D., Jelínek, E. & Mísař, Z., 1998. Prograde eclogite in the Gföhl Nappe, Czech Republic: new evidence on Variscan high-pressure metamorphism. *Journal of Metamorphic Geology*, **16**, 563–576.

Mehnert, K.R, 1971. Migmatites and the Origin of Granitic Rocks. Elsevier, Amsterdam.

Mehnert, K.R., Büsch, W. & Schneider, G., 1973. Initial melting at grain boundary of quartz and feldspar in gneisses and granulites. *Neues Jahrbuch Für Mineralogie Monatshefte*, **4**, 165–183.

Miller, C.F., McDowell, S.M. & Mapes, R.W., 2003. Hot and cold granites? Implications of zircon saturation temperatures and preservation of inheritance. *Geology*, **31**, 529–532.

Monecke, T., Kempe, U., Monecke, J., Sala, M. & Wolf, D., 2002. Tetrad effect in rare earth element distribution patterns; a method of quantification with application to rock and mineral samples from granite-related rare metal deposits. *Geochimica et Cosmochimica Acta*, **66**, 1185–1196.

Montel, J.M., 1993. A model for monazite/melt equilibrium and application to the generation of granitic magmas. *Chemical Geology*, **110**, 127–146.

Nabelek, P.I. & Glascock, M.D., 1995. REE-depleted leucogranites, Black Hills, South Dakota: a consequence of disequilibrium melting of monazite-bearing schists. *Journal of Petrology*, **36**, 1055–1071.

O'Brien, P.J., 2006. Type-locality granulites: high-pressure rocks formed at eclogite-facies conditions. *Mineralogy and Petrology*, **86**, 161–175.

O'Brien, P.J. & Carswell, D.A., 1993. Tectonometamorphic evolution of the Bohemian Massif: evidence from high pressure metamorphic rocks. *Geologische Rundschau*, **82**, 531–555.

O'Brien, P.J. & Rötzler, J., 2003. High-pressure granulites: formation, recovery of peak conditions and implications for tectonics. *Journal of Metamorphic Geology,* **21**, 3–20.

Olsen, S.N. & Grant, J.A., 1991. Isocon analysis of migmatitization in the Front Range, Colorado, USA. *Journal of Metamorphic Geology*, **9**, 151-164.

Olsen, S.N., Marsh, B.D. & Baumgartner, L.P., 2004. Modelling mid-crustal migmatite terrains as feeder zones for granite plutons: the competing dynamics of melt transfer by bulk versus porous flow. *Transactions for the Royal Society of Edinburgh: Earth Sciences*, **95**, 49–58.

Owen, J.V. & Dostal, J., 1996. Prograde metamorphism and decompression of the Gföhl gneiss, Czech Republic. *Lithos*, **38**, 259–270.

Petford, N., Lister, J.R. & Kerr, R.C., 1994. The ascent of felsic magmas in dykes. *Lithos*, **32**, 161–168.

Petford, N., Cruden, A.R., McCaffrey, K.J.W. & Vigneresse, J.-L., 2000. Granite formation, transport and emplacement in the Earth's crust. *Nature*, **408**, 669–673

Petrakakis, K., 1986a. Gneisses from the Moldanubikum, Lower Austria, and the metamorphic evolution of the southern Bunte-Serie. *Tschermaks mineralogische und petrographische Mitteilungen*, **35**, 243–259.

Petrakakis, K., 1986b. Metamorphism of high-grade gneisses from the Moldanubian Zone, Austria, with particular reference to the garnets. *Journal of Metamorphic Geology*, **4**, 323–344.

Petrakakis, K., 1997. Evolution of Moldanubian rocks in Austria: review and synthesis. *Journal of Metamorphic Geology*, **15**, 203–222.

Pin, C. & Zalduegui, J.F.S., 1997. Sequential separation of light rare-earth elements, thorium and uranium by miniaturized extraction chromatography: Application to isotopic analyses of silicate rocks. *Analytica Chimica Acta*, **339**, 79-89.

Pin, C., Briot, D., Bassin, C. & Poitrasson, F., 1994. Concomitant separation of strontium and samarium-neodymium for isotopic analysis in silicate samples, based on specific extraction chromatography. *Analytica Chimica Acta*, **298**, 209-217.

Powell, R., Holland, T. & Worley, B., 1998. Calculating phase diagrams involving solid solutions via non-linear equations, with examples using THERMOCALC. *Journal of Metamorphic Geology*, **16**, 577–588.

Racek, M., Štípská, P., Pitra, P., Schulmann, K. & Lexa, O., 2006. Metamorphic record of burial and exhumation of orogenic lower and middle crust: a new tectonothermal model for the Drosendorf window (Bohemian Massif, Austria). *Mineralogy and Petrology*, **86**, 221–251.

Rapp, R.P. & Watson, E.B., 1986. Monazite solubility and dissolution kinetics; implications for the thorium and light rare earth chemistry of felsic magmas.*Contributions to Mineralogy and Petrology*, **94**, 304–316.

Reiners, P.W., 1998. Reactive melt transport in the mantle and geochemical signatures of mantle-derived magmas. *Journal of Petrology*, **39**, 1039–1061.

Rudnick, R.L., McLennan, S.M. & Taylor, S.R., 1985. Large ion lithophile elements in rocks from high-pressure granulite facies terrains. *Geochimica et Cosmochimica Acta*, **49**, 1645–1655.

Rushmer, T., 1995. An experimental deformation study of partially molten amphibolite: application to low-melt fraction segregation. *Journal of Geophysical Research*, **100**, 15681–15695.

Rushmer, T., 1996. Melt segregation in the lower crust: how have experiments helped us? *Transactions for the Royal Society of Edinburgh: Earth Sciences*, **87**, 73–83.

Rushmer, T., 2001. Volume change during partial melting reactions: implications for melt extraction, melt geochemistry and crustal rheology. *Tectonophysics*, **342**, 389–405.

Rutter, E.H. & Neumann, D.H.K., 1995. Experimental deformation of partially molten Westerly Granite under fluid-absent conditions, with implications for the extraction of granitic magmas. *Journal of Geophysical Research*, **100**, 15697–15715.

Sawyer, E.W., 1991. Disequilibrium melting and the rate of melt residuum separation during migmatitization of mafic rocks from the Grenville Front, Quebec. *Journal of Petrology*, **32**, 701–738.

Sawyer, E. W., 1999. Criteria for the recognition of partial melting. *Physics and Chemistry of the Earth (A)*, **24**, 269–279.

Sawyer, E.W., 2000. Grain-scale and outcrop-scale distribution and movement of melt in a crystallising granite. *Transactions for the Royal Society of Edinburgh: Earth Sciences*, **91**, 73–85.

Sawyer, E. W., 2001. Melt segregation in the continental crust: distribution and movement of melt in anatectic rocks. *Journal of Metamorphic Geology*, **19**, 291–309.

Schulmann, K., Melka, R., Lobkowicz, M.Z., Ledru, P., Lardeaux, J. & Autran, A., 1994. Contrasting styles of deformation during progressive nappe stacking at the southeastern margin of the Bohemian Massif (Thaya Dome). *Journal of Structural Geology*, **16**, 355–370.

Schulmann, K., Kröner, A., Hegner, E., Wendt, I., Konopásek, J., Lexa, O. & Štípská, P., 2005. Chronological constraints on the pre-orogenic history, burial and exhumation of deep-seated rocks along the eastern margin of the Variscan Orogen, Bohemian Massif, Czech Republic. *Americal Journal of Science*, **305**, 407–448.

Shaw, D.M., 1968. A review of K–Rb fractionation trends by covariance analysis. *Geochimica et Cosmochimica Acta*, **32**, 573–601.

Spiegelman, M. & Kenyon, P., 1992. The requirements for chemical disequilibrium during magma migration. *Earth and Planetary Science Letters*, **109**, 611–620.

Steiger, R.H. & Jäger, E., 1977. Subcommission on Geochronology; convention on the use of decay constants in geo- and cosmochronology. *Earth and Planetary Science Letters*, **36**, 359-362.

Streckeisen, A. & Le Maître, R.W., 1979. A chemical approximation to the modal QAPF classification of the igneous rocks. *Neues Jahrbuch fur Mineralogie-Abhandlungen*, **136**, 169–206.

Suess, F.E., 1912. Die moravische Fenster und ihre Beziehung zum Grundgebirge des Hohen Gesenkes. *Akademie der Wissenschaften, Denkschrift Matematisch - Naturwissenschaftliche Klasse*, **88**, 541–631.

Svoboda, J., 1966. Regional Geology of Czechoslovakia. Part I The Bohemian Massif. Czech Geological Survey in the Publishing House of Czechoslovak Academy of Sciences, Prague.

Sylvester, P.J., 1998. Post-collisional strongly peraluminous granites. *Lithos*, **45**, 29–44.

Štípská, P. & Powell, R., 2005. Does ternary feldspar constrain the metamorphic conditions of high-grade meta-igneous rocks? Evidence from orthopyroxene granulites, Bohemian Massif. *Journal of Metamorphic Geology*, **23**, 627–647.

Štípská, P., Schulmann, K. & Kröner, A., 2004. Vertical extrusion and middle crustal spreading of omphacite granulite: a model of syn-convergent exhumation (Bohemian Massif, Czech Republic). *Journal of Metamorphic Geology*, **22**, 179–198.

Tajčmanová, L., Konopásek, J. & Schulmann, K., 2006. Thermal evolution of the orogenic lower crust during exhumation within a thickened Moldanubian root of the Variscan belt of Central Europe. *Journal of Metamorphic Geology*, **24**, 119–134.

Taylor, S.R. & McLennan, S.M., 1985. The Continental Crust: Its Composition and Evolution. Blackwell, Oxford.

Tollmann, A., 1982. Großräumiger variszischer Deckenbau im Moldanubikum und neue Gedanken zum Variszikum Europas. *Geotektonische Forschungen*, **64**, Stuttgart.

Urban, M., 1992. Kinematics of the Variscan thrusting in the Eastern Moldanubicum (Bohemian Massif, Czechoslovakia): evidence from the Námě granulite massif. *Tectonophysics*, **201**, 371–391.

Valbracht, P.J., Vrána, S., Beetsma, J.J., Fiala, J. & Matějka, D., 1994. Sr and Nd isotopic determinations in three Moldanubian granulite massifs in southern Bohemia. *Journal of the Czech Geological Society*, **39**, 114.

van Breemen, O., Aftalion, M., Bowes, D.R., Dudek, A., Mísař, Z., Povondra, P. & Vrána, S., 1982. Geochronological studies of the Bohemian Massif, Czechoslovakia, and their significance in the evolution of Central Europe. *Transactions for the Royal Society of Edinburgh: Earth Sciences*, **73**, 89–108.

Van der Wal, D. & Bodinier, J.L., 1996. Origin of the recrystallisation front in the Ronda peridotite by km-scale pervasive porous melt flow. *Contributions to Mineralogy and Petrology*, **122**, 387–405.

Vanderhaeghe, O., 1999. Pervasive melt migration from migmatites to leucogranite in the Shuswap metamorphic core complex, Canada: control of regional deformation. *Tectonophysics*, **312**, 35–55.

Veksler, I.V., Dorfman, A.M., Kamenetsky, M., Dulski, P. & Dingwell, D.B., 2005. Partitioning of lanthanides and Y between immiscible silicate and fluoride melts, fluorite and cryolite and the origin of the lanthanide tetrad effect in igneous rocks. *Geochimica et Cosmochimica Acta*, **69**, 2847–2860.

Vellmer, C., 1992. Stoffbestand und Petrogenese von Granuliten und granitischen Gesteinen der südlichen Böhmischen Masse in Niederösterreich. Unpublished PhD. thesis, Georg-August-Universität, Göttingen.

Vigneresse, J.-L., Barbey, P. & Cuney, M., 1996. Rheological transitions during partial melting and crystallization with application to felsic magma segregation and transfer. *Journal of Petrology*, **37**, 1579–1600.

Villaseca, C., Martin Romera, C., De la Rosa, J. & Barbero, L., 2003. Residence and redistribution of REE, Y, Zr, Th and U during granulite-facies metamorphism: behaviour of accessory and major phases in peraluminous granulites of central Spain. *Chemical Geology*., **200**, 293–323.

Vielzeuf, D. & Holloway, J. R., 1988. Experimental determination of the fluid-absent melting relations in the pelitic system-consequences for crustal differentiation. *Contributions to Mineralogy and Petrology*, **98**, 257–276.

von Bargen, N. & Waff, H.S., 1986. Permeabilities, interfacial areas and curvatures of partially molten systems: results of numerical computations of equilibrium microstructures. *Journal of Geophysical Research*, **91**, 9261–9276.

Watson, E.B., 1996. Dissolution, growth and survival of zircons during crustal fusion; kinetic principles, geological models and implications for isotopic inheritance. *Transactions for the Royal Society of Edinburgh: Earth Sciences*, **87**, 43–56.

Watson, E.B. & Harrison, T.M., 1983. Zircon saturation revisited: temperature and composition effects in a variety of crustal magma types. *Earth and Planetary Science Letters*, **64**, 295–304.

Watson, E.B. & Harrison, T.M., 1984. Accessory minerals and the geochemical evolution of crustal magmatic systems: a summary and prospectus of experimental approaches. *Physics of the Earth and Planetary Interiors*, **35**, 19–30.

Watson, E.B., Vicenzi, E.P. & Rapp, R.P., 1989. Inclusion/host relations involving accessory minerals in high-grade metamorphic and anatectic rocks. *Contributions to Mineralogy and Petrology*, **101**, 220–231.

Watt, G.R. & Harley, S.L., 1993. Accessory phase controls on the geochemistry of crustal melts and restites produced during water-undersaturated partial melting. *Contributions to Mineralogy and Petrology*, **114**, 550–566.

Wedepohl, K.H., 1995. The composition of the continental crust. *Geochimica et Cosmochimica Acta*, **59**, 1217–1232.

Weinberg, R.F., 1999. Mesoscale pervasive felsic magma migration: alternatives to dyking. *Lithos*, **46**, 393–410.

Weinberg, R.F. & Searle, M.P., 1998. The Pangong Injection Complex, Indian Karakoram: A case of pervasive granite flow through hot viscous crust. *Journal of Geological Society*, **155**, 883–891.

Whittington, A.G. & Treloar, P.J., 2002. Crustal anatexis and its relation to the exhumation of collisional orogenic belts, with particular reference to the Himalaya. *Mineralogical Magazine*, **66**, 53–92.

Whittington, A., Richet, P., Behrens, H., Holtz, F. & Scaillet, B., 2004. Experimental temperature-X($H_2O$)-viscosity relationship for leucogranites and comparison with synthetic silicic liquids.*Transactions for the Royal Society of Edinburgh: Earth Sciences* , **9**, 59–71.

Wickham, S.M., 1987. The segregation and emplacement of granitic magmas. *Journal of the Geological Society of London*, **144**, 281–297.

Williamson, B.J., Downes, H., Thirlwall, M.F. & Beard, A., 1997. Geochemical constraints on restite composition and unmixing in the Velay anatectic granite, French Massif Central. *Lithos*, **40**, 295–319.

Závada, P., Schulmann, K., Konopásek, J., Ulrich, S. & Lexa, O., in press. Extreme ductility of feldspars – melt enhanced grain boundary sliding (GBS) and creep failure: rheological implications for felsic lower crust. *Journal of Geophysical Research*.

Zhao, Z.H., Xiong, X.L., Hen, X.D., Wang, Y.X., Qiang, W., Bao, Z.W. & Jahn, B., 2002. Controls on the REE tetrad effect in granites: Evidence from the Qianlishan and Baerzhe granites, China. *Geochemical Journal*, **36**, 527–543.

Zeng, L., Asimow, P.D. & Saleeby, J.B., 2005. Coupling of anatectic reactions and dissolution of accessory phases and the Sr and Nd isotope systematics of anatectic melts from a metasedimentary source. *Geochimica et Cosmochimica Acta*, **6**, 3671–3682.

# CHAPTER IV:

## Influence of mechanical anisotropy and melt proportion on recurrent brittle and ductile response of partially molten crust exemplified by structural and AMS study, Central Vosges, France

# Influence of mechanical anisotropy and melt proportion on recurrent brittle and ductile response of partially molten crust exemplified by structural and AMS study, Central Vosges, France

*Karel Schulmann [1], Jean-Bernard Edel [1], Pavlína Hasalová [1, 2], Ondrej Lexa[1, 2], John Cosgrove [3] and Josef Ježek [2]*

[1] Université Louis Pasteur, CGS/EOST, UMR 7516–7517, 1 rue Blessig, Strasbourg 67084, France

[2] Institute of Petrology and Structural Geology, Charles University, Albertov 6, 12843, Prague, Czech Republic

[3] Department of Earth Sciences, Imperial College of London, Prince Consort Road 1, UK

## Abstract

Complex behaviour of solid state rocks including granitic melts in region of fertile magma segregation was studied in the metasedimentary and gneissic migmatites of the Central Vosges. The metasedimentary metatexites and diatexites were deformed by homogeneous viscous flow, but show a complete continuity between pre-rheological critical melt percentage AMS fabrics and associated viscous flows AMS fabrics. Metatexites with low proportion of melts (<50%) and metagraywacke mesosomes exhibit rather high degree of anisotropy associated with plane strain to oblate ellipsoid shapes. The leucosomes show plane strain ellipsoid shapes and weaker degree of anisotropy. The diatexites and granites (>50% of melts) show very weak degree of anisotropy and highly variable ellipsoid shapes which may reflect undisturbed rotation of careers of magnetic anisotropy (biotite) in freely moving melts.

Mechanical behaviour of rocks with low ability to melt also depends on the volume of granitic magma. In regions with low volume of melts, the magma is ascending along the main anisotropy in the form of sills. Low proportion of melt is characterized by preservation of homogeneous AMS fabric of solid state network at high angle to fabric pattern of pervasive homogeneous viscous flow. High proportion of melt is identified by disintegration of pre-melting fabric elements and their progressive reorientation towards directions of main magma flow.

**Keywords:** migmatites, migmatite rheology, superposed fabrics, AMS, Vosges

## Introduction

The common spatial and also temporal relation between migmatites and crustal scale shear zones led several authors to propose a mechanism of magma rise by exploiting crustal weaknesses (Brown, *et al.*, 1995; Brown & Solar, 1998a; Brown & Solar, 1998b; Collins & Sawyer, 1996; Weinberg & Searle, 1998). These authors argued that the magma intrudes pervasively, parallel to main anisotropy represented by foliation planes, fold hinges and boudin necks (Brown, 1994; Brown *et al.*, 1995). The most common observation indicates that the vein-like leucosomes are injected into extensional fractures provided the magma pressure is high enough (Lucas & St-Onge, 1995; Wickham, 1987) or parallel to the axial surface of folds (Vernon & Paterson, 2001) indicating magma injection perpendicular to the direction of active contraction.

Vanderhaeghe (1999) suggested that in fertile metapelite lithologies the melt fraction forms a diffuse network of concordant veins feeding discordant dikes that are dominantly perpendicular to regional stretching direction. In contrast, the refractory lithologies show intrusive character of granitic fraction displaying sharp contacts with the host rocks. In these areas the melt migrated through a network of fractures using mechanically weak foliation planes or along fractures oriented at high angle to main anisotropy. This field example emphasises different rheological properties of hot country rocks and pervasive flow of melt in either ductile deforming matrix or invading hydraulically opened fractures. Brown *et al.* (1995) and Vanderhaeghe (2001) further discussed problem of transition from metatexites (stromatitic migmatites of Mehnert (1971)) marked by pervasive flow of melt through network of foliation parallel veins to melt dominated diatexites (nebulitic migmatites of Mehnert (1971)) which is marked by disruption of solid network and development of true magmatic flow in granites.

Brown *et al.* (1981) emphasised that in nature it is almost impossible to draw a line between solid network intruded by granitic veins and between migmatitic or gneissic enclaves passively rotating in viscous melt. This is because none of above mentioned studies provided full information about orientation, symmetry and intensity of fabrics of contemporaneously deformed solid state network and granitic veins. Moreover, there exists no study which quantifies the gradual evolution of fabrics in solid rocks and in veins with increasing proportion of molten material. It is only recently, that analogue modelling (Barraud *et al.*, 2001; Barraud *et al.*, 2004; Rosenberg, 2001; Rosenberg & Handy, 2001) and structural studies (Brown, 2004; Brown & Solar, 1998b; Cosgrove, 1997; Vernon & Paterson, 2001) proposed mechanical models explaining geometry of melt enhanced shear zones and feedback to the melting and deformation.

To answer all these problems, the analysis of anisotropy of magnetic susceptibility (AMS) represents an ideal method to describe orientation of fabric ellipsoid directions, shape of fabric ellipsoid and degree of anisotropy in both migmatitic veins and host rock (Ferré *et al.*, 2003) . The interpretation of quantitative AMS fabrics in migmatites is possible if the solid state rock fabric is distinguished from magmatic one in veins or partially molten rocks and if the magnetic mineralogy is well known (Ferré *et al.*, 2004). Therefore, combined structural, AMS and petrographic analysis is needed to identify precisely the rock type in terms of melt proportion and corresponding magnetic mineralogy and susceptibility.

The migmatite domain of the Vosges Mountains offers an excellent example of crustal cross-section through orthogneisses, metasedimentary migmatites to diatexites, granites and leucogranites. In this area, structural relationships between a variety of migmatites and adjacent granites were studied together with their AMS fabrics correlated with different degree of melt proportions and intensity of bulk deformation. These data are used to discuss the relative role of solid rock mechanical anisotropy, proportion of granite melt and viscosity contrast between different types of host rocks, granite veins and surrounding granite. We establish a model of transient mechanical behaviour of solid state rock–melt system from buckling of rock–melt multilayer, formation of melt bearing heterogeneous shear zones to development of hybrid fractures with increasing melt proportion and bulk strain intensity. Numerical modelling of AMS fabric complemented with detailed microstructural study is used to explain the complex evolution of AMS pattern during contemporaneous melt flow and deformation of solid network.

## Geology of the studied area

The internal part of the Vosges Mountains is built of high-grade gneisses, granulite rocks, granites and migmatites and it is bordered to the south and north by external zones formed by low-grade to non-metamorphosed Palaeozoic volcano-sedimentary sequences (Fig. 1a). The high grade zone in the Vosges (Mts.) consists of the gneiss-granulite complex and migmatite mostly metasedimentary complex (Fluck, 1980), which is subject of this study (Fig. 1b). The gneiss-granulite complex consists of medium pressure mafic to felsic granulites (T = 750°C, P = 9–11 kbar) derived from a variety of protoliths that underwent amphibolite facies re-equilibration (T = 650°C, P = 4–6 kbar) (Latouche, *et al.*, 1992; Rey *et al.*, 1989). The age of early metamorphism at around 335 Ma was determined in various granulites using U–Pb zircon method (Schaltegger *et al.*, 1999). This unit is separated from northerly lying migmatite complex by several ENE–WSW trending crustal granite intrusions (Fluck, 1980), partly emplaced along large-scale sinistral shear zone (Kratinová *et al.*, 2007; Wickert & Eisbacher, 1988). The structural fabric of migmatite region is, according to Blumenfeld & Bouchez (1988) and Rey *et al.* (1992) dominated by extensional Carboniferous tectonics associated with pervasive anatexis and intrusions of voluminous anatectic granites dated at 325.8±4.8 Ma using the U–Pb zircon technique (Kratinová *et al.*, 2007; Schaltegger *et al.*, 1999; Schulmann *et al.*, 2002). The K–Ar and Ar–Ar geochronology carried out in the migmatites indicates cooling

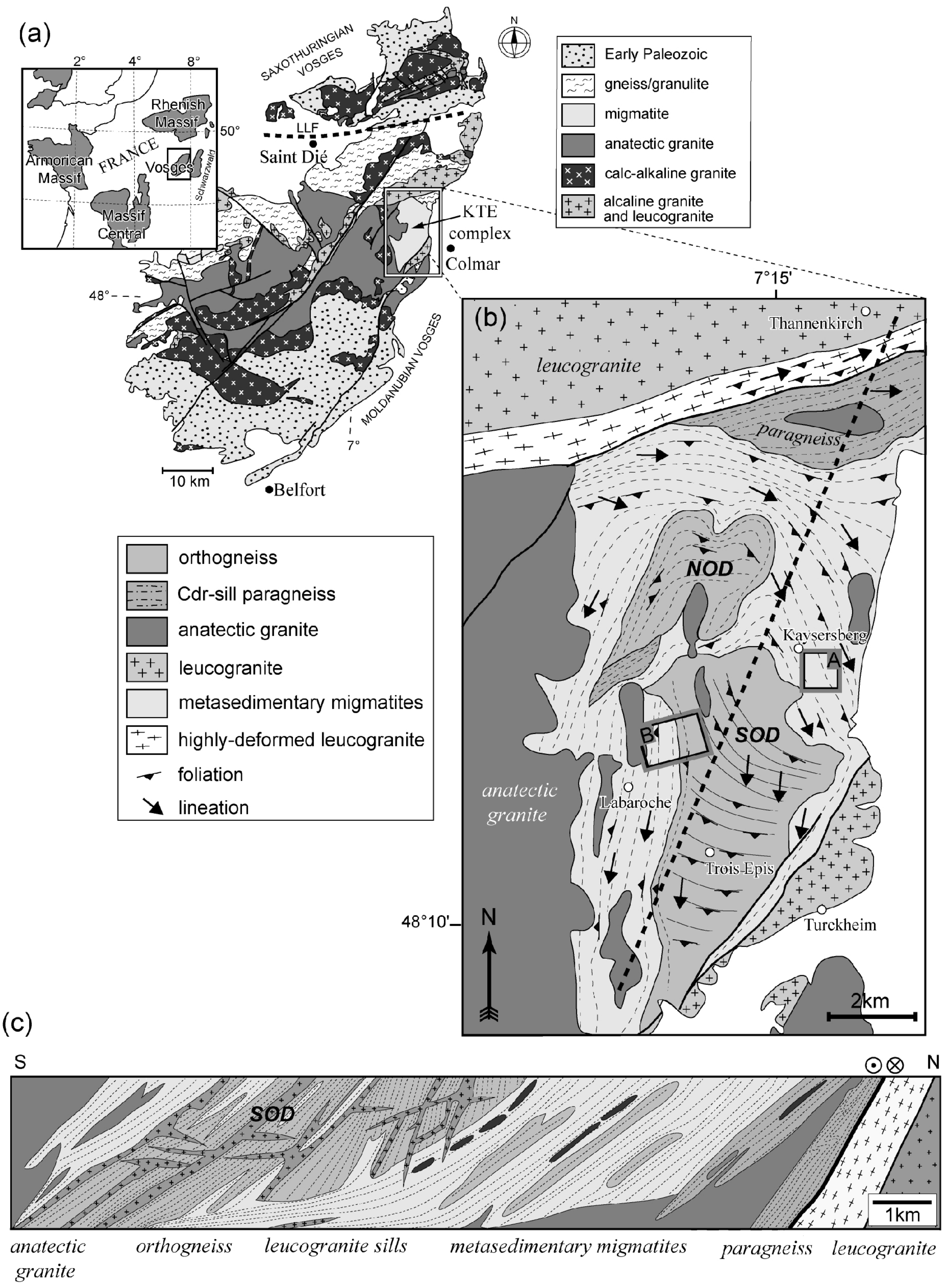


**Fig.1:** *(a) Simplified geological map of Vosges (modified after Fluck, 1980) with the location of the studied area (white rectangle). The upper left inset shows the general location of Vosges within the European Variscides. (b) Detail geological map of the studied migmatitic complex of southern Vosges (modified after Fluck, 1980). The map is modified according to field structural observations and an attempt is made to underline the degree of anatexis in the map scale. Black dashed line corresponds to location of the cross-section. NOD=North Orthogneiss Domain, SOD=South Orthogneiss domain. (c) Schematic geological N–S cross-section through the migmatitic complex showing main structural features of the studied area. Vertical axes not to scale.*

through the biotite and muscovite closure temperatures of 280–350°C (Harrison *et al.*, 1985), which occurred at 327±10 Ma and 333±10 Ma, respectively (Boutin *et al.*, 1995).

## Petrography and microstructures of principal rock types

The studied migmatitic complex (Fig. 1) consists basically of two main lithologies: (i) metasedimentary migmatites connected with variable proportions of anatectic granites surrounding (ii) two orthogneiss domains (Fluck, 1980). The dominant rock type is represented by biotite-rich *metasedimentary migmatites* which are most abundant in the eastern and western parts of the studied area (Fig. 1b). The migmatites exhibit various degree of melting from metatexites (Fig. 2a) to diatexites (Fig. 2b). The biotite-rich metatexite is medium to coarse grained rock and consists mostly of plagioclase (40 modal %), less abundant K-feldspar (20 modal %), quartz (20–30 modal %) and biotite up to 15 modal %. The alumosilicates are absent. Diatexites (Fig. 3a) show idiomorphic plagioclase and K-feldspar indicating crystallization from melt. K-feldspar is also characterized by a Carlsbad twinning suggesting its igneous origin (Vernon, 1986). Quartz exhibits signs of incipient recrystallization (Fig. 3a) possibly developed during the cooling (McLellan, 1983). The planar fabric of meta- and diatexites is formed by characteristic migmatite layering and preferred orientation of dispersed biotite, respectively (Fig. 2a, b). The metasedimentary migmatites are associated with medium grained anatectic biotite-rich granite which is locally porphyritic and form 30–50 modal % of single outcrops (Fig. 2c). In anatectic granites the fabric is underlined by weak alignment of biotite and locally by shape preferred orientation of K-feldspar.

Second important lithology is represented by the biotite bearing gneiss (Fig. 2d & 3b, c) interpreted by Fluck (1980) as a product of a static recrystallization of a high-grade orthogneisses or granulites. Microstructure of this rock is characterized by presence of fine-grained equigranular matrix composed of plagioclase, quartz and K-feldspar (Fig. 3b), with relics of monomineralic aggregates of recrystallized feldspars (Fig. 3c). Perthitic K-feldspar (30 modal %) shows irregular shapes with straight to slightly lobate boundaries, while plagioclase (25–30 modal %) is sub-equant with straight to weakly lobate boundaries (Fig. 3b, c). Plagioclase grains display normal zoning with andesine core ($An_{30-50}$) and thin distinct albite/oligoclase rims ($An_{10-18}$). Quartz (20 modal %) is variable in size and shows highly irregular shapes and strongly curved boundaries. Interstitial quartz and plagioclase grains tracing feldspar boundaries (Fig. 3c) as well as distinct K-feldspar and plagioclase rims represent incipient amount (< 5%) of former melt (Sawyer, 1999). Straight crystal faces of feldspars against quartz also point to crystallization from melt (Kenah & Hollister, 1983;

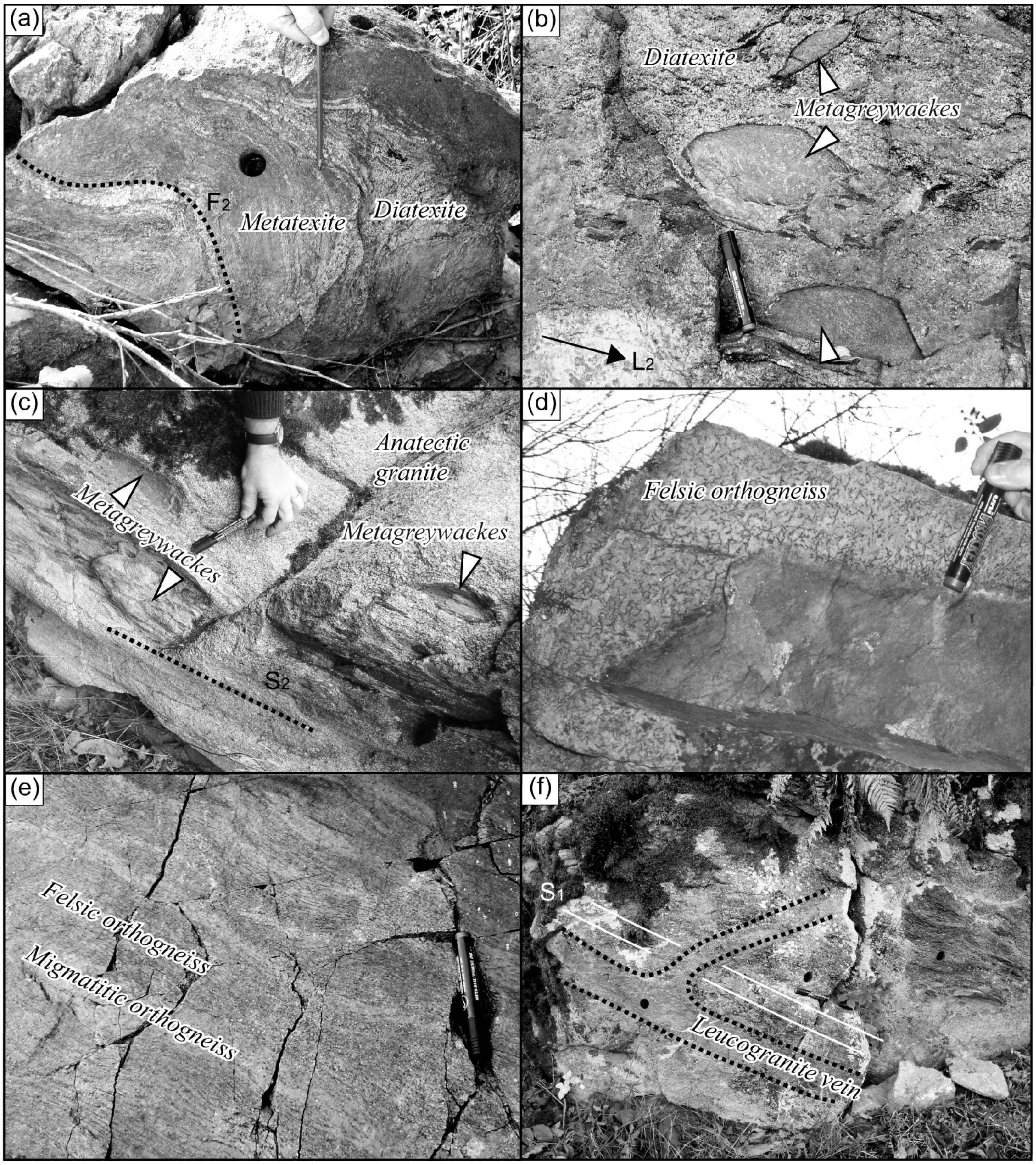


**Fig. 2:** *Field photographs illustrating the main rock types in studied area and their structural characteristics. (a) Disharmonically folded biotite-rich meta- and diatexite by decimetre to metre scale $F_2$ folds. The leucosome veins are located in fold hinge regions or parallel to mesosome foliation (locality K16). (b) Diatexite containing boudins of metagraywackes (white arrows). The boudins are oriented either parallel to the $L_2$ lineation or perpendicular to it (locality K1). (c) Heterogeneous enclaves of gneisses and metagraywackes arranged parallel to the magmatic fabric of surrounding anatectic granite with well developed magmatic $S_2$ fabric (black dashed line) (locality TE40). (d) Migmatitic orthogneiss displaying layer-parallel gneissosity $S_1$ marked by arrangement of planar biotite aggregates (locality TE6). (e) Alternation of the felsic orthogneiss and migmatitic orthogneiss in an outcrop scale. Biotite aggregates underline $S_1$ foliation. These two rock types show diffuse boundaries and it is locally difficult to define structural relationships between them in the field (locality TE27). (f) Leucogranite vein (black dashed lines) cross-cutting surrounding migmatites (locality K16).*

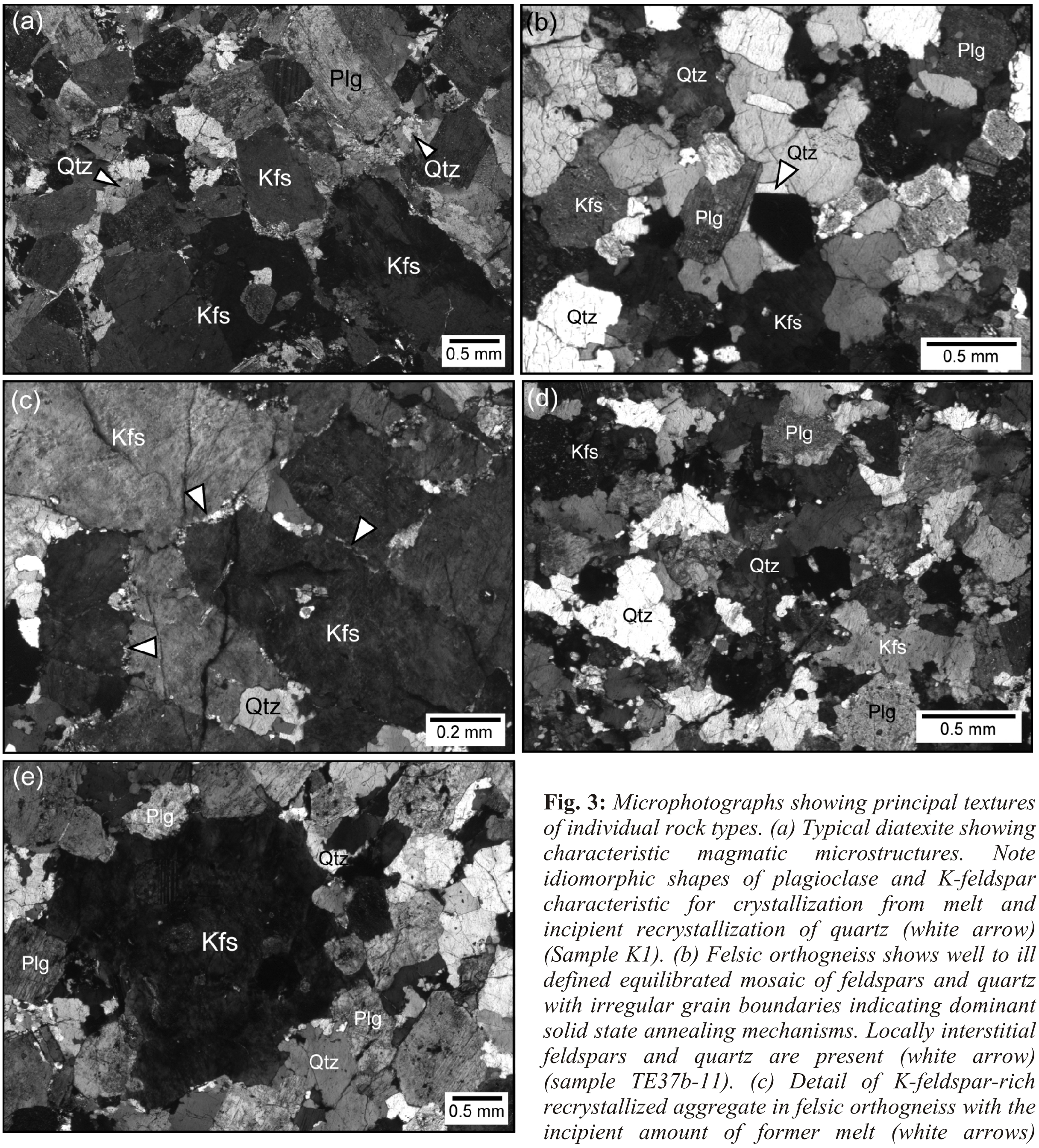


**Fig. 3:** *Microphotographs showing principal textures of individual rock types. (a) Typical diatexite showing characteristic magmatic microstructures. Note idiomorphic shapes of plagioclase and K-feldspar characteristic for crystallization from melt and incipient recrystallization of quartz (white arrow) (Sample K1). (b) Felsic orthogneiss shows well to ill defined equilibrated mosaic of feldspars and quartz with irregular grain boundaries indicating dominant solid state annealing mechanisms. Locally interstitial feldspars and quartz are present (white arrow) (sample TE37b-11). (c) Detail of K-feldspar-rich recrystallized aggregate in felsic orthogneiss with the incipient amount of former melt (white arrows) crystallizing along grain boundaries in the form of interstitial quartz, plagioclase and K-feldspar grains (sample TE37b-11). (d) Typical microstructure of migmatitic orthogneiss that is composed of large irregular corroded feldspar grains with highly lobate boundaries traced with a newly crystallized interstitial feldspars and quartz grains. Quartz forms large irregular grains with highly lobate boundaries. Microstructure of this rock type corresponds to orthogneiss with a high proportion of crystallized melt (sample TE6-72). (e) Detail of corroded relict large K-feldspar grain completely coated by new interstitial feldspars and quartz grains crystallizing along its boundaries (sample TE31-21).*

Marchildon & Brown, 2003). Biotite (10 modal %; Ti = 0.12–0.16 p.f.u., $X_{Mg}$ = 0.32–0.36) shows decussate microstructure (Fig. 4a, c) (Vernon, 1976) and is arranged into irregular elongate polycrystalline aggregates with strong preferred orientation underlying internal anisotropy of this rock type (Fig. 2d). Poikilitic garnet partially replaced by biotite is locally present. Microscopic structure of this gneiss (Fig. 3b) corresponds to highly annealed, solid-state rock which experienced only subordinate melting and we call it further *felsic orthogneiss*.

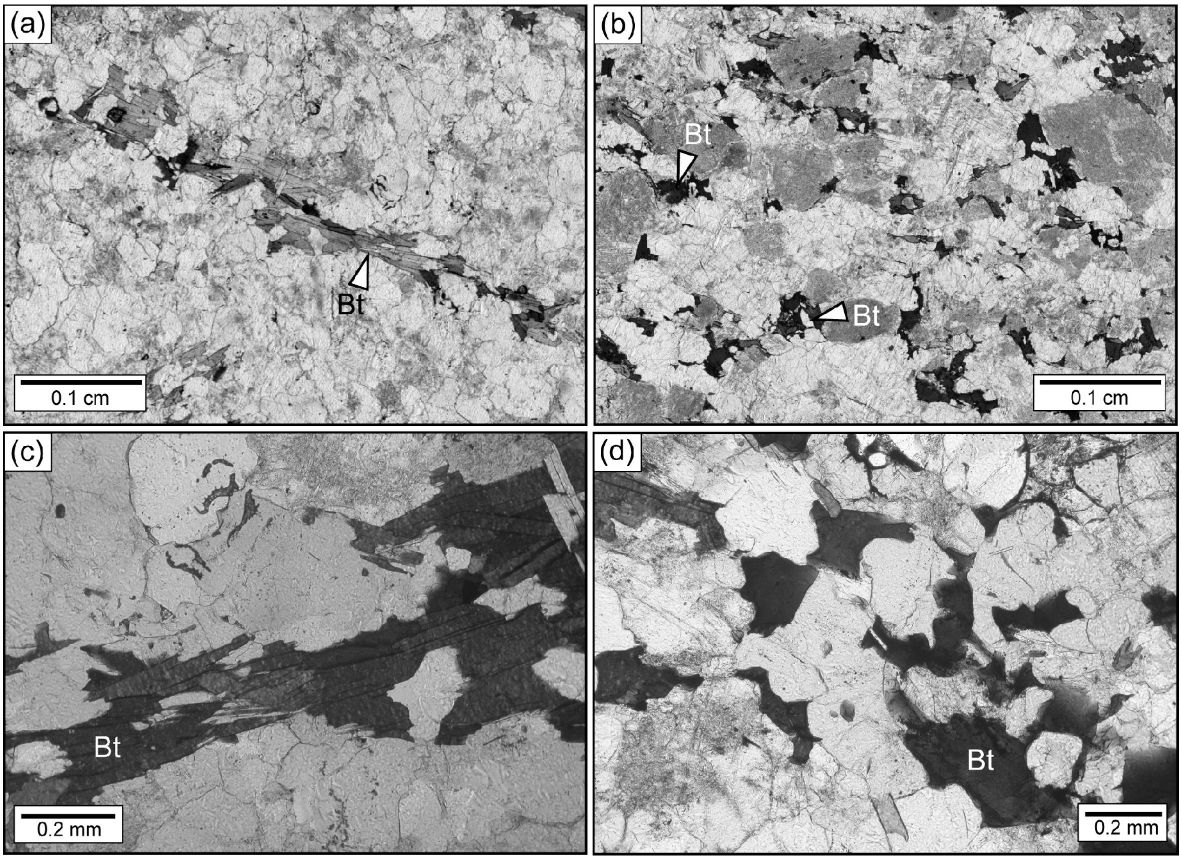


**Fig. 4:** *Micrographs showing the textural difference between biotite in felsic orthogneiss and migmatitic orthogneiss. (a) Biotite aligned into irregular elongate polycrystalline aggregates with strong preferred orientation in felsic orthogneiss (sample TE37b-11). (b) Completely dispersed biotite in migmatitic orthogneiss (sample TE37b-11). (c) Detail of biotite aggregate in felsic orthogneiss. Biotite shows decussate microstructure (sample TE34-512). (d) Detail of dispersed biotite in migmatitic orthogneiss. Biotite display strongly corroded shapes as typical reaction microstructures of reactant minerals with melt (sample TE34-512).*

In some places, this felsic orthogneiss is interlayered with more isotropic rock type of microgranite appearance (Fig. 2e & 3d). This rock type is fine-grained and quartz–feldspathic in composition but the biotite is completely dispersed in equigranular matrix of plagioclase, K-feldspar and quartz (Fig. 3d & 4b). K-feldspar and twinned plagioclase form irregular corroded grains with highly lobate boundaries overgrown with newly crystallized feldspars and quartz and myrmekites (Fig. 3d, e). Quartz occurs in form of large irregular grains with highly lobate boundaries (Fig. 3d). Biotite (Ti = 0.15–0.18 p.f.u., $X_{Mg}$ = 0.4–0.45) show strongly corroded shapes (Fig. 4d) that correspond to those described by Büsch *et al.* (1974) and Mehnert *et al.* (1973) as typical reaction microstructures of reactant minerals with melt. Biotite is locally replaced by muscovite as a 'back-reaction' caused by hydratation due to the crystallization and concentration of the melt in the source rock. Microstructure of this rock type (Fig. 3d) corresponds to orthogneiss with a relatively high proportion of melt. Therefore, we suggest that the dispersed type of rock represents a partially molten and disintegrated equivalent of felsic orthogneiss and we will call it the *migmatitic orthogneiss* further in the text. The felsic and migmatitic orthogneisses show diffuse boundaries and it is difficult to define structural relationships between them in the field (Fig. 2e).

In several places, the both orthogneisses are cross-cut by leucogranite veins with highly variable orientation with respect to host rock fabric (Fig. 2f). Locally, discordant granite dykes of variable dimensions were observed.

## Macroscopic structures and melt proportions within the migmatite complex

The whole migmatite complex represents a large portion of partially molten crust immersed in the heterogeneous and porphyritic anatectic granites (Fig. 1b, c), which show uniform flow fabric marked by west to SW dipping magmatic foliation and S to SSE plunging mineral lineation. The structural evolution is characterised by two main fabric forming events. The early deformation $D_1$ is represented by solid state deformation fabrics well preserved in felsic orthogneiss and locally also in metasedimentary migmatites. These early structures are reworked by flat $D_2$ fabric associated with subsequent extensional deformation and extensive melting (Blumenfeld & Bouchez, 1988; Kratinová *et al.*, 2007; Rey *et al.*, 1992).

### *Metasedimentary migmatites and associated anatectic granites*

The $S_1$ foliation in meta- and diatexites is only rarely preserved in form of fabric folded by decimetre to metre scale $F_2$ folds (Fig. 2a). The leucosome veins are located often in fold hinge regions or parallel to mesosome foliation. At highly molten regions, the enclaves of folded metatexites and metagraywackes are freely floating in surrounding anatectic granites which exhibit well developed magmatic $S_2$ fabric (Fig. 2c). Here, the planar fabric of metatexites is commonly concordant with dominant $S_2$ fabric of surrounding diatexites and anatectic granites. The SW dipping foliation of anatectic granites is marked by preferred orientation of feldspar phenocrysts and by alignment of enclaves of migmatites (Fig. 2c). Locally, transition from magmatic to sub-magmatic and even solid state deformation was observed leading to the development of C/S structures (Berthé *et al.*, 1979) indicating top to the SSE movement. In this case, the $S_2$ foliation bears strong mineral and stretching lineation plunging to the SSE (Fig. 1b).

The diatexites and associated anatectic granites show a less pronounced mineral or stretching lineation. In these rocks the regional stretching direction is defined by preferred orientation of elongate boudins of metagraywackes (Fig. 2b). The boudinage of metagraywackes follows two directions: parallel to the SSE trending $L_2$ mineral lineation or perpendicular to it. Within the YZ section of $D_2$ fabric, some rotation of boudins marked by deflections of surrounding layers of biotite rich schlierens can be observed.

### *South and north orthogneiss domains*

The large NE–SW elongated orthogneiss domain occupies the southern part of the studied area and is composed dominantly by felsic and migmatitic orthogneisses. This southern orthogneiss domain (SOD) is surrounded by metasedimentary migmatites from the east and anatectic granites from the west (Fig. 1b). In order to quantify relationships between deformation and melt proportion, the melt percentage in individual outcrops was estimated on the basis of both macroscopic and microscopic observations (Fig. 5). The melt proportion was calculated as a percentage of individual lithologies from single outcrops using 1321 drilled specimens. This analysis shows that the SOD is globally dominated by felsic (*c.* 40%) and migmatitic orthogneiss (*c.* 20%) but it can be divided into three zones according to melt proportion (Fig. 8):

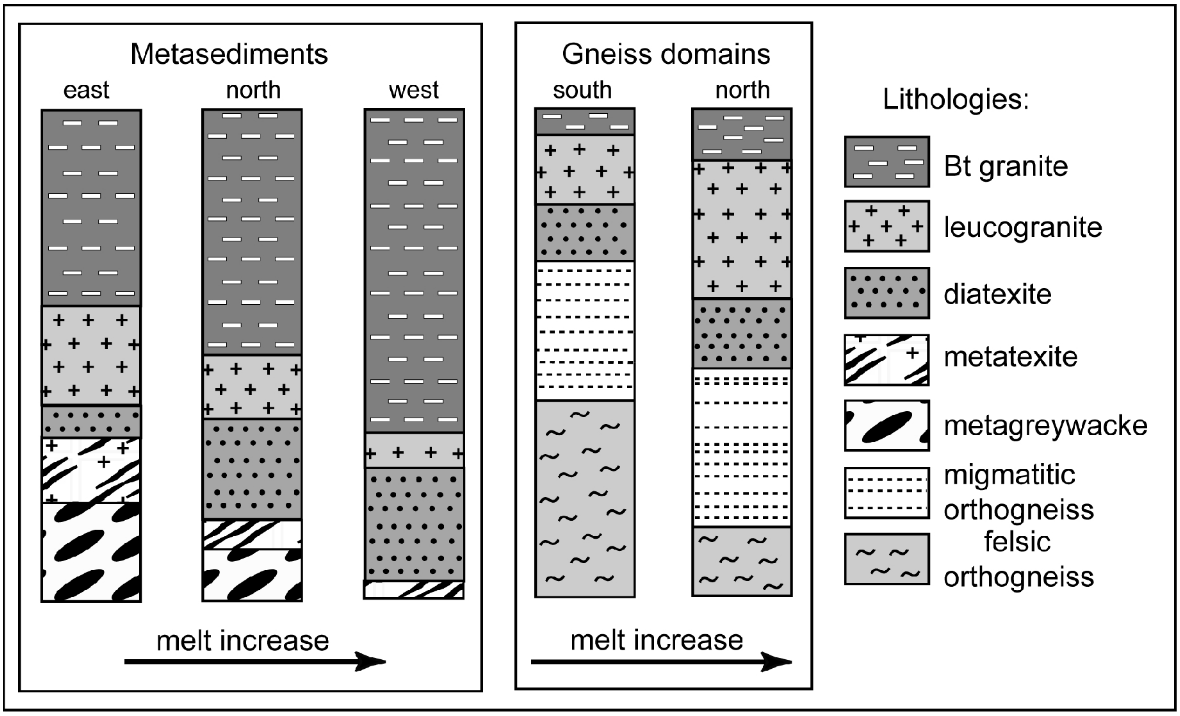


**Fig. 5:** *Histograms representing the melt proportions in individual rock types within both orthogneiss domains and metasedimentary migmatites. Melt proportion increases from left to the right in the diagrams and from east to west or south to north in the map, respectively.*

1) the central and eastern zone 3km wide marked by *c.* 20–30% of melt represented by granite veins cross cutting orthogneiss, 2) up to 1 km wide internal margin dominantly developed at the western part of the SOD with *c.* 30–50% of melt represented by synfolial granites and proportion of diatexites and, 3) narrow 0.5–1 km wide external margin characterized by 50–80% of melt represented by anatectic and porphyritic granites mostly developed along the SW margin of the SOD. Statistics of drilled samples from the central part of the SOD show approximately 80% of felsic orthogneiss and 20% of migmatitic orthogneiss, while the percentage of migmatitic orthogneiss increases up to 40% in the internal marginal zone and to 70% in the external marginal zone.

The general structure of gneiss domains is characterized by dominant layer-parallel gneissosity $S_1$ which is formed by arrangement of planar biotite aggregates (Fig. 2c, d). The $S_1$ gneissosity in central part of the SOD is steeply dipping to the south or to the southwest (Fig. 1). In some places granitic veins without any internal fabric intrude sub-parallel to the $S_1$ foliation of the host rock (Fig. 1c). Occasionally, the distinct granite and leucogranite veins several dm to metre in width cross-cut orthogneisses at high angle with respect to foliation or almost perpendicular to it. In the western internal margin of the SOD the gneissosity changes direction and dips to the west under medium to steep angles. The westerly dipping layers of felsic orthogneiss or migmatitic orthogneiss are interlayered and/or cross-cut by granitic and leucogranitic veins several decimetres to metres in width.

Further to the west, in the external margin of the SOD the layers of orthogneisses form enclaves arranged parallel to the magmatic fabric of anatectic granite. Out of the SOD the medium-grained locally porphyritic anatectic granites predominate with a few migmatitic enclaves strictly oriented parallel to the $D_2$ fabric (Fig. 2c). The change in geometry of solid-state fabric in the internal and external margin of the SOD associated with gradual increase of magma proportion is interpreted to occur during $D_2$ reworking of original $S_1$ fabric.

In the northern part of studied region small NE–SW elongate northern orthogneiss domain (NOD) occurs and contains c. 15% felsic orthogneiss and c. 35% migmatitic orthogneiss which represent by maximum 50% of outcrops. The small centre of domain is characterized by 30–50% of melt (equivalent to internal margin of the SOD), while most of the NOD surface exhibits 50–80% of melt corresponding to external margin of the SOD. The melt is represented by diatexites of indistinguishable protoliths, anatectic granites and leucogranites which also surround the whole composite orthogneiss body (Figs. 1b, c). $S_1$ foliation is locally preserved and dips mostly to the south and southwest under shallow to medium angles (Fig. 1b). At some places, the $S_1$ fabric is disharmonically folded and cross-cut by flat leucogranite veins. Large granitic veins cross-cut interlayered orthogneiss and diatexite at high angle to foliation are present (Fig. 2f).

## The AMS fabrics

Macroscopic structural analysis cannot distinguish between deformation of solid state rocks and that of different kinds of migmatites and granites in terms of coupling between flow of melt and deformation of solid state rocks. In order to propose a consistent model of melt behaviour with respect to the solid network of host rocks or vice versa the relationship between magma flow and deformation of solid enclaves a detailed fabric characterization is needed. Therefore, we carried out an AMS study of main types of lithologies in regions where variable proportion of melt was determined.

### *Sampling strategy and methods*

Measurements of the bulk magnetic susceptibility and of the anisotropy of magnetic susceptibility were performed on 1321 specimens from 108 sites distributed regularly within the whole migmatitic complex and the adjacent granites. For the purpose of AMS study four types of main lithologies were evaluated separately: 1) metasedimentary migmatites (meta- and diatexites), 2) felsic and migmatitic orthogneisses, 3) anatectic granite and 4) leucogranite veins. In single outcrops, which include several lithologies, the samples were regrouped according to detailed petrographic investigations of drill cores described above. The statistical processing and evaluation of 138 AMS sub-groups was carried out using the ANISOFT package of programs (Hrouda *et al.*, 1990; Jelínek, 1978). The susceptibility and the AMS were measured with modified AGICO instruments. The variations in the mean susceptibility with temperature were obtained using a CS–3 apparatus and a KLY–3S Kappabridge (Parma, 1988). The mean susceptibility is $K_m = (K_1 + K_2 + K_3)/3$, where $K_1 > K_2 > K_3$ represent the shape of the ellipsoid of the susceptibility. The corrected degree of anisotropy $P' = \exp[(\ln K_1 - \ln K_m)^2 + (\ln K_2 - \ln K_m)^2 + (\ln K_3 - \ln K_m)^2]$ gives the intensity of preferred orientation of magnetic minerals in a rock. The shape parameter $T = 2\ln(K_2/K_3)/\ln(K_1/K_3) - 1$ (Jelínek, 1981) indicates the symmetry of magnetic fabric, being linear when $-1 < T < 0$ and planar when $1 > T > 0$.

### *Magnetic volume susceptibility and thermomagnetic curves*

The leucogranites are characterized by the weakest susceptibilities (average $K_m = 88.10^{-6}$, standard deviation  $= 61.10^{-6}$) (Fig. 6a). The K/t thermomagnetic curves of leucogranite samples (Fig. 6b) reveal the coexistence of paramagnetic minerals and low amount of magnetite characterized by a decrease of the susceptibility around 580°C.

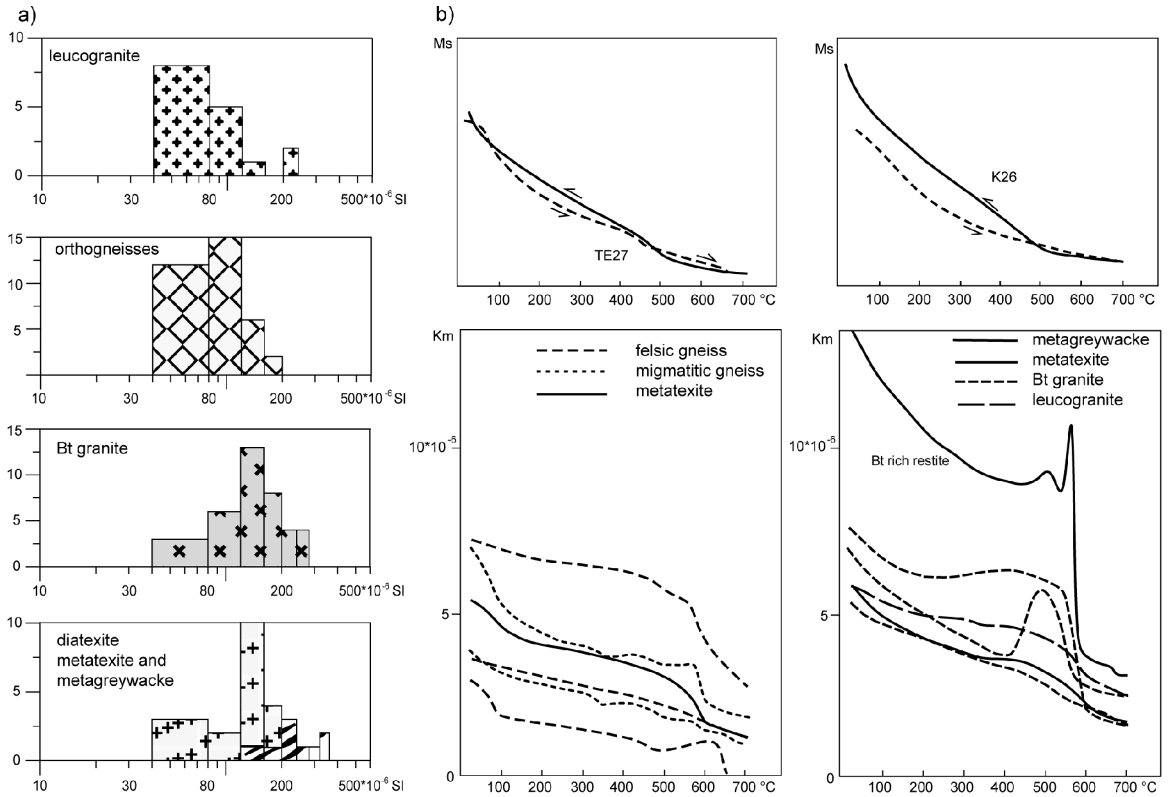


**Fig. 6**: *(a) Mean magnetic susceptibility ($K_m$) histograms showing the distribution of value of susceptibility for four major examined lithologies. Number of sites is plotted on ordinate and the $K_m$ values on abscissa. The mean values and standard deviations are given for each rock type. (b) Representative diagram of granite total susceptibility versus temperature from sample of four major lithologies show dominantly hyperbolic heating curve documenting presence of paramagnetic phases within granites and migmatitic orthogneisses except metagraywacke samples containing significant amount of ferromagnetic minerals.*

The felsic and migmatitic orthogneisses show similar distribution of mean susceptibilities with a slightly higher average (average $K_m = 103.10^{-6}$,  $= 35.10^{-6}$) (Fig. 6a). The K/t and Ms/t thermomagnetic curves indicate that paramagnetic minerals, specifically the biotites, are the main carriers of the magnetization. Magnetite and occasionally hematite, with a Curie temperature of 680°C (Fig. 6b), are the secondary contributors.

Biotite bearing anatectic granites and porphyritic granites exhibit susceptibilities around $K_m = 152.10^{-6}$ with standard deviation $= 53.10^{-6}$ (Fig. 6a) which, according to the thermomagnetic curves result from the coexistence of paramagnetic biotites with a variable amount of ferromagnetic magnetite (Fig. 6b). The thermomagnetic curves of diatexites are similar to curves of Bt-granites and reveal the coexistence of paramagnetic minerals with weak proportion of magnetite (Fig. 6b). Compared to previously described rocks, the greywackes, restite-dominated schlierens and metatexites show the highest bulk susceptibility (average $K_m = 242.10^{-6}$, $= 65.10^{-6}$). This is mainly due to high amounts of paramagnetic biotite and significant amount of magnetite (Fig. 6b).

### *AMS fabric of metasedimentary migmatites and anatectic granites*

The melt proportions indicate an increasing proportion of granites and products of partial melting from east to west and from south to north (Fig. 5). The map of AMS fabrics (Fig. 7) and pole diagrams (Fig. 8) show that both magnetic foliations and lineations exhibit consistent fabric pattern in metasedimentary migmatites surrounding two orthogneiss domains. The magnetic foliations are dipping to the SW under shallow angle in the east and under moderate to steep angle in the west (Fig. 7a & 8a). The magnetic lineations are sub-horizontal and oriented in NNW–SSE direction (Fig. 7b & 8a). The changes of AMS fabric to E–W direction in the northern and southern part of studied area are related to sinistral shearing associated with emplacement of leucogranite sheet-like intrusions and is discussed elsewhere (Kratinová *et al.*, 2007).

The degree of magnetic anisotropy expressed by P' parameter is generally low in diatexites and anatectic granites and the AMS ellipsoid of these rocks is mostly of prolate to plane strain shape (Fig. 8b). A biotite-rich metatexites yield higher degree of anisotropy and more oblate shapes of AMS ellipsoid compared to diatexites and anatectic granites (Fig. 8b). Competent metagraywackes imbedded in metasedimentary migmatites and anatectic granites show identical orientation of AMS directions to those in the surrounding rocks. Their degree of anisotropy increases compared the diatexites and anatectic granites and the shape of AMS ellipsoid develop towards strongly oblate (Fig. 8b).

### *AMS fabric of felsic and migmatitic orthogneisses*

The AMS foliations of orthogneisses in the core and eastern part of the SOD (*c.* 20–30% of melt) are uniformly dipping to the SSW or SW under steep to shallow angles and bear magnetic

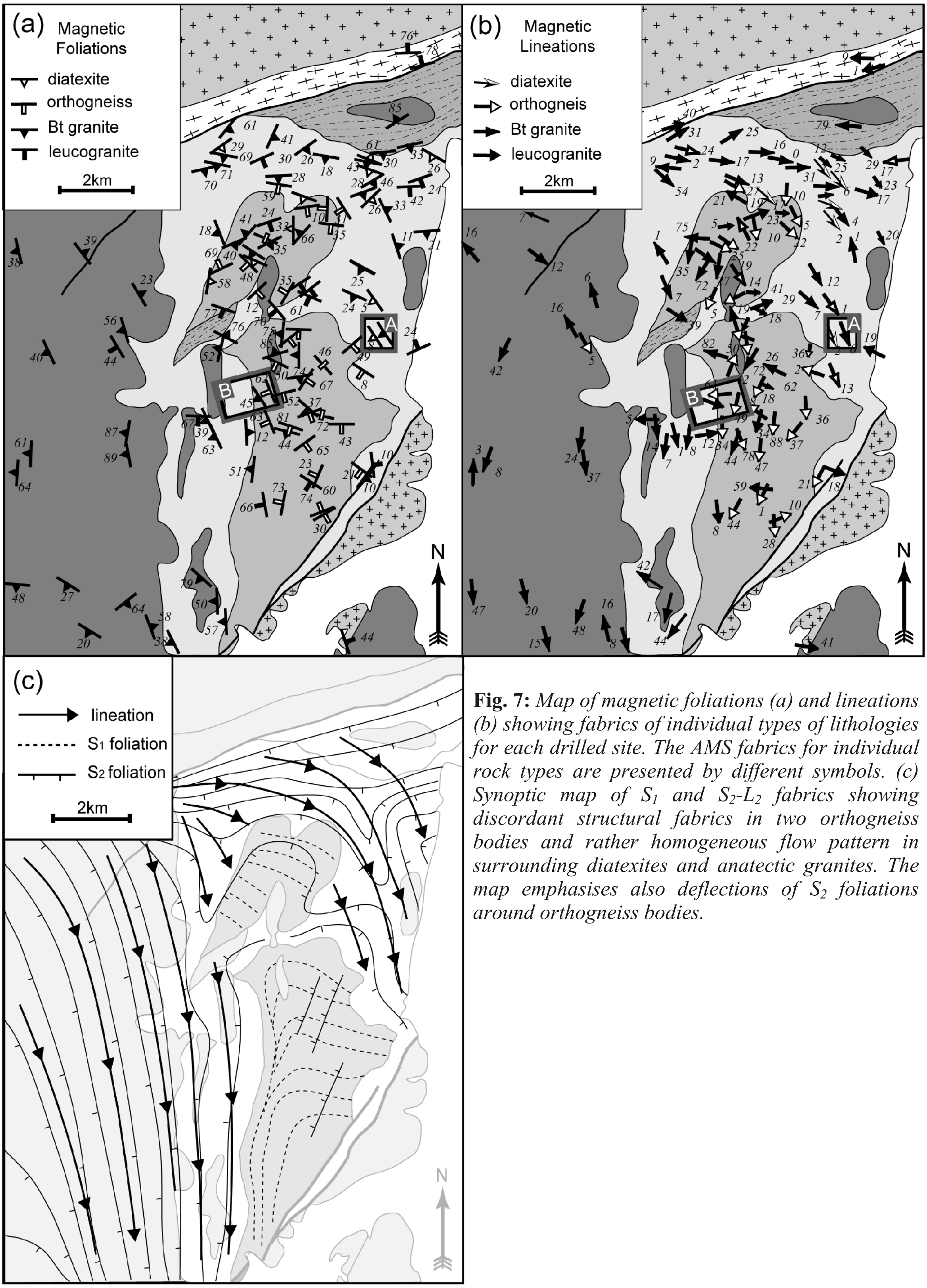


**Fig. 7:** *Map of magnetic foliations (a) and lineations (b) showing fabrics of individual types of lithologies for each drilled site. The AMS fabrics for individual rock types are presented by different symbols. (c) Synoptic map of $S_1$ and $S_2$-$L_2$ fabrics showing discordant structural fabrics in two orthogneiss bodies and rather homogeneous flow pattern in surrounding diatexites and anatectic granites. The map emphasises also deflections of $S_2$ foliations around orthogneiss bodies.*

lineation plunging to the SSW under variable angles (Figs. 7 & 8). The degree of AMS anisotropy of felsic orthogneiss is rather low and the shapes of fabric ellipsoid vary from weakly oblate to weakly prolate (Fig. 8c). The AMS fabric of rare leucogranite and granite veins is generally sub-parallel to host orthogneiss fabric (Fig. 8c).

At the western internal margin of the SOD (*c.* 30–50% of melt) the AMS fabrics from felsic orthogneisses show magnetic foliations dipping either to the S or to the W and form a girdle of planes which intersects in SSW direction (Figs. 7 & 8a). The magnetic lineation of these rocks is steeply to moderately plunging either to the south or to the west parallel to the dip of magnetic foliation, which is consistent with passive rotation of both structural elements (Fig. 9a). The magnetic ellipsoids of these rocks show variable shapes and weak degree of anisotropy. The AMS fabric of migmatitic orthogneisses reveal magnetic foliations generally dipping to the SW bearing sub-horizontal magnetic lineation oriented in SSE direction, i.e., nearly parallel to the magnetic lineations of surrounding anatectic granites. The degree of anisotropy of migmatitic orthogneisses is generally low and associated with plane strain to prolate shapes of magnetic susceptibility ellipsoid (Figs. 7 & 8c).

In the external margin of the SOD (*c.* 50–80% of melt, Area B in Fig. 1b) the felsic orthogneiss is almost absent and migmatitic orthogneiss sheets alternate with leucogranites and granites and their magnetic foliations are almost uniformly dipping to the west. The magnetic lineation in felsic migmatite show mixed pattern characterized by lineation plunge to the west or to the SSW (Fig. 9). The granite and leucogranite veins in the external margin of the SOD show identical AMS parameters to those of interlayered migmatitic orthogneiss (Figs. 7 & 8c).

The NOD exhibits the most complex AMS fabric pattern in the studied area due to almost equal proportion of felsic and migmatitic orthogneisses and various types of granites (Fig. 5). The felsic and migmatitic orthogneisses show magnetic foliations dipping to the SW under shallow to moderate angles. Magnetic lineations are forming a broad maximum plunging under shallow angle to the SE (Fig. 8a). AMS fabrics of felsic orthogneiss show oblate ellipsoid and medium degree of magnetic anisotropy. In contrast migmatitic orthogneiss show plane strain to prolate shapes of ellipsoid of magnetic anisotropy and the degree of AMS slightly weaker compared to felsic orthogneiss (Fig. 8d). The AMS fabric patterns of granite and leucogranite veins developed in the NOD area may be subdivided into two main groups according to their orientations and dominant vein composition (Fig. 8d). The first group of leucogranite veins is represented by bundle of NW and SE dipping planes intersected in SW direction. These planes bear sub-horizontal E–W oriented magnetic lineation and show dominantly plane strain to oblate shapes of ellipsoid of magnetic susceptibility (Fig. 8c). The second group of biotite granite veins is characterized by two sets of sub-vertical magnetic foliations trending NW–SE and N–S, respectively (Fig. 8c). These foliations bear sub-horizontal magnetic lineations and exhibit mostly plane strain to weakly prolate shapes of ellipsoids of magnetic susceptibility.

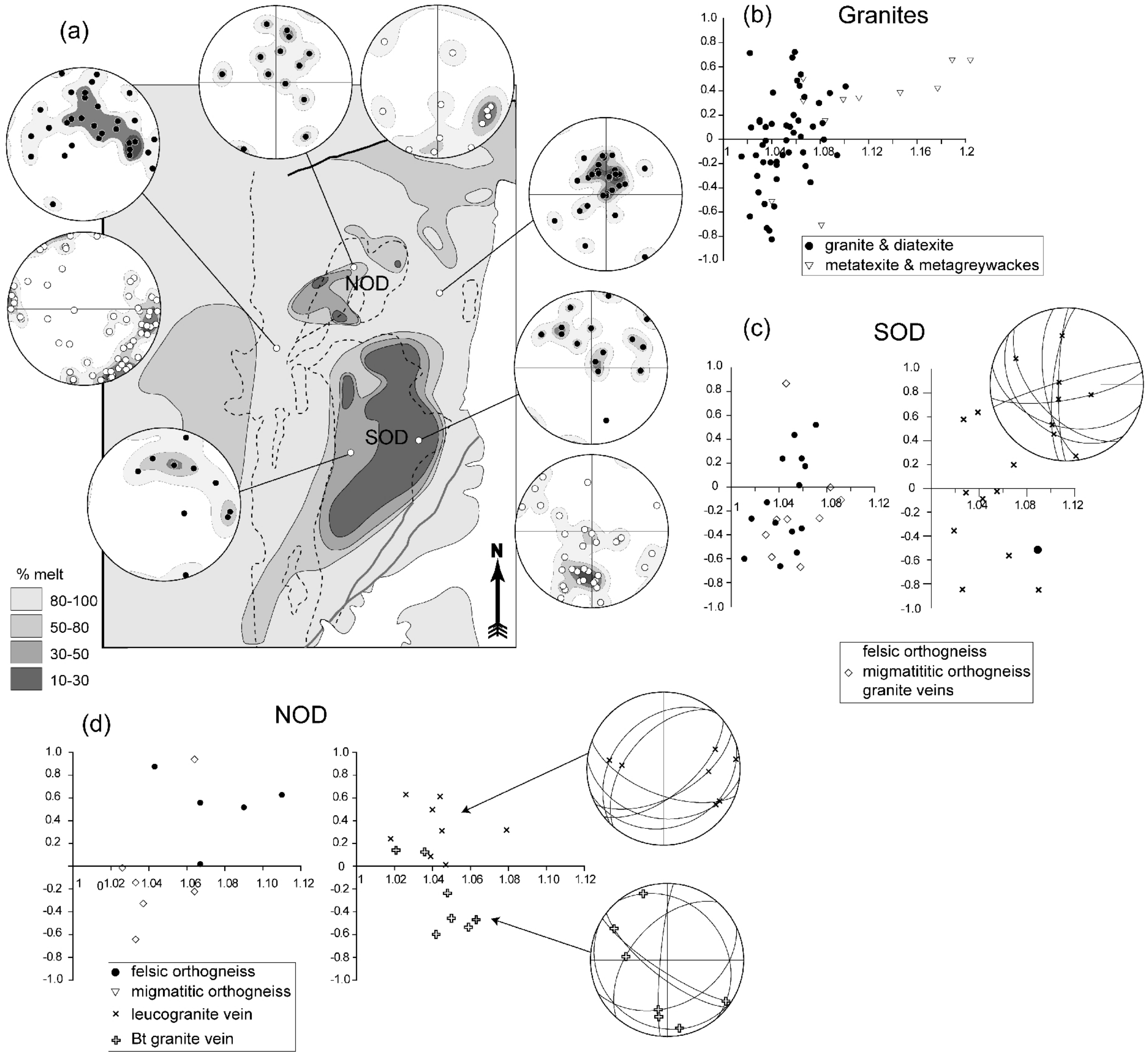


**Fig. 8:** *(a) Map of melt proportion and AMS fabric data for four both orthogneiss domains and surrounding metasedimentary migmatites. Pole diagrams of magnetic foliations (full circle) and lineations (open circle) are shown. Lower hemisphere projection, contoured at multiples of uniform distribution. (b) P–T diagrams constructed after Jelinek (e) Idem for the NOD. Left – data for felsic orthogneiss and migmatitic orthogneiss, right – data for leucogranite dykes and for granite dykes. (1981).*

## Discussion

The structural relations and AMS study of felsic and migmatitic orthogneisses, metasedimentary migmatites (meta- and diatexites) and anatectic granites allowed us to discuss the relations between relative melt proportion, deformation style and mechanical behaviour of solid state rock-melt system. Moreover, we are able to define the bulk flow parameters characterized by fabric in the anatectic granites and diatexites and study complex deformation pattern of orthogneiss bodies which are regarded as highly anisotropic inclusions surrounded by viscously flowing melt bearing migmatites. We examine the mechanical response of anisotropic rocks to external stress exerted by viscously flowing rocks which dramatically changes with increasing melt proportion. We also discuss the complexity of AMS fabrics in felsic orthogneiss as well as in migmatitic orthogneiss using numerical modelling approach and demonstrate that the variations in shape of fabric ellipsoid originate probably due to deformational overprints. This fabric evolution model is subsequently expanded to metasedimentary migmatites and we argue that large variety of AMS fabrics in partially molten rocks and in some intrusions may originate due to complex overprints.

### *Kinematic interpretation of AMS fabrics in metasedimentary migmatites and anatectic granites (homogeneous viscous flow)*

These rocks show high proportion of foliation parallel veins of granites as shown by 63–90% of granite samples used for AMS measurements drilled from these domains (Fig. 5). AMS fabrics measured in metatexites and metagraywackes show the same orientation of magnetic foliations and lineations as those determined in diatexites and anatectic granites. The degree of AMS and degree of oblatness decrease with increasing melt proportion from metagraywackes, metatexites to diatexites and anatectic granites and from east to the west (Fig. 10). The variations of AMS fabric and melt proportion could be explained by model of strain partitioning suggested for deformation of partially molten rocks by Vigneresse & Tikoff (1999). These authors suggest that when the melt escape threshold (Vigneresse *et al.*, 1996) is achieved and melt is segregated into coherent bands and the bulk strain tensor is split into coaxial part in restites and non-coaxial part in melt. In this model the degree of anisotropy of "weakly deformed" restites (metagraywackes boudins) should be lower than that of "strongly deformed" melt (diatexites and anatectic granites), which is not a case in studied area. Moreover, the metagraywacke boudins are strongly elongated in a direction parallel to granite lineation, which is not in agreement with oblate shapes of AMS ellipsoid in surrounding rocks (Fig. 10c). This incompatibility indicates that the structural and fabric histories of solid rocks, granite leucosomes and viscously flowing granite are more complicated than it would be predicted from simple strain partitioning model of Vigneresse & Tikoff (1999) or homogeneous and pervasive flow model proposed by e.g. Vanderhaeghe (1999).

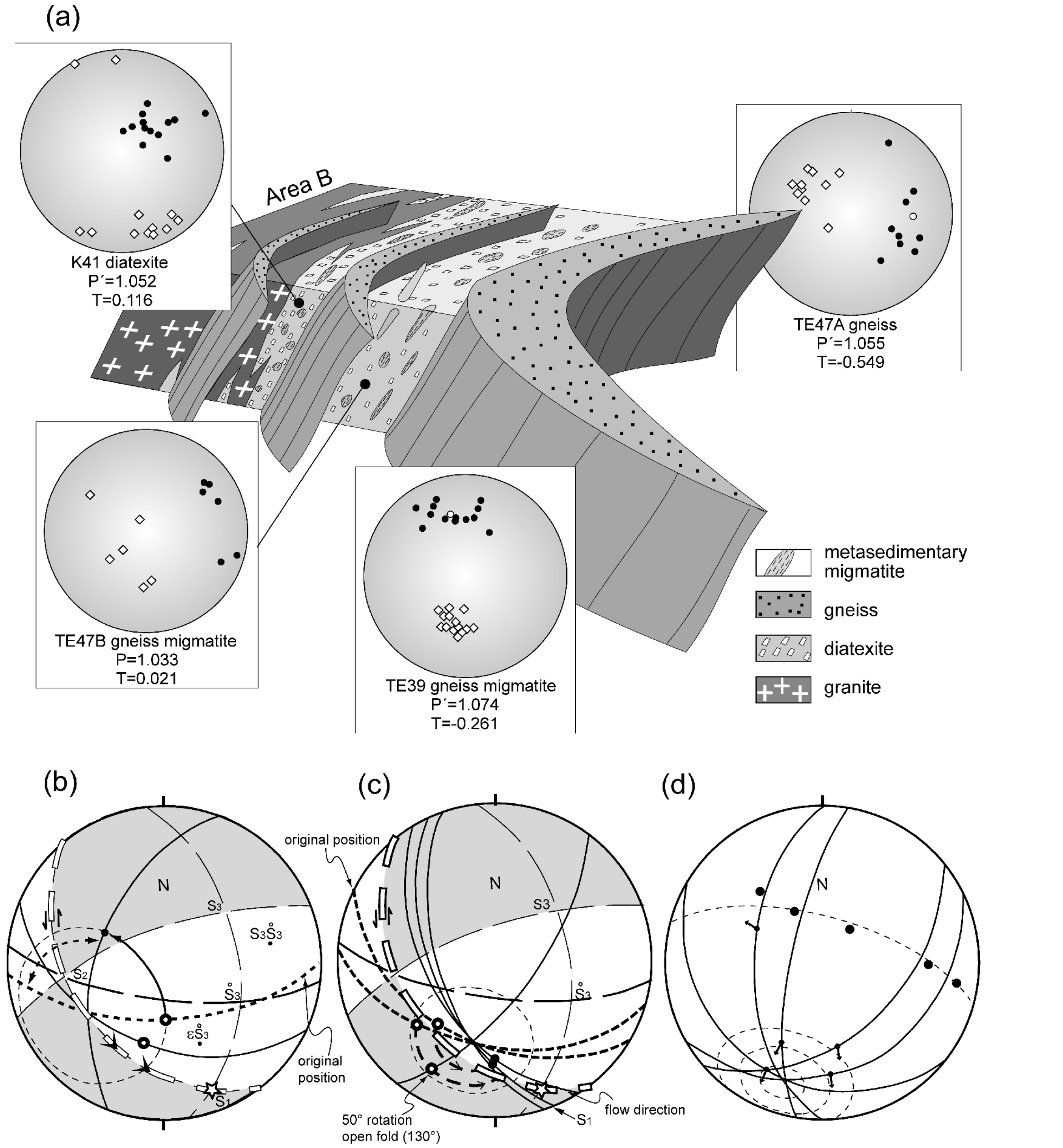


**Fig. 9:** *(a) The structural relationships between the solid state fabric of felsic orthogneiss migmatitic orthogneiss and between surrounding anatectic granite and diatexite along the transition from internal and external core margins of the SOD (area A). Pole diagrams of magnetic foliations and lineations show passive rotation of magnetic fabric within felsic orthogneiss and progressive reworking toward anatectic granite. (b) Stereogram showing the relationships of external migmatite flow framework and fabric within internal SOD core margin. The orientation of AMS average foliation from adjacent anatectic granites (white dashed line) and position of average AMS lineation of anatectic granites (white star) is shown. The diagram is separated into dark (extension) and white (compression) sectors of instantaneous strain for the dextral simple shear flow. Dashed line represents a $S_2$, $S_3$ plane of instantaneous deformation. Note that the original orientation of orthogneiss fabric (dotted thick curve) is located close to the instantaneous compression axis $S_3$. Two thin full curves indicate rotated limbs of large fold together with passively rotated lineations (open circle for original position and close circle for finite position). (c) Idem for external margin of the core of the SOD. Note that the rotated foliations are close to the main flow plane (white dashed curve) and that the fold axis (bundle intersection) rotates towards direction of regional stretching (white star). (d) Example of folded planes in the internal and external margin transition of the SOD core. Lower hemisphere equal area projections.*

The western and eastern domains of metasedimentary migmatites and anatectic granites can be considered as regions that accommodated the same deformation during the melt production and magma flow with increasing proportion of melt towards east. Statistics of AMS fabric data also show that from east to west the shape of AMS ellipsoid evolves from weakly oblate to plane strain or weakly prolate in conjunction with decrease in degree of anisotropy (Fig. 10a,b). Structural observations indicate that the major deformational regime was controlled by non-coaxial deformation with main elongation axis oriented in NNW-SSE direction and with flow plane gently to moderately dipping to the southwest. Kinematic observations suggest normal sense of movement component down to the SSE. Therefore, combination of AMS data with melt proportion estimates and constant orientation of AMS fabric of granites and diatexites indicate that fabric pattern east of orthogneiss bodies represent a stable kinematic framework in which the solid state rocks are deformed. This framework allows us to estimate orientations of instantaneous and finite stretching axes and principal stress directions for homogeneous simple shear flow. Assuming, that the average plane of finite strain ellipsoid is dipping under 30° to the SW and the $S_1$ direction is plunging 10° to the SE, the instantaneous and finite directions can be defined as shown in Figure 9b. Because the instantaneous strain axes are parallel to the axes of principal stress we can determine the orientation of $_1$ to be plunging 50° to east and $_3$ plunging 15° to the north. In case of combined simple and pure shear, the stress axes will rotate towards direction of principal axes of finite strain (Weiellmars, 1983). These assumptions allows defining the orientations of principal stress axes of stress tensor that will act on more rigid orthogneiss domains that are surrounded by flowing molten material.

### *The kinematic interpretation of orthogneiss AMS fabrics for low to intermediate melt proportions*

It was also shown that the amount of melt in the central part of the southern orthogneiss domain is low as documented by only 30% of drilled leucogranite samples (Fig. 5). Here, the magnetic foliations and lineations of orthogneiss samples are generally dipping to the S or SSW at medium to steep angles. The magnetic fabrics of leucogranites are either sub-parallel or dipping under shallower angles than those in surrounding orthogneiss. This indicates that the viscous flow in veins is often parallel or to lesser extent oblique with respect to walls represented by the main anisotropy of host orthogneiss. Orientation of leucogranite veins parallel to the orthogneiss anisotropy and AMS fabrics in granites and diatexites surrounding the SOD form mutual angle, that compatible with the orientation of tensile fractures for given orientations of principal stress axes ${}_1$ and ${}_3$ defined previously for external magma flow. Figure 10a shows, that theaxes are roughly parallel to internal anisotropy of large orthogneiss domain and therefore, we suggest that the veins cutting the central part of orthogneiss body originated by dilation of highly mechanically anisotropic orthogneiss. Because principal compressional stress direction was sub-parallel to mechanical anisotropy we suggest that the intrafolial dilation is due to layer parallel shortening similar to that described by Barraud *et al.* (2001; 2004).

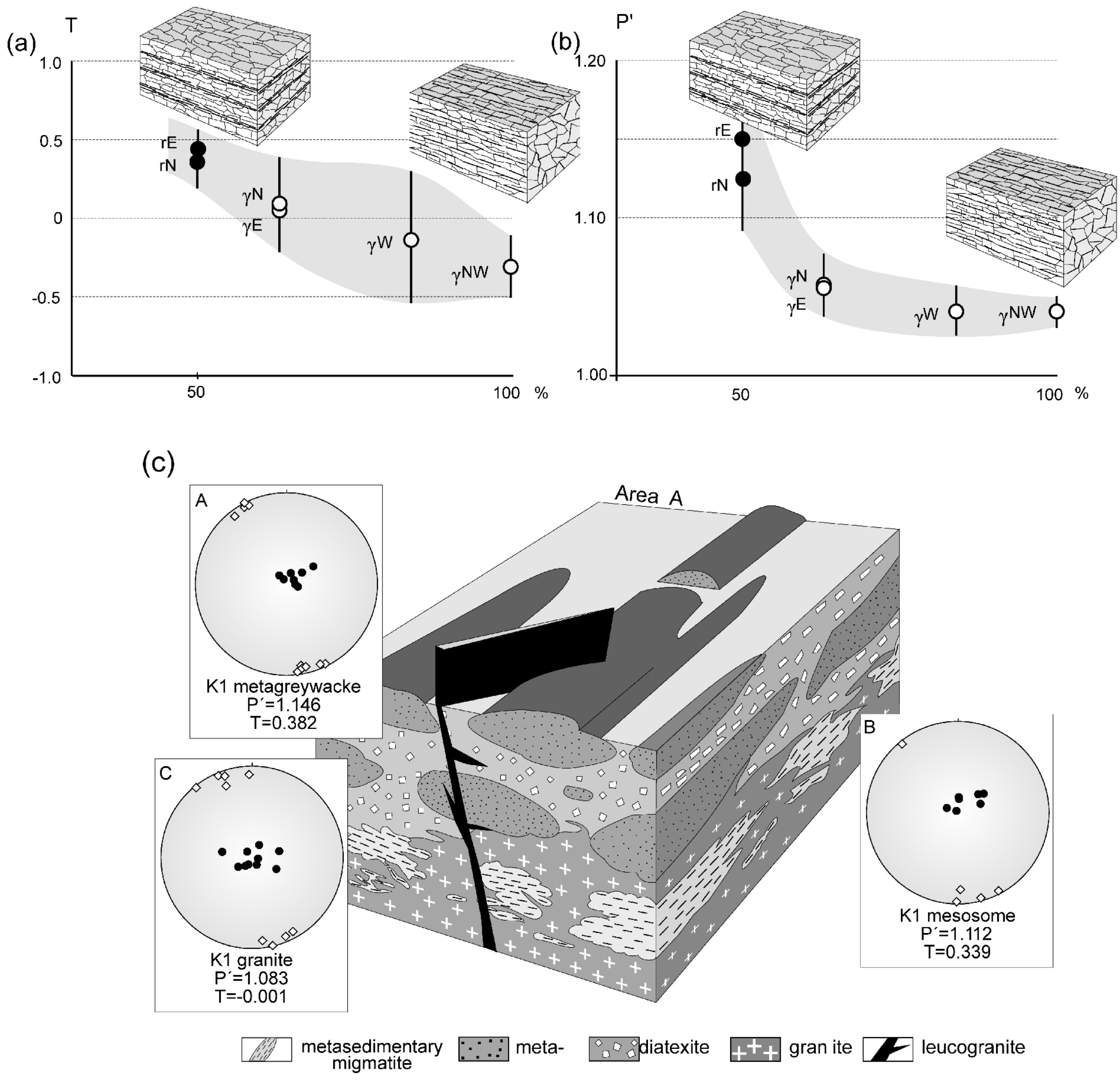


**Fig. 10:** *Relationship between the melt proportion and fabric elements in metasedimentary migmatites. (a) The upper left diagram shows the development of fabric symmetry expressed by T parameter for metatexites in the northeast and east and northwest and west of the studied area. (b) The upper right diagram shows the development of degree of anisotropy P´ with melt proportion from east to west. (c) The upper inset shows the three-dimensional relationship between melt proportion and AMS fabric of metagraywacke boudins, surrounding migmatites and anatectic granites (area A).*

Western and more intensely molten part of the SOD reveals higher amount of granitoids associated with highly variable orientations of felsic orthogneiss AMS fabrics. We argue, that AMS foliation and lineation patterns described above are compatible with rotations of gneissic fabric due to hundred metre scale buckling of originally E–W trending steep mechanical anisotropy. The intersections of AMS foliations in different parts of orthogneiss domain are plunging to the SSW or to the W under 40–50° and coincide with the orientations of hinges of large scale folds (Fig. 9a,b). The folding of orthogneiss foliation is easy to initiate because of highly favourable orientation of mechanical anisotropy with respect to $_1$ direction. Figure 10a,b shows orientation of this large scale fold with interlimb angle of 90° with axial plane parallel to the external $S_1S_3$ plane of magmatic flow. In the external margin of the SOD core the AMS pattern is modified (Fig. 9c). The AMS lineations are located along a small circle around fold hinge axis which indicates that the folding was governed by active amplification without any contribution of post-buckle flattening. (In the latter case the lineations on folded surfaces would be distributed along great circle; e.g. Twiss & Moores (1992, p. 318)). With ongoing deformation the folds become close to tight with interlimb angle of 30°, axial plane close to external granite flow plane and hinge close to the direction of regional stretching (Fig. 9c). The AMS lineations are still distributed along small circle suggesting dominant active buckling mechanisms up to very high strains. The shapes of ellipsoids of magnetic susceptibility are highly variable ranging from oblate to prolate. This kind of fabric distribution may reflect the strain variations in long and short limbs associated with shearing superimposed on gneissic fabric in more attenuated fold limbs.

The orientation of AMS fabric of migmatitic orthogneiss samples as well as the degree of anisotropy and shapes of magnetic ellipsoids entirely coincides with fabrics of surrounding granites (Fig. 8). At the same time these fabrics are discordant to folded surfaces of migmatitic gneisses. This particular orientation of AMS fabric of migmatitic orthogneisss is similar to orientation of axial plane leucosomes in meso-scale folds as shown e.g. by Vernon & Paterson (2001). The axial planar orientation of magnetic foliation and orientation of $K_1$ direction with respect to geometry of open and close folds (Fig. 9a, b) may imply that these fabrics represent domains of complete transposition of original orthogneiss fabrics in regional scale shear zones and disintegration of original gneissic anisotropy by either in-situ melting process or pervasive flow melt at grain scale (Hasalová *et al.*, 2008).

### *The kinematic interpretation of the orthogneiss AMS fabrics for high melt proportions*

The AMS fabric pattern of external margin of the SOD and the whole NOD shows coherent orientation of magnetic foliations of felsic orthogneiss and migmatitic orthogneisss with respect to the orientation of fabrics in surrounding granites. The main difference in between both types of rocks was found in shape of AMS ellipsoid which is of plane strain to oblate for felsic orthogneiss samples and plane strain to prolate for migmatitic orthogneiss. The other important feature is a single SE plunging maximum of magnetic lineations of orthogneiss samples sub-parallel to regional lineation in granites. However, the migmatitic orthogneiss samples show larger spread of magnetic lineations and show prominent SE–NW maximum and subordinate E–W lineations. We suggest that the felsic orthogneiss and migmatitic orthogneiss form a layered system with orientation of layering sub-parallel to the general flow direction of surrounding diatexites and granites. This interpretation is supported by presence of recumbent often rootless folds with sub-horizontal hinges (Fig. 2a) suggesting that the whole system represent isoclinally folded migmatite-gneiss multilayer system. The AMS lineation of felsic orthogneiss and in migmatitic orthogneiss as well as in mesoscopic fold hinges become almost parallel with linear fabric in surrounding granites due to passive rotation of fold hinges in viscous flow (Skjernaa, 1989). The E–W oriented AMS lineations in migmatitic orthogneiss can be explained by change in regional stretching direction from SE–NW to E–W typically developed in the northern part of the studied region.

The veins of leucogranites that are oriented at low angles to the main anisotropy of gneiss-migmatite multilayer are interpreted as conjugate normal kink-bands or extensional shears filled by granitic magma (Cosgrove, 1997). The orientations of magnetic lineations suggest that the extensional shears developed in the same kinematic framework as main foliation, i.e. vertical shortening and SE–NW extension. The general oblatness of AMS ellipsoid indicates combined pure and simple shear that operated during movement along shears and their filling by melt. In conclusion the geometrical relationship between leucogranite veins and fabric of felsic orthogneiss–migmatitic orthogneiss multilayer is fully compatible with model of shear band development during layer perpendicular shortening of highly anisotropic multilayer (Cosgrove, 1997; Kidan & Cosgrove, 1996).

The vertical veins filled by granites are interpreted as strike slip zones developed as hybrid fractures (transition between tensional and shear failure) filled with melt (Price & Cosgrove, 1990). The sharp angle between these fractures is bisected in NE–SW direction indicating horizontal compression direction that is perpendicular to vertical compression related to development of low angle extensional shears. In addition, the orientation of principal compressive stress is sub-parallel to the principal extension direction recorded in migmatites which is incompatible with shear failure theory. Therefore, we suggest that the late granite veins developed later and under different stress regime than earlier leucogranite vein array.

### *Role of mechanical anisotropy on rheology of partially molten crust*

This study shows that the proportion of melt directly controls the resistance and the degree of mechanical anisotropy of foliated rocks. The orthogneiss with low melt proportion deforms by layer parallel dilation when compressed parallel to mechanical anisotropy. This is in agreement with analogue model of Barraud *et al.*, (2001) who demonstrated that at low strain intensities the melt segregation is controlled by orientation of mechanical anisotropy perpendicular to the shortening which creates foliation parallel dilatant veins (Fig. 11). We note that the fluid (melt) pressure generated cohesion-less fracturing of orthogneiss is not only controlled by SSE orientation of  only but also by favourable pre-melting orientation of orthogneiss foliation.
However, for increased proportion of melt the anisotropic rock compressed parallel to layering significantly weakens and the melt-solid rock multilayer starts to buckle. The active amplification of large scale folds indicates high mechanical anisotropy and/or strong viscosity contrast between melt and rock (Fig. 11). At the same time, axial surface layers of partially molten rocks called here migmatitic orthogneiss develop approximately perpendicular to the direction of active contraction. Our microstructural and petrological study shown that within the migmatitic orthogneiss layers the biotite grains are corroded and resorbed and that the whole rocks show important resorptions of old feldspars and precipitation of new mineral phases. The topology of new feldspars and quartz indicate that these minerals crystallized from melt (Sawyer, 1999, 2000) and resorptions of biotite and feldspars indicate disequilibrium reaction with melt (Büsch *et al.*, 1974). The temperature of this event was higher than that of original orthogneiss origin, because of increase of $X_{Mg}$ and Ti content in biotite. Therefore, we suggest that zones of migmatitic orthogneiss indicate regions of important interaction of melt and host rock at increasing temperature – i.e. during regional anatectic event as suggested already by Rey *et al.* (1992). We suggest that these domains represent zones of active deformation associated with grain scale percolation of melt (Hasalová *et al.*, 2008). This corroborates well with the geometry of these zones which is fairly similar to axial planar leucosomes described by Vernon & Paterson (2001). This hypothesis is supported by disintegration of original biotite aggregates,

which became dispersed in the matrix. The deformation was probably accommodated by grain boundary sliding of feldspars which enhanced complete mixing and randomization biotites in the host rocks. However, to which extent the shape of deformation ellipsoid reflects the shape, of bulk deformation or result of strain superposition cannot be satisfactorily resolved using existing dataset.

Ongoing shortening and increase of melt proportion further weakens melt-solid rock

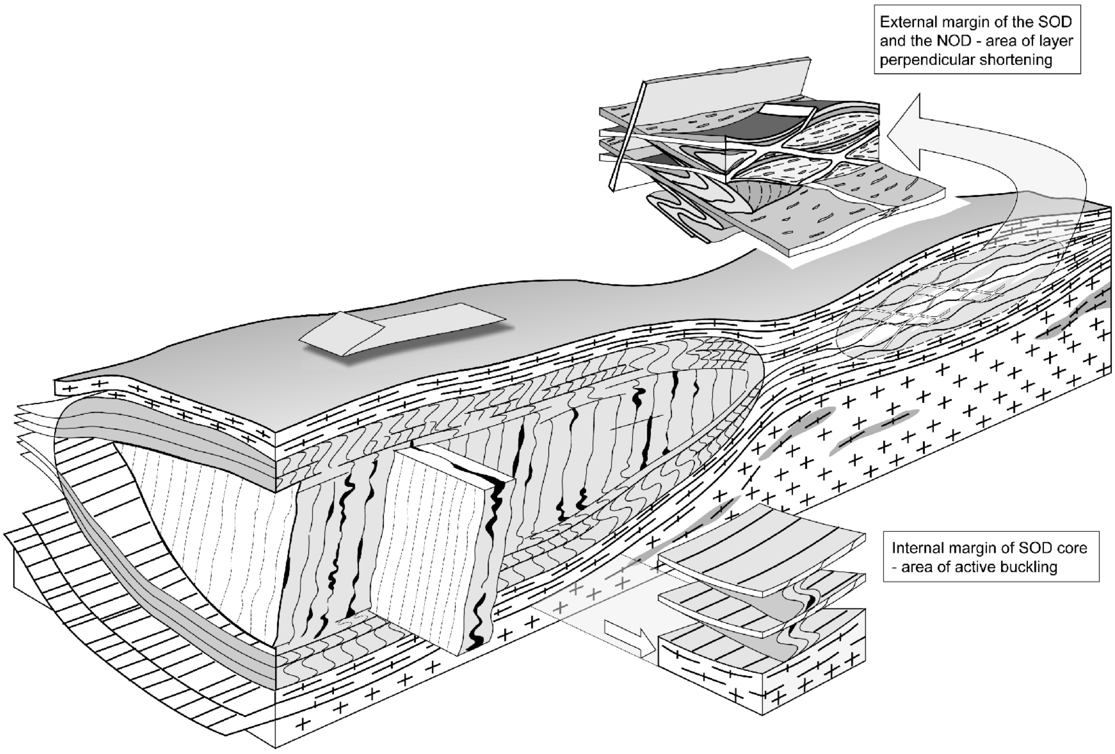


**Fig. 11:** *The schematic figure of deformation of anisotropic orthogneiss domain surrounded by metasedimentary migmatites and anatectic granites. The central domain suffers layer parallel dilation as result of superimposed $D_2$ deformation. The internal margin of the SOD suffers active buckling of orthogneiss/melt multilayer and the external margin of the SOD exhibit structures compatible with layer perpendicular shortening. The significantly deformed NOD with developed $S_2$ fabric and accompanied shear bands filled by leucogranites are shown in enlarged inset.*

multilayer which progressively developing main anisotropy perpendicular to the main shortening direction. Because of vertical principal compressive stress, the process of extension induces sub-horizontal planar anisotropy within the rock (Fig. 11). This is progressively more intense as the stretching increases thus enhancing already existent anisotropy in orthogneiss and mineral alignment in felsic orthogneiss. Important results of layer perpendicular shortening of layered rocks is development of the pinch and swell structures in the single layers and the conjugate normal kink-bands (extensional shears) in the matrix (Kidan & Cosgrove, 1996).

The implication of above described suite of structures indicate that partially molten orthogneiss contain units with highly different strengths - less competent migmatitic orthogneiss and granites and competent felsic orthogneiss, the rock has a high mechanical anisotropy and experiences bulk rheological changes during progressive deformation. We explain the mechanisms of layers of melt in planes perpendicular to direction of active contraction using model of Cosgrove (1997). According to this model, the general condition for fluid fracturing is that the fluid pressure is equal or greater than tensile strength of the rock normal to that plane ($T_n$) and the normal stress acting across it. In the well-laminated rock tensile strength normal to the foliation $T_n$ is lesser than that parallel to it $T_p$. In addition, in extensional settings the vertical stress $_v$ coincides with the maximum principal compression $_1$, while $_3$ coincides with $_h$ and is sub-horizontal. In our case, the condition for tensile failure $P_{fluid\ (melt)} > T_n + {}_v$ is easily satisfied indicating that the differential stress is less than difference between two tensile strength ( $_1$ - $_3$)<( $T_p$ - $T_n$). In this case the extensional fracture is formed parallel to foliation. We suggest that this is the mechanisms, by which the multilayer of felsic/migmatitic orthogneiss is forming i.e., parallel to the regional flow plane. In addition fracturing along the low angle normal extensional shears promotes movements of granitic melts through and out of the partially molten crust.

### *A numerical model of AMS development in migmatites*

Based on described structural history we suggested that in internal margin of SOD the felsic/migmatitic orthogneiss multilayer suffered large scale folding and AMS patterns confirmed active buckling mechanisms. This means that the internal fabric in rheologically stronger felsic orthogneiss layers was only passively rotated in short and long limbs of large scale folds. Consequently, the short limbs regions of large folds are likely to be affected by layer parallel shortening and dilating during $D_2$ deformation. In contrast the superposition of $D_2$ deformation on long limbs, which are entirely rotated into X–Y plane of $D_2$, causes continuous flattening.

The hypothesis of superposed deformation on fold-like pattern was testified by numerical simulation of AMS fabric development (Ježek & Hrouda, 2002). The magnetic mineralogy study shows that the magnetic carriers are dominantly biotite grains with highly oblate single grain AMS ellipsoid (Martín-Hernández & Hirt, 2003). Our modelling shown that development of overall prolate fabrics in felsic orthogneiss and migmatitic orthogneiss can results from either strongly constrictional flow or from nearly orthogonal superposition of deformation on existing mineral fabric (Fig. 12). To constrain the parameters controlling AMS fabrics developed by superposed deformation we used stochastic approach, where two perpendicular fabrics were defined by randomly varying symmetry of superposed strains from plane strain to oblate parameterized by symmetry index (SI) and randomly varying fabric intensity parameterized by time index (TI). The values of SI vary from 1 (plane strain in XZ plane) past 0.5 (fully oblate strain) to 0 (plane strain in YZ plane). The TI is relative finite strain varying from 0 to 1. The results of individual simulations were projected onto PT space (Jelínek, 1981) and from range of observed data (-0.7<T<0 and 1<P<1.1) the statistics of input parameters were depicted (Fig. 13). This model shows that symmetries and intensities found in orthogneiss and migmatitic orthogneiss can result from superposition of nearly perpendicular fabrics when 1) intensities of both fabric developments are similar and 2) symmetries of both fabrics are similar and 3) the X axes of both fabrics are sub-parallel. Consequently, the alternate development of prolate and oblate fabrics in felsic orthogneiss could results from superposition of $D_2$ deformation on short and long limbs of large folds.

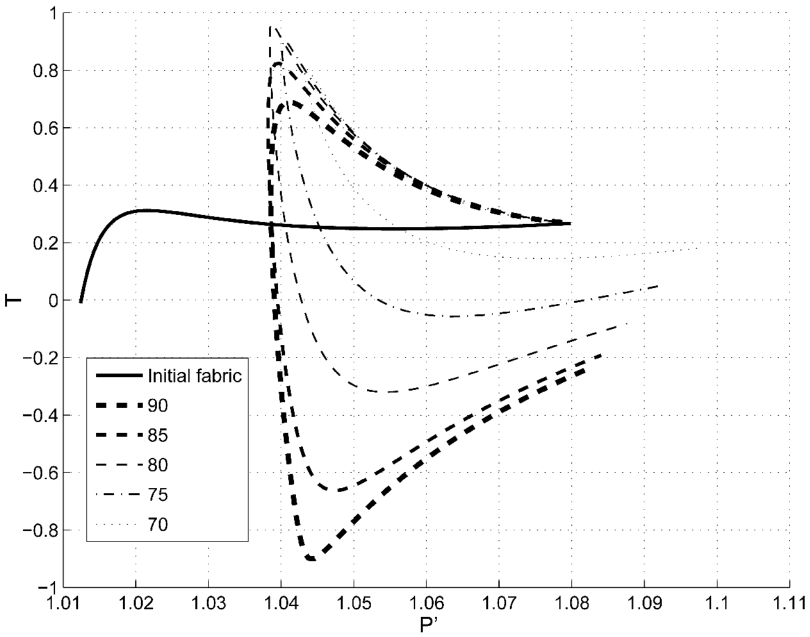


**Fig. 12:** *Evolution of P' and T parameters of superposed coaxial plain strain deformations with perpendicular stretching direction. The different trajectories are shown for different angles between shortening directions. The prolate symmetries are obtained for maximum 15° deviations from mutually perpendicular direction.*

## Conclusions

This study shows a complex deformational behaviour of solid state rocks and granitic melts in fertile region of magma segregation. The regions of metasedimentary metatexites and diatexites are akin to deform by homogeneous viscous flow. Rocks with low proportion of melts exhibit

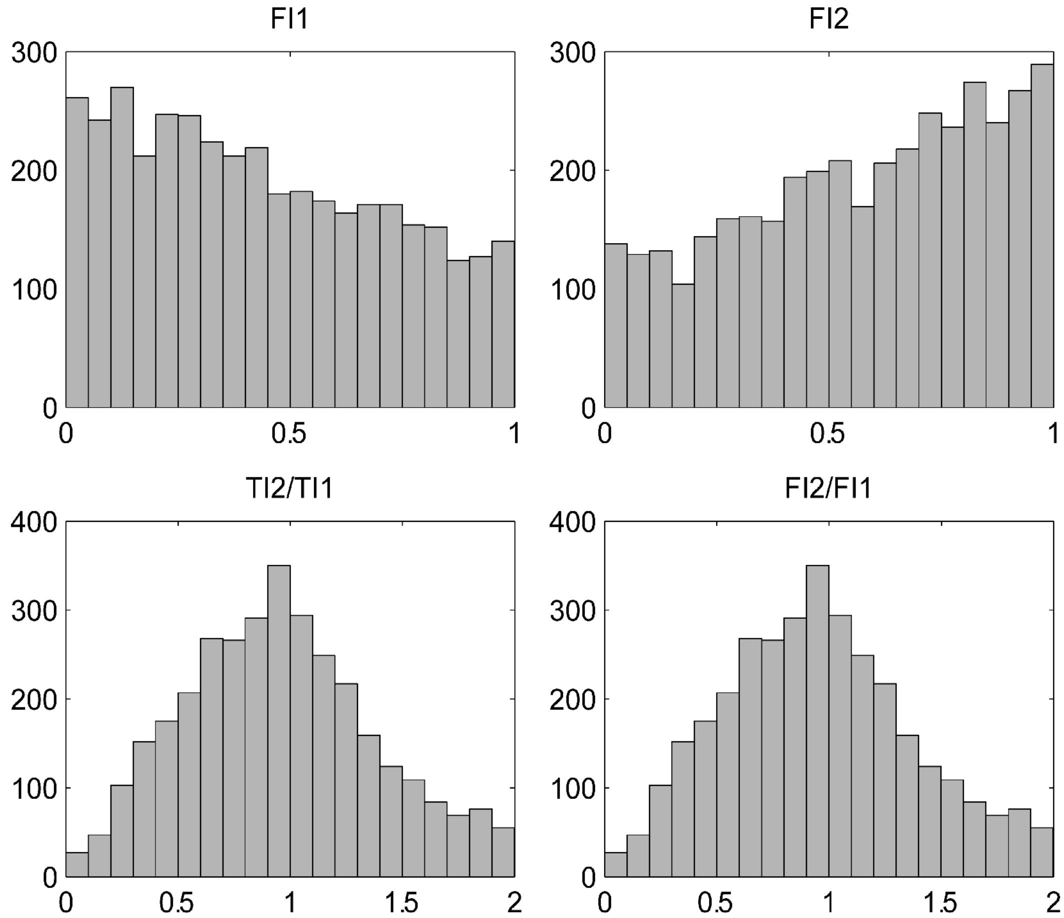


**Fig. 13:** *Four histograms of parameters of stochastic model resulting in prolate symmetries of superposed AMS fabric: FI1 – fabric index of original fabric (0 – plane strain, vertical lineation, 0.5 – oblate strain, 1 – plane strain, horizontal lineation), FI2 – fabric index of superposed deformation (0 – plane strain, horizontal lineation parallel to intersection with original fabric, 0.5 – oblate strain, 1 – plane strain, horizontal lineation, perpendicular to intersection with original fabric), TI1, TI2 – relative times of fabric development.*

high or variable degree of anisotropy associated with plane strain ellipsoid to oblate shapes. The surrounding leucosomes show plane strain ellipsoids shapes and weaker degree of anisotropy reflecting strain partitioning. In contrast, rocks with low ability to melt are behaving as rigid bodies, so that in regions with low amount of melts the magma is ascending along the main anisotropy in the form of sills. In our model the two orthogneiss domains are considered as two giant anisotropic inclusions immersed in homogeneously flowing viscous granites and diatexites reflecting regional flow related to regional transtensional deformation. Internal parts of orthogneiss domains preserve their original solid state fabrics as well as fabrics that are imposed by flow of surrounding partially molten rocks. It is important to understand when this deformation occurred. It is likely that the deformation of orthogneiss multilayer occurred when the surrounding system was not entirely molten and when the contractional stress was transmitted across the whole metasedimentary and orthogneiss domain. These stress transfer is responsible for initial layer parallel shortening which cause the homogeneous deformation, dilation and reorientation of magnetic minerals documented by development of prolate fabrics in both felsic and migmatitic orthogneisses. With ongoing shortenings and melting the rheological contrast to surrounding metasedimentary migmatites certainly increased and the orthogneiss domains become relatively rigid and almost undeformable by ongoing deformation.

Even if these conclusions are semi-quantitative in terms of the volume of liquids and fabric patterns, we can estimate the mechanical threshold when the rigid framework is still present and when it becomes disintegrated in viscous magma flow. Such mechanical threshold may be considered an indirect expression of rheological critical melt percentage or melt escape threshold, which is however, studied by magmatic petrologists only on grain scale. In order to quantify the influence of volume of magmatic liquid on mechanical threshold of disintegration of solid network in nature, more detailed fabric study of migmatitic terrains with significantly better outcrop quality is required. This may stimulate future research in making a bridge between experimental estimates of melt proportion vs. rock rheology and mechanical behaviour of rocks in molten crust in nature.

## Acknowledgements

This work was finantially supported by the CNRS and Université Louis Pasteur Strasbourg (UMR 7516-7517), the Ministry of Education of the Czech Republic ( No. MSM0021620855 to Josef Ježek) and the French National Grant Agency (No.06-1148784 to K. Schulmann). J. Ježek also benefited from an invited professorship at ULP, Strasbourg. Stays of Pavlína Hasalová at ULP were founded by the French Government Foundation (BGF).

## References

Barraud, J., Gardien, V., Allemand, P. & Grandjean, P., 2001. Analog modelling of melt segregation and migration during deformation. *Physics and Chemistry of the Earth (A)*, **26**, 317–323.

Barraud, J., Gardien, V., Allemand, P. & Grandjean, P., 2004. Analogue models of melt-flow networks in folding migmatites. *Journal of Structural Geology*, **26**, 307–324.

Berthé, D., Choukroune, P. & Jegouzo, P., 1979. Orthogneiss, mylonite and non coaxial deformation of granites; the example of South Armorican shear zone. *Journal of Structural Geology*, **1**, 31–42.

Blumenfeld, P. & Bouchez, J. L., 1988. Shear criteria in granite and migmatite deformed in the magmatic and solid states. *Journal of Structural Geology*, **10**, 361–372.

Boutin, R., Montigny, R. & Thuizat, R., 1995. Chronologie K–Ar et $^{39}Ar/^{40}Ar$ du métamorphisme et du magmatisme des Vosges. Comparaison avec les massifs varisques avoisinants et détermination de l'âge de la limite Vise´en inférieur - Viséen supérieur. *Géologie de la France*, **1**, 3–25.

Brown, M., 1994. The generation, segregation, ascent and emplacement of granite magma: the migmatite-to-crustally-derived granite connection in thickened orogens. *Earth-Science Reviews*, **36**, 83–130.

Brown, M., 2004. The mechanism of melt extraction from lower continental crust of orogens. *Transactions of the Royal Society of Edinburgh, Earth Sciences*, **95**, 35–48.

Brown, M., Averkin, Y. A., McLellan, E. L. & Sawyer, E. W., 1995. Melt segregation in migmatites. *Journal of Geophysical Research*, **100**, 15.655–15.679.

Brown, M., Friend, C. R. L., McGregor, V. R. & Perkins, W. T., 1981. The late archaean Qôrqut granite complex of southern West Greenland *Journal of Geophysical Research*, **86**, 10617–10632.

Brown, M. & Solar, G. S., 1998a. Granite ascent and emplacement during contractional deformation in convergent orogens. *Journal of Structural Geology*, **20**, 1365–1393.

Brown, M. & Solar, G. S., 1998b. Shear-zone systems and melts: Feedback relations and self-organization in orogenic belts. *Journal of Structural Geology*, **20**, 211–227.

Büsch, W., Schneider, G. & Mehnert, K. R., 1974. Initial melting at grain boundaries. Part II: Melting in rocks of granodioritic, quartz dioritic and tonalitic composition *Neues Jahrbuch Für Mineralogie Monatshefte*, **8**, 345–370.

Collins, W. J. & Sawyer, E. W., 1996. Pervasive granitoid magma transfer through the lower-middle crust during non-coaxial compressional deformation. *Journal of Metamorphic Geology*, **14**, 565–579.

Cosgrove, J. W., 1997. The influence of mechanical anisotropy on the behaviour of the lower crust. In: *Thermal and mechanical interactions in deep-seated rocks.* (ed Schulmann, K.) *Tectonophysics*, pp. 1–14, Elsevier, Amsterdam, Netherlands.

Ferré, E. C., Martin-Hernandez, F., Teyssier, C. & Jackson, M., 2004. Paramagnetic and ferromagnetic anisotropy of magnetic susceptibility in migmatites: Measurements in high and low fields and kinematic implications. *Geophysical Journal International*, **157**, 1119–1129.

Ferré, E. C., Teyssier, C., Jackson, M., Thill, J. W. & Rainey, E. S. G., 2003. Magnetic susceptibility anisotropy: A new petrofabric tool in migmatites. *Journal of Geophysical Research,* **108**, EPM 5–1 – 5–14.

Fluck, P., 1980. Métamorphisme et magmatisme dans les Vosges moyennes d'Alsace. Contribution a l'histoire de la chaine Varisque. *Mémoires des Sciences Géologiques*, **62**, 248.

Harrison, T. M., Duncan, I. & McDougall, I., 1985. Diffusion of $^{40}$Ar in biotite; temperature, pressure and compositional effects. *Geochimica et Cosmochimica Acta*, **49**, 2461–2468.

Hasalová, P., Schulmann, K., Lexa, O., Štípská, P., Hrouda, F., Ulrich, S., Haloda, J., Týcová, P., 2008. Origin of migmatites by deformation enhanced melt infiltration of orthogneiss: a new model based on quantitative microstructural analysis. *Journal of Metamorphic Geology*.

Hrouda, F., Jelínek, V. & Hrušková, L., 1990. A package of programs for statistical evaluation of magnetic anisotropy data using IBM-PC computers. *EOS, Transactions, American Geophysical Union*, **71**, 1289.

Jelínek, V., 1978. Statistical processing of anisotropy of magnetic susceptibility measured on groups of specimens. *Studia geophysica et geodaetica*, **22**, 50–62.

Jelínek, V., 1981. Characterisation of the magnetic fabric of rocks. *Tectonophysics*, **79**, 63–67.

Ježek, J. & Hrouda, F., 2002. Software for modeling the magnetic anisotropy of strained rocks. *Computers & Geosciences*, **28**, 1061–1068.

Kenah, P. & Hollister, L. S., 1983. Anatexis in the Central Gneiss Complex, British Columbia. In: *Migmatites, Melting and Metamorphism* (eds Atherton, M. P. & Gribble, C. D.), pp. 142–162, Cheshire, Shiva.

Kidan, T. W. & Cosgrove, J. W., 1996. The deformation of multilayers by layer - normal compression; an experimental investigation. *Journal of Structural Geology*, **18**, 461–474.

Kratinová, Z., Schulmann, K., Edel, J. B., Ježek, J. & Schaltegger, U., 2007. Multiple magmatic fabrics in episodically emplaced magma batches in transtensional setting: tectonic model based on AMS study and numerical modelling. *Tectonics*.

Latouche, L., Fabries, J. & Guiraud, M., 1992. Retrograde evolution in the Central Vosges mountains (north-eastern France): implications for the metamorphic history of high-grade rocks during the Variscan orogeny. *Tectonophysics*, **205**, 387–407.

Lucas, S. B. & St-Onge, M. R., 1995. Syn-tectonic magmatism and the development of compositional layering, Ungava Orogen (northern Quebec, Canada). *Journal of Structural Geology*, **17**, 475–491.

Marchildon, N. & Brown, M., 2003. Spatial distribution of melt-bearing structures in anatectic rocks from Southern Brittany, France: implications for melt transfer at grain- to orogen-scale. *Tectonophysics*, **364**, 215–235.

Martín-Hernández, F. & Hirt, A. M., 2003. Paramagnetic anisotropy of magnetic susceptibility in biotite, muscovite and chlorite single crystals. *Tectonophysics*, **367**, 13–28.

McLellan, E. L., 1983. Contrasting textures in metamorphic and anatectic migmatites - an example from the Scottish Caledonides. . *Journal of Metamorphic Geology*, **1**, 241–262.

Mehnert, K. R., 1971. *Migmatites and the Origin of Granitic Rocks* Elsevier, Amsterdam.

Mehnert, K. R., Büsch, W. & Schneider, G., 1973. Initial melting at grain boundary of quartz and feldspar in gneisses and granulites. *Neues Jahrbuch Für Mineralogie Monatshefte*, **4**, 165–183.

Parma, J., 1988. An automated torque meter for rapid measurement of high-field magnetic anisotropy of rocks. *Physics of The Earth and Planetary Interiors*, **51**, 387–389.

Price, M. J. & Cosgrove, J. W., 1990. *Analysis of Geological Structures*. Cambridge University Press, Cambridge.

Rey, P., Burg, J.-P. & Caron, J.-M., 1992. Middle and late Carboniferous extension in the Variscan Belt: structural and petrological evidences from Vosges Massif (Eastern France). *Geodinamica Acta*, **5**, 17–36.

Rey, P., Burg, J.-P., Lardeaux, J. M. & Fluck, P., 1989. Evolutions métamorphiques contrastées dans les Vosges orientales: témoins d'un charriage dans la chaine varisque *Comptes Rendus de Académie des Sciences Français*, **309**, 815–821.

Rosenberg, C. L., 2001. Deformation of partially molten granite: A review and comparison of experimental and natural case studies. *International Journal of Earth Sciences*, **90**(1), 60–76.

Rosenberg, C. L. & Handy, M. R., 2001. Mechanisms and orientation of melt segregation paths during pure shearing of a partially molten rock analog (norcamphor-benzamide). *Journal of Structural Geology*, **23**, 1917–1932.

Sawyer, E. W., 1999. Criteria for the recognition of partial melting. *Physics and Chemistry of the Earth*, **24**, 269–279.

Sawyer, E. W., 2000. Grain-scale and outcrop-scale distribution and movement of melt in a crystallising granite. *Transactions for the Royal Society of Edinburgh: Earth Sciences*, **91**, 73–85.

Schaltegger, U., Fanning, C. M., Günther, D., Maurin, J. C., Schulmann, K. & Gebauer, D., 1999. Growth, annealing and recrystallization of zircon and preservation of monazite in high-grade metamorphism: conventional and in situ U–Pb isotope, cathodoluminiscence and microchemical evidence. *Contributions to Mineralogy and Petrology*, **134**, 186–201.

Schulmann, K., Schaltegger, U., Ježek, J., Thompson, A. B. & Edel, J. B., 2002. Rapid burial and exhumation during orogeny: Thickening and synconvergent exhumation of thermally weakened and thinned crust (Variscan orogen in Western Europe). *American Journal of Science*, **302**, 856–879.

Skjernaa, L., 1989. Tubular folds and sheath folds: definitions and conceptual models for their development, with examples from the Grapesvare area, northern Sweden. *Journal of Structural Geology*, **11**, 689–703.

Twiss, R. J. & Moores, E. M., 1992. *Structural Geology*. W.H.Freeman & Co Ltd, New York.

Vanderhaeghe, O., 1999. Pervasive melt migration from migmatites to leucogranite in the Shuswap metamorphic core complex, Canada: control of regional deformation. *Tectonophysics*, **312**, 35–55.

Vanderhaeghe, O., 2001. Melt segregation, pervasive melt migration and magma mobility in the continental crust: The structural record from pores to orogens. *Physics and Chemistry of the Earth,* **26**, 213–223.

Vernon, R. H., 1986. K-feldspar megacrysts in granites-phenocrysts, not porphyroblasts. *Earth-Science Reviews*, **23**, 1–63.

Vernon, R. H. & Paterson, S. R., 2001. Axial-surface leucosomes in anatectic migmatites. *Tectonophysics*, **335**, 183–192.

Vigneresse, J. L., Barbey, P. & Cuney, M., 1996. Rheological transitions during partial melting and crystalization with application to felsic magma segregation and transfer. *Journal of Petrology*, **37**, 1579–1600.

Vigneresse, J. L. & Tikoff, B., 1999. Strain partitioning during partial melting and crystallizing felsic magmas. *Tectonophysics*, **312**, 117–132.

Weinberg, R. F. & Searle, M. P., 1998. The Pangong injection complex, Indian Karakoram: a case of pervasive granite flow through hot viscous crust. *Journal of the Geological Society*, **155**, 883–891.

Wickert, F. & Eisbacher, H., 1988. Two-sided Variscan thrust tectonics in the Vosges Mountains, north-eastern France. *Geodinamica Acta*, **2**, 101–120.

Wickham, S. M., 1987. The segregation and emplacement of granitic magmas. *Journal of Geological Society*, **144**, 281–297.

# General conclusions

The results of the thesis are presented in four manuscripts that concerns on origin of migmatitic rocks and melt transport in the crust. Based on these studies, the following points should be emphasized to conclude the research.

To understand better the melt transport in the crust and origin of migmatitic rocks field observations has to be combined with detail microstructural study. Modern quantitative microstructural analysis may provide important information about reorganization of the rock structure associated with melt migration in terms of grain contact distributions, characterization of dynamic or static conditions of melt movement through rocks using analysis of grain boundaries and shape orientations and cooling or heating histories of rocks using crystal size distribution theory. Additionally, petrological and geochemical data provide important information about P–*T* conditions and allow estimation of composition, amount and bahaviour of melt involved in the process.

For an origin of migmatitic rocks new model of '*melt infiltration'* was introduced. In this model melt from an external source passes pervasively along grain boundaries through the whole rock volume and changes macroscopic and microscopic appearance of the rock. This process is characterized by resorption of old phases, nucleation of new phases along grain boundaries and modification of mineral and whole-rock compositions. It is suggested that the individual migmatite types represent different degrees of equilibration between the host rock and migrating melt. All these processes occur along a retrograde path during exhumation of the Gföhl Unit.

The melt infiltration was modeled using thermodynamic and geochemical data as an open-system process characterised by changes of the total mass/volume, accompanied by gains/losses in many of the major- and trace-elements. The numerical modelling of the mass balance resulted in identification of a component added by a heterogeneous nucleation of feldspars, quartz and apatite from the passing melt.

The infiltrating melt may have been lost from similar protoliths at any point on the *P–T* path, moving up through the rock pile, or it can be of foreign derivation, for example from granulitic migmatites outside the Gföhl orthogneiss migmatite body.

The infiltration occurs during exhumation, corresponding to the implied decreasing equilibration *P–T* conditions from 790°C and 8.5–6 kbar, to 690°C and 5–4 kbar.

For large-scale melt movement '*pervasive melt flow*' was proposed. In this model melt migrates penetratively along grain boundaries and does not require formation of channelized pathways. Although our data seem to be consistent with such a model, there is still a number of issues to be resolved. A key problem is the expected involvement of small volumes of penetrating acid melts, which should theoretically have high viscosities. The process of reactive porous flow is very slow even for mantle-derived melts (tens to hundreds centimetres per year) and is likely to be even more so in the crust. This would make the system vulnerable to freezing, and subsequently render the long-distance melt percolation impossible.

Generally, the melt infiltration and pervasive melt flow in the crust has profound consequence for the petrogenesis of migmatites in high-grade metamorphic terrains, would strongly influence the rheology of large crustal domains with potential consequences for deformation mechanism in collisional orogens and would have profound implications for chemical development of large crustal segments overlaying anatectic regions and the melt transport therein.

An attempt to estimate the mechanical threshold when the rigid framework is still present and when it becomes disintegrated in viscous magma flow was made. This can make a bridge between experimental estimates of melt proportion vs. rock rheology and mechanical behaviour of rocks in molten crust in nature.

# Résumé de la these en français

Cette these de doctorat présente les résultats d'études détaillées de terrain, microstructures, pétrologie et géochimie, effectuées sur une large terrane migmatitique d'âge Varisque: l'unité Gföhl de la zone Moldanubienne, du massif de Bohęme (République Tcheque). Les données obtenues par cette approche multi-disciplinaires ont été utilisé pour contraindre l'origine des roches migmatitiques, ainsi que permettre une meilleure compréhension du transport de produits fondus dans la croűte. Cependant les résultats de cette these sont aussi discuté comme mécanismes pour tout terrain migmatitique.

Un nouveau modele est proposé pour l'infiltration des produits fondus, a partir d'une source externe, pour expliquer (1) les variations dans l'apparence des migmatites et (2) le modele 'reactive porous melt flow' par le mouvement de produits fondus dans la croűte.

Le complexe migmatitique-gneissique de Gföhl forme l'unité anatectique la plus large de la racine orogénique Varisque. Il est situé a la bordure est du massif de Bohęme et est constitué d'orthogneiss de haut grade indiquant différents degrés de migmatisation, ainsi que dec corps granulitiques mineurs, des péridotites et amphibolites. L'unité Gföhl présente l'opportunité exceptionnelle d'étudier l'origine des roches migmatitiques, du fait qu'il offre la possibilité d'observer directement *in-situ*, sur le terrain, les relations spatiales et structurales entre les migmatites et leurs protoliths granitiques. De plus ces migmatites montrent différentes proportions de produits fondus. Cela engendre la possibilité d'étudier les changements graduels dans l'apparence microscopique des roches mais aussi les changements de microstructures et proportions modales des minéraux.

Basés sur l'étude détaillée de terrain et l'étude microstructutrale **(chapitre 1)**, 4 types de migmatites sont décrits dans la région du Gföhl:

(i) *Des orthogneiss rubanés (Type I)* présentant des couches mono minérales de plagioclase, K-feldspath et quartz recristallisé d'une part, distinctement séparées, des couches de biotites.

(ii) *Les migmatites stromatitiques (Type II)* composées d'agrégats de plagioclase te K-feldspath ainsi que parfois de quartz, et d'agrégats irréguliers de quartz. Les limites entre chaque agrégat sont mal définies et plutôt diffuses.

(iii) *Des migmatites schlieren (Type III)* qui montrent des domaines distinctement enrichis en plagioclase-quartz et une foliation définie seulement par l'orientation préférentielle des biotites et sillimanites, dispersés dans la roche.

(iv) *Des migmatites nébulitiques* isotropiques *(Type IV).*

Cette thése montre que ces roches appartiennent a une séquence continue, en partant des orthogneiss rubanés jusqu'aux migmatites nébulitiques par un processus de déformation en présence de produits fondus. Les orthogneiss et migmatites nébulitiques formeraient ainsi, les extrémités d'une évolution graduelle. Les orthogneiss rubanés ($S_1$ représenté par les différentes couches minéralogiques) sont transposés lors de la déformation $D_2$ en migmatites stromatitiques qui contiennent des reliques des othogneiss rubanés et de la foliation $S_1$. Les migmatites stromatitiques sont transformées graduellement, en migmatites isotropiques Schlieren, alternant avec les corps allongés de migmatites nébulitiques.

La destruction de la structure rubanée des orthogneiss, ainsi que le développement progressif des migmatites nébulitiques sont caractérisées par des changements systématiques de texture. Une étude des textures de ces roches a été réalisé pour permettre de quantifier ces changements. Cette étude a inclue une analyse de la taille des grains, une analyse de la distribution de la taille des cristaux (CSD) ainsi qu'une analyse de l'orientation et la forme de la limites des grains. Cette quantification a été réalisé par l'intermédiaire de l'utilisation de l'extension PolyLX du logiciel GIS ArcView, ainsi que de l'utilitaire PolyLX sous MATLAB. Toutes les phases principales ont été étudié (Pl, Kfs, Qtz and Bt), et ceci de façon systématique a travers toute la séquence. Les statistiques sur la taille des grains montrent une croissance continuelle de la taille des grains associée a une décroissance de la déviation standard, ceci pour une évolution des orthogneiss rubanés jusqu'aux migmatites nébulitiques. Les courbes de la distribution de la taille des grains (CSD) indiquent systématiquement une augmentation du taux de nucléation et une diminution du taux de croissance pour toutes les phases felsiques, en considérant une évolution des othogneiss rubanés aux migmatites nébulitiques. Les nouvelles phases nucléent préférentiellement le long des limites de grains a haute énergie, imposant une distribution réguliere des phases individuelles. En mẹme temps, les proportions modales des phases felsiques évoluent vers une composition 'minimum granitique'. Cette tendance est accompagnée d'une décroissance de l'orientation préférentielle de la forme des grains (SPO) pour toutes les phases felsiques.

Tous ces changements précédemment mentionnés, sont en accord avec un model de nucléation progressive et hétérogene des plagiclases, K-felspaths et Quartz, a partir de produits fondus, associé a une résorption des phases originelles.

Pour expliquer ces changements observés macroscopiquement, mais aussi en composition, un nouveau modele d'infiltration de produits fondus a été développé. Il implique une infiltration de matériel a partir d'une source externe, ou ce matériel se déplace le long des limites de grains, a travers l'ensemble du volume des roches, changeant ainsi l'apparence macroscopique et microscopique des roches.

La quantité de produits fondus et sa connectivité sont des parametres critiques qui contrôlent la mobilité des fondus, ainsi que le comportement rhéologique des roches semi-fondues. Pour contraindre ces parametres les méthodes d'anisotropie de susceptibilité magnétique (AMS) et EBSD ont été utilisé sur les roches du Gföhl.

La topologie des produits fondus dans les orthogneiss rubanés, Type I exhibe des poches de matériel fondu, qui sont allongées et sont orientées a un angle important avec les rubans, indiquant que la distribution de ce matériel fondu était contrôlée par la déformation du solide. Dans ce cas, les microstructures montrent des structures compatibles avec des mécanismes de déformation combinat 'dislocation creep' et 'grain boundary sliding'. Les types II a IV ont été développé par 'granular flow' accompagné par une diffusion accrue par la présence de matériel fondu ou/et par la flux direct de matériel fondu. Cependant la quantité de produits fondus présent, durant la déformation, n'a jamais surpassé la limite critique pour permettre la rotation libre des grains de biotite.

Le **chapitre 2** présente une discussion sur les aspects pétrologiques de la transition des orthogneiss rubanés aux migmatites nébulitiques. Le but de cette étude est de comprendre quelle sorte de fluide aurait pu participer a l'évolution de la minéralogie et géochimie de la roche, quelle aurait pu ętre sa composition et comment il a pu interagir avec la roche originelle.

L'assemblage de la séquence étudiée est Grenat –Biotite–Sillimanite– K-feldspath–Plagiclase–Quartz. Aucune muscovite est présente ce qui indique que le fluide impliqué est de composition granitique. Les compositions minéralogiques montrent des changements systématiques avec l'augmentation du degré de désintégration (augmentation de $X_{Fe}$ dans les grenats et biotites, diminution de Ca dans les plagioclases). Ceci est compatible avec une diminution de la température et pression d'équilibration de 790–850°C a 7.5 kbar pour les orthogneiss rubanés a 690–770°C a 4.5 kbar pour les migmatites nébulitiques (modélisation THERMOCALC). Les changements observés dans les analyses de roches completes, indiquent le comportement d'un systeme ouvert, interprété comme le résultat de la percolation de produits fondus le long de la limite de grains. Pour permettre un changement significatif de composition, le passage d'une quantité importante de produits fondus a dű ętre nécessaire.

La disparition des structures dans les diatexites sont décrites dans la majorité de la littérature, comme le résultat de la production *in-situ* d'une grande quantité de produits fondus. Dans le cas de cette étude, des arguments sont présentés, supportant l'idée que le 'reactive porous melt flow' a été responsable de la formation de ces migmatites. De plus, les calculs des trajets P, T ont montré que les produits fondus infiltrés, ont été équilibré avec la roche lors de la partie rétrograde du trajet P, T, c'est a dire pendant l'exhumation, a partir de la croűte inférieure, du complexe gneissique de Gföhl.

La section géochimique de cette these **(chapitre 3)** décrit les variations géochimiques des analyses des éléments majeurs, de trace et les isotopes Sr–Nd effectuées sur la roche complete. Alors que tous les types montrent une empreinte géochimique et isotopique distincte, l'analyse de la séquence complete montre une évolution le long d'une tendance plus ou moins réguliere pour la plupart des éléments. Cette évolution est en accord avec le modele proposé d'infiltration de produits fondus, dans lequel les othogneiss rubanés sont infiltrés par du matériel fondu felsique dérivé d'une source externe. L'infiltration a été modelisé comme un processus ouvert, caractérisé par des changements de masse/volume, et accompagné par des pertes/gains en éléments majeurs et traces. La modélisation numérique de la balance massique a permis désertification d'un composant additionné par la nucléation hétérogene des K-felspaths, quartz et Apatites, a partir du passage du matériel fondu. Aux stages plus avancés, les variations chimiques dans les migmatites Schlieren et nébulitiques requiarent le rôle croissant de la cristallisation fractionnée de K-feldspath et plagioclases, et en quantité moindre de la monazite riche en Th et apatite.

L'ensemble de ces informations démontrent que la séquence des types gneiss/migmatites de l'unité du Gföhl peut etre interprété par un processus dans lequel les orthogneiss rubanés ont été infiltré par du matériel fondu felsique dérivé d'une source externe. Un tel processus, impliquant un large volume de produits fondus, qui a l'échelle microscopique ne montrent aucun signe de ségrégation ou channelisation majeur, pourrait ętre un mécanisme important de transport de produits fondus dans la croűte. Dans le cas de cette étude, l'unité Gföhl représente une portion significative de la racine orogénique. La démonstration de ce processus d'infiltration présent a l'échelle du massif entier montre que ce processus pourrait ętre crucial dans le cadre de la différenciation crustale, mais aussi pourrait gouverner la rhéologie de la pile crustale lors d'événements orogéniques.

Le dernier chapitre **(chapitre 4)** présente des données et analyses additionnelles qui ont été effectue dans la cadre d'une étude sur les Monts Vosgiens, qui consistait en une étude des textures et pétrologique des migmatites des Vosges. Cette étude a montré un comportement complexe des roches a l'état solide et fondues. Il a été démontré que le flux visqueux est fortement dépendant de la lithologie de la roche, c'est a dire des propriétés mécaniques des roches durant leur fusion, ainsi que leur anisotropie pre-fusion. Les diatexites et granites montrent un degré faible d'anisotropie, des formes d'ellipsoďdes tres variables, ce qui pourrait refléter la rotation libre des biotites dans les matériel fondu. Au contraire les roches montrant une forte pre-fusion anisotropie et faible habilité de fusion se comportent comme des corps rigides. Leur comportement dépend aussi de la quantité de liquide granitique. En effet dans les régions a forte quantité de liquide, leur comportement est rigide et les corps rigides tournent pour se placer dans la direction du flux. Par contre dans les domaines ou une faible quantité de liquide était présente, le matériel fondu se déplace le long des anisotropies majeures, sous la forme de sills. Il est donc possible de faire une corrélation entre la proportion de matériel fondu et les réseaux AMS. Une faible proportion de liquide est caractérisé par la préservation de la fabrique homogene AMS. Dans le cas d'une forte proportion de liquide la fabrique pre-fusion est détruite et les éléments se réorientent progressivement dans la direction du flux de liquide.

# List of figures

## Chapter 1:



## Chapter 2:

## Chapter 3:



## Chapter 4:

# List of tables

## Chapter 1:



## Chapter 2:



## Chapter 3: